Integrating silicon carbide spintronics quantum systems

Von der Fakultät 8 Mathematik und Physik der Universität Stuttgart
zur Erlangung der Würde eines Doktors der Naturwissenschaften
(Dr. rer. nat.) genehmigte Abhandlung

Vorgelegt von

Charles Babin

aus Chambray-lès-Tours

Hauptberichter:	Prof. Dr. Jörg Wrachtrup
Mitberichter:	Prof. Dr. Tilman Pfau
Tag der mündlichen Prüfung:	28.03.2022

3. Physikalisches Institut
Universität Stuttgart
2022

À toi Clémence, pour ton amour et nos fou rires,
pour ces moments passés ensemble et ton sourire.
À toi Malo, la plus merveilleuse des surprises,
à ton émerveillement et à nos bêtises.

Contents

List of Figures

Acknowledgments

That's it. The end is nigh. Tomorrow, I will hand in the manuscript, start to prepare the defense, after which life will move on. Yet, as dusk settles, a few hours are left for me to reflect on the past three and half years of my life and to thank the people who helped me along in this journey.

My parents are the ones who come first in my mind, the ones with whom this voyage started. They offered me, thorough my entire life, unconditional love and support, they allowed me to grow and become the person I am today. I could never thank them enough for all they did. My siblings also played an incredible role in the story of my life. Despite our differences, we understand and deeply love each other.

I am thankful to Prof. Wrachtrup, who welcomed me into his group nearly four years ago when I was still a master's student, a decision I hope he doesn't regret in hindsight. He, and Dr. Kaiser, gave me professional opportunities, as well as guidance on the work accomplished. Thanks also to Prof. Pfau, who agreed to be my second referee.

I had the chance to collaborate with several groups and many talented scientists without whom this manuscript would not have been submitted already, if ever. I was fortunate to have many insightful discussions with each and every one of them. I realized how much there is still for me to learn in many fields of science. I am also grateful for the three generations of master students who worked with me in the lab, their various skills and talents allowed the project to be what it is today.

The energies and good vibes of the squad members, past and present, cheered me up and made my days in the lab more entertaining. I would like to also thanks all my colleagues of pi3, for the shared ice creams, cakes, cups of coffee, beers, and even sometimes pieces of advice. I am also thankful for the help provided by all the technicians, secretaries, and workers of the institute.

I feel in a forever debt toward Raphael (a.k.a Raphiki), his light-hearted company is the best I could hope for. He never hesitated to help me, to listen to my rants, or to proofread this entire manuscript. I'm grateful for all the time we spent together. Thanks to him and Fiammetta (a.k.a Fifi), I *kicked it* at the climbing gym.

Many other friendships have been precious to me during these demanding times: the Jugendfarm crew, always willing to do something or nothing together. My old roommates of Challemel-Lacour, the ones with a room or simply a couch, and their loved

ones; were always here for me if I needed someone to talk to. The Improfesseurs, these weeks together have been real highlights of my life and will stick with me forever.

On many levels, things have changed since a young *Charlie Boy* started his PhD. I grew up, learned valuable lessons, cried and laughed, and hopefully, I also matured. I even have a child now, a lovely and joyful Malo who brightens every single one of my day with his smiles and laughter. This family we started together with Clémence, my wonderful fiancée, is the closest to my heart. I cherish every moment together, and I could not be happier to share with them the rest of my journey.

Dear reader, who went through this acknowledgment or some parts of this thesis, I wish you all the best in your life. For my part, I will now go to bed and hopefully, the printer will be functional tomorrow.

Zusammenfassung

Die erste Quantenrevolution begann mit der Wende zum 20. Jahrhundert, als Max Planck die Schwarzkörperstrahlung durch eine neuartige Idee erklärte: die Quantisierung der elektromagnetischen Energie. Die physikalische Bedeutung, die sich dahinter verbarg, war ihm ein Rätsel, doch dieses Konzept ebnete den Weg zu einem völlig neuen Forschungsgebiet. Auf den verschiedenen Solvay-Konferenzen legten die Begründer der Quantenmechanik die theoretischen Grundlagen dieses kontraintuitiven Paradigmas fest und diskutierten über dessen Bedeutung und Reichweite. Dieses neue Verständnis des Universums ermöglichte der Menschheit die Entwicklung bahnbrechender Technologien wie Laser, Transistoren oder Atomuhren, die uns die Glasfaserkommunikation, Computer oder das globale Positionsbestimmungssystem (GPS) ermöglichten. Auch wenn die Steuerung komplexer Quantensysteme nach wie vor eine Herausforderung darstellt, entwickelt eine neue Generation von Physikern und Mathematikern Theorien über neue Wege zur Nutzung dieser Systeme. Maschinen mit beispielloser Rechenleistung, die in der Lage sind, die Realität zu simulieren, wurden erstmals 1981 von Richard Feynmann erdacht [1]. Im Laufe der nächsten Jahrzehnte wurden Quantenalgorithmen eingeführt, die im Vergleich zu entsprechenden klassischen Algorithmen einen beispiellosen Geschwindigkeitszuwachs aufweisen. Lehrbuchbeispiele wie die Algorithmen von Grover [2] oder Deutsch–Jozsa [3, 4] sind einige davon. Der Algorithmus, der alle Erwartungen über den Haufen warf, wurde jedoch 1994 von Peter Shor vorgestellt: die Faktorisierung einer ganzen Zahl in ihre Primfaktoren in polynomieller Zeit, im Gegensatz zur subexponentiellen Skalierung bekannter klassischer Algorithmen [5]. Dies war eine so große Bedrohung für die auf moderner Kryptographie basierende sichere Kommunikation, dass zwei Forschungsbereiche aufblühten, die nach neuen Verschlüsselungsmethoden suchten: Post-Quanten-Kryptographie [6] und Quantenkommunikation [7, 8, 9]. Letztere nutzt grundlegende Quantenprinzipien wie das No-Cloning-Theorem und die Quantenverschränkung, um nachweislich sichere Netzkanäle zu etablieren. Die zweite Quantenrevolution ist nun im Gange: die Verfeinerung der Kontrolle über komplexe und große Systeme zur Entwicklung und Konstruktion innovativer Quantentechnologien. Die Forschung an einer Vielzahl von neu entstehenden Plattformen floriert und hat in den letzten zwei Jahrzehnten an Schwung gewonnen. [10, 11, 12, 13, 14, 15, 16, 17, 18, 19]

Jedoch könnte der Hype um die zweite Quantenrevolution in Frage gestellt werden. Erstens im Hinblick auf den tatsächlichen Wert, den die Quantentechnologien der Menschheit bringen könnten. Zum anderen könnten angesichts der aktuellen Klimakrise, die laut dem Zwischenstaatlichen Ausschuss für Klimaänderungen (IPCC) höchstwahrscheinlich durch menschliche Aktivitäten ausgelöst wurde, die in diese Forschungs-

bereiche gesteckten Energien und Ressourcen wahrscheinlich besser an anderer Stelle eingesetzt werden. Dennoch sind die Herausforderungen, die sich daraus ergeben, faszinierend, und der wissenschaftliche Fortschritt ermöglicht uns ein besseres Verständnis der zugrunde liegenden Realität unseres Universums. Außerdem könnte uns der Zufall möglicherweise zu nützlichen Lösungen für vorübergehende Probleme führen. Es lohnt sich also, die Quantentechnologien bis zu einem gewissen Grad zu erforschen.

Optisch aktive Spins in Festkörpern sind vielversprechende Kandidaten für fortgeschrittene Quanteninformationsverarbeitung und Quantenmetrologie, und vielversprechende chipbasierte Quantentechnologien. Faszinierende Möglichkeiten ergeben sich durch die Verknüpfung von atomähnlichen optischen Übergängen und langlebigen Elektronen- und Kernspin-Qubit-Clustern [20]. Die Verschränkung mehrerer Knotenpunkte bestehend aus Stickstoff-Fehlstellen-Zentren (NV) in verschiedenen Diamanten wurde nachgewiesen [21, 22]. Darüber hinaus haben neuere Forschungen gezeigt, dass "unsterbliche Festkörper-Spin-Qubits" auf der Grundlage des Shor'schen Neun-Qubit-Fehlerkorrekturcodes realistisch in Reichweite sind [23, 24]. Um solche Qubits effizient zu verschränken, wird inzwischen allgemein anerkannt, dass die Skalierung über die grundlegenden Szenarien mit wenigen Qubits hinaus einen Sprung in der Wechselwirkungseffizienz der Spin-Photonen-Schnittstelle erfordert, z. B. unter Verwendung der Hohlraum-Quantenelektrodynamik (cQED) [25, 26]. Eine große Herausforderung in diesem Prozess besteht darin, die spinoptischen Kohärenzen zu schützen und gleichzeitig einen hochgradig zuverlässigen Zugang zu Qubit-Clustern, wie z. B. Kernspins, zu ermöglichen [27]. Trotz erheblicher Anstrengungen ist die Entwicklung einer skalierbaren cQED-Plattform im Festkörper für die üblicherweise verwendete Diamanttechnologie eine außerordentliche Herausforderung geblieben. Die optische Stabilität der NV-Zentren ist stark beeinträchtigt, sobald sie in nanophotonische Strukturen integriert sind, was auf die Kopplung mit nahegelegenen Spins und Ladungsfallen zurückzuführen ist [28, 29]. Andererseits haben Gruppe-IV-Defekte in Diamant dank ihrer strukturellen Inversionssymmetrien in den letzten Jahren mit bahnbrechenden Spin-Photonen-Experimenten robuste optische Kohärenzen gezeigt [30, 31, 32]. Für eine zuverlässige Spinmanipulation sind jedoch Millikelvin-Temperaturen erforderlich, bei denen eine direkte Kontrolle über Kernspincluster schwierig wird [33, 34]. In den letzten Jahren hat Siliziumkarbid (SiC), ein gut etablierter industrieller Halbleiter mit großer Bandlücke, als Träger mehrerer vielversprechender Farbzentren an Bedeutung gewonnen [35, 36, 37], insbesondere das Silizium-Vakanzzentrum (V_{Si}), das dank des Schutzes der Wellenfunktionssymmetrie robuste Spektral- und Spineigenschaften aufweist [38, 39, 40].

Ziel meiner Arbeit war es, zu untersuchen, ob V_{Si} erfolgreich in einen nanophotonischen Kristallhohlraum integriert werden kann. Wie in dieser Dissertation erörtert, umfasste dieses Problem mehrere Aspekte, die analysiert werden mussten. Um die Vorteile dieser Hohlräume voll ausnutzen zu können, müssen sich die Quantenemitter innerhalb des Modenvolumens befinden, in dem das elektromagnetische Feld eingeschränkt ist. Darüber hinaus müssen die spinoptischen Kohärenzen gegenüber Nanofabrikationstechniken widerstandsfähig sein. Schließlich müssen integrierte Punktdefekte die Fähigkeit aufweisen, nahe gelegene Kernspins kohärent zu manipulieren und so Multi-

QuBit-Register zu bilden, die für eine fehlertolerante Quanteninformationsverteilung erforderlich sind. Die wichtigsten Ergebnisse sind veröffentlicht in [41].

In diesem Manuskript ist Kapitel 1 der Beschreibung des behandelten Punktdefekts gewidmet: V_{Si} in SiC, die grundlegenden spin-optischen Eigenschaften und die Bedeutung für die heutige Forschung. Kapitel 2 stellt den Rahmen der cQED vor und beweist, dass V_{Si} theoretisch den Bereich hoher Kooperativität erreichen kann. In Kapitel 3 werden unsere Ergebnisse zur ionenunterstützten Implantationstechnik vorgestellt. Diese Technik ermöglicht die Erzeugung hochwertiger flacher V_{Si}-Zentren mit nanometer genauer räumlicher Auflösung. In Kapitel 4 werden Wellenleiter mit dreieckigem Querschnitt um bereits existierende V_{Si}-Zentren herum hergestellt. Die integrierten V_{Si}-Zentren zeigen robuste spinoptische Kohärenzen, die denen von ungestörten Bulkdefekten ähneln. Kapitel 5 baut auf früheren Modellen auf und erweitert den theoretischen Rahmen der Kernspinkontrolle durch Entkopplungssequenzen auf den Bereich niedriger Magnetfeldstärken und beliebiger Elektronenspinquantenzahlen. Auf der Grundlage eines präziseren Modells demonstrieren wir die kohärente Kontrolle von zwei integrierten Kernspin-Qubits mit hoher Zuverlässigkeit. Schließlich konnte ich dank der Forschungsprojekte, die ich während meines Studiums durchgeführt habe, ein experimentelles Projekt unseres Instituts unterstützen, das nicht mit Spins in Festkörpern zusammenhängt. Ein modifiziertes Mach-Zehnder-Interferometer hat eine Phasenempfindlichkeit jenseits der Schrotrauschgrenze (SNL) erreicht, die ich in Kapitel 6 theoretisch hergeleitet habe. Das Experiment verwendet gequetschte Lichtzustände, und im Gegensatz zu Standard-Homodyn-Detektionsverfahren erfolgt die Messung der optischen Phasenverschiebung durch Standard-Intensitätsmessungen, was sich als robust gegenüber Verlusten erweist. Die in dieser Arbeit verwendeten Abkürzungen und Symbole sind in Anhang A-B zu finden. Anhang C enthält das Protokoll zur Stabilisierung eines Lasers auf Resonanz mit einem spezifisch driftenden Farbzentrum. Darüber hinaus werden in Anhang D die Techniken beschrieben, mit denen ein Magnetfeld entlang der *c*-Achse des Kristalls ausgerichtet wird, das für die Untersuchung der Spineigenschaften eines Farbzentrums erforderlich ist.

Tiefliegende V_{Si}-Zentren in 4H-SiC haben ausgezeichnete optische Kohärenzen mit nahezu transformationsbegrenzten optischen Linien und enger inhomogener Verteilung gezeigt [38, 39, 42], wie in Kapitel 1 erläutert. Außerdem zeigten sie Spin-Kohärenzzeiten im Millisekundenbereich und eine kohärente Kopplung mit nahegelegenen Kernspins [40, 43]. Wie die ersten experimentellen Ergebnisse meiner Doktorarbeit zeigen, die in [44, 45] veröffentlicht wurden, behalten V_{Si}-Zentren ihre interessanten Spektral- und Spineigenschaften bei außergewöhnlich hoher Betriebstemperatur ($T = 20$ K). Der Schutz der Wellenfunktionssymmetrie trägt zur hohen Ununterscheidbarkeit der Photoemission bei, was zur Demonstration einer kohärenten Licht-Materie-Grenzfläche mit einem Elektronenspin und zwei Photonen geführt hat, die für die Erzeugung von Clusterzuständen geeignet ist. Allerdings leidet das V_{Si}-Zentrum unter einer schlechten Spin-Photonen-Schnittstelle aufgrund einer geringen Sammeleffizienz, dem inhärenten Problem optisch adressierbarer Spinsysteme in Festkörpern. Die geringe Spin-Photonen-Wechselwirkungswahrscheinlichkeit ist ein wesentlicher Engpass für die Skalierbarkeit der Plattform und schränkt den Anwendungsbereich ein.

Durch die Integration in eine cQED wird die Kopplung zwischen einem Quantenemitter und einem im Hohlraum eingeschlossenen Photon verstärkt [26], wie in Kapitel 2 erläutert. Die wichtigsten zu berücksichtigenden Parameter sind der Purcell-Faktor (P) und die Kooperativität (C). Theoretisch können mit modernen Nanofabrikationstechniken Hohlräume hergestellt werden, die so konstruiert sind, dass sie den Bereich hoher Kooperativität ($C > 1$) für das V_{Si}-Zentrum erreichen [46, 47, 48]. In diesem Bereich ist eine deterministische kohärente Wechselwirkung zwischen einem integrierten Quantenemitter und einem einzelnen injizierten Photon möglich [49, 50, 51, 52]. Im Vergleich zu anderen Punktdefekten haben alle V_{Si}-Zentren die gleiche Dipolausrichtung, was die Integration in nanophotonische Resonatoren erleichtert. Darüber hinaus ist SiC ein für die Nanofabrikation geeignetes Material, das in Wafergröße im Handel erhältlich ist. Das breite optische Trans- parenzfenster und die nichtlinearen optischen Koeffizienten im sichtbaren und nahen infraroten Bereich ermöglichen die Frequenzumwandlung auf dem Chip und die Vier-Wellen-Mischung [53, 54]. V_{Si} in SiC scheint daher ein vielversprechendes System für die Integration in nanophotonische Resonatoren zu sein.

Ionenimplantationstechniken können zur Erzeugung einzelner Defekte mit hoher räumlicher Auflösung eingesetzt werden [55, 56, 57, 58]. Es bleibt jedoch unbekannt, ob die spinoptischen Eigenschaften nach einer solchen Erzeugung erhalten bleiben. In Kapitel 3 wurden drei Ionensorten in eine epitaktisch gewachsene SiC-Schicht implantiert: Silizium (Si^{++}), Protonen (p^{+}) und Helium (He^{+}). Die mit Hilfe eines fokussierten Ionenstrahls (FIB) implantierten Silizium-Ionen erzeugen Monovakanzen im Kristallgitter. Die Defekte weisen jedoch breite Emissionsspektren auf, was wahrscheinlich auf eine starke Beschädigung der Farbzentren zurückzuführen ist; daher können keine spin-erhaltenden optischen Übergänge beobachtet werden. Protonen und Heliumionen werden mit Energien von einigen keV durch eine Anordnung von Löchern implantiert, die durch eine lithografierte Polymethylmethacrylat (PMMA)-Maske definiert sind. Beide Ionenarten erzeugen flache Einzeldefekte mit langsam driftenden transformationsbegrenzten optischen Linien. Die räumliche Genauigkeit wurde mit etwa 50 nm gemessen, begrenzt durch die Lochgröße, was mit dem geringen Modenvolumen nanophotonischer Hohlräume kompatibel ist. Ein softwaregestütztes Protokoll stabilisiert den Resonanzlaser auf den driftenden Linien und ermöglicht die Messung der Spineigenschaften der erzeugten Defekte. Die durch He^{+}-Ionenimplantation erzeugten Defekte zeigen die längste jemals gemessene Hahn-Echo-Spinkohärenzzeit für das System: $1{,}4 \pm 0{,}1$. Für zukünftige Untersuchungen wäre es interessant, die Möglichkeit zu untersuchen, eine Helium-FIB-Quelle zur Erzeugung von Farbzentren zu verwenden, die eine maskenfreie Implantation in vorcharakterisierte nanophotonische Resonatoren ermöglicht.

Wellenleiter mit dreieckigem Querschnitt können, wie in Kapitel 4 erläutert, im Einmodenbetrieb mit einer Lichtleitereffizienz nahe der Eins betrieben werden [59]. Um die spinoptischen Zusammenhänge integrierter V_{Si}-Zentren zu untersuchen, werden die Nanostrukturen in einem SiC-Kristall mit vorcharakterisierten, durch Elektronenbestrahlung erzeugten Farbzentren hergestellt. Die Wellenleiter sind 400 nm und 1000 nm breit und haben einen halben Öffnungswinkel von 45°. Alle untersuchten Defekte in den 1000 nm breiten Strukturen weisen langsam driftende spinselektive

Übergänge auf, wobei die Hälfte von ihnen nahezu umwandlungsbegrenzte optische Linien zeigt. In den 400 nm breiten Wellenleitern wurden jedoch keine V_{Si}-Zentren identifiziert. Die spektrale Wanderung war wiederum so langsam, dass ein Resonanzlaser auf den optischen Übergängen praktisch unendlich lange stabilisiert werden kann, indem unser Rückkopplungsprotokoll einmal pro Minute periodisch aktiviert wird. Mit der nachgewiesenen Stark-Abstimmung von V_{Si} [60, 61] könnte man das Protokoll umkehren, um die Defekte auf einen Referenzlaser zu stabilisieren. Wir haben auch die Hahn-Echokohärenzzeit der integrierten Defekte gemessen, die mit tiefen Bulk-Defekten derselben Probe vergleichbar ist ($0{,}85 \pm 0{,}03$ ms). Unsere Arbeit stellt die erste erfolgreiche Integration von nicht-zentrosymmetrischen Punktdefekten in Nanostrukturen dar. Auf der Grundlage unserer Ergebnisse schlagen wir ein alternatives Wellenleiterdesign vor, das für Defekte in einer Tiefe von $30 - 40$ nm unter der Oberfläche optimiert ist - die Tiefe der durch He^+-Ionenimplantation erzeugten Defekte.

Kernspins, die von Natur aus im Wirtsmaterial vorhanden sind, können genutzt werden, um lokale Multi-Qubit-Cluster mit langen Speicherzeiten zu erzeugen [62, 63, 64]. Dank der langen Kohärenzzeit, die die integrierten V_{Si}-Zentren aufweisen, können wir zwei eingebettete Kernspins durch Impulsfolgen auf den Elektronenspin kohärent manipulieren. Die Dynamik des zweistufigen Systems während einer Entkopplungssequenz wird in Kapitel 5 beschrieben. Die Carr-Purcell-Meiboom-Gill (CPMG)-Sequenz [65], die aus gleichmäßig verteilten Refokussierungspulsen besteht, ist durch Resonanzen gekennzeichnet, bei denen ein gekoppelter Kernspin verschiedene Rotationen durchläuft, was eine deterministische Kontrolle seines Quantenzustands ermöglicht. Der theoretische Rahmen, der auf der Hyperfein-Wechselwirkung basiert, wurde gegenüber früheren Modellen [66, 67] erweitert, um unseren experimentellen Bedingungen gerecht zu werden: niedrige Magnetfeldstärke und ein halbzahliges Elektronenspinsystem. Die genauere Beschreibung wird an den identifizierten integrierten Kernspins verifiziert, wobei die experimentellen Bedingungen optimiert werden, um den Kernspinzustand mit hoher Genauigkeit zu kontrollieren. Schließlich wird ein Protokoll vorgestellt, mit dem sich der Zustand des Elektronenspins trotz einer nicht einheitlichen Sammeleffizienz mit einem einzigen Schuss auslesen lässt, wobei ein Kernspin als Ancilla-Qubit verwendet wird [68].

Gequetschte Zustände des Lichts entsprechen Photonen, bei denen die Unsicherheit einer ihrer Feldquadraturen kleiner ist als die eines kohärenten Zustands [69, 70]. In die Laserinterferometrie ermöglicht das quetschen einer Empfindlichkeit jenseits der Schrotschussgrenze (SNL) [71, 72]. Gequetschte Lichtzustände sind jedoch sehr empfindlich gegenüber optischen Verlusten im gesamten Aufbau und erfordern komplexe Verfahren [73]. Unsere Gruppe hat kürzlich an einem neuartigen System gearbeitet, das die Stabilität eines klassischen Interferometers mit der Empfindlichkeitsverbesserung eines nichtlinearen Interferometers kombiniert. Es wurde ein Verbesserungsfaktor von $1{,}13 \pm 0{,}02$ über einen breiten Frequenzbereich von bis zu 100 kHz erreicht. Dies sind Raten, die mit der N00N-Zustandsinterferometrie aufgrund der geringen optischen Sättigung von Photonenzahl-auflösenden Detektoren unerreichbar sind [74, 75]. In Kapitel 6 modellieren wir den Versuchsaufbau und untersuchen die Auswirkungen von Verlusten auf die Empfindlichkeit. Der Kontrast der Inter-

ferenzstreifen ist mit der Verbesserung der Phasenempfindlichkeit verknüpft, was es ermöglicht, die theoretische Herleitung zu bestätigen. Obwohl das Experiment bei niedrigem Photonenpaarfluss durchgeführt wird, erweitere ich den Rahmen auf stärker gequetschte Zustände. Der dann erreichte Verbesserungsfaktor kann bis zu zwei betragen und ist noch widerstandsfähiger gegen Verluste.

Zusammenfassend lässt sich sagen, dass V_{Si}-Zentren ihre ausgezeichneten spinoptischen Eigenschaften auch nach der Erzeugung durch Ionenimplantationstechniken und nach der Integration in nanophotonische Strukturen beibehalten. Auf der Grundlage dieser Fortschritte haben wir die nahegelegenen Kernspins kohärent und mit nahezu gleicher Genauigkeit kontrolliert. Um die optischen Übergänge zu stabilisieren, wären weitere Untersuchungen zur Oberflächenpassivierung durch Graphenabscheidung erforderlich [76, 77]. Dank der bestehenden p-i-n-Strukturen des Halbleiters SiC hat die Ladungsverarmung um das Fehlstellenzentrum zu einer verbesserten spinoptischen Stabilität geführt [78], Techniken, die auch auf V_{Si}-Zentren angewendet werden könnten. Die Skalierung der Anzahl adressierbarer Kernspin-Qubits ist durch eine präzise Steuerung der Isotopenkonzentration während des Wachstums der epitaktischen Kristallschicht möglich [79]. Dank der zweiatomigen Beschaffenheit von Siliziumkarbid können außerdem zwei verschiedene Kernspinbäder kohärent gesteuert werden, wodurch sich die Anzahl der verfügbaren Kernspins im Vergleich zur Diamantplattform verdoppelt [27, 80]. Aufgrund des halbzahligen Spins von V_{Si} hebt die Hyperfeinwechselwirkung die Entartung der Kernspinniveaus mit einer einzigartigen Aufspaltung auf, die vom Gitterplatz des Kerns abhängt. Somit sind Flip-Flops in den Kernspin-Clustern verboten, was die Implementierung eines beliebigen Quantencomputer-Algorithmus erleichtert [23, 81, 82].

Diese Dissertation stellt einen bedeutenden Schritt in Richtung integrierter Quantencomputer-Cluster mit effizienten Spin-Photonen-Schnittstellen unter Verwendung von Farbzentren in SiC dar.

Summary

The first quantum revolution started at the turn of the 20th century, as Max Planck explained the black-body radiation via a novel idea: the quantization of electromagnetic energy. The physical meaning behind it puzzled him, yet this concept paved the way to an entirely new field of research. Through the different Solvay conferences, the founders of quantum mechanics laid the theoretical principles of this counter-intuitive paradigm, debating its meaning and reach. This new understanding of the universe allowed humanity to develop breakthrough technologies such as lasers, transistors, or atomic clocks which gave us optical fiber communication, computers, or global positioning system (GPS). Even though the control of complex intricate quantum systems remained a challenge, a new generation of physicists and mathematicians theorized new ways to utilize those systems. Machines with unprecedented computing power, capable of simulating reality, were first imagined by Richard Feynmann in 1981 [1]. For decades to come quantum algorithms were introduced, showcasing unprecedented speed-up compared to equivalent classical algorithms. Textbook examples, such as the Grover [2] or Deutsch–Jozsa [3, 4] algorithms are some of them. Yet, the one that shattered anyone's expectation was presented by Peter Shor in 1994: the factorization of an integer into its prime factors in a polynomial time as opposed to the sub-exponential scaling of known classical algorithms [5]. Enough of a threat to modern cryptography-based secured communications, that two fields of research blossomed searching for new encryption methods: post-quantum cryptography [6] and quantum communication [7, 8, 9]. The second one utilizes fundamental quantum principles, such as the no-cloning theorem and quantum entanglement, to establish provably secure network channels. The second quantum revolution is now in motion: refining the control over complex and large systems to develop and engineer innovative quantum technologies. Research on a variety of emerging platforms is thriving and gaining momentum for the last two decades [10, 11, 12, 13, 14, 15, 16, 17, 18, 19].

However, the hype around the second quantum revolution could be questioned. First, in regards to the real value that quantum technologies could bring to Humankind. In a second time, considering the current climate crisis, most likely induced by human activities as reported by the Intergovernmental Panel on Climate Change (IPCC), the amount of energies and resources poured into these research fields could probably be better used elsewhere. Yet, the challenges arising are fascinating and the scientific advancement provides us with a better understanding of the underlying reality of our universe. Additionally, serendipity could potentially lead us to useful solutions to contemporary problems. Thus, quantum technologies are worth investigating to some extent.

Optically active spins in the solid are promising candidates for advanced quantum information processing and quantum metrology, promising chip-based quantum technologies. Fascinating opportunities emerge by linking atom-like optical transitions and long-lived electron and nuclear spin qubit clusters [20]. Multinode entanglement distribution between nitrogen-vacancy (NV) centers in distinct diamonds have been demonstrated [21, 22]. Furthermore, recent research has shown that "immortal solid-state spin qubits" based on Shor's nine-qubit error correction code are realistically within reach [23, 24]. To efficiently entangle such qubits, it is now well-accepted that scaling beyond basic few-qubit scenarios requires a leap forward in the interaction efficiency of the spin-photon interface, e.g. using cavity quantum electrodynamics (cQED) [25, 26]. A major challenge in this process is to protect spin-optical coherences while granting high-fidelity access to qubit clusters, such as nuclear spins [27]. Despite considerable efforts, the development of a scalable solid-state cQED platform has remained extraordinarily challenging for the commonly-used diamond technology. The optical stability of the NV centers is severely compromised once integrated into nanophotonic structures, due to coupling to nearby spins and charge traps [28, 29]. On the other hand, group-IV defects in diamond, thanks to their structural inversion symmetries, have shown robust optical coherences with groundbreaking spin-photon experiments obtained in recent years [30, 31, 32]. Yet, high-fidelity spin manipulation requires millikelvin temperatures at which direct control over nuclear spin clusters becomes challenging [33, 34]. In recent years silicon carbide (SiC), a well-established industrial wide-bandgap semiconductor, has gained traction as a host of multiple promising color centers [35, 36, 37], in particular the silicon vacancy (V_{Si}) center which provides robust spectral and spin properties thanks to wavefunction symmetry protection [38, 39, 40].

The objective of my thesis was to study whether V_{Si} could be successfully integrated into a nanophotonic crystal cavity. As discussed in this dissertation, this problem encompassed several aspects that needed to be analyzed. To take full advantage of those cavities, the quantum emitters have to be within their mode volumes, where the electromagnetic field is confined. Furthermore, the spin-optical coherences have to be resilient against nanofabrication techniques. Lastly, integrated point defects have to show the ability to coherently manipulate nearby nuclear spins, building multi-qubit registers required for fault-tolerant quantum information distribution. The main results obtained are published in [41].

In this manuscript, Chapter 1 is dedicated to the description of the point defect of interest: V_{Si} in SiC; its fundamental spin-optical properties, and its relevance in today's research. Chapter 2 introduces the framework of cQED and proves that V_{Si} can theoretically reach the high-cooperativity regime. In Chapter 3, our results on ion-assisted implantation techniques are presented. The technique allows a high-yield generation of high-quality shallow V_{Si} centers, with nanometric spatial accuracy. In Chapter 4, triangular cross-section waveguides are fabricated around preexisting V_{Si} centers. The integrated V_{Si} centers display robust spin-optical coherences, similar to the one of unperturbed bulk defects. Chapter 5, builds upon previous models to extend the theoretical framework of nuclear spin control via decoupling sequences to the low

magnetic field strength regime and arbitrary electron spin quantum number. Capitalizing on a more precise model, we demonstrate high-fidelity coherent control on two integrated nuclear spin qubits.
Finally, thanks to research projects accomplished during my studies, I have been able to help an experimental project of our institute, uncorrelated to spins in solid. A modified Mach-Zehnder interferometer has reached phase sensitivity beyond the shot-noise limit (SNL), which I give a theoretical derivation of in Chapter 6. The experiment uses squeezed states of light, and contrary to standard homodyne detection schemes, the optical phase shifts measurement is done through standard intensity measurements which proves to be robust against losses.
Abbreviations and symbols used in this dissertation can be found in Appendix A-B. Appendix C provides the protocol used to stabilize a laser on resonance with a spectrally drifting color center. Moreover, the techniques used to aligned a magnetic field along the *c*-axis of the crystal, needed to probe the spin properties of a color center, are described in D.

Deep-bulk V_{Si} centers in 4H-SiC have shown excellent optical coherences, with nearly transform-limited optical lines and narrow inhomogeneous distribution [38, 39, 42], as explained in Chapter 1. Additionally, they displayed millisecond of spin-coherence times and coherent coupling to nearby nuclear spins [40, 43]. As demonstrated during the first experimental results obtained in my PhD thesis, published in [44, 45], V_{Si} centers maintain their interesting spectral and spin properties at exceptionally high operation temperature ($T = 20$ K). The wavefunction symmetry protection contributes to the high indistinguishability of the photoemission, which has led to the demonstration of a coherent light–matter interface comprising one electron spin and two photons, suitable for cluster state generation. Yet, the V_{Si} center suffers from a poor spin-photon interface due to a low collection efficiency, the inherent problem of optically addressable spin systems in solids. The low spin-photon interaction probability is a major bottleneck to the scalability of the platform, limiting the scope of the application. By integration in a cQED, the coupling between a quantum emitter and a photon confined in the cavity is enhanced [26], as discussed in Chapter 2. The main parameters to consider are the Purcell factor (P) and the cooperativity (C). Theoretically, state-of-the-art nanofabrication techniques can create cavities engineered such as to reach the high-cooperativity regime ($C > 1$) for the V_{Si} center [46, 47, 48]. At this regime, deterministic coherent interaction between an integrated quantum emitter and a single injected photon is possible [49, 50, 51, 52]. Compared to other point defects, all V_{Si} centers have the same dipole orientation which facilitates the integration into nanophotonic resonators. Furthermore, SiC is a nanofabrication friendly material, with wafer-size materials commercially available off-the-shelf. The broad optical transparency window and the optical non linear coefficients in the visible and near-infrared region allow for on-chip frequency conversion and four-wave mixing [53, 54]. As such, V_{Si} in SiC seems a promising system for integration into nanophotonic resonators.

Ion implantation techniques can be used to generate single defects with a high spatial resolution [55, 56, 57, 58]. However, it remains unknown if the spin-optical properties are preserved after such a generation. In Chapter 3, three ion species have

been implanted in an epitaxially grown SiC layer: silicon (Si^{++}), proton (p^{+}), and helium (He^{+}). Silicon ions, implanted using a focused ion beam device (FIB), generate monovacancies within the crystal lattice. Yet, the defects show broad emission spectra, probably due to heavy damage surrounding the color centers; thus no spin-preserving optical transitions can be observed. Protons and helium ions are implanted at energies of a few keV through an array of holes, defined from a lithographed polymethyl methacrylate (PMMA) mask. Both ion species generate shallow single defects with slowly drifting transform-limited optical lines. The spatial accuracy was measured to be around 50 nm, limited by the hole size, which is compatible with the low mode volume of nanophotonic cavities. A software-assisted protocol stabilizes the resonant laser onto the drifting lines, allowing the measurement of the spin properties of the generated defects. The defects created via He^{+} ion implantation present the longest-ever measured Hahn echo spin coherence time for the system: 1.4 ± 0.1 ms. For future investigations, it would be interesting to study the possibility to use a helium FIB source to generate color centers, allowing mask-free implantation into precharacterized nanophotonic resonators.

Triangular cross-section waveguides can have a single-mode operation with near-unity light-guiding efficiencies [59], as discussed in Chapter 4. To study the spin-optical coherences of integrated V_{Si} centers, the nanostructures are fabricated in a SiC crystal with precharacterized color centers generated via electron irradiation. The waveguides are 400 nm and 1000 nm wide with a half-opening angle of 45°. All investigated defects in the 1000 nm wide structures present slowly drifting spin-selective transitions, with half of them displaying near-transform-limited optical lines. Yet, no V_{Si} centers are identified in the 400 nm wide waveguides. The spectral wandering was once again slow enough that a resonant laser is stabilized on the optical transitions, for virtually an infinite amount of time, only by periodically activating our feedback protocol once per minute. Using the demonstrated Stark tuning of V_{Si} [60, 61], one could reverse the protocol to stabilize the defects onto a reference laser. We also measured the Hahn echo coherence time of the integrated defects, which is similar to deep bulk defects of the same sample (0.85 ± 0.03 ms). Our work represents the first successful integration of non-centrosymmetric point defects in nanostructures. Capitalizing on our results, we propose alternative waveguides design optimized for defects $30 - 40$ nm beneath the surface; the depth of defects generated via He^{+} ion implantation.

Nuclear spins, naturally present in the host material, can be utilized to create local multi-qubit clusters with long storage times [62, 63, 64]. Thanks to the long coherence time displayed by the integrated V_{Si} centers, we coherently manipulate two embedded nuclear spins via pulse sequence on the electron spin. The dynamics of the bipartite system, during a decoupling sequence, is described in Chapter 5. The Carr-Purcell-Meiboom-Gill (CPMG) sequence [65], consisting of equally spaced refocusing pulses, is characterized by resonances at which a coupled nuclear spin undergoes various rotations, enabling deterministic control of its quantum state. The theoretical framework, based on hyperfine interaction, is extended from previous models [66, 67] to be faithful to our experimental conditions: low magnetic field strength and half-integer electron spin system. The more accurate description is verified on the identified integrated

nuclear spins, with optimized experimental conditions to reach high-fidelity control of the nuclear spin state. Finally, a protocol is given to reach a single-shot readout of the electron spin state, despite a non-unity collection efficiency, using a nuclear spin as an ancilla qubit [68].

Squeezed states of light correspond to photons with the uncertainty of one of their field quadratures smaller that of a coherent state [69, 70]. Utilized in laser interferometry, squeezing allows reaching sensitivity beyond the shot-noise limit (SNL) [71, 72]. However, squeezed states of light are highly sensitive to optical losses over the complete setup and require complex schemes [73]. Our group recently worked on a novel scheme combining the stability of a classical interferometer with the sensitivity enhancement of a non-linear interferometer. An enhancement factor of 1.13 ± 0.02 was reached across a wide frequency range, up to 100 kHz. Rates that are unattainable using N00N-state interferometry due to the low optical saturation levels of photon number resolving detectors [74, 75]. In Chapter 6, we model the experimental setup, studying the effect of losses on the sensitivity. The fringe visibility is linked to the phase sensitivity enhancement, which allows us to confirm the theoretical derivation. Even though the experiment is performed at low photon pair flux, the framework is extended to the high squeezing regime. The enhancement factor then achieved can be up to two and is even more resilient to losses.

In conclusion, V_{Si} centers retain their excellent spin-optical properties after generation via ion-implantation techniques as well as after integration in nanophotonic structures. Capitalizing on those advances, we coherently controlled nearby nuclear spins with near-unity fidelity. To stabilize the optical transitions, further study on surface passivation via graphene deposition would be necessary [76, 77]. Moreover, benefiting from existing p-i-n structures of the semiconductor SiC, charge depletion around the divacancy center has led to improved spin-optical stability [78], techniques which could be applied to V_{Si} centers. Additionally, Scaling up the number of addressable nuclear spin qubits is possible via precise control of the isotope concentration during the growth process of the epitaxial crystal layer [79]. Furthermore, thanks to the diatomic nature of silicon carbide, two distinct nuclear spin baths could be coherently controlled, doubling the number of available nuclear spins compared to the diamond platform [27, 80]. Ultimately, due to the half-integer spin of V_{Si}, the hyperfine interaction always lifts the nuclear spin level degeneracy with a unique splitting dependent on the nucleus lattice site. As such, flip-flops in the nuclear spin clusters are forbidden, facilitating the implementation of any quantum computing algorithm [23, 81, 82].

This dissertation represents a significant step towards integrated quantum computational clusters with efficient spin–photon interfaces using color centers in SiC.

Scientific publications

1. Y.-C. Chen, P. S. Salter, M. Niethammer, M. Widmann, F. Kaiser, R. Nagy, N. Morioka, C. Babin, *et al.*, "Laser writing of scalable single color centers in silicon carbide", *Nano Letters* **19**, 2377–2383 (2019) [55]

2. P. Udvarhelyi, G. Thiering, N. Morioka, C. Babin, F. Kaiser, *et al.*,"Vibronic states and their effect on the temperature and strain dependence of silicon-vacancy qubits in 4h-SiC",*Physical Review Applied* **13**, 054017 (2020) [45]

3. D. Lukin, A. D. White, R. Trivedi, M. A. Guidry, N. Morioka, C. Babin, *et al.*,"Spectrally reconfigurable quantum emitters enabled by optimized fast modulation", *npj Quantum Information* **6**, (2020) [60]

4. N. T. Son, C. P. Anderson, A. Bourassa, K. C. Miao, C. Babin, *et al.*,"Developing silicon carbide for quantum spintronics", *Applied Physics Letters* **116**, 190501 (2020). [37]

5. N. Morioka, C. Babin, R. Nagy, I. Gediz, E. Hesselmeier, *et al.*, "Spin-controlled generation of indistinguishable and distinguishable photons from silicon vacancy centres in silicon carbide," *Nature Communications* **11**, 2516 (2020) [44]

6. P. Vergyris, C. Babin, R. Nold, E. Gouzien, H. Herrmann, *et al.*,"Two-photon phase-sensing with single-photon detection", *Applied Physics Letters* **117**, 024001 (2020) [83]

7. R. Nagy, D. B. R. Dasari, C. Babin, D. Liu, V. Vorobyov, *et al.*, "Narrow inhomogeneous distribution of spin-active emitters in silicon carbide", *Applied Physics Letters* **118**, 044001 (2021). [42]

8. C. Babin, R. Stöhr, N. Morioka, T. Linkewitz, T. Steidl, *et al.*, "Fabrication and nanophotonic waveguide integration of silicon carbide colour centres with preserved spin-optical coherence", *Nature Materials* **21**, 67–73 (2022). [41]

9. R. Nold, C. Babin, J. Schmidt, T. Linkewitz, M. Zaballos, *et al.*, "A Quantum Optical Microphone in the Audio Band", *under review* (2022)

10. N. Morioka & D. Liu, O. O. Soykal, I. Gediz, C. Babin, R. Stöhr, *et al.*,"Spin-optical dynamics and quantum efficiency of single V1 center in silicon carbide", *under review* (2022)

Chapter 1

Silicon vacancy centers in silicon carbide

In this chapter, the color center studied during the entirety of my time as a PhD student will be presented, namely the silicon vacancy (V_{Si}) center in silicon carbide (SiC). We will first introduce the host crystal: silicon carbide, before giving a quick overview of the different color centers present in SiC. The experimental setup used to characterize color centers will then be shown. We will proceed with the presentation of the V_{Si} center, its energy level structure and its spin-optical properties. We will demonstrate the relevance of this spin defect in regard to the DiVincenzo criteria and introduce an achievable spin-photon entanglement scheme. Finally, we will discuss the fundamental differences between the V1 and the V2 centers, the two types of V_{Si} in 4H-SiC, and why our efforts are leaning towards the development of the V2 center as a quantum platform.

1.1 Silicon carbide, a promising platform

Silicon carbide is a wide-bandgap (between $2.3 - 3.3$ eV depending on the crystal structure) semiconductor and plays a critical role in today's high-power and high-temperature electronics industry, thanks to its thermal conductivity being three times higher compared to silicon [84, 85, 86, 87] and further technological progress might go hand in hand with the development of electric vehicles [88]. Interestingly, the first electroluminescence from SiC was observed in 1907 [89]. Thereafter, SiC has been a key material for the development of commercial light emitting diodes (LEDs) [90, 91].

1.1.1 Properties of SiC

The crystal lattice of SiC is composed equally of silicon and carbon atoms tetrahedrally bonded by covalent bonds. There exist more than 250 non-equivalent spatial arrangements of the tetrahedra called *polytypes* [92]. As carbon and silicon belong to the same group of the periodic table, their properties are similar, and the SiC crystal attributes land between the ones of silicon and diamond with a density and hardness close to that of diamond. In contrast to diamond however, SiC is also piezoelectric [93], the presence of an electric field can generate local strain in the crystal. This could lead

to potential ways to manipulate the photoemission of color centers [45]. Further, compared to diamond, SiC can be precisely doped [94, 95] and p-i-n junction devices are achievable with benefits to the control of the color center [78, 96].

The optical properties of SiC are also interesting, showing a broad optical transparency window (0.37 - 5.6 µm) [97], as well as optical nonlinear coefficients in the visible and near-infrared regions [48, 98, 99], which allow for on-chip frequency conversion [53] and four-wave mixing [54].

Furthermore, SiC is a nanofabrication-friendly material, with the recent development of diverse nanofabrication techniques such as SiC-on-insulator [47, 100], doping-selective photo-electrochemical etching [101, 102] or reactive ion etching [103].

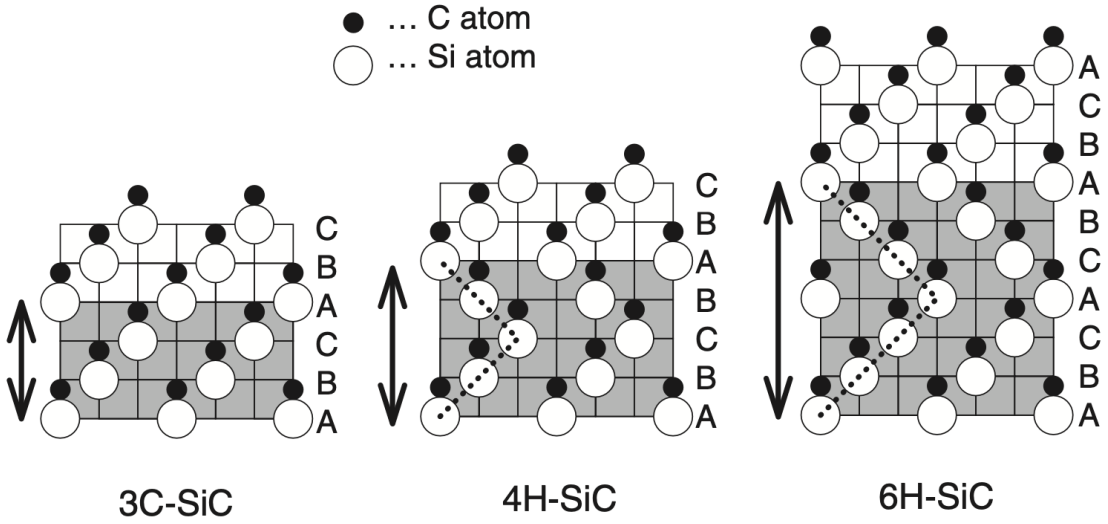

Figure 1.1: **Crystal lattice of SiC polytypes.** Stacking sequence of three common SiC polytypes: 3C-, 4H- and 6H-SiC. Adapted from [85].

As of today, three polytypes of SiC are mainly studied as host for quantum defects: 3C-, 4H- and 6H-SiC [104, 105]. The letters C and H correspond to the type of crystal structure: cubic[1] and hexagonal respectively, while the numbers are the length of the unit cell (the shortest stacking sequence). In a given atomic layer, the atoms can be arranged in three distinct ways to achieve closest packing labelled A, B and C. For example the fundamental stacking sequence for 4H-SiC is ABCB (length of 4) and for 6H-SiC is ABCACB (length of 6). In FIGURE 1.1, the crystal lattice stacking sequences of the three mentioned polytypes are given (adapted from [85]).

1.1.2 Optically active spin defects in SiC

Color centers have unique properties (spin, energy levels, coherence time ...) depending on the lattice site they are occupying in the host crystal, as well as their charge state. SiC is the host of large varieties of color centers [35, 36, 37]: divacancies, transition metal defects, monovacancies and even nitrogen vacancies. Those defects can be formed

[1]It is more exactly a zincblende structure: a diatomic faces centered cubic structure.

during the growth of the material, but are mainly introduced afterwards via particle irradiation.

The neutral divacancy ($V_{Si}V_C^0$) consists of neighboring silicon and carbon vacancies. Divacancies exist in four configurations according to the lattice sites of the missing silicon and carbon atoms (hexagonal and cubic). It is a spin-1 system emitting at a near-IR wavelength (∼1100 nm) with a Debye–Waller factor (DWF) around 7% and a Hahn echo coherence time around a millisecond even at room temperature [79, 106, 107, 108]. Integration in p-i-n structures, to deplete the charges surrounding the neutral divacancy, has shown the stabilization of the spin defect which displayed nearly lifetime-limited optical transitions [78]. The highly-cycling optical transitions combined with the high-contrast readout even at room temperature [109] have made the divacancy an interesting candidate for a spin-photon interface. Further, first results on the spin to charge conversion have been recently published [110], where the spin state is mapped onto the charge state of the divacancy. Integration in photonic crystal cavities also has been already realized [102]; yet, it has led to severe degradation of spin-optical coherences due to coupling to surface spins and charge traps.

Transition metal defects like chromium (Cr^{4+}) [111, 112, 113] or vanadium (V^{4+}) [114, 115] ions have been recently explored showing promising quantum properties. Particularly, around 75 % of the Cr^{4+} ($S = 1$) emission is in the zero-phonon line (ZPL) in the near-infrared (∼1050 nm). However, the excited state is long lived with a lifetime of around 150 µs, which could limit the repetition rate of any given protocols, and the spin-optical coherence of single defects still has to be investigated. Interestingly, the photon emission of the V^{4+} defect ($S = 1/2$) is in the telecom O-band, thus compatible with the optical fiber infrastructure, with a high ratio in the ZPL (∼ 20%). Furthermore, contrary to the Cr^{4+} defect, V^{4+} has a short excited state lifetime (∼ 100 ns), which is of great value for quantum information processing. Yet, the spin properties are to be investigated.

In our work we solely focus on the monovancy, formed by a missing silicon atom in the crystal lattice, namely silicon vacancy conventionally written as V_{Si}. We are motivated by the promising results obtained in the past years [39, 40, 45], which we will discuss later in this manuscript. However, before diving into the properties of V_{Si} in SiC, we will present the experimental setup used to study the spin system.

1.2 Experimental setup

Most of the experiments have been conducted at cryogenic temperatures. The various samples were placed inside a Montana Instruments cryostat and subsequently cooled down to 10 K. To study the spin-optical properties of single V_{Si} we developed a state-of-the-art home built confocal setup with electronic devices controlled by our own python-based software, which also allows for automatization of protocols as well as the stabilization of different components of the setup. The last two points have been the key aspects to the pursuit of the experiments during the different covid-related lockdowns, as most of the experiments could be performed and supervised remotely.

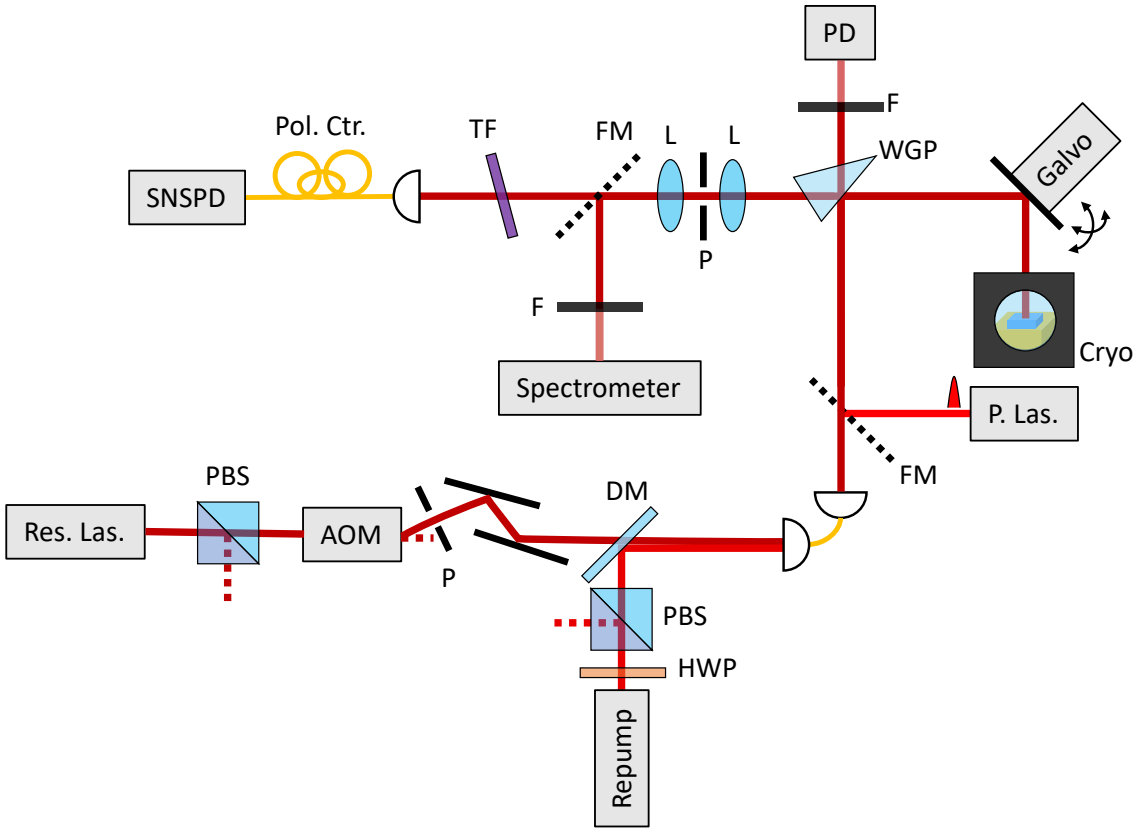

Figure 1.2: **Optical setup.** Sketch of the home built confocal setup. The description is given in the main text. Res. Las.: Tunable diode laser emitting at 917 nm. PBS: Polarization beam splitter. AOM: Acousto-optic modulator. P: Pinhole; DM: Dichroic mirror. Repump: Laser diode emitting at 785 nm. HWP: Half-waveplate. FM: Flip mirror. P. Las.: 2-ps pulsed laser. WGP: Wedged glasse plate. Galvo: Nanopositioning mirror tip/tilt actuators. Cryo: Cryostat. PD: Amplified photodetector. L: Lense. F: Filter. TF: Tunable filter. Pol. Ctr.: Fiber-based polarization controller. SNSPD: Superconducting nanowire single-photon detectors.

1.2.1 Optical path

A sketch of the optical setup is depicted in FIGURE 1.2. The setup can be separated into the excitation, collection and microscope paths. The first path combines the various lasers used to probe the system, while the second one is intended to analyze the emitted photons from the color centers. The last path is specifically conceived to control the position of the laser beam and of the sample to image a specific area of the sample. These three paths are spatially separated by a wedged glass plate (WGP).

Excitation path

Three different lasers are used to excite the system: a tunable diode laser at 917 nm (Toptica DL pro) resonant with the spin-selective transitions of the V2 center; a laser-diode (Roitner RLT785-150MGS) operating at 785 nm used to excite the defects off-resonantly and to recapture an electron when the defect's charge state has been altered

(also called repump laser); a 2-ps-pulsed laser (PicoQuant LDH-P-C-780) operating at a central wavelength of 780 nm.

The first two laser beams are combined at a dichroic mirror (DM) before being coupled into a single-mode fiber to perfectly overlap their spatial modes. The beams are later collimated in a free-space beam path. To make sure that both beams have the same polarization, we use polarization beam splitters (PBS) to only select vertically polarized light. A half-waveplate (HWP) is used to manually control the repump laser power. Whereas the repump laser can be switched on/off rapidly using a simple TTL signal (given by a Pulse Streamer from Swabian Instruments), the resonant laser has to be kept running[2]. Thus, we used an acousto-optic modulator (AOM EQ Photonic 3200-124) which is a diffraction grating optics: upon receiving a microwave signal it splits the laser beam into different diffraction modes. This configuration has two advantages. First, by collecting the 1^{st} diffraction mode using an iris or a pinhole (P), we can effectively turn on/off the resonant laser (typically in a timescale of around 15 ns). Second, the power ratio between the 0^{th} order mode and the 1^{st} one is controlled by the microwave power, hence allowing the control of the resonant laser power used to excite the system.

It is to be noted that all three lasers cannot be used simultaneously. A flip mirror (FM) is placed in the free-space beam path which, when actuated, reflects the pulse-laser and blocks both continuous-wave (CW) lasers. To make sure that all the lasers excite the same region of the sample, we optimize the optics alignment such that both beams (reflected and transmitted) are virtually overlapping.

A wedged glass plate (WGP) separates the excitation and collection path. It transmits $\sim 97\%$ and reflects $\sim 3\%$ of the incoming light, maximizing the number of collected photons. We used the 97% of "wasted" excitation light to measure the resonant laser power with an amplified photodetector (PD), after a spectral filtering of the 780 nm laser via a 850 nm longpass filter (F). Using a self-developed python-based software, we can automatically set the resonant laser to any power reachable by the laser. An analog output of the NIDAQ card controls the output power of the AOM driver, thus changing the resonant laser power and using the PD signal as feedback. A more comprehensive description of the electronics dependency will be given in the next section.

Microscope path

The laser beams are focused onto the SiC crystal through a microscope objective with a numerical aperture of NA = 0.9 (Zeiss). The color centers fluorescence is collected through this microscope objective as well. The most efficiently excited defects will be the ones placed in the focal plane of the microscope objective. The rough positioning of the sample is performed using linear XYZ-nanopositioners (Attocube ANPx101 and ANPz101), while a more precise positioning is done via scanning the laser beams in the XY-plans of the sample using a closed-loop nanopositioning mirror tip/tilt actuator (Galvo, Mad City Labs Inc. Nano-MTA2X10, 20 nradian resolution) and an open-loop z-scanner (Attocube ANSz100) to move the sample along the z-axis. Importantly, a microwave drive is provided through a 50 µm diameter copper wire placed within a few hundreds of µm to the sample. The microwave field is generated via several

[2]The rising and falling time of the laser power being to slow for any pulsed measurements.

signal generators (Rohde & Schwarz SMIQ03b and SMIQ02b) and amplified by a 20 dB amplifier[3].

Collection path

As mentioned above, the fluorescence is transmitted through the WGP. Yet, the lasers do not only excite the color center of interest but also the material surrounding it and other color centers in its vicinity. In order to suppress as much background signal as possible, the fluorescence is spatially filtered by being focused onto a 50 µm pinhole (P) before to be recollimated. The focal point of the microscope objective is imaged onto the collimated fluorescence after the pinhole. From here, two detection schemes are present. With the FM actuated, the fluorescence is sent to a Peltier cooled spectrometer (Ocean Insight QE pro, 0.3 nm resolution) to obtain an emission spectrum of the fluorescence. In this case the signal is spectrally filtered using an 850 nm longpass filter (F). Whereas when the flip mirror is not actuated, the signal is collected into a single-mode fiber after being also spectrally filtered using a tunable longpass filter (Semrock, Versa Chrome Edge) to suppress any laser breakthrough and to only collect the phonon sideband (PSB) of the V2 centers. Finally, the coupled photons are sent to one (or two using a 50/50 fiber beam-splitter) superconducting nanowire single-photon detector(s) (SNSPD, PhotonSpot). Furthermore, as the detection efficiency of the detectors is polarization-dependent, we 3D-printed polarization controller (Pol. Ctr.) to optimize the polarization of the detected photons.

1.2.2 Electronic control

The different experimental apparatus are controlled via a self-written python-based software, called *pi3diamond*. We inherited the code from previous successful experiments conducted at our institute and built upon it to further optimize the measurement protocols and automatize tasks that were previously done manually. A sketch of all electronic dependencies is given in FIGURE 1.3.

The signal from the spectrometer is directly extracted onto our computer (PC) using a python library of the manufacturer, while the SNSPD sends a electronic pulse at each detection event, which is first processed by a time-tagger (TT, Swabian Instruments) according to the measurement protocol and then treated by our own software. The software sends digital instructions to the flip mirrors to change their positions and to the pulse streamer. The pulse streamer is used to synchronize all the devices and to control the pulse sequences, sending TTL signals to the repump/pulsed laser and also to the AOM driver. As the rising time of the microwave signal generators is rather large, the microwave signals are sent to switches (MiniCircuits, ZASWA-2-50DRA+) controlled via TTL signals from the pulse streamer.

The National Instrument card (NIDAQ) reads the analog output of the photodiode, and subsequently (after computational processing) sends an analog signal to the AOM driver to change its output power. The NIDAQ also sends an analog signal to control the positions of the z-scanner and the tilt stage. Importantly, the NIDAQ is also used to trigger the frequency change of the microwave signal generator in a pulse sequence

[3]Typical mw power level at the wire is around 15-20 dBm.

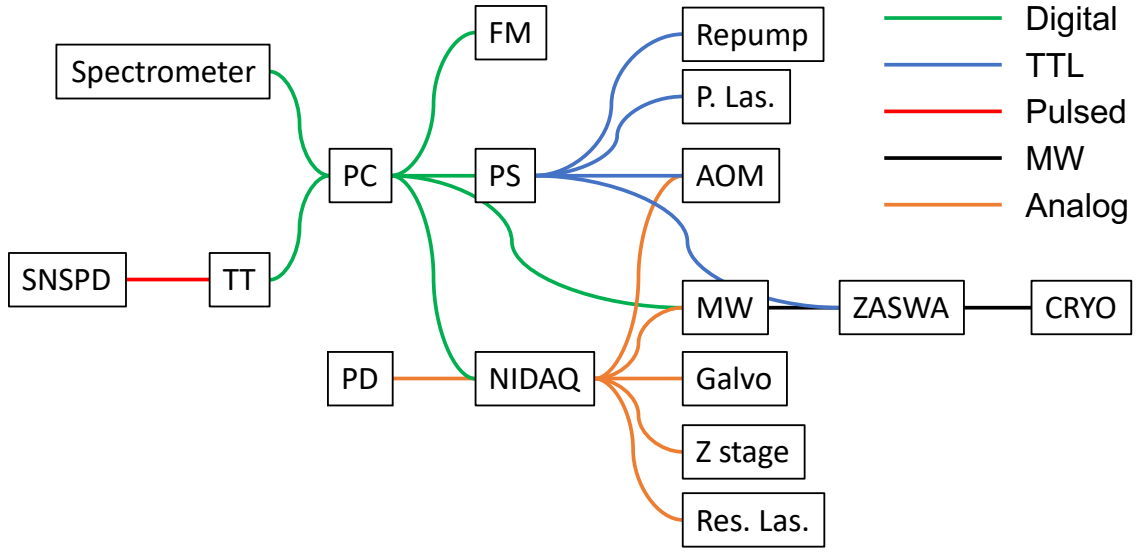

Figure 1.3: **Electronic setup.** Sketch of the dependency of the various electronic devices (drawn in rectangles) used to control the setup. The description is given in the main text. The colors of the lines correspond to the type of signal exchanged between the devices. SNSPD: Superconducting nanowire single-photon detectors. TT: Time tagger. PC: Computer. PD: Amplified photodiode. FM: Flip mirror. PS: Pulse streamer. Repump: Laser diode emitting at 785 nm. P. Las: Pulsed laser. AOM: Acousto-optic modulator. MW: Microwave source. Galvo: Closed-loop nanopositioning mirror tip/tilt actuators. Res. Las.: Tunable diode laser emitting at 917 nm. ZASWA: Microwave switch. CRYO: cryostat.

requiring a sweep of the microwave frequency. The frequency of the resonant laser can be changed by tuning the laser cavity, which is also dictated by an analog signal from the NIDAQ.

Since we answered the question "How to study?", let's answer the questions "What to study?" and "Why this system?".

1.3 Silicon vacancy in 4H-SiC

Silicon vacancies are one of the most fundamental point defects in SiC and have been observed in different polytypes such as 3C-, 4H- and 6H-SiC [104, 105, 116, 117]. It is a monovacancy, a single missing silicon atom. The lattice structure of 4H-SiC hosts two non-equivalent silicon lattice sites which gives rise to two different color centers: V1 [118] and V2 [119] for the hexagonal and cubic lattice site respectively; as illustrated in FIGURE 1.4**a**. As a sidenote, we mention that 6H-SiC hosts two different hexagonal sites with color centers labeled V1 and V3 for the sites k1 and k2, respectively [120].

High-energy particle irradiation is used to generate V_{Si} within the crystal lattice. The particles can be for example, electrons [43, 118], protons [57, 122], neutrons [123, 124] or ions [56, 58]. The irradiation will create a localized homogeneous distribution of defects in a given volume of the crystal depending on the particles, their energies

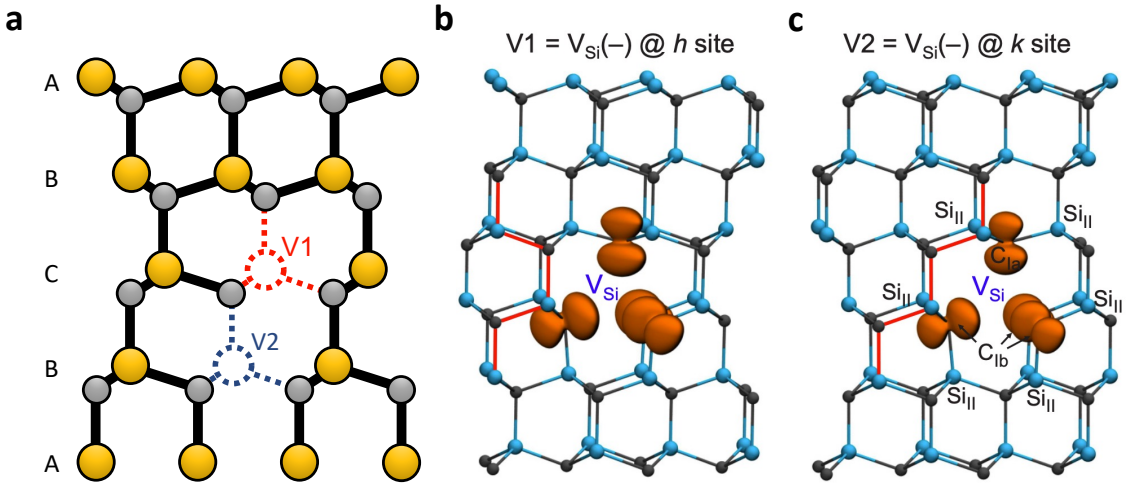

Figure 1.4: **Silicon vacancy in 4H-SiC. a** Crystal structure of 4H-SiC. The V1 (V2) center is formed by a missing silicon atom at a cubic (hexagonal) lattice site **b** (**c**) Spin density model, orange lobes, of the V1 (V2) center. Adapted from [121].

and the irradiation doses [125]. Direct femtosecond laser writing can also be used to create single V_{Si} defects [55, 126]. A deeper study on defect generation via particle bombardment will be given in Chapter 3.

1.3.1 Electronic structure

The theoretical energy level is derived from group theory and has been obtained in [117]. The missing silicon atom, in both hexagonal (V1) and cubic (V2) lattice sites of 4H-SiC, results in four dangling bonds from the nearest neighbors (carbon atoms). The symmetry of the system: C_{3v}, corresponding to a symmetry per rotation of an angle of 120° and 240°, is preserved independently of charge state the V_{Si} center. A spin density representation of the electrons wavefunctions can be seen in FIGURE 1.4**b,c** (adapted from [121]). The dangling bonds form two a_1 and one e levels. The first a_1 level is within the valance band while the second one as well as the e level are within the bandgap. In the case of negatively charged V_{Si}, five electrons are distributed between these three levels. One possible distribution of the electrons is two electrons in the lowest a_1 level, one electron in the second a_1 level and finally two electrons in the e level. This particular repartition would be written as $a_1^2 a_1^1 e^2$ and is believed to be the ground state of V_{Si} center [117]. It is a spin quartet $^4A_2$ with a total spin: $S = 3/2$. The electronic structure of the ground state is given in FIGURE 1.5**a**. The first and second excited states of V_{Si} arise when an electron is promoted, via absorption of a photon, from the lower a_1 level to the second a_1 level $^4A_2$ ($a_1^1 a_1^2 e^2$) or to the e level ^4E ($a_1^1 a_1^1 e^3$). The first excited state corresponds to the V_i and the second one to the V_i' ($i \in \{1, 2\}$). Even though the V_2' has been theoretically predicted, it has not yet been observed experimentally.

A more recent study of the V_{Si} center [127] provides a more complex energy level structure with the description of intersystem-crossing states (ISC): metastable-state

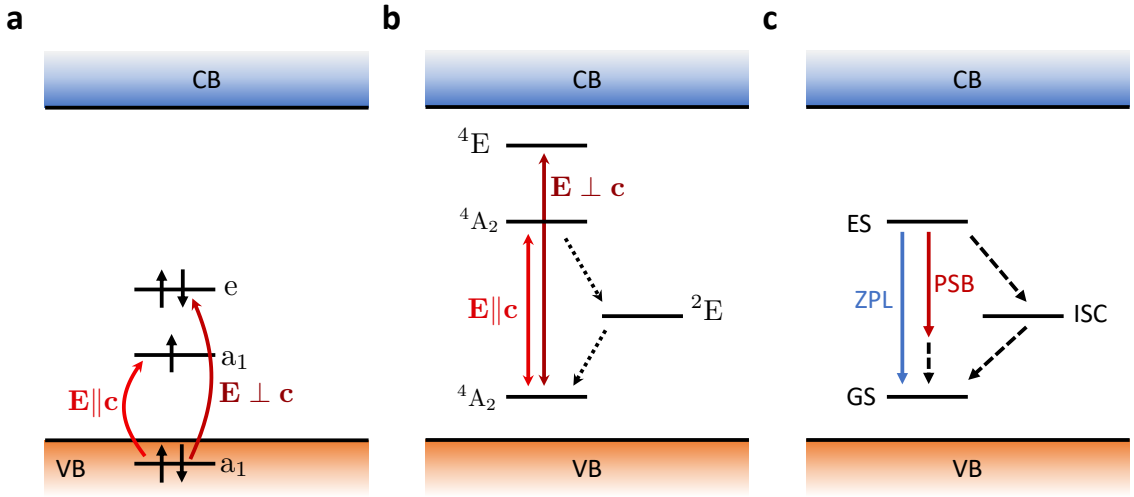

Figure 1.5: **Band diagram of V_{Si} centers. a** Distribution of the five electrons of the negatively charged V_{Si} in the ground state. The red arrows correspond to the electron promotion pathways from the first a_1 level to the second a_1 or the e level to form the first or second excited state, respectively. The electronic transition corresponds to optical transitions with the polarization given in the sketch. **b** Energy levels of the V_{Si} within the bandgap of the material with their respective symmetries. The red solid arrows represent the optical transitions (with their polarization) from the ground state to the first (second) excited state: V_i (V_i'). The decay channels from and to the metastable state are illustrated as dotted lines. **c** Representation of the decay pathways from the first excited state (ES) to the ground state (GS). Either the system emits a photon with or without emission of phonons, the photon is then within the zero-phonon line (ZPL) or the phonon sideband (PSB), respectively. The system can also decay non-radiatively through the intersystem-crossing states (ISC).

manifold that are coupled to the ground and first excited state.

To understand the dynamics of such a system, we need to look at the allowed transitions between the levels. From group theory and experimental findings [117, 118], we know that the optical transition from the $^4A_2$ ground state to the $^4A_2$ excited state is polarized along the *c*-axis of the crystal, while the one to the ^4E excited state is polarized perpendicular to the *c*-axis. Furthermore, the system can also decay from the first excited state to the ground state through one of the metastable states: a ^2E multiplet[4].

A general sketch of the energy level structure for both V_{Si} in 4H-SiC is shown in FIGURE 1.5**b** together with their optical transitions.

1.3.2 Fluorescence properties

Both negatively charged silicon-vacancy centers in 4H-SiC have shown fluorescence in the near-infrared region [43, 118, 128, 129]: 861 nm for the V1 center and 917 nm

[4]The other states can be considered in a rate model as deshelving states, however in this manuscript we will only take into account the ISC as a spin-mixing long-live state.

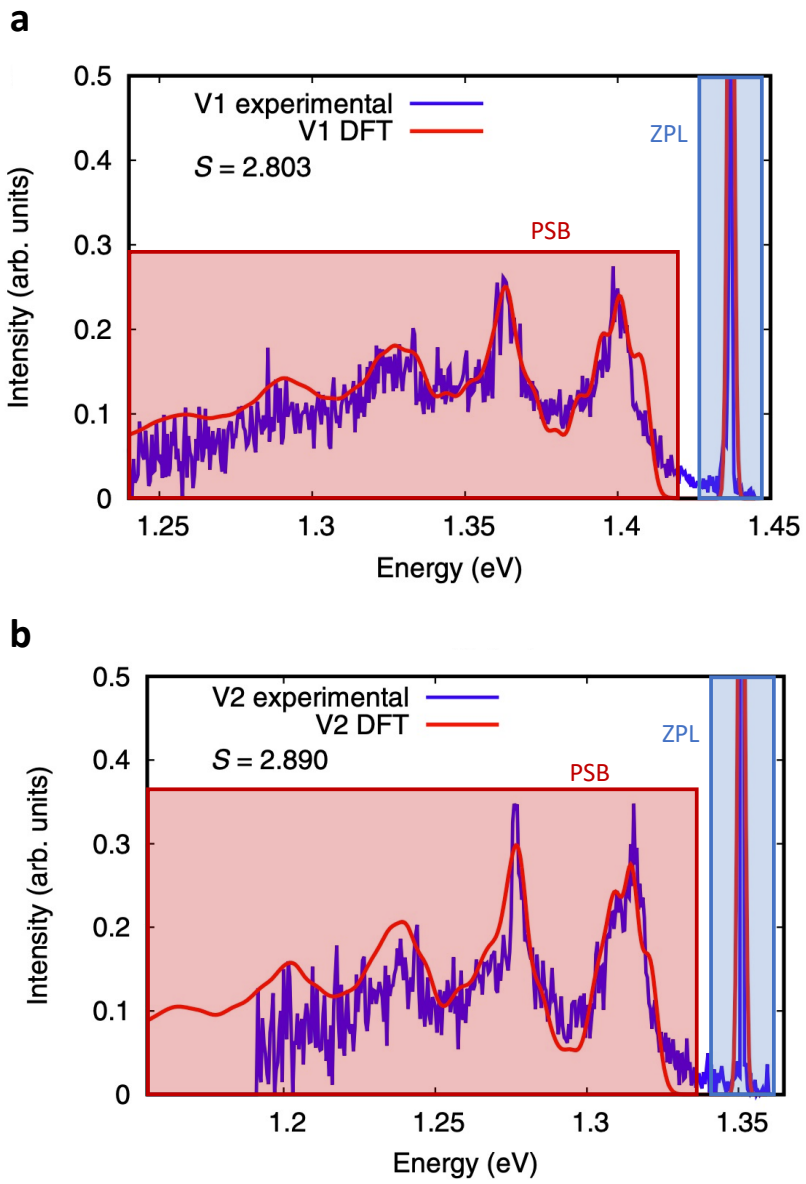

Figure 1.6: **V_{Si} centers emission spectra. a** (**b**) Typical emission spectra of a V1 (V2) color center. The blue lines are the experimental data and the red lines are calculated emissions using Huang-Rhys theory [132]. The red (blue) transparent box visualizes the ZPL (PSB) part of the spectrum. Adapted from [45].

for the V2 center. An emitted photon could then be relatively easily converted to a telecom C-Band photon ($\sim$ 1550 nm); to be compatible with existing fiber network, via frequency conversion. Indeed, it would correspond to less than frequency doubling such as a pump power would be far longer than the target frequency and would not lead to an excessive photonic noise at the converted wavelength. Such techniques have already been implemented for quantum dots [130] using a pump beam at 2.2 µm. Following recent nanophotonic device fabrications in SiC [36, 47, 48, 131], the frequency conversion could be realized on-chip in an integrated quantum node.

Emission spectra of both V_{Si} can be seen in FIGURE 1.6**a,b**. They have been obtained during an international collaboration between the groups of Prof. Vučković (Stanford), Prof. Wrachtrup (Stuttgart) and Prof. Gali (Budapest). The University of Stuttgart provided a working sample to the E. L. Ginzton Laboratory with whom we[5] analyzed the spin-optical properties of the V1 and V2 centers and the theoretical analysis of the results has been conducted by the Budapest university (P. Udvarhelyi and G. Thiering). The results obtained in this collaboration have been summarized in [45].

The defects studied were situated a few micrometers apart and cooled down at 4 K. Subsequently, they were excited using a continuous-wave off-resonant optical excitation at 730 nm, the fluorescence was sent to a spectrometer (see FIGURE 1.2). Both spectrum (FIGURE 1.6**a,b**) present similar features: a sharp peak at 1.44 eV (V1) or 1.35 eV (V2) then a series of broad peaks. The first peak corresponds to the zero-phonon line (ZPL), when photons are emitted during the decay of the system from the excited to the ground state without the emission of phonons. The other photons emitted correspond to decay channels in which phonons are emitted at the same time as photons (hence lower energies of the emitted photons), those photons are in the phonon sideband (PSB). A sketch of the different decay channels can be seen in FIGURE 1.5**c**. The experimental spectra are fitted using Huang-Rhys theory [132], which accounts for the interaction strengths between the electronic bounds and crystal phonons. To do so our collaborators employed a simplified Franck-Condon principle [133, 134].

From this analysis, we can extract the Debye-Waller factor (DWF): the ratio of ZPL emission to the total photoemission. For both centers the DWF obtained using the fit parameters is around 6%, while the one measured using the experimental data is about 8% and 9% for V1 and V2 respectively. Those results are similar to independently reported measurements [135]. However, it deviates from older reported value (40%) [118] as the previous spectra did not cover the full extent of the phonon sideband. As we will see in Chapter 2, this information allows us to estimate the efficiency of a given entanglement protocol.

Another important property of a given electron spin system is the excited state lifetime, as this will directly translate into the linewidth of emitted photons. It has been estimated to be around 6 ns [118, 124, 129] for both the V1 and V2 center in 4H-SiC. In Chapter 3, we have measured an excited state lifetime around 7 ns, thus on par with previous measurements.

1.3.3 Spin Hamiltonian

As stated earlier, the ground and excited states are spin quartets with a total spin of: $S = 3/2$, thus allowing the electron spin system to be in four different spin sublevels: $m_s \in \{-3/2, -1/2, +1/2, +3/2\}$ (where m_s is the spin quantization along the z-direction[6]). The general Hamiltonian describing an electron spin quartet system [136, 137] is

$$\mathcal{H} = \mathcal{H}_{\text{ZFS}} + \mathcal{H}_{\text{EZ}}, \tag{1.1}$$

[5] The experiments have been realized by N. Morioka, D. Lukin and I.

[6] here, the c-axis of the crystal.

where $\mathcal{H}_{\text{ZFS}}$ and $\mathcal{H}_{\text{EZ}}$ are the zero-field splitting (ZFS) and electron Zeeman (EZ) contributions. The so-called zero-field splitting corresponds to a level splitting occurring even without any external electromagnetic field. It is due to the interaction between the unpaired electron spins, a more detailed spin-spin interaction model given in [138]. The ZFS is characterized by the tensor $\mathbf{D}$:

$$\mathcal{H}_{\text{ZFS}} = \widetilde{\mathbf{S}}\mathbf{D}\mathbf{S}, \tag{1.2}$$

where $\mathbf{S}$ is the vector of the spin operators $\mathbf{S} = (\hat{S}_x, \hat{S}_y, \hat{S}_z)$ and $\mathbf{D}$ is the following tensor:

$$\mathbf{D} = \frac{1}{2}\begin{pmatrix} -\frac{D}{3} + E & 0 & 0 \\ 0 & -\frac{D}{3} - E & 0 \\ 0 & 0 & \frac{2D}{3} \end{pmatrix}. \tag{1.3}$$

D and E are the longitudinal and transversal crystal field splitting parameters, such that:

$$\mathcal{H}_{\text{ZFS}} = D\left(\hat{S}_z^2 - \frac{1}{3}S(S+1)\right) + E\left(\hat{S}_x^2 - \hat{S}_y^2\right). \tag{1.4}$$

For V_{Si} in SiC, without crystal strain, we have $E \ll D$ [105, 139]; thus:

$$\mathcal{H}_{\text{ZFS}} = \begin{pmatrix} D & 0 & 0 & 0 \\ 0 & -D & 0 & 0 \\ 0 & 0 & D & 0 \\ 0 & 0 & 0 & -D \end{pmatrix}. \tag{1.5}$$

The ZFS keeps the state $|\pm 1/2\rangle$ and $|\pm 3/2\rangle$ degenerate with an energy difference of $2D$ between the two spin doublets. Using different experimental protocols, at room and cryogenic temperatures, the zero-field splitting has been estimated for the ground and excited states of both, the V1 and V2 centers [40, 45, 119, 140, 141]. Interestingly, both color centers have approximately the same excited state zero-field splitting of around 1 GHz, while their ground state zero-field splitting differs quite significantly with 4.5 MHz compared to 70 MHz for V1 and V2 respectively. The sign of the D parameter for the ground and excited states have been measured to be the same [142], whereas the absolute sign is still debated. In this manuscript, we will assume that D is positive[7]. The spin-sign degeneracy is lifted in the presence of an external magnetic field via the electron Zeeman term:

$$\mathcal{H}_{\text{EZ}} = \tilde{\gamma}_e\, \mathbf{B}\hat{\mathbf{S}}. \tag{1.6}$$

$\mathbf{B}$ is the external magnetic field and $\tilde{\gamma}_e = g_e\mu_b/\hbar$ is the gyromagnetic ratio, predicted to be the same for all ground and excited states: 2.8 MHz/G [39, 40]. Let us assume the magnetic field lies in the (X,Z) plane: $\mathbf{B} = B\sin(\theta)\mathbf{e_x} + B\cos(\theta)\mathbf{e_z}$. Then the full Hamiltonian, equation (1.1), can be written as:

$$\mathcal{H} = D(\hat{S}_z^2 - \frac{1}{3}S(S+1)) + \tilde{\gamma}_e B\cos(\theta)\hat{S}_z + \tilde{\gamma}_e B\sin(\theta)\hat{S}_x. \tag{1.7}$$

[7] If a tree falls in a forest and no one is around to hear it, does it make a sound?

If $\theta \neq 0$, then the eigenstates of the Hamiltonian of the two spin quartets are different due to the difference in the ZFS, mixing the spin states in distinct manners. Thus, for most experiments, the magnetic field is aligned along the c-axis of the crystal ($\theta = 0$), see Appendix D. This lift the spin state degeneracy via the Zeeman effect while conserving the spin states $|m_s\rangle$ as eigenstates of both the ground and excited state Hamiltonians. A sketch of the energy levels for the ground and excited states of the V2 center under a magnetic field of $B = 0$ G and $B \neq 0$ G is depicted in FIGURE 1.7**a**. Similar to the magnetic field, the electric field also impacts the energy levels of the electron spin system via the Stark effect [60, 61]. However, in all of our experiments, we worked without any applied external electric field, thus, this energy contribution will only be discussed in the scope of spectral diffusion in section 2.4.

1.3.4 Electron spin transitions

The optical transitions from the ground to the excited states are spin-conserving and are conventionally labeled[8] A_1 and A_2 for the transitions $|\pm 1/2\rangle_{gs} \leftrightarrow |\pm 1/2\rangle_{es}$ and $|\pm 3/2\rangle_{gs} \leftrightarrow |\pm 3/2\rangle_{es}$, respectively, as seen in FIGURE 1.7**a**. Thanks to a similar gyromagnetic ratio in both spin quartets, the energy differences of the optical transitions are independent of the magnetic field strength, so we have:

$$f_{A_1} = \Delta - (D_{gs} + D_{es}), \tag{1.8}$$
$$f_{A_2} = \Delta + (D_{gs} + D_{es}). \tag{1.9}$$

Where Δ is the energy difference between the ground and excited state. The splitting between the optical transitions is then a fixed parameter:

$$f_{A_2} - f_{A_1} = 2D_{gs} + 2D_{es} \sim 1 \text{ GHz}. \tag{1.10}$$

We currently do not know how to tune this frequency difference, which will turn out to be a limitation of the system as discussed in Chapter 2. It is to be noted, that the system can also be optically excited using an off-resonant laser, operating at 780 nm for example, addressing every optical transition.

The ground state spin transitions ($\Delta m_s = \pm 1$) can be addressed via a microwave field resonant with the energy difference. The theoretical framework for this is introduced in Appendix E. The microwave transitions are labeled ν_1, ν_2, ν_3, see FIGURE 1.7**a**. In the presence of a magnetic field $\mathbf{B}$ aligned along the c-axis of the crystal, the transitions are equal to:

$$|-3/2\rangle \leftrightarrow |-1/2\rangle : \quad \nu_1 = |2D_{gs} - \tilde{\gamma}_e B|, \tag{1.11}$$
$$|-1/2\rangle \leftrightarrow |+1/2\rangle : \quad \nu_2 = \tilde{\gamma}_e B, \tag{1.12}$$
$$|+3/2\rangle \leftrightarrow |+1/2\rangle : \quad \nu_3 = 2D_{gs} + \tilde{\gamma}_e B. \tag{1.13}$$

The frequency dependency as a function of the magnetic field is plotted in FIGURE 1.7**b**. Interestingly, after a given magnetic field (B_0^{gs}) the difference $\nu_3 - \nu_2$ and

[8] The subscripts are not linked to the type of V_{Si} center, both the V1 and V2 centers have an A_1 and A_2 transitions.

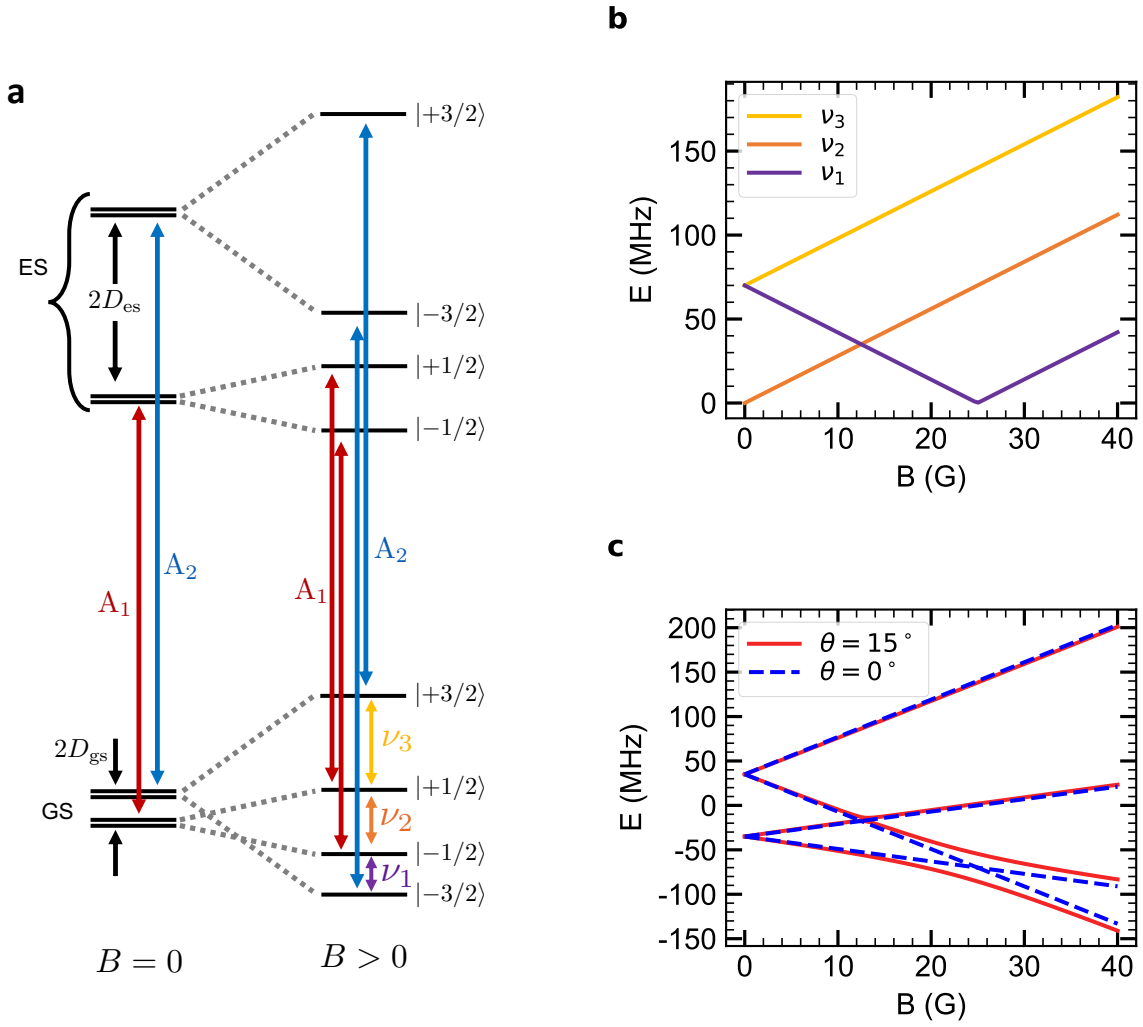

Figure 1.7: **Energy level diagram of V_{Si} center.** **a** Energy level diagram of V_{Si} centers without (left) and with (right) an external magnetic field applied along the c-axis. The ground (GS) and excited states (ES) are spin quartets linked via spin-conserving optical transitions (A1, red; A2, blue). The magnetic field lifts the Kramers degeneracy in the ground and excited state, allowing to address each ground state microwave transition (ν_i, color-coded). **b** Ground state transition frequencies for the V2 center according to the magnetic field strength (parallel to the c-axis); based on the equations (1.11). The frequencies are color-coded according to the color scheme introduced in **a**. **c** Eigenvalues of the V2 ground states for a tilted magnetic field (angle color-coded). For $B = 25$ G, the ground states are mixing when the magnetic field is not parallel to the c-axis, hence the anticrossing observed.

$\nu_2 - \nu_1$ is constant and equal to $4D_{gs}$. The spin system at $B = B_0^{gs} = 2D_{gs}/\tilde{\gamma}_e$ is at the ground state level anti-crossing (GSLAC): if $\theta = 0$ both spin states $|-3/2\rangle$ and $|-1/2\rangle$ have the same energies; yet any small misalignment of the magnetic field will lift the degeneracy where the eigenstates are coherent superposition of the states $|-3/2\rangle$ and

$|-1/2\rangle$. A simulation of the eigenvalues (energies) of the Hamiltonian for $\theta = 0$ and $\theta = 15°$ is shown in FIGURE 1.7**c**, where we can see the energies not "crossing" for $\theta \neq 0$, hence the name anti-crossing. The same phenomenon happens for the excited states, however at a much higher magnetic field: $B = B_0^{es} = 2D_{\text{es}}/\tilde{\gamma}_e$. For example for V2:$B_0^{gs} = 25$ G while $B_0^{es} = 356$ G. A possible application of the anti-crossing will be explored in section 1.5.1.

Now we will explain the two main experimental protocols to characterize the spin-optical transitions of a single V_{Si} at low temperature: optically detected magnetic resonance (ODMR) and photoluminescence excitation (PLE) scan.

ODMR

To understand this protocol, we will place ourselves in the absence of any magnetic field such that the Kramers doublets are degenerates. As seen in FIGURE 1.8**a**, if the electron spin is in the states $|\pm 3/2\rangle_{\text{gs}}$ and is continuously excited along the resonant optical transition A_2, after few cycles (leading to photoemission) between the ground and excited states, the electron spin will end up in the ISC, from which the system can decay, with equiprobability, in all four spin states. The system has a 50% chance to be in the states $|\pm 3/2\rangle_{\text{gs}}$, in which the system cannot be re-excited anymore and is *dark*. Studying the probability tree diagram one find that the system will always end up in the dark subspace under continuous resonant laser excitation. However, if a microwave (mw) radiation, resonant with the zero-field splitting ($2D_{\text{gs}}$), is simultaneously applied, the system will be driven back to bright subspace and will emit photons again.

So we see that under continuous resonant laser and mw excitation, the system will emit a constant photon flux. However, if the microwave is not in resonance with the ground state transition the system will not be able to emit photons. Hence the experimental protocol, shown in the inset of FIGURE 1.8**b**, which consists of a microwave frequency sweep under resonant optical excitation. A typical ODMR signal is shown in FIGURE 1.8**b**. The maximum of the fluorescence corresponds to the zero-field splitting 70 MHz. Due to spin-dependent rates, this protocol can also be used with an off-resonant laser (e.g. 780 nm). Even though this technique can be used at any temperature, it leads to drastically reduced contrast. As such, if each spin-transition can be addressed separately, it is preferred to use a resonant laser.

In the case of a non-zero magnetic field, the levels are split, and following the same thought process, if the system is under continuous laser and mw excitation, for example along A_2 and ν_1, respectively, the spin system will end up in the state $|+1/2\rangle_{gs}$: a steady state, from which the color center cannot be re-excited. This allows initialization of the spin system [40] in a few tens of microseconds with fidelity up to 98 %. Therefore, in the presence of an external magnetic field, two microwave radiations are required: one fixed at a given frequency resonant with one of the transitions while the second one can be swept across the two other transitions. FIGURE 1.8**c** shows a more refined protocol, where we can measure all three transitions in a single frequency scan. To do so, while the first microwave is tuned across the transitions ν_i, the second microwave is resonant with the transition $\nu_{(i+1)\equiv 3}$. An ODMR signal acquired at a magnetic field of $B = 36$ G using this protocol is shown in FIGURE 1.8**d**, revealing all three ground state transitions.

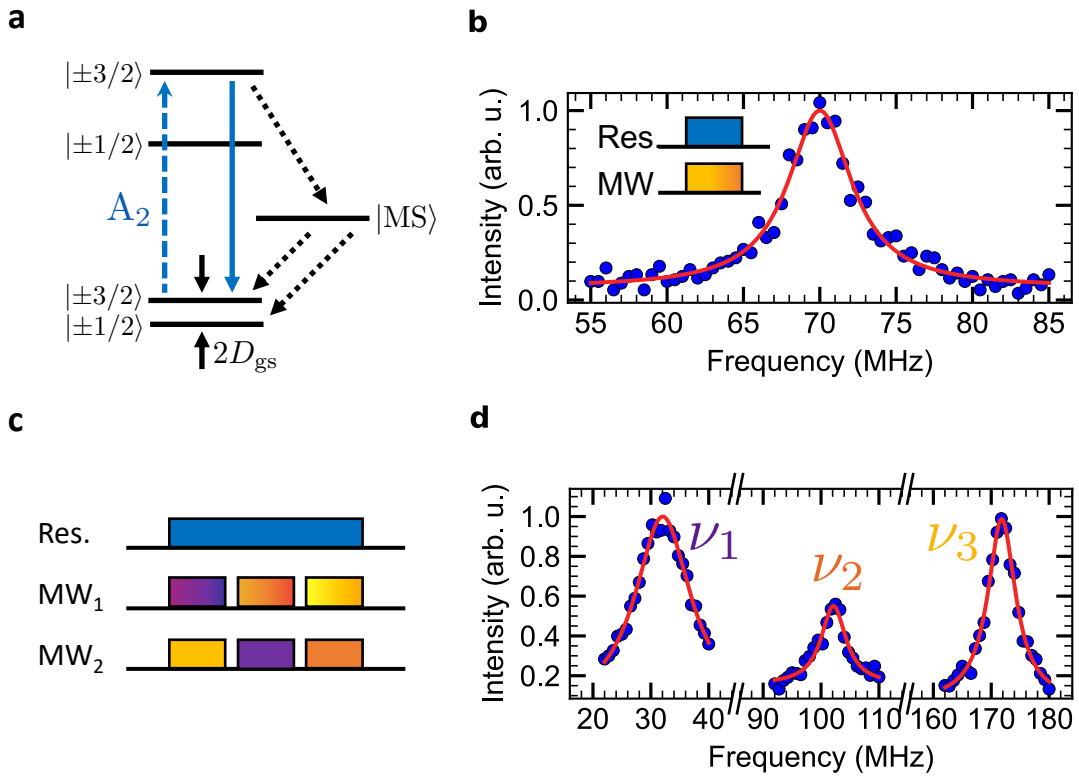

Figure 1.8: **Optically detected magnetic resonance.** **a** Model of the spin system evolution. Thanks to spin flips occurring in the metastable states, under continuous laser excitation along the A_2 transition the states $|\pm 1/2\rangle_{gs}$ are steady states of the system. **b** ODMR signal (blue dots) of the ground state fitted with a Lorentzian function (red line) in the absence of a magnetic field. Inset: pulse sequence, the microwave frequency is tuned while the system is continuously excited with a laser resonant with the A_2 transitions. The maximum of the signal corresponds to the zero-field splitting of the ground states $2D_{gs}$. **c** Pulse sequence needed to measure all three ground state transitions (ν_i) in a single scan. The microwave has two frequency components. The first is tuned across all three transitions while the second one will take successively the value of an other transition to avoid spin pumping. E.g. to measure the ν_1 transition, the second microwave is resonant with the ν_3 transitions. **d** ODMR signal for a non-zero magnetic field ($B = 36$ G). Each local maximum corresponds to a ground state microwave transition (labeled).

PLE

Photoluminescence excitation (PLE) scan is similar to an ODMR experiment, see Figure 1.9**b**. But instead of scanning the microwave frequency, the resonant laser frequency is swept, while the microwave radiation is resonant with the relevant ground states transitions. Two microwave sources are then required in the presence of a magnetic field, see Figure 1.9**a**. A peak in the fluorescence is observed when the laser is in resonance with an optical transition. A typical series of PLE scans can be see in Figure 1.9**c**, and the sum of all the scans is displayed in Figure 1.9**d**. Two peaks

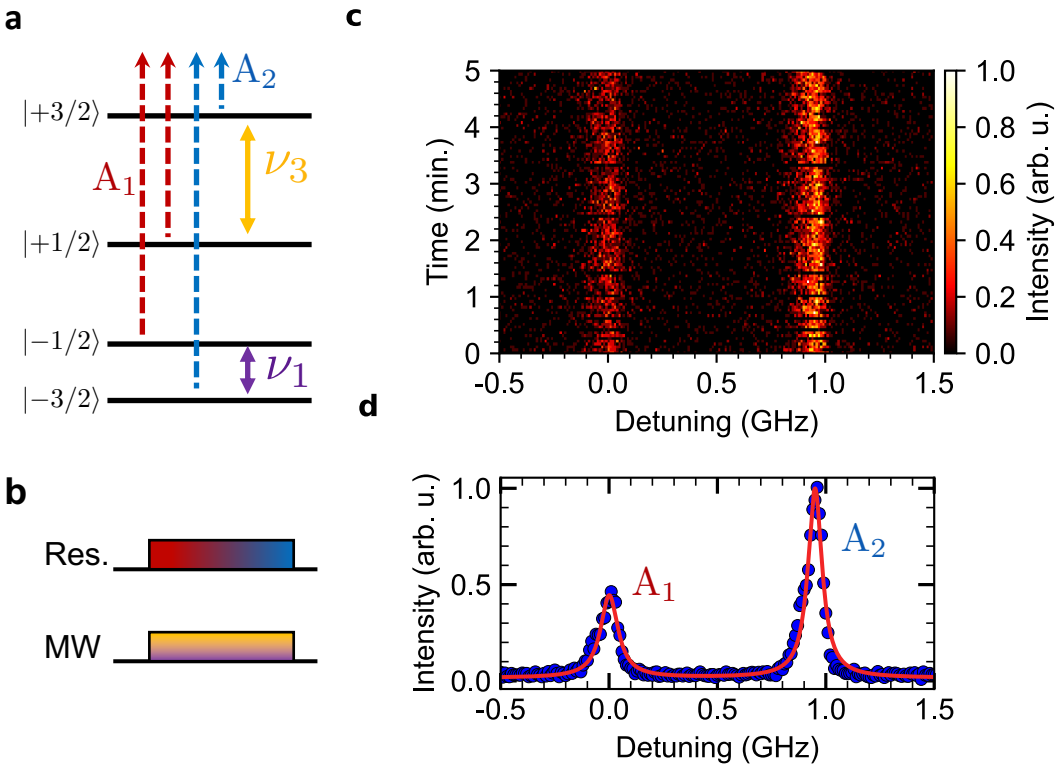

Figure 1.9: **Photoluminescence excitation scans.** **a** Sketch of the relevant ground state transitions for PLE measurements in the presence of an external magnetic field. **b** Sketch of the PLE protocol: the frequency of the resonant laser is scanned across both optical transitions (A_1 and A_2) while the microwave field drives the ground state transitions $|\pm 3/2\rangle \leftrightarrow |\pm 1/2\rangle$ (ν_1 and ν_3) simultaneously. **c** Repeated resonant excitation scans for 5 minutes. The scans are vertically stacked, and the measured intensity is color-coded. No frequency drift is observed. **d** Sum of each measured scan (blue dots). The data is fitted with a double Lorentzian (red line) from which we yield a full width at half maximum (FWHM) of 98 ± 5 MHz and 78 ± 2 MHz for the A_1 and A_2 transitions, respectively.

separated by 1 GHz can be seen, the splitting corresponds to the energy difference between the spin-conserving optical transitions (1.10). Furthermore, the left and right peaks correspond to the A_1 and A_2 transitions respectively and they are narrow (80 MHz broad) and stable over time.

As described so far, the methods to measure the energy ν_i and A_i are interdependent, like an Ouroboros: one wouldn't know where to start, as we need ODMR to do a PLE and vice-versa. However, for the PLE scans, we can use a low intensity off-resonant laser to mix the state with the ISC having a similar effect to microwave driving, as a spin-mixing mechanism. Further, as we often start to characterize a sample without any magnet, the ground state transition is known to be $2D_{gs}$, and we introduce a magnet in a second step, to lift the degeneracy at a point when the optical transitions are known for a given defect. While we observe a distribution of the optical lines [42],

the ground state transitions are robust and are the same for all V_{Si} at a given magnetic field. Therefore, once the microwave transitions are known at a given magnetic field, we can investigate the optical transitions of other color centers using PLE scans.

In this section, we have described the V_{Si} in SiC and how we can characterize its spin-optical properties combining microwave and laser radiations. In the next section, we will show how one can use color centers as stationary qubits and why they are relevant in quantum information processing.

1.4 DiVincenzo's criteria

To utilize a given spin system as a stationary qubit in any given quantum protocols, here for quantum information processing, the system has to demonstrate few key elements summarized in the DiVincenzo's criteria [143]:

(1) Initialization capability.

(2) Ability to readout the qubit state.

(3) A set of *universal* quantum gates.

(4) Long-lived quantum state, compared to the time of a given protocol.

(5) Strong spin-photon interface.

The criteria (5) is unique to quantum communication protocols. In the following sections, we will show why, if we define the qubit as: $|0\rangle = |+1/2\rangle_{gs}$ and $|1\rangle = |+3/2\rangle_{gs}$ from the V_{Si} center, most of the criteria are fulfilled. We already explored the way to initialize the system in the above manuscript (1) [40]. Further, we can distinguish between the states $|+1/2\rangle_{gs}$ and $|+3/2\rangle_{gs}$ using a laser excitation resonant with the A_1 transition: the system will be bright or dark according to its spin state (2). The efficiency of this readout protocol will be further discussed at several points in this manuscript (section 2.3 and section 5.5). We will now study how to deterministically manipulate the electron spin (3) and examine the coherence time of the system (4).

1.4.1 Coherent manipulation of single V_{Si} center

The qubit state can be deterministically and coherently manipulate utilizing microwave control, see Appendix E. To demonstrate our ability to control the qubit state experimentally, one can induce Rabi oscillations between the states $|0\rangle$ and $|1\rangle$. If the electron spin system is initially in the state $|0\rangle$ then after a time τ under continuous microwave drive at ν_3, the state of the V_{Si} center is [144]:

$$|\Psi(\tau)\rangle = \cos\left(\frac{\Omega_R \tau}{2}\right)|0\rangle + \sin\left(\frac{\Omega_R \tau}{2}\right)|1\rangle\,, \tag{1.14}$$

where Ω_R is the Rabi frequency, proportional to the square root of the microwave power. We can define the $\pi/2$ and π times as relevant driving times after which the qubit state is sent from the state $|0\rangle$ to the states $|+\rangle = (|0\rangle + |1\rangle)/\sqrt{2}$ and $|1\rangle$

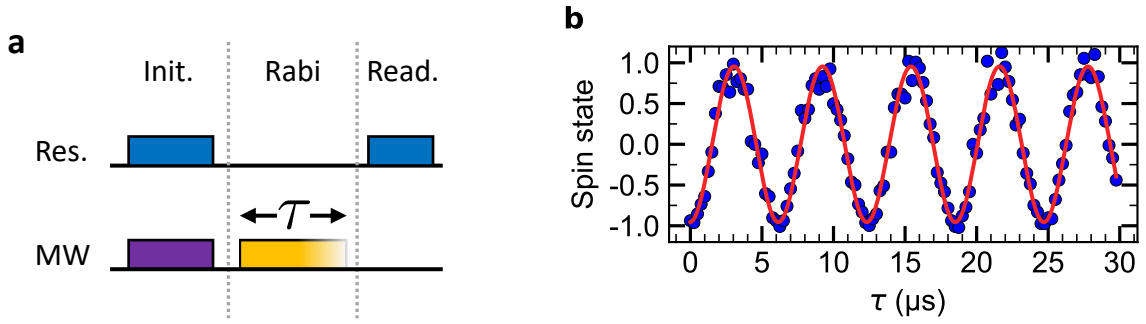

Figure 1.10: **Rabi oscillation. a** Sketch of the Rabi cycle protocol. The system is initialized in the state $|+3/2\rangle$, then a microwave pulse along the ν_3 transition is applied for variable times. The spin system is then read out in the state $|+3/2\rangle$. **b** Rabi oscillation for a V2 center. The spin state $+1$ corresponds to $m_s = 3/2$ and -1 to $m_s = 1/2$.

respectively. To read out the spin state, we use resonant laser excitation (along A_2); the protocol to observe Rabi oscillation is given in FIGURE 1.10**a** and a typical signal, performed on a V2 center at 10 K, in FIGURE 1.10**b**. The $\pi/2$ time is 3.091 ± 0.006 μs and the π time is 6.182 ± 0.012 μs. The high contrast of $95.5 \pm 0.1\%$ underlines the high control we have over the electron spin state.

Equation (1.14) corresponds to a rotation around the Y axis in the Bloch sphere representation. By controlling the phase of the microwave field we can change the rotation axis in the (X, Y) plane. Finally, free evolution with the Hamiltonian given in (1.7) allows the spin to precess around the Z axis, such that we are able to perform rotations around the 3 main orthogonal axes (X, Y, Z) and, by combining those, rotation around any axis. As we will see in Chapter 5, we can perform CNOT gates on a two-qubit system, thus fulfilling the third DiVincenzo's criterion (3).

1.4.2 Spin coherence

Thanks to our ability to initialize and coherently manipulate the quantum state of the V_{Si}, we can measure the dephasing (T_2^*) and coherence (T_2) times. The protocols to measure those characteristic times are similar: after being initialized in the state $|0\rangle$, the system undergoes two $\pi/2$-pulses separated by a time interval τ before being read out in the state $|0\rangle$ via a resonant laser pulse. Experimentally, to increase the signal-to-noise ratio and avoid background noise, the last microwave pulse is alternatively[9] a $\pi/2$ or $3\pi/2$-pulse, to read out if the electron spin is in the states $|0\rangle$ or $|1\rangle$; both signals are then subtracted. The only difference between a free induction decay experiment (to measure T_2^*), and a Hahn echo experiment (to measure T_2) is that for the latter, a refocusing pulse (π-pulse) is performed halfway through the waiting time τ. The pulse sequences for both experiments are given in FIGURE 1.11**a**,**c**.

With decoherence sources, for example, electromagnetic field noise or dipole-dipole interaction with other spins (electron or nucleus) in the crystal lattice, the qubit state

[9] In successive experimental realization.

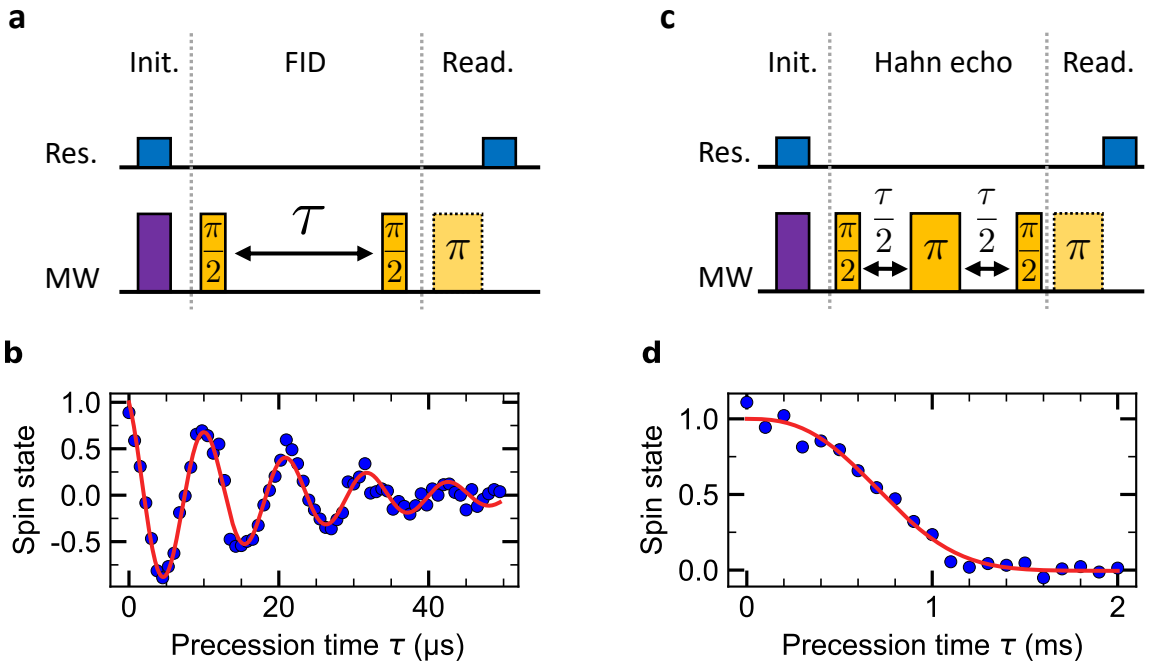

Figure 1.11: **Spin properties.** **a** Sketch of the free induction decay (FID) protocol. explained in the main text. **b** Spin dephasing time of a V2 center. The fit (red line) of the data (blue dots) yields $T_2' = 21 \pm 1$ μs. **c** Sketch of the Hahn echo sequence. It is similar to the FID but has an extra π-pulse in the middle of the free evolution. **d** Spin coherence time of a V2 center. The fit (red line) to the data (blue dots) yields $T_2 = 0.85 \pm 0.03$ ms. For both, **b** and **d**, the spin state $+1$ corresponds to $m_s = 3/2$ and -1 to $m_s = 1/2$.

will lose some of its purity over time, until no coherence is left. The time scale of the decaying envelope (see FIGURE 1.11**b**) in a Ramsey interferometry experiment is called the dephasing time: T_2^* while the decay time in the Hahn echo experiment (see FIGURE 1.11**d**) is the coherence time: T_2. The oscillation seen in the free induction decay comes from a frequency mismatch between the microwave source and the energy difference of the qubit, strongly coupled nuclear spins also contribute to the oscillation.

For the V_{Si} in 4H-SiC, a coherence time of 0.8 ms at low temperatures and at least 160 μs at room temperature have been reported [40, 43]; on par with other solid-state spin systems and adequate for to entanglement protocols (4). We measured, as seen in FIGURE 1.11**b**,**d** typical dephasing times of 21±1 μs, and coherence times of 0.85±0.03 ms for bulk defects at 10 K. Furthermore, strategies exist to increase the coherence times, i.e the time a coherent state can survive, using decoupling sequences [63, 110] or utilizing nuclear spins in the defect's vicinity as a quantum information storage [24]. These aspects will be discussed in Chapter 5.

1.5 Spin-photon entanglement scheme

The question about the strength of a spin-photon interface is complex: the system should be able to transfer its quantum information to a photon and vice versa. Furthermore, this process should be near-deterministic to be usable for real-world quantum applications. The first point will be discussed in this section, where a spin-photon entanglement protocol will be given, while the second will be extensively discussed in Chapter 2.

1.5.1 λ-scheme

Several experiments [145, 146, 147, 148] have demonstrated the possibility of using λ-schemes to transfer and store the information from and to a photon. A λ-scheme is a three-level system with two electric-dipole transitions: $|1\rangle \leftrightarrow |3\rangle$ and $|2\rangle \leftrightarrow |3\rangle$ while the transition $|1\rangle \leftrightarrow |2\rangle$ is forbidden[10]; see FIGURE 1.12**a**.

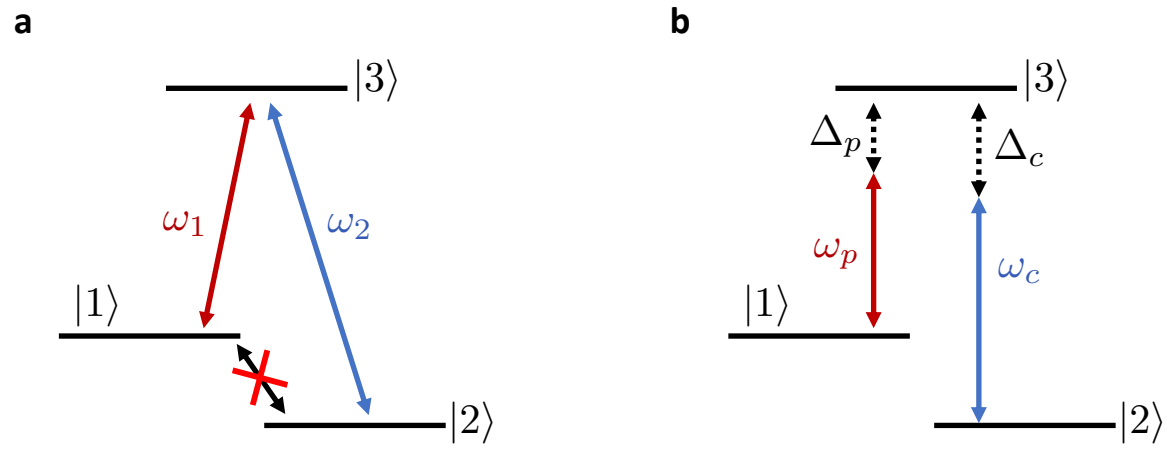

Figure 1.12: **λ-scheme. a** Sketch of a λ-system: three-level system composed of an excited state ($|3\rangle$) and two ground states ($|1\rangle, |2\rangle$). The two electric-dipole transitions are shown with colored arrows (frequencies: ω_i). **b** Representation of the lasers used to create a coherent population trapping. A probe (control) lasers at frequency ω_p (ω_c) detuned from the resonant transition ω_1 (ω_2) by Δ_p (Δ_p).

The excited state $|3\rangle$ can radiatively decay to both ground states, $|1\rangle$ and $|2\rangle$, with the same probability for a balanced λ-scheme. Once excited, the system will emit a photon with a wavelength that depends on the decay channel. In other terms, the spin-photon system will be in the quantum state

$$\frac{|1\rangle_e |\omega_1\rangle_\gamma + |2\rangle_e |\omega_2\rangle_\gamma}{\sqrt{2}}. \tag{1.15}$$

A maximally entangled electron spin(e)-photon(γ) state, allowing for spin-photon information transfer. A marker of such a three-level system is coherent population trapping (CPT).

[10] More precisely, the transitions is not used and the two ground states do not interact.

Coherent population trapping

If both optical transitions, $|1\rangle \leftrightarrow |3\rangle$ and $|1\rangle \leftrightarrow |2\rangle$, are excited at the same time, the system is trapped in a dark state: a coherent superposition of the states $|1\rangle$ and $|2\rangle$ from which it cannot be excited. To understand this phenomenon, we need to describe the Hamiltonian of the three-level system interacting with a probe (along $|1\rangle \leftrightarrow |3\rangle$) and a control (along $|2\rangle \leftrightarrow |3\rangle$) laser at Rabi frequencies: Ω_p and Ω_c, see FIGURE 1.12**b**. In the basis $\{|3\rangle, |1\rangle, |2\rangle\}$, the Hamiltonian of the system reads:

$$\hat{H} = -\hbar \begin{pmatrix} 0 & \Omega_p \cos(\omega_p t) & \Omega_c \cos(\omega_c t) \\ \Omega_p \cos(\omega_p t) & \Delta_p + \omega_p & 0 \\ \Omega_c \cos(\omega_c t) & 0 & \Delta_c + \omega_c \end{pmatrix}. \tag{1.16}$$

Under the rotating wave approximation, see Appendix E, the effective Hamiltonian is [149]

$$\hat{H}_{int}^{RWA} = -\frac{\hbar}{2} \begin{pmatrix} -2\Delta_p & \Omega_p & \Omega_c \\ \Omega_p & 0 & 0 \\ \Omega_c & 0 & -2(\Delta_p - \Delta_c) \end{pmatrix}. \tag{1.17}$$

The CPT arises when the detuning of both lasers is the same ($\Delta_p = \Delta_c = \Delta$). In this case, the eigenstates of the Hamiltonian are:

$$|e_0\rangle = \cos(\theta)|1\rangle - \sin(\theta)|2\rangle, \tag{1.18}$$
$$|e_+\rangle = \sin(\theta)\sin(\phi)|1\rangle + \cos(\theta)\sin(\phi)|2\rangle + \cos(\phi)|3\rangle, \tag{1.19}$$
$$|e_-\rangle = \sin(\theta)\cos(\phi)|1\rangle + \cos(\theta)\cos(\phi)|2\rangle - \sin(\phi)|3\rangle, \tag{1.20}$$

with $\theta = \arctan(\Omega_p/\Omega_c)$ and $\tan(2\phi) = \sqrt{\Omega_p^2 + \Omega_c^2}/\Delta$[11]. Interestingly, the state $|e_0\rangle$ has no contribution of the state $|3\rangle$, thus $|e_0\rangle$ cannot be excited, as no spontaneous emission can be observed.

Experimentally, a spin population in the superposition state $|e_0\rangle$ can be achieved by continuous optical pumping into the excited state $|3\rangle$ using a control laser and using a second laser to sweep its frequency across the second transition. A drop of fluorescence is observed when the detuning of both lasers is equal. This technique is used in spectroscopy and is characteristic of a λ-scheme. This phenomenon can be used to transfer the information from a flying photon to the electron spin: the first brick to build a quantum network.

Many systems have achieved λ-schemes and coherent population trapping: ions, quantum dots, NV-centers [150, 151, 152, 153]; yet, V_{Si} present spin-conserving transitions with no λ-scheme available at first glance. In the next section, we will describe how to use the magnetic field to engineer a λ-scheme.

λ-scheme in V_{Si}

As seen earlier, in equation (1.7), by using a tilted magnetic field with respect to the c-axis of the crystal, the eigenstates of the Hamiltonian become superposition of spin

[11] A more precise mathematical derivation can be made using the master equation for the density matrix, nevertheless the description and conclusion are the same.

states. Thanks to the large difference in the zero-field splitting between the ground and excited states of V_{Si}, the spin-mixing is different in each subspace. We can then create a balanced λ-scheme at the excited state level anticrossing (ESLAC). In this regime, the mixing induced from a small tilt angle (θ) is negligible for the ground states but significant for the excited states $|-3/2\rangle_{es}$ and $|-1/2\rangle_{es}$.

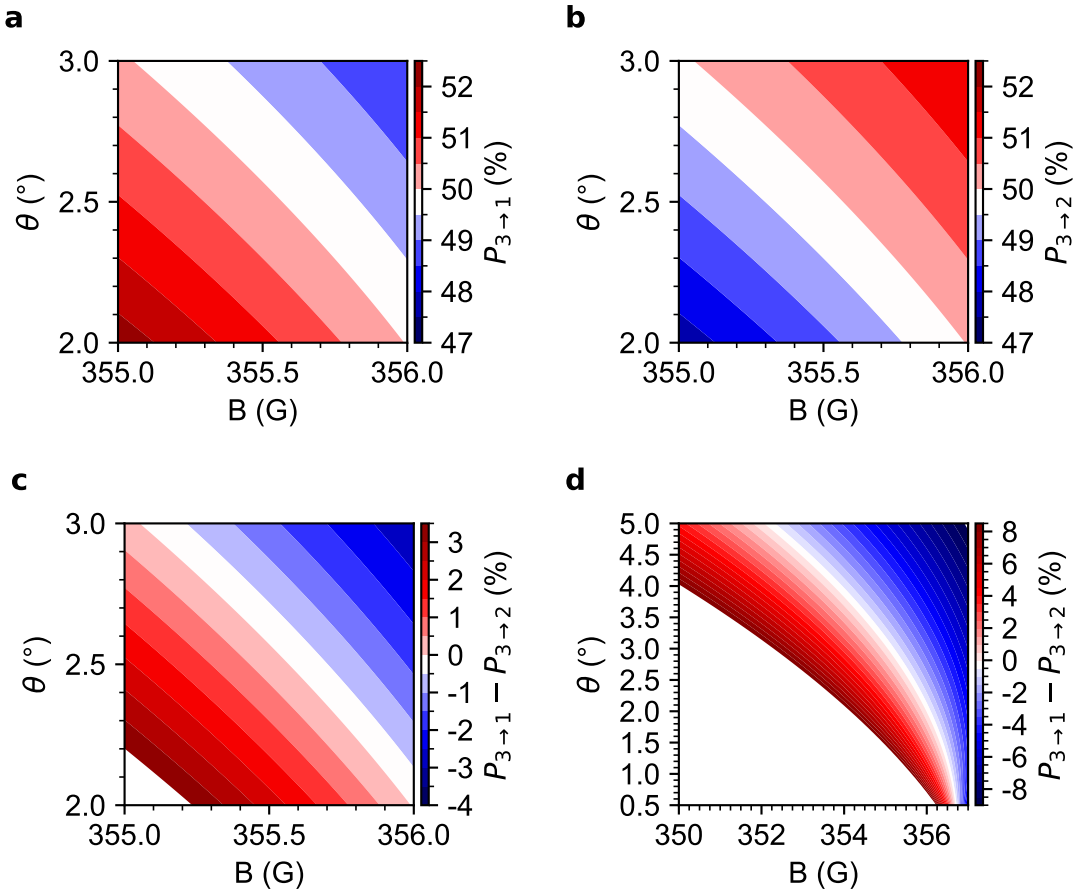

Figure 1.13: **ESLAC-induced spin mixing.** Contour plot showing the probability (color-coded), to decay from the states $|+\rangle_{es} = |3\rangle$ to the state $|-1/2\rangle_{gs} = |1\rangle$ (**a**) or to the state $|-3/2\rangle_{gs} = |2\rangle$ (**b**) when the system is in an external magnetic field (B, θ). The difference between both probabilities is given in **c** and **d**. The figure **d** simply covers a wider set of the parameter space. A balance λ-scheme is achieved when the magnetic field is set to an operating point along the line passing by the point 355.5 G and 2.6°. The probability difference is larger than 1% for a magnetic field misalignment of 0.1 G or 0.2°.

We simulated for the V2 center at which magnetic field the eigenstates for the excited states would be $|\pm\rangle_{es} = (|-3/2\rangle_{es} \pm |-1/2\rangle_{es})/\sqrt{2}$, while the ground state energy eigenstates would still be the spin states. FIGURE 1.13 showns the probability to decay from $|+\rangle_{es} = |3\rangle$ to $|-3/2\rangle_{gs} = |2\rangle$ and $|-1/2\rangle_{gs} = |1\rangle$ for various magnetic field strengths and angles, from which we can extract the functioning point: $B = 355.5$ G and $\theta = 0.6°$.

Yet, to realize such a system one needs to study the required stability of the magnetic field. Our criterion is: the magnetic field fluctuation should not lead to a 49.5%/50.5% unbalanced. Then, the angle of the magnetic field has to be adjusted within 0.2° and the magnetic field strength needs to be stable within ± 0.1 G. This requirement is fulfilled by state-of-the-art available equipment [154, 155]. Thus, a λ-scheme is achievable for the dichroic vacancies in SiC and can be used for spin-photon entanglement protocols where the spin of the electron system is entangled with the wavelength of the emitted photon.

To interface two spin systems via photon entanglement, the successive emitted photons from one stationary qubit should be identical to match the optical transitions of the second qubit. To this end, we studied the indistinguishability of the generated photons in [44].

1.5.2 V_{Si} center, source of indistinguishable photons

Some results from [44] will be briefly present in this section. To quantify the indistinguishability of photons emitted from a V_{Si} (here V1), we study the interference pattern of two successive emitted photons by a V_{Si} center. To this end, we excite the system twice using two off-resonant laser pulses (PicoQuant) separated by $\delta t = 48.7$ ns every $10\delta t = 487$ ns. Thanks to the long ISC's lifetime, the spin system can not decay through the ISC in the time δt. Therefore, if two photons are detected during an instance of the experimental sequence, they were emitted along the same spin-conserving transition. We only collect ZPL photons thanks to a narrow spectral filtering. The ZPL photons are coupled into a single-mode fiber before being sent to an unbalanced Mach–Zehnder interferometer with a path travel time difference of δt. The two outputs of the interferometer are connected to a SNSPD. A sketch of the experimental setup is shown in FIGURE 1.14**a** (adapted from [44]).

Both ZPL collected photons, the early and the late one, have the same chance to go through the short or long path of the interferometer. However only if the early photon goes through the long path and the late photon through the short path will the photons arrive simultaneously at the second beam splitter of the interferometer. In all other cases, they will arrive at different times and their detector paths will be uncorrelated. In the event of simultaneous arrival of the photons at the second beam splitter, a phenomenon of *bunching* can occur if the photons are indistinguishables: both photons will output the interferometer along the same path. This phenomenon is the Hong-Ou-Mandel effect [156] (HOM).

Experimentally, we detect this photon bunching by measuring the coincidence events between both detectors. In FIGURE 1.14**b** is shown a typical raw data for our measurements, the peaks ratio follows the 1:2:0:2:1 rule [157] linked to the probability of each photonic distribution within the interferometer. The raw HOM interference visibility is estimated to be $69 \pm 2\%$, on par with those reported for quantum dots[12] using off-resonant excitation ($53 - 86\%$) [158, 159, 160] and which is sufficient for the implementation of two-photon entanglement protocols [161, 162, 163]. By time-filtering the laser noise and possible phase kicks due to pure dephasing, we can reach interference visibility up to $85 \pm 4\,\%$ (see supplementary information of [44]).

[12] State-of-the-art system for photoemisson Indistinguishability

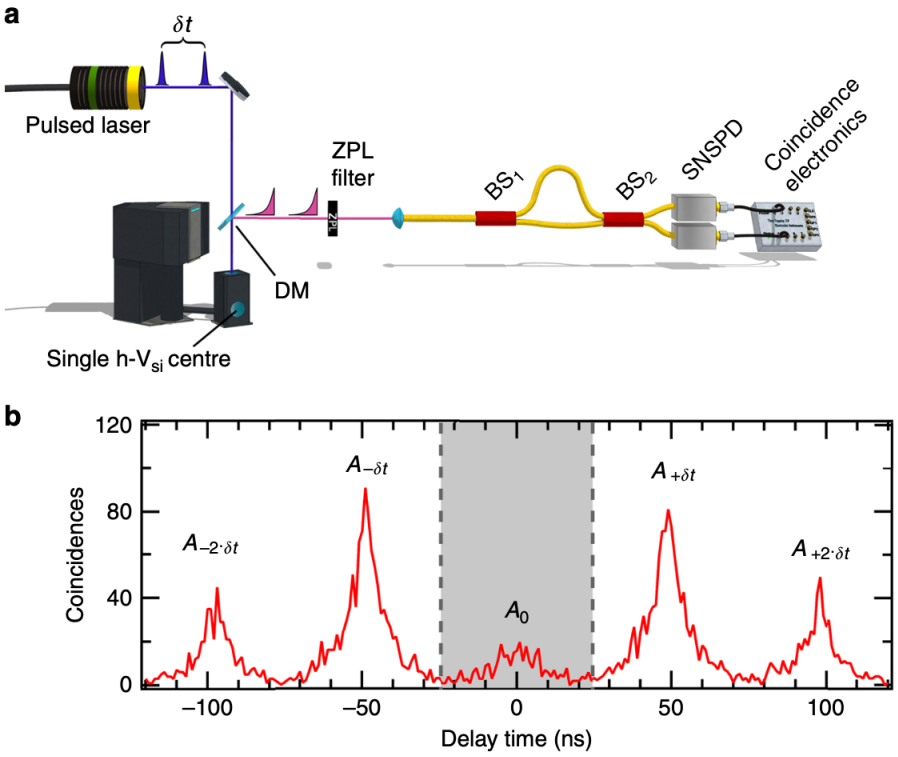

Figure 1.14: **Hong-Ou-Mandel experiment.** **a** Sketch of the setup used to realize HOM interference. Two laser pulses, separated by $\delta t = 48.7$ ns, excite the V1 center twice. The emitted ZPL photons are collected in an unbalanced Mach–Zehnder interferometer, the outputs of which are sent to SNSPDs to measure coincidence counts. **b** Two-photon coincidence counts as a function of the detection time delay. The suppressed peak at a delay time of zero reveals the Hong-Ou-Mandel interference. Using the grey area as the integration interval, and the raw data without any time gating, we yield a contrast of $69 \pm 2\%$. Adapted from [44].

In conclusion of this section, we have demonstrated that V_{Si} centers can be used to generate highly indistinguishible photons which could be entangled with the electron spin of the system. Thus, V_{Si} centers in SiC are promising candidates for quantum information processing. But, which one, the V1 or V2 center, is the most promising and should be considered for further work?

1.6 V1 or V2?

In this manuscript, we have presented the V1 and the V2 as having similar spin-optical properties. Yet, in this section we will show that the V2 center seems to be the more appealing system between the two. First, we will discuss the implication of the difference in the ground state zero-field splitting, then we will study the temperatures at which each system can operate.

1.6.1 Temperature dependence of the optical lines

As shown in FIGURE 1.2, the SiC crystal is placed in a cryostat which is cooled down to a few Kelvins. The main reason for cooling down a color center is to mitigate the interaction between the electron spin and the crystal phonons. At room temperature, the spin-conserving transitions for the V_{Si} are not spectrally resolved, in contrast to measurements performed at 4 K, where both transitions are spectrally separated [40, 119].

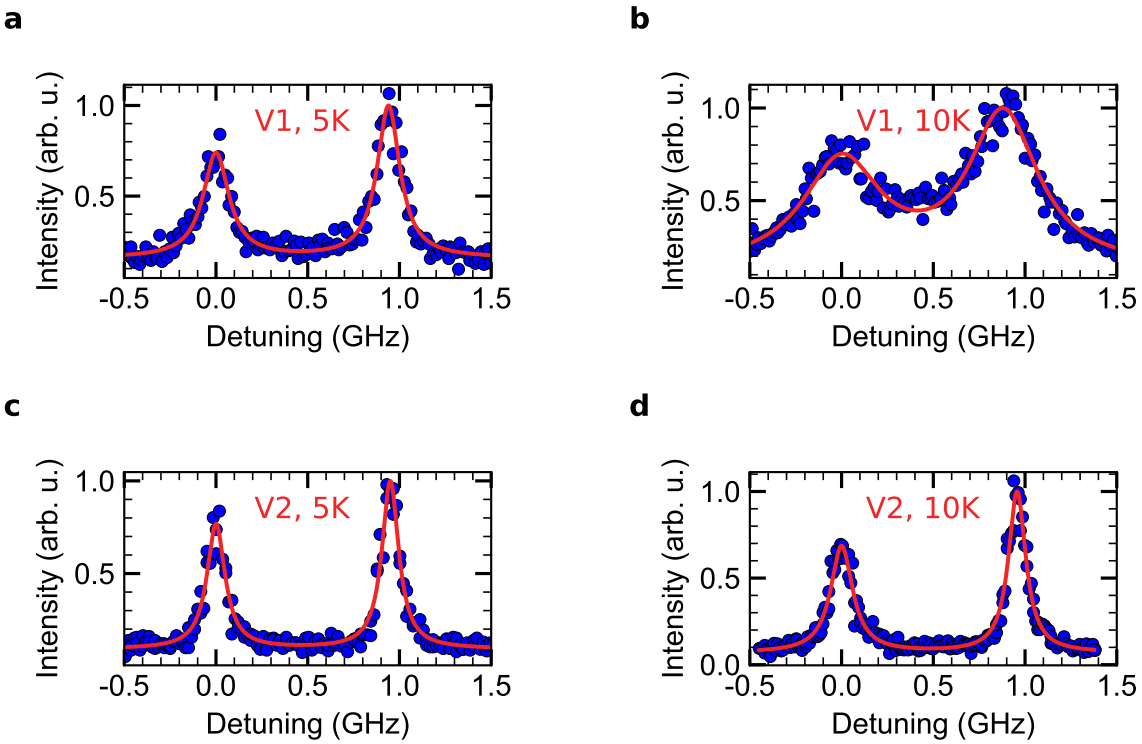

Figure 1.15: **Temperature dependent PLE scans.** PLE scans for the V1 (**a**,**b**) and V2 center (**c**,**d**) performed when the crystal was cooled down at 5 (**a**,**c**) and 10 Kelvins (**b**,**d**). Each data set (blue dots) are fitted with a double Lorentzian (red line). While the linewidths of the optical transitions increased with the temperature for the V1 center, they remain unchanged for the V2 center.

In our collaborative work [45], we studied the temperature dependence of the V1 and V2 center's optical lines. The experimental results were obtained by N. Morioka, D. Lukin and me, while the computational/theoretical analysis was performed by the group of Prof. Gali using advanced density functional theory (DFT) [164, 165] and the Perdew-Burke-Ernzerhof functional [166]. PLE scans of two spatially closed V1 and V2 centers are recorded at various temperatures. In FIGURE 1.15 are displayed a single scan for both color center at 5 and 10 Kelvin. Interestingly, as the V2 center optical linewidths are unchanged as the temperature increases, a clear broadening of the V1 optical line is observed. We studied the defects up to 25 Kelvin and the linewidths of the optical transitions are shown in FIGURE 1.16. While the V1 center optical lines start to broaden at 5 Kelvin, the V2 ones are narrow up to 20 Kelvin, thanks to a larger vibronic

gap. The temperature dependence is based on the interaction of the spin system with the acoustic phonons [167]. Interestingly, 4 K is the current temperature limit reached by the standard liquid-helium cryostat running full duty cycles. Below that, dilution fridges are required. Thus any heat generated by microwave drive will cause an increase in temperature. However at $T = 10$ K, a high-power drive is achievable with a stable operating temperature.

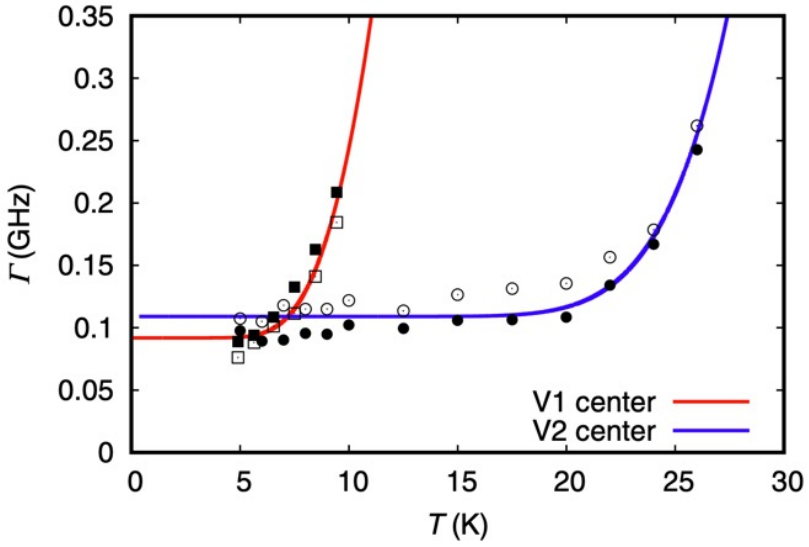

Figure 1.16: **Temperature dependence of the optical linewidths.** Temperature dependent linewidth of the A_1 (hollow points) and A_2 (solid points) transitions for the V1 (squared points) and the V2 (circular points) centers. The data is fitted using the theoretical model given in [45]. While the V2 center transitions remain narrow up to 20 K, the V1 center transitions broaden at 5 K. Adapted from [45].

1.6.2 Speed of microwave drive

As discussed previously, the power linewidth of the ODMR lines, i.e the spectral range within which a ground state transition can be driven, is dependent to the microwave field strength [168]

$$\Delta\nu_i \approx \Delta\nu^{(0)} + \alpha\sqrt{P_{\text{mw}}}. \tag{1.21}$$

Where P_{mw} is the microwave field power and $\Delta\nu^{(0)}$ the transform-limit of the ODMR linewidth (the inverse of the dephasing time $1/T_2^*$). Furthermore, as seen in equation (1.11), the spectral difference between two successive transitions ($\nu_3 - \nu_1$, $\nu_2 - \nu_1$) is $2D_{\text{gs}}$. Therefore, to drive a single transition via microwave radiation, the power should be kept below a certain level:

$$P_{mw} < P_{\text{max}} = \left(\frac{D_{\text{gs}} - \Delta\nu^{(0)}}{\alpha}\right)^2. \tag{1.22}$$

As the V2 center has a larger ground state zero-field splitting than the V1 center (70 MHZ vs 4 MHz), the maximum allowed microwave power is also larger for V2. Further

as the Rabi frequency increases with the microwave power, it is clear that working with the V2 center will allow for faster deterministic manipulation of the spin system. Thus, the V2 center is more promising than the V1 center for quantum information technologies applications. Its spin-optical properties are more resilient to temperature changes up to $T = 20$ K, at which standard cryogenic equipment can compensate for additional heat from a high-power spin drive, allowed thanks to a larger ground state ZFS.

1.7 Conclusion and outlook

In this chapter, we have introduced the main protagonist of this manuscript: the V_{Si} center in 4H-SiC, an electron spin system trapped within a crystal lattice. We have seen its spin-optical properties: 3/2 spin system with spin-conserving optical transitions, long-lived ground state, and highly indistinguishable photon emission. We have described how to characterize and manipulate such a color center using microwave and laser pulses; and how to create a spin-photon entanglement scheme using a well-engineered magnetic environment. We have also shown in which aspect the V2 center is more promising as a quantum platform compared to the V1 center. It is convincing that the V2 center fulfills the DiVincenzo's criteria, in every aspect considered so far. Yet the elephant in the room needs to be addressed: the low spin-photon interaction. Indeed, as will be discussed in the next chapter, the collection efficiency of bulk defects via standard confocal microscopy is close to 1% rendering the system inapplicable for immediate quantum information applications. We will also introduce the theoretical framework of cavity quantum electrodynamics, and a way to potentially realizes near-deterministic spin-photon interaction.

Chapter 2

Cavity quantum electrodynamics

In this chapter, we will finally address the bottlenecks which restrict the positioning of solid-state color centers as the leading platform for quantum information processing: the weak interaction between the electron spin and the photon. In other words, each photon emitted by a color center should be collected by a potential quantum network. Vice versa, each network-photon has to coherently interact with the targeted spin qubit. However, this dream scenario faces multiple limitations that need to be addressed.

First, the emission of an optical dipole covers usually a solid angle of 4π, limiting the coupling towards free-space modes. This effect is accentuated by the internal reflection of the light at the surface of the host crystal due to refractive index mismatch. This situation is illustrated in FIGURE 2.1**a**, where the total reflection occurs for angles larger than $\phi = \arcsin(1/n_{\mathrm{SiC}}) \sim 22°$, according to the Snell–Descartes law. Furthermore, while the coupling of the optical transitions to optical phonons is utilized for the characterization of color centers, as it allows the probing of the system with resonant laser pulses and the collection of photons in the phonon sideband (PBS), these photons cannot be used for entanglement purposes. The Debye-Waller factor (DWF) refers directly to the fraction of emitted photons in the zero-phonon line (ZPL), used for entanglement distribution, which is only around 8% [45, 135] for V_{Si} centers in SiC. Also, as seen earlier, not every excitation yields a photon due to nonradiative pathways, e.g. phonon-assisted spin-mixing transitions; affecting the electron spin information and thus reducing the entanglement distribution rate. In this chapter, we will study the different solutions to expand the applicability scope of color centers in solid through the improvement of the spin-photon interface. First, we will briefly describe solid immersion lenses which are aimed to increase the collection efficiency. Secondly, we will describe theoretically a more complete solution: the integration of quantum emitters in cavity quantum electrodynamics systems and investigate if V_{Si} in SiC can be integrated into such structures.

2.1 Solid immersion lense

A first solution to the limited collection efficiency is the fabrication of solid immersion lenses (SILs) [169, 170, 171]. If they are perfectly hemispherical and the color center is placed at the center of them, then all photons emitted upward will be transmitted to free-space modes, see FIGURE 2.1**b**. SiLs fabricated using focused ion beam (FIB) have

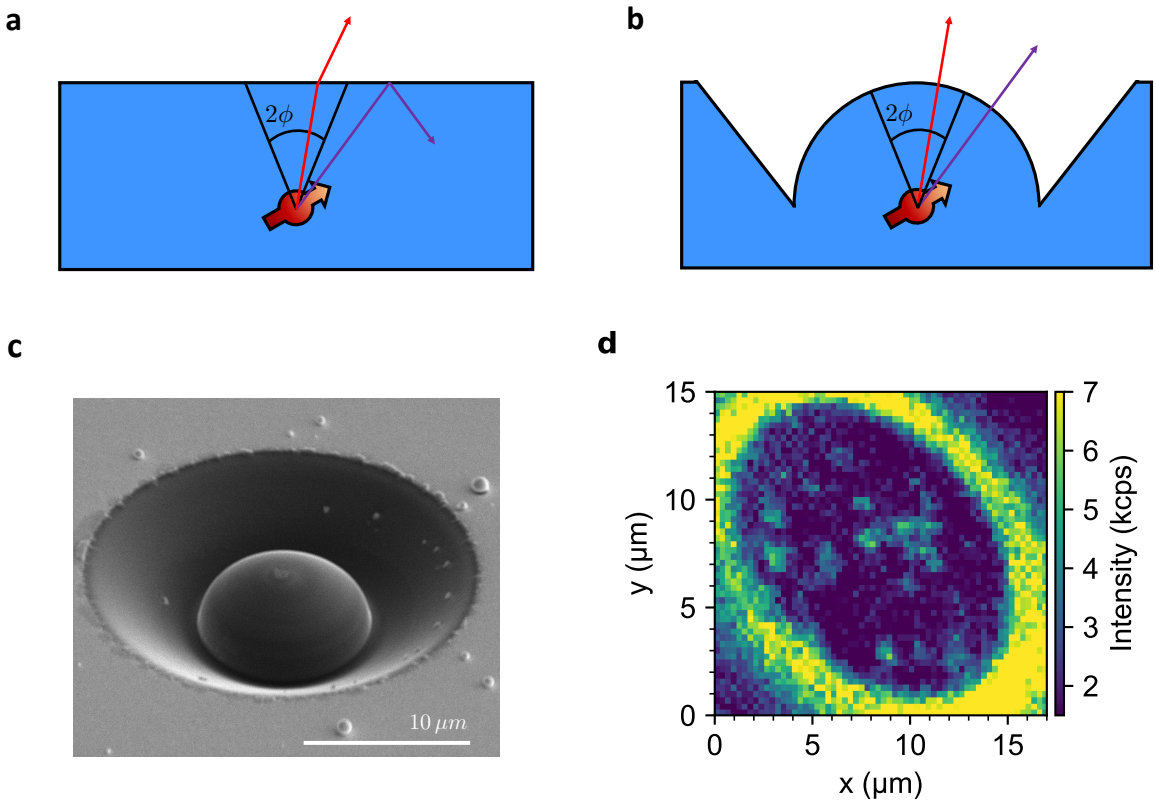

Figure 2.1: **Solid immersion lense. a** (**b**) Schematic representation of a color center in bulk (solid immersion lense). The red arrows represent photon paths coupled to free-space modes in both cases while the purple arrows correspond to the photon paths that are only collected in the case of the emitter in the SIL. **c** Scanning electron microscope image of a fabricated SIL. **d** Confocal scan of the SIL, bright spots correspond to quantum emitters in the SIL.

yielded an enhancement of 2.7 [43] for the SiC platform and up to 8 for NV centers in diamond [172, 173]. The difference essentially comes from non-perfect SIL shape and non-ideal color centers positions. FIGURE 2.1**c** shows a SEM image of a SIL that we fabricated in our facility at the start of my PhD, and in FIGURE 2.1**d** is given a low-temperature confocal scan of the corresponding SIL. The fabrication recipe followed is given in [43]. Other fabrication approaches are currently under investigation, for example, based on the reflow of a mask giving it a circular shape and then imprinting this shape to SiC via ion etching. So far this has led to a collection efficiency enhancement up to 3.4 [174]. Yet, due to an etching rate mismatch between the mask and SiC, this process creates non-spherical lenses.

While increasing the collection efficiency of the photoemission of color centers is an important aspect, a SIL has no effect on the intrinsic spin-optical properties of the emitters. The low DWF, as well as the spin-mixing rates, are the same for bulk or SIL defects and the main bottlenecks remain. The integration of quantum emitters in cavities is the way forward, according to the scientific community, as we will present in this chapter.

2.2 Photonic crystal cavity

The embedding of a quantum emitter in a photonic cavity is a promising solution to engineer the electromagnetic local density of states in order to enhance the interaction strength between the spin system and a cavity-confined photon. To understand the framework of cavity quantum electrodynamics, we will follow the explanation given in the excellent review [26]. We will study a standard two-level quantum system with radiative and non-radiative decay pathways between the ground and excited states. The respective rates are γ_{r} and γ_{nr}. The radiative decay pathway is composed of ZPL and PSB channels, we will denote γ_{ZPL} and γ_{PSB} the respective associated decay rates. A sketch of the emitter decay channels can be seen in FIGURE 2.2**a**.

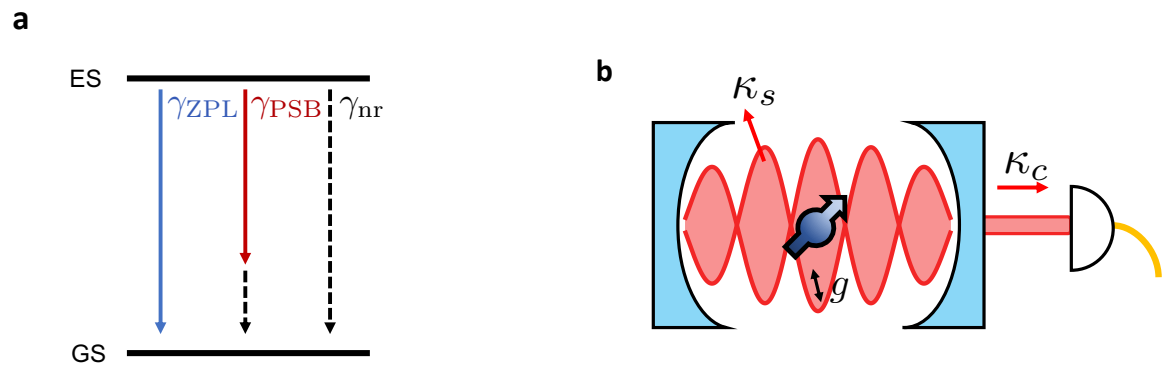

Figure 2.2: **Quantum emitter coupled to a cavity. a** Representation of the different decay paths from the excited state to the ground state. Either the system emits a photon with or without emission of phonons or the system can decay non-radiatively. The red solid (black dashed) lines correspond to the emission of a photon (phonons). **b** Schematic of an integrated quantum emitter coupled to a cavity quantum electrodynamics system. The coupling rate between the color center and a cavity photon is g, and the confined photon can either scatter out of the cavity at a rate κ_s or be collected into a single-mode fiber at a rate κ_c.

In this framework, the excited state decay rate is:

$$\gamma = \frac{1}{\tau} = \gamma_{\mathrm{r}} + \gamma_{\mathrm{nr}} = \gamma_{\mathrm{ZPL}} + \gamma_{\mathrm{PSB}} + \gamma_{\mathrm{nr}}, \tag{2.1}$$

where τ is the excited state lifetime. The Debye-Waller factor (denoted as ξ) is then:

$$\xi = \frac{\gamma_{\mathrm{ZPL}}}{\gamma_{\mathrm{r}}}, \tag{2.2}$$

so that:

$$\gamma_{\mathrm{ZPL}} = \xi\,\gamma_{\mathrm{r}},\ \gamma_{\mathrm{PSB}} = (1-\xi)\,\gamma_{\mathrm{r}}. \tag{2.3}$$

The quantum efficiency (η) is the probability for the system to decay radiatively once excited [175]:

$$\eta = \frac{\gamma_{\mathrm{r}}}{\gamma}, \tag{2.4}$$

thus:

$$\gamma_{\mathrm{r}} = \eta\,\gamma,\ \gamma_{\mathrm{nr}} = (1-\eta)\,\gamma. \tag{2.5}$$

We can reinject those terms in equation (2.3) such that we can express all the rates in term of the intrinsic properties of the color center (γ, ξ, η) :

$$\gamma_{\mathrm{ZPL}} = \xi\,\eta\,\gamma,\ \gamma_{\mathrm{PSB}} = (1-\xi)\,\eta\,\gamma,\ \gamma_{\mathrm{nr}} = (1-\eta)\,\gamma. \tag{2.6}$$

Once we have defined the spin system, we can introduce a general model for the photonic resonator. The cavity itself is defined by the rate at which the confined photon is dissipated: κ. The photon can be either collected (κ_c) or scattered (κ_s), thus $\kappa = \kappa_c + \kappa_s$. For example, in the case of a photonic crystal cavity [176, 177] the collected photons are the ones guided along the waveguide coupled to the measurement apparatus while the scattered light is lost in free space. We denote g the coupling strength between the cavity and the emitter. A sketch of the spin-cavity system is depicted in FIGURE 2.2**b**.

2.2.1 Purcell factor

When an emitter is embedded in an optical cavity tuned in resonance with the emitter optical transitions, the local photonic density of state is enhanced; leading to an increase of the radiative emission's rate of the color center inside the cavity mode. The cavity mode's frequency is designed to be resonant with the ZPL, to only increase the number of photons used for entanglement purposes. We denote Γ_{ZPL}[1], the emission rate in the enhanced mode (here the ZPL) after integration inside a cavity. This enhancement is characterized by the Purcell factor:

$$P = \frac{\Gamma_{\mathrm{ZPL}}}{\gamma_{\mathrm{ZPL}}}. \tag{2.7}$$

We define Γ as the total decay rate from the excited to the ground state after integration of the spin system in the cavity, such that we have the following identity:

$$\Gamma = \Gamma_{\mathrm{ZPL}} + \gamma_{PBS} + \gamma_{\mathrm{nr}} = P\,\gamma_{\mathrm{ZPL}} + \gamma_{\mathrm{PSB}} + \gamma_{\mathrm{nr}}. \tag{2.8}$$

The Purcell factor P can be expressed with the well-known formula [178, 179]:

$$P = \frac{3}{4\pi^2}\left(\frac{\lambda}{n}\right)^3\left(\frac{Q}{V}\right). \tag{2.9}$$

Where $Q = \omega/\kappa$ is known as the quality factor, with ω being the resonance frequency of the cavity and n is the index of refraction. V is the cavity mode volume [180], the volume of the cavity in which the electromagnetic field is confined. Often, the mode volume V is expressed as a fraction of a fundamental mode volume:

[1] In the literature, the enhanced rate is often denoted Γ but for clarity I decided against, as it will become clear to the reader in this section

$$V_0 = \left(\frac{\lambda}{n}\right)^3. \tag{2.10}$$

The quality factor can be interpreted as how well the cavity can store the photon, similar to classical mechanics and the description of harmonic oscillators and their damping behaviors. Hence, the quality factor is also defined as the frequency to bandwidth ratio:

$$Q = \frac{\omega}{\Delta\omega}. \tag{2.11}$$

In the case of V_{Si} center, we aim to enhance both A_1 and A_2 transitions with no enhancement of the PSB, a minimum quality factor of a few thousand should then be achieved. Indeed, from the emission spectra we measured (see FIGURE 1.6), the spectral separation between the ZPL and PSB is around 5 nm, so the bandwidth should be at most 1 nm. Interestingly, the Purcell factor P (equation (2.9)) only depends on the cavity geometry, this dependency is often encapsulated in the formula:

$$P \propto \frac{Q}{V}. \tag{2.12}$$

This latest equation explains the drive of the community to create high-quality factor cavities with low mode volume, maximizing the Purcell factor.

In the literature, there have been many successful fabrications of nanophotonic cavities for the SiC and diamond platforms with various designs and geometries: 1D [47, 101, 177, 181, 182] or 2D [131, 183, 184] photonic crystal cavities, ring resonators [47, 48, 185] or microdisks [186], as well as Fabry-Perot microcavities [187, 188]. Due to complex schemes, which are required to stabilize the Fabry-Perot at low temperatures to counteract the vibrations of the cooling system, the photonic structures are more promising. There have been demonstrations of quality factors up to $10^5 - 10^6$ [48, 131]. Furthermore, as of today one of the most promising approaches is 1D photonic crystal cavities coupled via tapered fibers [177] combining easy in/out coupling (up to 90 % collection efficiency) with scalable fabrication techniques.

Experiments studying integrated color centers in SiC have shown Purcell enhancement up to 75 (20) for the V1' (V1) ZPL [46, 47, 189] as well as 50 for the divacancy [102]. Thus, it is a reasonable to assume that similar Purcell factors could be reached for the V2 center. Further, in those cases a mode volume of V_0 (see equation (2.10)) [101, 181] or half of V_0 [47, 177] have been reached. At the V2 center ZPL emission (917 nm), it corresponds to a typical width of $\sqrt[3]{V_0} \sim 350$ nm, thus the defect should be positioned with a nanometric precision to optimize the emitter-cavity coupling. Interestingly, new designs of photonic crystal cavities have been simulated with an ultra small mode volumes: $V_0 \cdot 10^{-2}$ [190], $V_0 \cdot 10^{-4}$ [191].

From our bibliographic review, we see that high Purcell factor cavities are achievable for the SiC platform. However, studying the ratio between the different decay branches is not sufficient to determine which Purcell factor should be aimed for a given quantum emitter, one should also consider the cooperativity: C.

2.2.2 Cooperativity

While the Purcell factor P describes the increase in the photoemission within the ZPL, it doesn't give a complete image of the coupling between a cavity-confined photon and an electron spin. Indeed, the probability of coherent spin–photon interaction, when a single photon is inserted in the cavity, depends on the cooperativity C:

$$C = \frac{\Gamma_{\mathrm{ZPL}}}{\gamma}. \tag{2.13}$$

While similar to the definition of the Purcell factor, see equation (2.7), the denominator is here the full decay rate from the exited to the ground state (γ) and not the one of interest (γ_{ZPL}). In other words, the cooperativity compares the cavity-assisted radiation rate to all other dephasing mechanisms. A spin-photon interface is greatly improved once the high cooperativity regime ($C > 1$) is reached; in this regime deterministic coherent interaction between an integrated quantum emitter and a single injected photon is possible [49, 50, 51, 52] as well as on-demand generation of single photons [192]. Thus, it is a prerequisite for quantum information processing [16, 193, 194]. Utilizing the equations (2.6-2.8), we can express the cooperativity as:

$$C = \frac{P\,\gamma_{\mathrm{ZPL}}}{\gamma}, \tag{2.14}$$

$$C = \frac{P\,\xi\,\eta\,\gamma}{\gamma}, \tag{2.15}$$

$$C = P\,\eta\,\xi = P \cdot (\eta\,\xi). \tag{2.16}$$

The cooperativity is then a fraction of the Purcell factor, depending on the spin system properties: the Debye-Waller factor and the quantum efficiency. Thus to achieve high cooperativity, $C > 1$, the Purcell factor should satisfy:

$$P > (\eta\,\xi)^{-1}. \tag{2.17}$$

An arbitrary large P, while allowing for a high cooperativity cavity, would also results in a broadening of the optical transitions.

2.2.3 Spectral broadening

The transform-limited linewidth of the direct radiative transition is inversely proportional to the excited state lifetime:

$$\Delta\nu = (2\pi\tau)^{-1} = \frac{\gamma}{2\pi}. \tag{2.18}$$

If we define $\Delta\nu_P$ the natural linewidth of the optical transitions once integrated in a cavity of Purcell factor P, then using the equation (2.8) we have:

$$\Delta\nu_P = \frac{\Gamma}{2\pi}, \tag{2.19}$$

$$\Delta\nu_P = \frac{\gamma}{2\pi}\Big[P\,\xi\,\eta + (1-\xi)\,\eta + (1-\eta)\Big], \tag{2.20}$$

$$\Delta\nu_P = \Delta\nu\Big[(P-1)\,\xi\,\eta + 1\Big]. \tag{2.21}$$

The increase of the radiative emission via Purcell enhancement broadened the optical lines. Also, as expected, if $P = 1$ (no enhancement) then $\Delta\nu_P = \Delta\nu$. For a cooperativity of $C = 1$ ($P = (\xi\,\eta)^{-1}$), the natural linewidth is:

$$\Delta\nu_P = \Delta\nu\,[2 - \xi\,\eta]. \tag{2.22}$$

And in general, in order to reach a cooperativity of $C = x$ then the Purcell factor should be $P = x\,(\xi\,\eta)^{-1}$ and thus will lead to an optical linewidth of:

$$\Delta\nu_P = \Delta\nu\Big[(x+1) - \xi\,\eta\Big]. \tag{2.23}$$

We can summarize the main results of this section in the following theorem.

Theorem 1 *For a given quantum emitter (γ, ξ, η) embedded in a cavity in resonance with the emitter zero-phonon line. the enhancement of the resonant radiative decay channel is described by the Purcell factor P:*

$$P = \frac{3}{4\pi^2}\Big(\frac{\lambda}{n}\Big)^3\Big(\frac{Q}{V}\Big), \tag{2.24}$$

leading to a cooperativity, describing the strength of the interaction between a confined photon and the emitter, of:

$$C = P\,\xi\,\eta, \tag{2.25}$$

and to a broadening of the natural linewidth ($\Delta\nu$):

$$\Delta\nu_P = \Delta\nu\Big[(P-1)\,\xi\,\eta + 1\Big], \tag{2.26}$$

$$\Delta\nu_P = \Delta\nu\Big[(C+1) - \xi\,\eta\Big]. \tag{2.27}$$

2.3 Application to the V_{Si} center in SiC

In regards to the fixed frequency difference between the optical lines A_1 and A_2 for both V_{Si} in 4H-SiC, see equation (1.10), the preservation of spin-dependent optical transitions once the system is integrated in a cavity will need to be considered. An arbitrary large Purcell factor would lead to an overlapping of the A_1 and A_2 lines as their respective linewidths would be larger than 1 GHz.

2.3.1 Bounded Purcell factor

To give a first figure of merit and estimate the maximal Purcell factor allowed and the corresponding radiative rates, we will use a simplified rate model of the V_{Si} center with an excited state lifetime of $\tau = 7$ ns (corroborated by later measurements, see FIGURE 3.12) for both A_1 and A_2 lines. As presented in Chapter 1, we estimated the DWF (ξ) to be around 8% while the quantum efficiency is yet to be estimated. For example, the quantum efficiency of the NV center in diamond is measured to be close to being 100 % [195] while lower bounded by 15 % for the SiV center in diamond [196, 197, 198]. It remains a challenge to estimate precisely the quantum efficiency due to the high number of parameters. For the V1 center, the quantum efficiency (η) is at least $25 - 30\%$ for the A_1 and A_2 lines and at most $\approx 50 - 70\%$, as estimated by MSc Di Liu in a scientific paper which is currently under review and not yet (pre)published. The lower bound have been estimated by simulating the local effective electromagnetic field and the response of the dipole while the upper bound have been obtained by assuming that the decay channels through the metastable states are the only non-radiative decay pathways. The V2 center is currently under investigation, and we will assume in this manuscript that it behaves comparably to the V1 center with $\eta \in [10\,\%, 75\,\%]$.

To preserve the spin-dependent transitions, we decide on a maximum transform-limited linewidth of 200 MHz, such as the A_1 and A_2 lines are still separated by 10σ. A simulation with different linewidths is given in FIGURE 2.3, where we observe that from a full width at half maximum of 300 MHz upward, each absorption line contributes to the other one as the sum of both lines (in red) sits above each line at the resonance: the optical lines are not perfectly spin-dependent anymore. For simplicity, we assume the natural linewidth of bulk V_{Si} to be 20 MHz ($(2\pi\tau)^{-1} \approx 23$ MHz) such as $\Delta\nu_{max}/\Delta\nu = 10$. Using the equation (2.26), we obtained the maximal allowed Purcell factor:

$$P_{max} = 1 + \frac{\Delta\nu_{max}/\Delta\nu - 1}{\xi\,\eta}, \tag{2.28}$$

$$P_{max} \approx \frac{9}{\xi\,\eta}. \tag{2.29}$$

Where we used the approximation $\xi\,\eta \ll 10$, condition fulfilled for V_{Si} center as $\xi\eta \leqslant \xi = 0.08 \ll 10$. The cooperativity would then be:

$$C_{max} = 9. \tag{2.30}$$

Thus, a high-cooperativity ($C > 1$) regime is achievable while maintaining spin-conserving transitions.

2.3.2 Effective V_{Si} center

In the case of a Purcell factor of P_{max}, the new ZPL decay rate is:

$$\Gamma_{ZPL,max} = \left(\frac{\Delta\nu_P}{\Delta\nu} - 1\right)\gamma = 9\gamma, \tag{2.31}$$

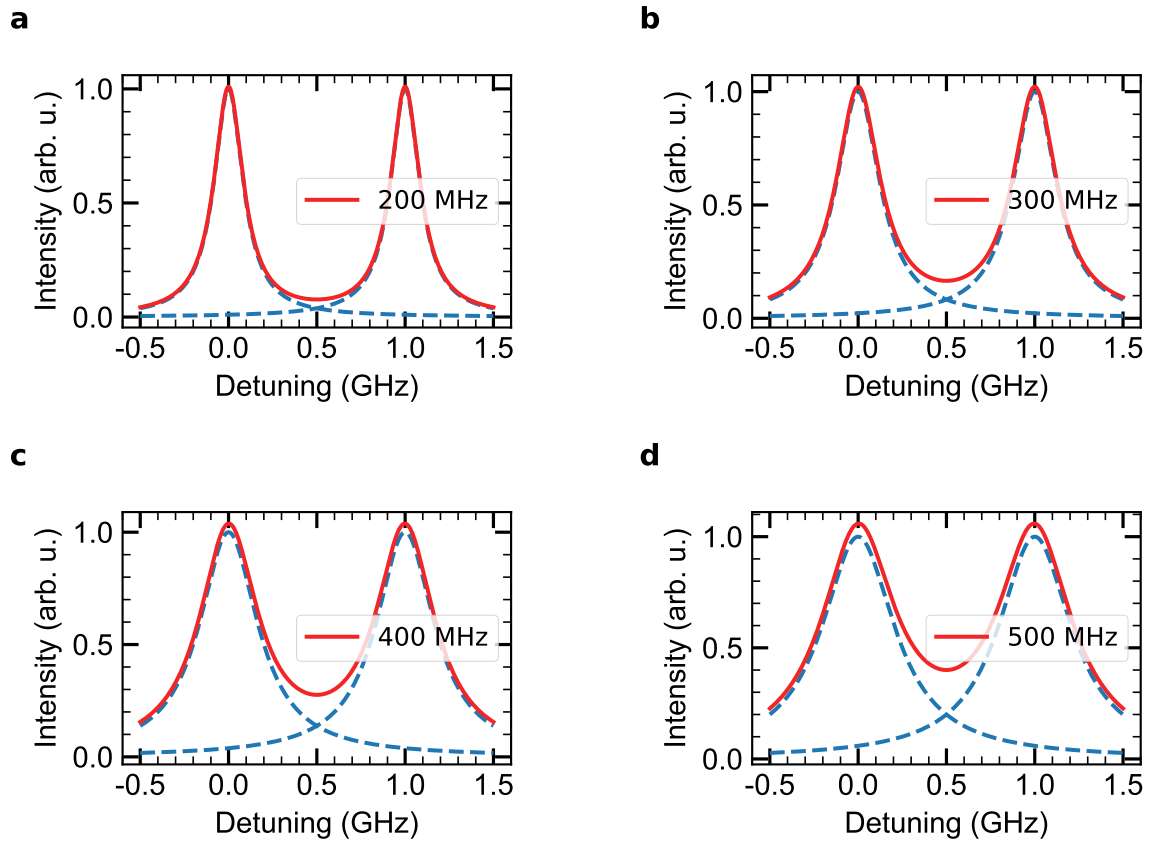

Figure 2.3: **Simulated V_{Si} centers optical lines.** Simulated optical absorption lines of a V_{Si} center, with various linewidths. The blue dashed lines are the Lorentzian curves for each optical transitions (A_1 and A_2) and the red solid lines the sum of both contributions.

and the other rates are let unchanged:

$$\Gamma_{\mathrm{PSB}} = \gamma_{\mathrm{PSB}} = (1-\xi)\,\gamma \text{ and } \gamma_{\mathrm{nr}} = \gamma_{\mathrm{nr}} = (1-\eta)\,\gamma. \tag{2.32}$$

The integrated color center is then described by an effective color center with the excited decay rate: γ_{eff}; Debye-Waller factor: ξ_{eff} and quantum efficiency η_{eff} given by the following equations:

$$\gamma_{eff} = (10-\xi\,\eta)\,\gamma \approx 10\,\gamma, \tag{2.33}$$

$$\xi_{eff} = \frac{9}{9+(1-\xi)\eta} \approx \frac{9}{9+\eta}, \tag{2.34}$$

$$\eta_{eff} = \frac{9}{10} + \frac{\eta}{10} - \frac{\xi\,\eta}{10} \approx \frac{9+\eta}{10}. \tag{2.35}$$

Thus, in the case of $P = P_{\max}$, the integrated V2 center will have an effective quantum efficiency and Debye-Waller factor above 90% while conserving spin-conserving transitions and achieving cooperativity of $C = 9$. This lets us perceive how solid-state

color centers once integrated in nanophotonic cavities can be used as highly efficient spin-photon interfaces.

In reality, the value of $P_{\max}$ is dependent on the quantum efficiency ($\eta \in [10\,\%, 75\,\%]$) thus bounded by: $130 \leq P_{\max} \leq 500$, which will be challenging to obtain, especially in the case of low η, as currently the maximal demonstrated Purcell factor in SiC photonic crystal cavities is around a hundred [46]. Improvement on the nanofabrication and cavity design, as well as more precise knowledge on the rate of the system, will allow us to unfold the full potential of V_{Si} centers.

Yet, we can ask ourselves if the current state-of-the-art of nanofabrication is enough to reach the high-cooperativity regime ($C > 1$). To answer this question, we can use a similar derivation method than previously used and obtain the following theorem:

Theorem 2 *For a given color center (γ, ξ, η), a Purcell factor of:*

$$P = \frac{C}{\xi\,\eta}, \tag{2.36}$$

is necessary to reach a cooperativity of C. The enhanced radiative decay rates is:

$$\Gamma_{ZPL} = C\,\gamma, \tag{2.37}$$

and the spin system can be described by an effective color center (γ_{eff}, ξ_{eff}, η_{eff}):

$$\gamma_{eff} = (C + 1 - \xi\,\eta)\,\gamma, \tag{2.38}$$

$$\xi_{eff} = \frac{C}{C + (1-\xi)\,\eta}, \tag{2.39}$$

$$\eta_{eff} = \frac{C + (1-\xi)\,\eta}{C + 1 - \xi\,\eta}. \tag{2.40}$$

Such that the effective Debye-Weller factor and quantum efficiency are both above $C/(C+1)$. The probability for the integrated system to emit a ZPL photon once excited is:

$$\xi_{eff}\,\eta_{eff} = \frac{C}{C + 1 - \xi\,\eta} \approx \frac{C}{C+1}. \tag{2.41}$$

Thus the minimal Purcell factor to reach the high-cooperativity regime ($C = 1$) is bounded for the V2 center by $10 \leq P_{min} \leq 110$: achievable with state-of-the-art nanofabrication techniques. In this regime, the system will emit a resonant photon half of the time it is excited, compared to potentially 1 % of the time in the bulk. In FIGURE 2.4**a-c** are visually represented what have been calculated so far in this chapter: the Purcell factor (P) needed to achieve a certain cooperativity (C) and the corresponding effective Debye-Weller factor/quantum efficiency given different quantum efficiencies of the bulk V_{Si} (η).

Interestingly, there exists an inflection point at $C \approx 3$: from which the change in the parameter of interest's values is slower. In other words, the increase of the cooperativity leads to a lower gain once a cooperativity of three is reached, which is achievable (as seen in FIGURE 2.4**a**) for a Purcell factor P of 100 even in the case of $\eta = 25\%$. Furthermore, we observe the opposite behavior of η_{eff} and ξ_{eff} according

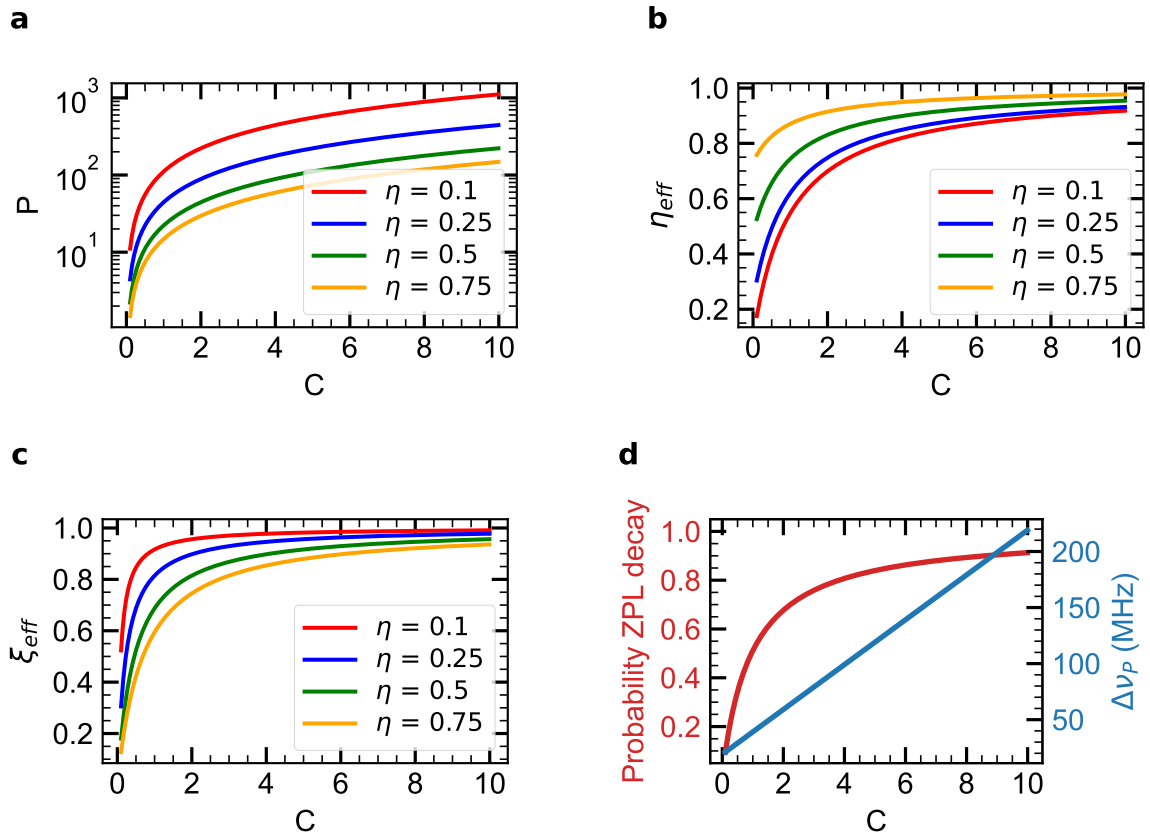

Figure 2.4: **Purcell factor and effective color center. a** Purcell factor of the cavity required to reach a cooperativity C, for different quantum efficiencies (color-coded). **b** (**c**) The effective quantum efficiency (Debye-Waller factor) of the integrated emitter in a cavity of cooperativiy C, for different quantum efficiencies (color-coded). **d** Key characteristics of the emitter placed in a cavity of cooperativity C: the probability of emission in the ZPL (red) and the optical linewidth (blue).

to the quantum efficiency η. While for a given cooperativity C the effective quantum efficiency increases with η (FIGURE 2.4**b**) the effective Debye-Waller factor decreases (FIGURE 2.4**c**). Yet, the probability to emit a ZPL photon (FIGURE 2.4**d**, red curve), once the emitter is coupled to a cavity of cooperativity C, is independent of η. Finally, as expected, the transform-limited linewidth is below the 200 MHz threshold for $C < 9$, as seen in FIGURE 2.4**d**.

2.3.3 Spin readout efficiency

While the emission rate in the ZPL is of utmost importance for quantum information technologies, the spin readout efficiency is also to be considered. With a highly-cycling optical transition, the average number of detected photons is significant when probed by a resonant laser. It allows for a single shot readout (SSR) of the system. Yet, in the case of bulk V_{Si} center in SiC, on average 0.01 photons are detected at each readout protocol. The integration in photonic cavities would also increase the average

number of emitted photons (N) before the system decays through the ISC and the spin information is lost. N is entirely fixed by the quantum efficiency, indeed the probability for the system to emit n photons is η^n, such that:

$$N = \sum_{n=0}^{\infty} n\,\eta^n = \frac{\eta}{(1-\eta)^2}. \tag{2.42}$$

Once integrated, N is determined by the effective quantum efficiency. In FIGURE 2.5 is shown the average number of photons emitted by an integrated spin system according to the cooperativity and various quantum efficiencies η. As we can see, even in the worst-case scenario ($\eta = 10\%$) the system, for $C = 3$, will already emit on average 10 photons under continuous excitation along a resonant transition before the loss of the spin information. If we assume a collection efficiency of 90% and a detector efficiency of 60 %, using tapered fibers [177] and SNSPD, each readout protocol will on average leads to the detection of 5 photons, thus allowing spin single-shot readout with a fidelity of 99.3 % (assuming no dark counts). However, one might need to also consider nuclear-spin-assisted readout protocol to increase the number of detected photons, as will be described in Chapter 5.

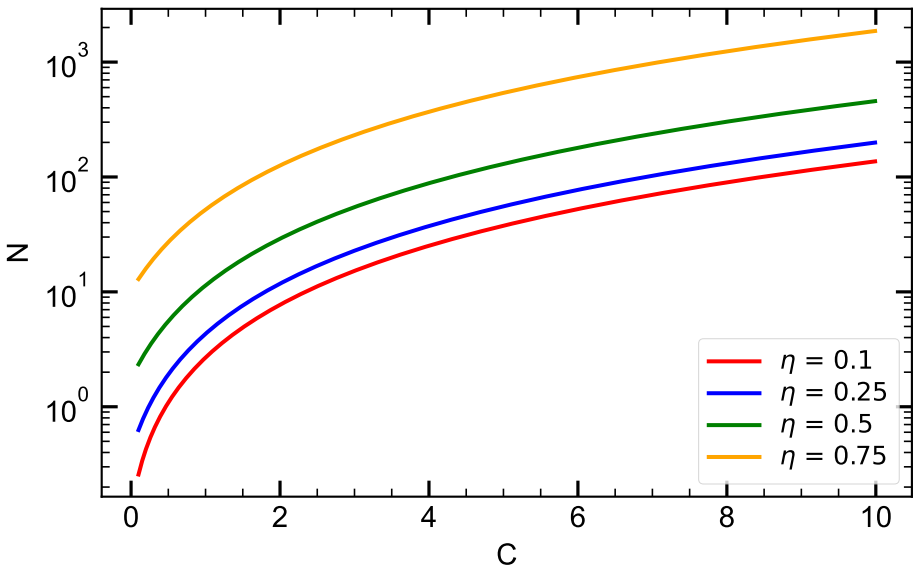

Figure 2.5: **Detected photons per readout.** Average number of photons emitted by the system integrated into a cavity with a cooperativity C, under continuous laser excitation, before the loss of the spin information through non-radiative spin-mixing decays. The number of emitted photons is estimated for various different quantum efficiencies of the color center (color-coded).

While it is possible to fabricate high-cooperativity cavities for the V2 center, taking into account the quantum efficiency and the natural splitting of the lines. Another challenge arises for integrated color centers: spectral diffusion.

2.4 Spectral diffusion

Spectral diffusion is an effect hindering the development of integrated solid-state color centers as quantum platforms for quantum information processing. It is a stochastic process, where e.g. the charge fluctuation in the host crystal leads to random spectral fluctuation of the optical transitions [199]. Other factors can cause spectral fluctuation of the emitters' optical lines such as temperature or magnetic field fluctuation. However, in this section, we will restrain ourselves to the study of the charge fluctuation. The spectral fluctuation can be understood with the Stark effect; where an additional energy splitting between the ground and excited states ($\hbar\,\delta\nu$) is caused by an electric field ($\mathbf{E}$):

$$\hbar\,\delta\nu = \Delta\mathbf{p}\cdot\mathbf{E}, \tag{2.43}$$

where $\Delta\mathbf{p}$ is the electric dipole moment of the emitter. A sketch of the modified energy levels under the Stark effect is given in FIGURE 2.7**a**. The first order electric dipole moment is linked to the wavefunction of the electronic-spin:

$$\Delta\mathbf{p} = \langle e|\,\mathbf{r}\,|e\rangle - \langle g|\,\mathbf{r}\,|g\rangle\,. \tag{2.44}$$

For color centers with inversion symmetry, such as Group IV defects in diamond [30], each term of the equation (2.44) is equal to zero and thus Group IV defects present excellent spectral stability of the optical lines [200]. For example, this has allowed for the interfacing of two bulk SiV defects [201]. In contrast, the wavefunctions of the ground and excited state of the NV centers are widely differents, as seen in FIGURE 2.6**a-b**, such as its dipole moment is relatively high $\sim$ 4 Debye [39]. Therefore, NV centers spectrally fluctuate [202], even deep in the bulk material [203]. Complex stabilization protocols are then required to interface two (or more) NV centers via resonant photons [22, 204], limiting the entanglement distribution rate.

The silicon vacancy in SiC doesn't present a centrosymmetry and the first order dipole moment is non-zero. However, using density functional theory (DFT), the dipole moment has been estimated to be 20 times lower for the V1 (0.2 Debye) center [39] compared to the NV-center. This is explained by the same symmetry of the wavefunctions for both ground and excited states (here: $^4A_2$) [117], as seen in FIGURE 2.6**c-d**. It is to be noted that due to the crystal arrangement of SiC, no centrosymmetric point defects can exist within its lattice. Yet, experimental measurements of the electric dipole moment don't agree with one another: with the measures of $\Delta\mathbf{p} = 0.18$ Debye [61] and $\Delta\mathbf{p} = 0.7$ Debye [60].

While the low electric dipole moment has led to high optical line stabilities in bulk material [40] with a small inhomogeneous distribution [42], the behavior of V_{Si} centers in nanostructured environements has yet to be investigated. Indeed, at the surface of the crystal, the energy fluctuation is higher due to unpaired electrons. This is especially true for NV centers, either in nanodiamond [202] or thin diamond membranes [205]. Even for the centrosymmetric SiV in diamond the integration in nanophotonic waveguides has led to spectral diffusion with stochastic jumps of the optical absorption lines [33]; due to a non-zero second-order electric dipole.

We can explain the spectral fluctuation for an integrated color center with a simple model, a sketch of the situation given in FIGURE 2.7**b**. We assume a color center to

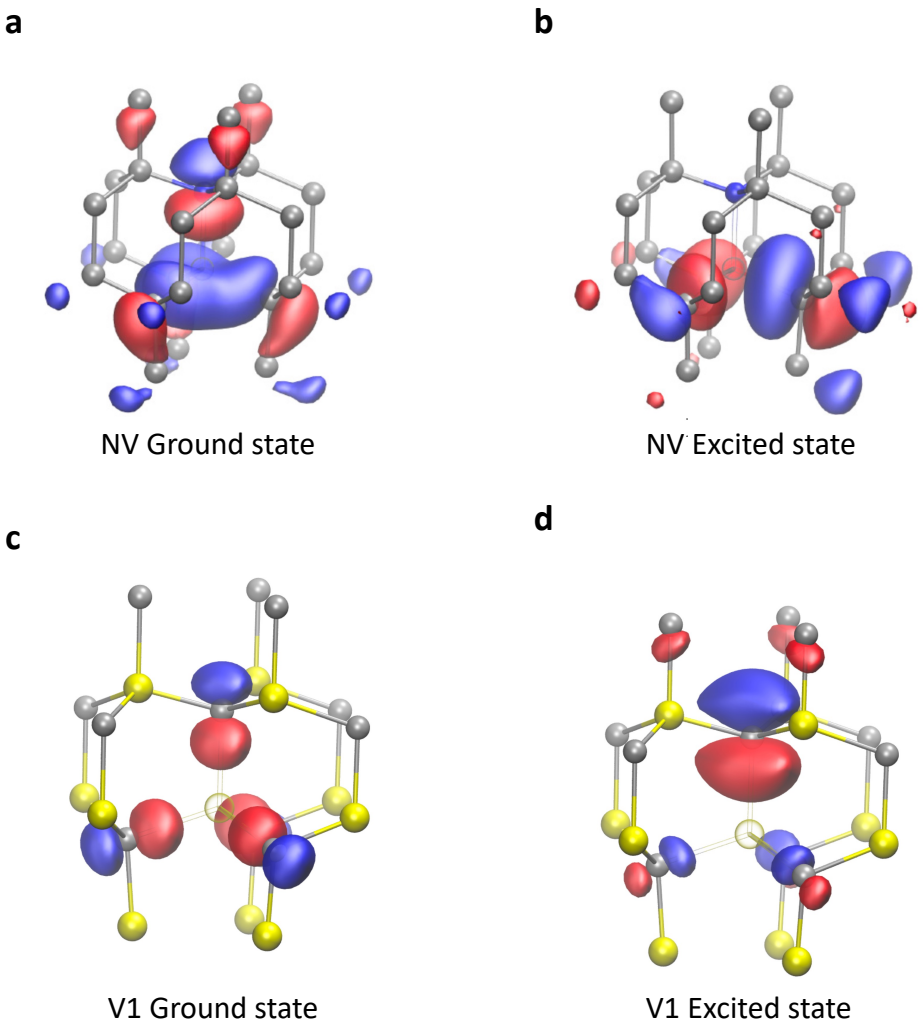

Figure 2.6: **Color centers wavefunctions.** Square moduli of the ground and excited states wavefunctions of the NV center (**a** and **b**) as well as the V1 center. (**c** and **d**) The wavefunctions are calculated by density functional theory. The red (blue) shaded area corresponds to positive (negative) sign of the wavefunction. The yellow and grey spheres represent silicon and carbon atoms. The figure is adapted from [39].

be at a distance r from the surface. When an electron passes by the spin system, it causes an electric field fluctuation which is given by the well-known equation:

$$\mathrm{E} = \frac{e}{4\pi\,\epsilon_0\,r^2}. \tag{2.45}$$

If we want the spectral diffusion to be negligible, the frequency shift caused by the electron should be less than the natural linewidth of the defect. Thus leading to a critical distance of around 50 nm for the V_{Si} in SiC (and 300 nm for the NV center in diamond). In reality, the electric charge fluctuation at the surfaces is more complex and depends on the surface termination and possible degradations due to the fabrication processes [28, 206]. Yet, the characteristics of V_{Si} center make it a good candidate to

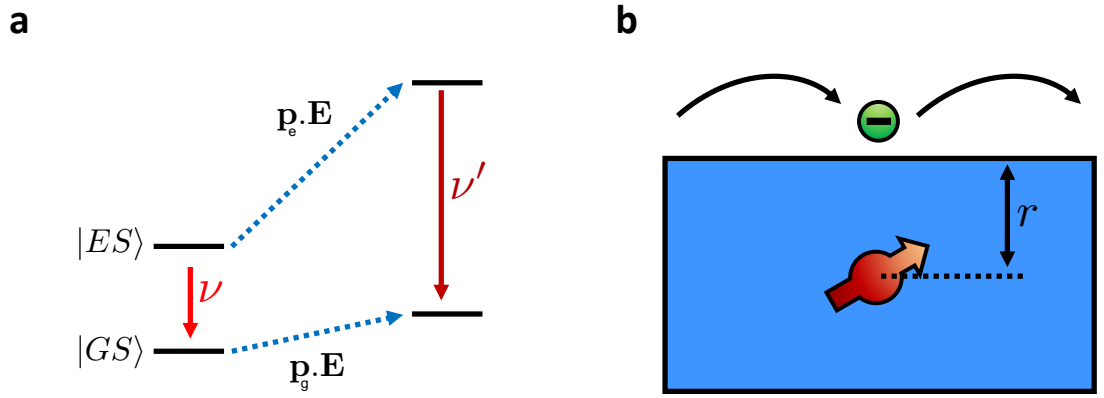

Figure 2.7: **Spectral fluctuation.** **a** Energy levels for an emitter before and after the presence of an electric field, for clarity, the Stark effect is exaggerated. **b** Schematic representation of a shallow color center in bulk, the green circle represents a surface electron which affects the energy levels of the quantum emitter by the Stark effect.

study for integration in a nanophotonic device with possible low spectral diffusion.

2.5 Conclusion and outlook

In this chapter, we have seen the inherent limitation of spin systems in solid: their low spin-photon interaction in bulk material hindering the development of next-generation quantum repeater protocols. The integration of point defects in photonic crystal tackles two important challenges: the low spin-photon interaction strength and the poor collection efficiency. This provides an enhancement of the radiative emission via Purcell effect and can lead to a very high collection efficiency thanks to a preferred mode for the photons leaking out of the cavity. We also have studied the relevant parameters and factors in order to optimize the spin-cavity coupling; namely the Purcell factor, the cooperativity and the natural linewidth broadening. We have introduced a method to estimate if a given color center could be successfully integrated into monolithic resonators. Our study has shown that the V_{Si} center could reach the high cooperativity regime, for a Purcell factor depending on the quantum efficiency of the emitter, while preserving spin-dependent optical transitions. However, this enhancement could be difficult to reach and single-shot readout might necessitate extra protocols, e.g. spin to charge conversion [110, 207] or the use of a nuclear spin as an ancilla qubit [68, 208]. As the V_{Si} center presents a high optical stability in bulk SiC, it is of high interest to evaluate if the V_{Si} center suffers or not from spectral diffusion once integrated into single-mode nanophotonic structures.

With the framework defined in the past two chapters, I can now introduce properly the main problematic of my PhD and of this manuscript:

Can the V2 center in SiC be successfully integrated into a nanophotonic crystal cavity?

To answer this question, from the description given in the above manuscript the following questions arise naturally:

1) Can we generate high-quality defects with a spatial accuracy compatible with the low mode volume of photonic resonators?

2) Are V2 centers spectrally stable in single-mode nanophotonic structures?

3) Can the V2 center, despite its non-integer spin $S = 3/2$, be used to coherently drive nuclear spins in its vicinity and form a local multi-qubit register?

If the V2 center in SiC answers to all of these interrogations, then it is a highly promising candidate to be considered for integration into photonic resonators.

In the next three chapters, I will answer each of the three interrogations via experimental studies on the V_{Si}:

Ch.3 will focus on ion-assisted implantation techniques to generate high-quality V_{Si} with a high spatial accuracy.

Ch.4 will be dedicated to the study of the spin-optical properties of integrated V_{Si} in nanophotonic waveguides.

Ch.5 will present the theoretical framework of the hyperfine interaction between an electron and a nuclear spin, followed by our results on the high-fidelity coherent manipulation of integrated nuclear spins using dynamical decoupling sequences

Chapter 3

Single V_{Si} centers generation via ion implantation

As seen in Chapter 2, the integration of single V2 centers into monolithic nanoresonators will provide near-deterministic light-matter interaction. To this end, it is fundamental to optimize the coupling of color centers with high spin-optical coherences to the cavity mode.

So far, only V2 centers generated via electron irradiation have demonstrated narrow optical lines with long coherence times [40, 45]. However, the defects are created randomly through all the epitaxial layer of the crystal [125]. Thus, the integration of defects in nanoresonators would require fabricating the structures around precharacterized defects, or one would have to use high fluence electron irradiation to obtain a high density of color centers at the risk of damaging the crystal lattice.

To overcome those challenges, the study of color center generation techniques allowing nanometric spatial resolution has been under investigation in the past few years [55, 56, 57, 58]. Different studies have shown the generation of single defect with a high spatial resolution using ion implantation or laser writing. However, it remains unknown if the spin-optical properties are preserved after such generation.

In this chapter, we will present our work on the study of ion-assisted generation of color centers in SiC. First, we will first present the reason why we were unsuccessful to generate single high-quality defects using a silicon focused ion beam (FIB), before demonstrating that helium ion and proton implantation can be used to generate single defects with a high spatial resolution. The resulting defects present for both cases near transformed limited optical transitions. Furthermore, the helium ion-implanted defects present the longest ever measured coherence time in a Hahn echo sequence.

The studies have been performed on a SiC sample grown along the c-side, with a nitrogen concentration of [N] $\sim 4 \cdot 10^{13}$ cm^{-3}. The sample was cleaved to investigate color centers along an a-side surface with smooth surface morphology. The sample was investigated prior to the implantation via fluorescence microscopy and no defect centers were found.

3.1 Silicon implantation

Mask-free implantation techniques are advantageous to generate defects as they provide high spatial resolution in a single step protocol. We implant silicon ions (Si^{2+}) using a FIB device operating at 35 keV acceleration voltage. The ion flux is varied from the minimal nominal dose of $1 \cdot 10^{-18}$ C per spot to $29 \cdot 10^{-18}$ C per spot corresponding to 3.1 and 91 ions respectively. After annealing the sample at 600°C for 30 minutes in an argon atmosphere to remove interstitial defects, we investigate the defect arrays at cryogenic temperatures ($T = 10$ K). A confocal scan of the implanted defects, performed with a continuous-wave excitation laser with an operation wavelength of $\lambda = 785$ nm, is shown FIGURE 1.2. A typical photoluminescence map, with optical excitation and collection from the top through a 0.9 NA objective, of the lowest implantation dose area is given in FIGURE 3.1, where well-spatially separated bright spots can be seen.

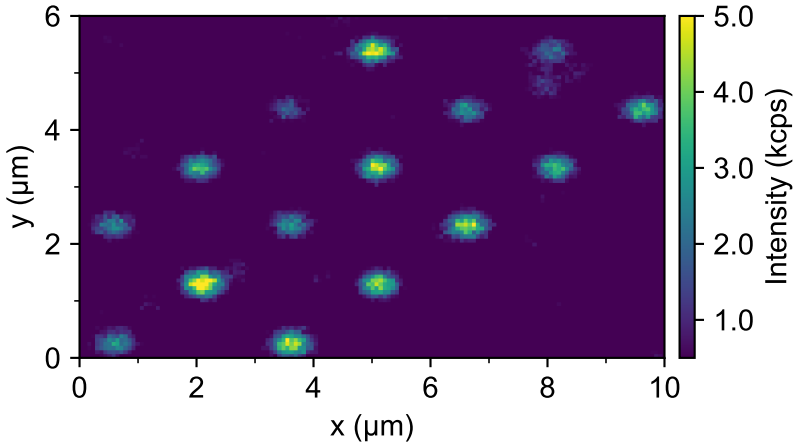

Figure 3.1: **Silicon-implanted defects array.** Confocal microscopy scan of the silicon implanted defects at the lowest dose (3.1 Si^{2+} ions per spot). No single defects can be seen.

To study the created defects, we first measure their emission spectra. A typical photoluminescence emission spectrum of the implanted spots using a Peltier cooled spectrometer (Ocean Insight QE pro, 0.3 nm resolution) is given in FIGURE 3.2.

In all implanted spots, we clearly identify the characteristic ZPL of V1 and V2 centers at 862 nm and 917 nm, respectively. However, the ZPL emission linewidths of V2 centers are around 1 nm (see inset of FIGURE 3.2) which is in contrast to the 0.3 nm spectrometer limited-linewidth, which is usually obtained for electron-implanted defects. Thus, without surprise, we were not able to identify resonant absorption lines for those defects. Furthermore, even at the lowest implantation dose, we did not observe any single defect; a sine qua non condition to claim the success of a defect generation technique. To further investigate the Si^{2+} implanted defects, and understand the broadening of the ZPL emission line, we perform additional measurements on the excited state lifetimes of the implanted defects. To this end, we record the fluorescence from an implanted defect after a 2-ps-pulsed excitation laser that operates at a central wavelength of 780 nm, a sketch of the protocol is given in FIGURE 3.3**a**.

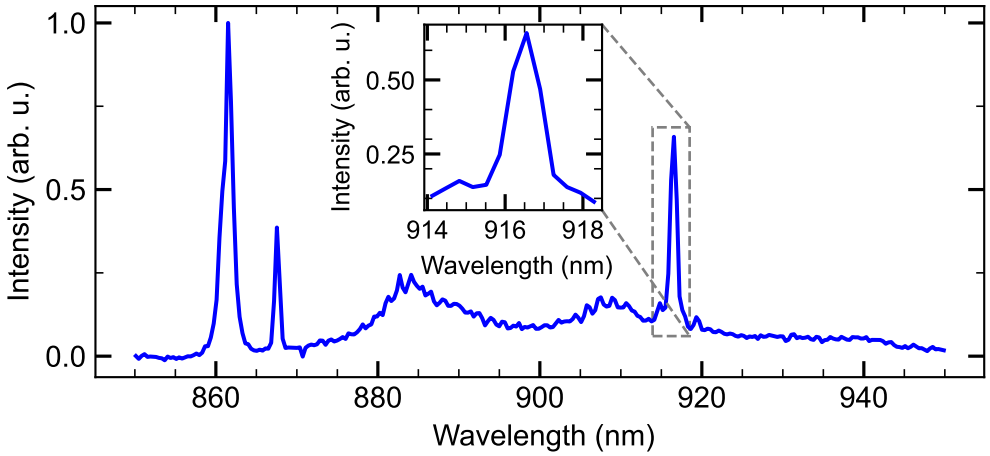

Figure 3.2: **Emission spectrum of silicon-implanted defects.** Typical photoluminescence spectrum of an implantation spot using the lowest possible Si^{2+} ion dose of $1 \cdot 10^{-18}$ C. The zero-phonon lines of both V1 and V2 are visible, which clearly show that multiple defects are being generated. The inset shows a zoom-in for the V2 ZPL, which is substantially wide.

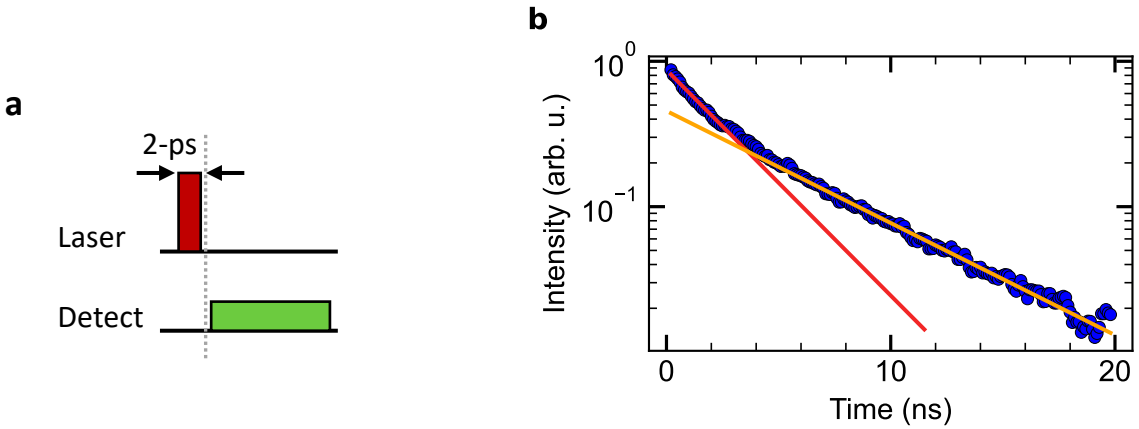

Figure 3.3: **Excited state lifetime (Si^{2+}).** **a** Measurement protocol of the excited state lifetime, a 2-ps pulsed laser excites the system and the fluorescence collection is time gated to avoid laser breakthrough and to increase the signal to noise ratio (SNR). **b** Pulsed off-resonant excitation lifetime measurement of a single implantation spot. The fit is based on a bi-exponential decay function, yielding 1/e-lifetimes of $\tau = 2.79 \pm 0.09$ ns and $\tau = 5.63 \pm 0.07$ ns, respectively.

The signal is temporally and spectrally filtered, as well as background corrected. The measured time-dependent phonon sideband fluorescence is displayed in FIGURE 3.3. We clearly observe a bi-exponential decay with 1/e-lifetimes of $\tau = 5.63 \pm 0.07$ ns and $\tau = 2.79 \pm 0.09$ ns, respectively. This contrasts with typical results obtained for off-resonant excitation of V1 and V2 centers [118, 124], where single exponential de-

cay have been observed. The longer decay constant closely resembles the deep bulk excited state lifetime, whereas the shorter decay time may indicate that additional non-radiative decay channels have been created due to substantial crystal damages associated with heavy Si^{2+} ions implantation [209, 210]. As we will see, lifetime measurements performed for helium and proton-implanted defects reveal single-decay behavior, strengthening our hypothesis.

In conclusion, silicon ions can be used to generate monovacancy clusters within the crystal lattice, however, the defects present broad emission spectra, which may be explained through heavy damage surrounding the color centers environment. In the future, to investigate the possibility to create a high-quality single V2 center utilizing silicon ions, the ion flux as well as its energy, could be reduced. In the next sections, we will present two successful ion-assisted implantation techniques.

3.2 Helium implantation

In this section, we will show how helium ions can be used to generate high-quality shallow V_{Si} centers in SiC.

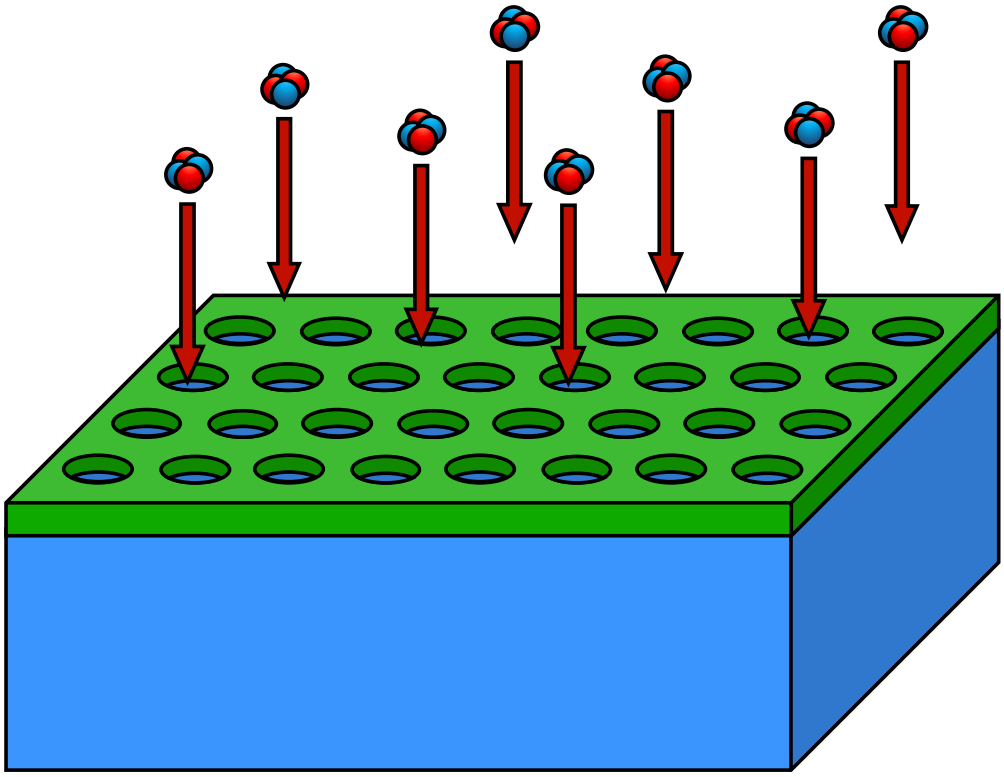

Figure 3.4: **Ion implantation sketch.** Schematics of V_{Si} centers creation via helium ion implantation. He^{+} ions are accelerated to 6 keV and implanted through a lithographed PMMA mask defining implantation spots.

3.2.1 Implantation protocol

The helium implanter used in our work is a micro-beam implanter (ion gun) with a limited spatial resolution due to the beam radius being around 100 µm. Therefore, the singly-charged He^+ ions beam is sent through a mask, as seen in FIGURE 3.4, made of an array of holes separated by 1 µm. Two hole diameter sizes have been experimentally considered: 100 and 200 nm. The mask is made of a single layer of spin-coated 200k-polymethyl methacrylate (PMMA), which has been electron-lithographed in Raith Eline apparatus with 20 kV acceleration voltage, 10 µm aperture, and an exposure dose of 270 $\mu C/cm^2$. The chemical structure of the exposed area is altered, thus modifying its solubility to a certain developer. In our case, after electron exposure, the sample is immersed, for two minutes, in a mixture of methyl isobutyl ketone (MIBK) and isopropyl alcohol (IPA) to develop the mask. Images of the resulting array under an optical microscope, as well as under a scanning electron microscope (SEM), can be seen in FIGURE 3.5.

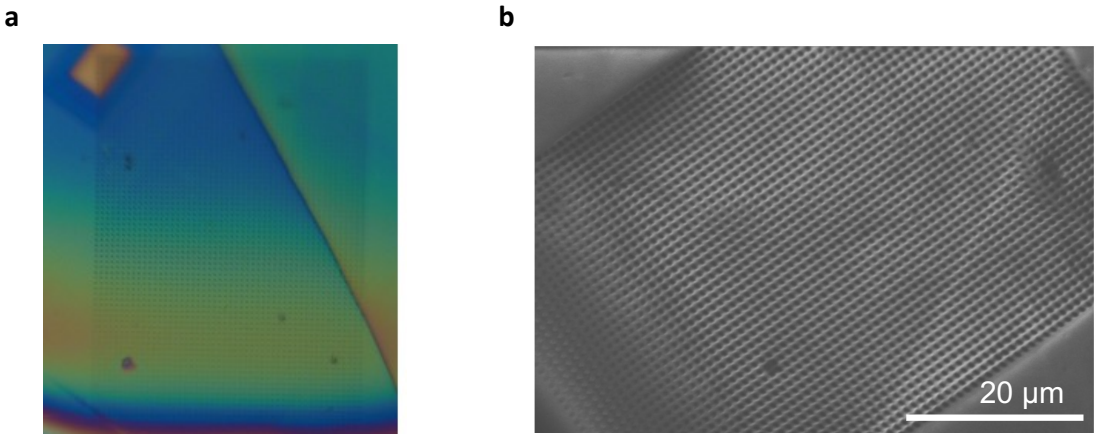

Figure 3.5: **Implantation mask.** Images of the PMMA mask defining the implantation array, using an optical microscope (**a**) or a scanning electron microscope (**b**).

Compared to previous work [56, 57, 58, 124, 211], we choose a low ion energy of 6 keV in order to minimize crystal damage, hoping to preserve the spin defects environment. The He^+ dose used of 10^{11} ions/cm correspond to 7.85 ions/hole (31.4 ions/hole) for the 100 nm (200 nm) diameter holes.

After removing the PMMA mask by immersion in an acetone solution, the sample was annealed at 600 °C for 30 min in an argon atmosphere to remove some interstitial-related defects and subsequently placed in our confocal microscopy setup for characterization.

3.2.2 Implantation yield

FIGURE 3.6 shows the photoluminescence map of the helium implanted defects, using continuous off-resonant excitation at 785 nm. To infer the implantation yield, i.e. the number of V2 centers created per implanted ion, we measure the number of defects

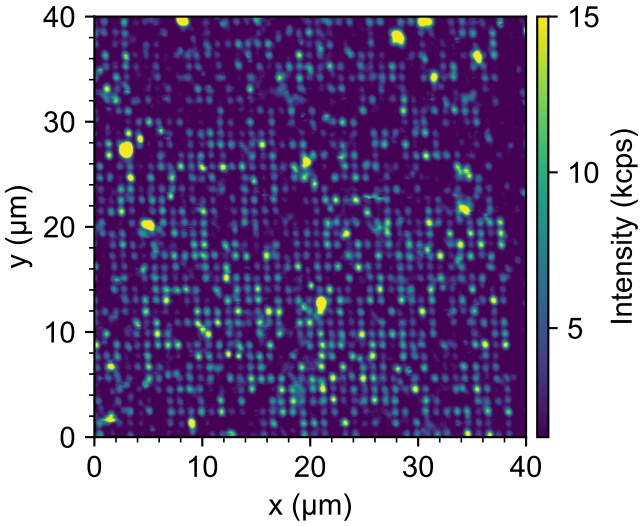

Figure 3.6: **Helium implanted defects array.** Confocal microscopy scan of the defects generated by Helium implantation through 100 nm diameter holes.

per implantation spot by performing second-order autocorrelation measurements ($g^{(2)}$), also known as Hanbury Brown and Twiss interferometry [212].

To this end, the fluorescence is sent into two single-photon detectors, using a 50/50 beam-splitter. The detector outputs are connected to a time-tagger which measures the time difference between the two detector signals and the measurements are histogrammed. The resulting histogram is background corrected and normalized such as the data is a faithful representation of $g^{(2)}(\tau)$ ($g^{(2)}(\tau \to \pm\infty) \to 1$). The measurement is done with an off-resonant excitation at 785 nm with 2 mW pump power. We find that V1 and V2 centers [118] are created at roughly the same rate. As we are only interested in the generation yield for the V2 centers, we suppress the phonon sideband emission of V1 centers during the $g^{(2)}$ measurements with an additional 950 ± 25 nm bandpass filter which rejects most of the V1 center's emission, and, at the same time, shows a high transmission for the first phonon sideband of the V2 center emission.

A typical measurement obtained for a single V2 center is shown in FIGURE 3.7**b**, where two features can be seen: a bunching and antibunching of the signal. Once the spin has emitted a photon, via radiative decay to the ground state, the second photon emission occurs when the system decays radiatively a second time, thus in a time scale of the excited state lifetime, i.e two photons are never emitted at the same time hence the antibunching observed. As explained in chapter 1, the V2 center can be considered as a three-level system composed of the ground state, the excited state and the metastable state, as depicted in FIGURE 1.5**c**. The latter is also called a shelving state, and transition through this long-lived spin state via non-radiative decay channels, can result in a large number of photons emitted separated by time intervals without emission. Thus explaining the bunching behavior observed in the $g^{(2)}$ measurement. For a single three-level system, the analytical expression of the autocorrelation function ($g^{(2)}$) is:

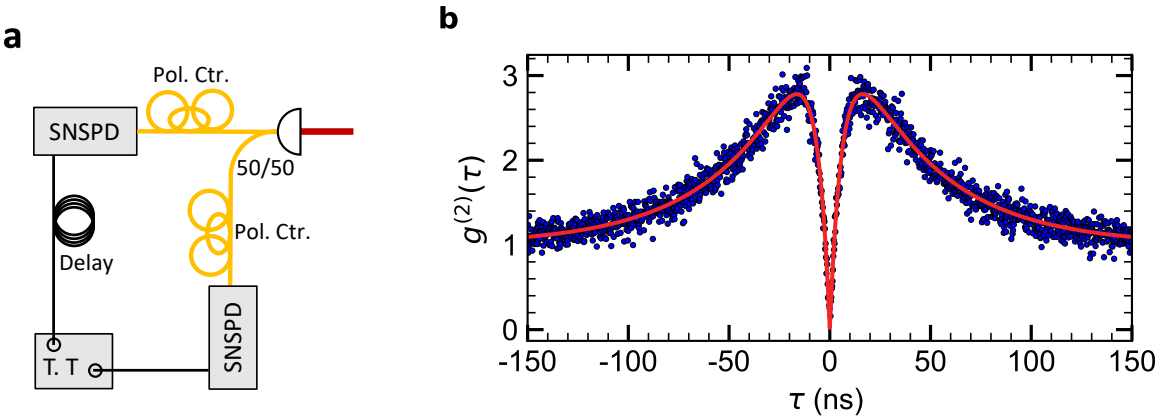

Figure 3.7: **Autocorrelation measurement. a** Sketch of the optical/electronic modification to the original setup (given in FIGURE 1.2). The collection path is split in two via a 50/50 fiber beam-splitter and sent to two different inputs of the SNSPD. The two resulting electronic signals are linked to the start and stop channels of the time-tagger, which measures the time delay between two successive pulses. **b** Typical second-order correlation measurement of a single V2 center (signal going below the 0.5 threshold). Blue dots are data and the red line is a fit taking into account the analytical formula of the function $g^{(2)}(\tau)$ (see equation (3.2)).

$$g^{(2)}(\tau) = 1 - (1+a)\exp\left(-\frac{|\tau|}{\tau_1}\right) + a\exp\left(-\frac{|\tau|}{\tau_2}\right). \tag{3.1}$$

Here, a, τ_1, τ_2 are linked to the different transition rates and state lifetimes and τ is the delay time between two detector clicks in the Hanbury Brown and Twiss setup. We will not investigate the different rates in this work as it is currently under investigation by MSc Di Liu, via novel pulse sequences. The equation (3.1) can be extended for multiple identical defects as:

$$g^{(2)} = 1 - \frac{1+a}{N}\exp\left(-\frac{|\tau|}{\tau_1}\right) + \frac{a}{N}\exp\left(-\frac{|\tau|}{\tau_2}\right). \tag{3.2}$$

Where N is the number of defects excited by the off-resonant laser. From the equation (3.2) and the fit of the signal, we can extract the number of V2 centers generated in a single spot: $N = \dfrac{1}{1 - g^{(2)}(\tau = 0)}$. In the measurement shown in FIGURE 3.7**b**, we find that $g^{(2)}(\tau = 0) \ll 0.5$, which correspond to a single emitter (value retrieves from the fit: $N = 1.01 \pm 0.02$). In other words, our implantation techniques is suitable to generate single V2 centers.

Performing a saturation study allows retrieving the saturation intensity of an implanted single V2 defect. We excite the system at varying excitation power and correct the resulting fluorescence by the background signal next to the implantation spot. The result is shown in FIGURE 3.8**a** and can be fitted by the following equation:

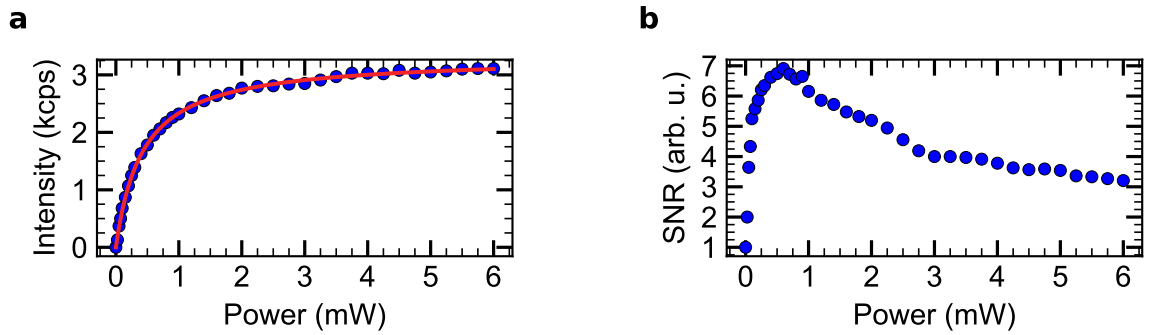

Figure 3.8: **Saturation study.** **a** Background corrected fluorescence rate of a single V2 center for various pump power. Blue dot are data and the red curve is the fit obtain using the equation (3.3). **b** Power dependent signal to noise ratio (SNR) of the fluorescence rate. The maximum is obtained for a laser power of 0.6 mW.

$$I(P) = \frac{I_S \cdot P}{P + P_S}. \tag{3.3}$$

Here, I_S (P_S) is the saturation intensity (power). We obtain for the single defect studied earlier a saturation intensity (power) of $I_S = 3\,319 \pm 9$ cts/s ($P_S = 422 \pm 5$ μW).

By inquiring 112 spots in the array of 100 nm implantation spot, under off-resonant excitation of 0.6 mW, where the SNR is maximal (see FIGURE 3.8**b**), we extract the statistical distribution of the number of defects per spot from the background-corrected count rate. The distribution is shown in FIGURE 3.9. The least-square fit to the data is based on a Poissonian function:

$$p(k) = \frac{\lambda^k}{k!} e^k, \tag{3.4}$$

corresponding to the probability to generate k defects in an implantation spot, and characterized by a single parameter λ: the average number of created defects. We determine the average number of V2 centers created per spot to be 0.66 ± 0.06. Considering the ion implantation dose ($1 \cdot 10^{11}\,\mathrm{cm}^{-2}$) and the mask's hole size (100 nm diameter), we obtain therefore an implantation yield of $8.5 \pm 0.8\,\%$ for generating V2 centers. The same study has been conducted on the array of 200 nm implantation spot, FIGURE 3.9, and from the defect number distribution, we yield an average of 2.4 ± 0.09 defects per spot thus leading to an implantation yield of $7.7 \pm 0.3\,\%$. In both implantation conditions, the number of defects created per helium ion is the same, which is expected as the yield is mainly dependent on the ion energy. Our implantation yield is thus similar to previous experiments conducted on the diamond platform [213, 214]. Higher energies could lead to higher implantation yields [56], however, it would also increase damage to the crystal lattice.

It seems more interesting to use the 100 nm diameter holes to create single V_{Si} centers, as when the implantation leads to the creation of defects, it will be most probably be a single defect. However, the 200 nm diameter holes will generally create

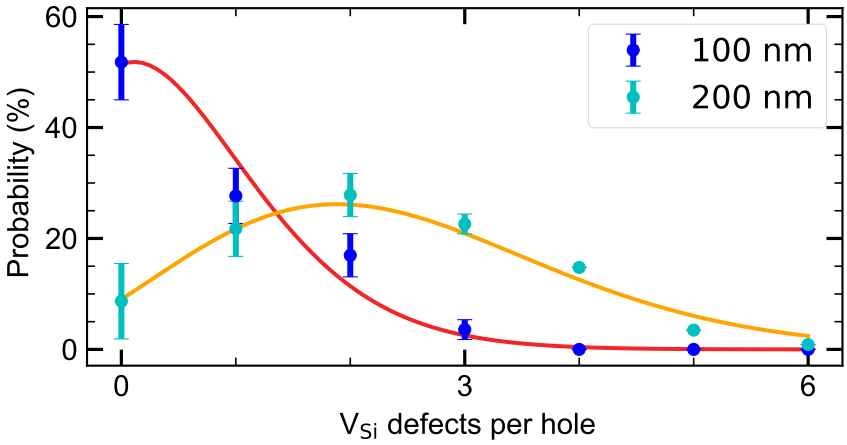

Figure 3.9: **Defect numbers distribution (He^+).** Probability distribution of the number of V2 centers per implantation site. Blue (Cyan) dots are data from the implantation array of 100 (200) nm holes and error bars correspond to the square root of the number of measurements; the red (orange) line is a fit to the data considering a Poissonian distribution (given in equation (3.4)).

more than one V2 center. Thus, we will only investigate the area of 100 nm diameter holes.

3.2.3 Spatial resolution

Due to the small mode volume of nanophotonic resonator devices (as discussed in Chapter 2), a high-accuracy three-dimensional positioning of defects generation is crucial for integration into photonic cavities. Here, we demonstrate the potential of He^+ implantation in this regard.

Defects depth

To determine the depth of the generated defects, we used standard Synopsys Sentaurus Monte Carlo (MC) simulations. Those have been conducted by our collaborators in Erlangen, from the group of Pr. Berwian at the Fraunhofer Institute for Integrated Systems and Device Technology IISB. Sentaurus MC takes into consideration the crystalline structure of 4H-SiC and uses the binary collision approximation (BCA).

Implantation was simulated at a temperature of $T = 300\,\mathrm{K}$ with an implantation energy of 6 keV and a dose of $1 \cdot 10^{11}\,\mathrm{cm}^{-2}$. As we do not have precise control on the implantation angle in our implanter device, simulations were done for varying tilt angles between 0° and 7°. For the simulation of vacancy generation, threshold displacement energies of 41 eV for Si and 16 eV for C have been chosen for the Frenkel pair defect model while taking into account all secondary recoils from cascades [215].

FIGURE 3.10**a** shows the results of the simulation for implantation at an angle of 0°. Here, even if we observe a He^+ ion channeling effect, no channeling is found in the depth profiles of carbon vacancies (V_C) and especially not for V_{Si}. The defects

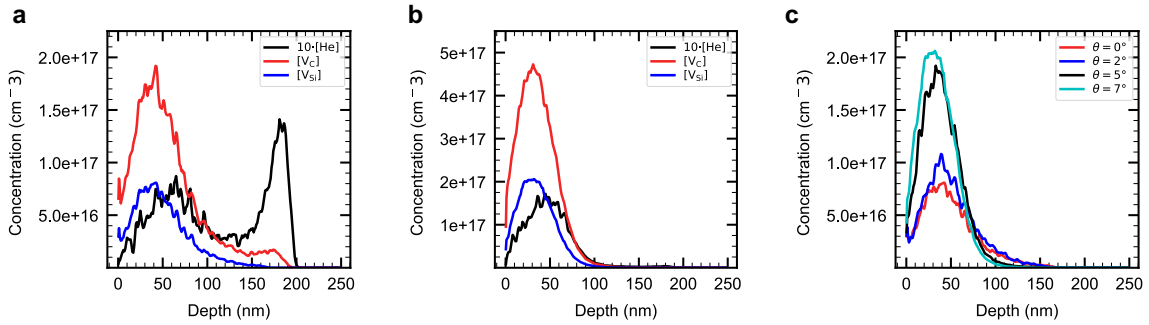

Figure 3.10: **He^+ implantation depth simulation.** **a** (**b**) Simulation of implantation depth for bombardment with He^+ ions at an energy of 6 keV at an angle $\theta = 0°$ ($\theta = 7°$). The black line represents the stopping distance for the He^+ ions, the green (blue) line represents the depths at which carbon (silicon) vacancies are created **c** Depth profiles of V_{Si} generation at different implantation angles θ ranging from 0° to 7°. The profiles are similar and thus we can conclude that V_{Si} centers are mainly generated at a depth of $30 - 40$ nm.

generated are shallow: in majority $30 - 40$ nm below the surface. The same depth profile of the defect generated can be observed at an increased implantation angle: $\theta = 7°$ in FIGURE 3.10**b**. Interestingly, the defect generation efficiency (implantation yield) is around three times higher. The simulated V_{Si} depth profiles for the varying implantation angles θ are regrouped in FIGURE 3.10**c**. The profiles present nearly identical shapes, thus confirming that the V_{Si} centers are created in majority at a depth of $30 - 40$ nm. We will now investigate the lateral accuracy of the defects positioning.

Lateral accuracy

To estimate the spatial implantation accuracy in lateral coordinates, we use a closed-loop piezo scanner (Mad City Labs Inc. Nano-LPMW, 0.4 nm resolution) and determine the position of 36 single V2 centers within a 12×12 array. Each single-defect position is determined using a two-dimensional Gaussian fit. Subsequently, the positions of the implanted defects are compared with a simulated grid. We minimize error squares between data and simulation by allowing the simulated grid to account for sample rotation and scanner linearity error in both directions. The fitted grid as well as the positions of the defects can be seen in FIGURE 3.11**a**, whereas the deviation between the measured data and the simulated grid is shown in FIGURE 3.11**b**. The extracted variance of the defect positions is 53.6 nm and is represented by a circle in FIGURE 3.11**b**. Thus, the variance is comparable to the implantation hole size (50 nm radius), such that the lateral straggle of He^+ ions during implantation is minimal.

To confirm our experimental results, we ran a "Stopping and Range of Ions in Matter" (SRIM) [216] simulation, analyzing the ion-matter interaction via Monte-Carlo method. We simulated the implantation of 6 keV He^+ ions into SiC and it resulted in a lateral straggle of 22 nm. The implantation accuracy at this low energy is thus sufficient for creating defects in the center of photonic crystal cavities [46]. Furthermore, higher

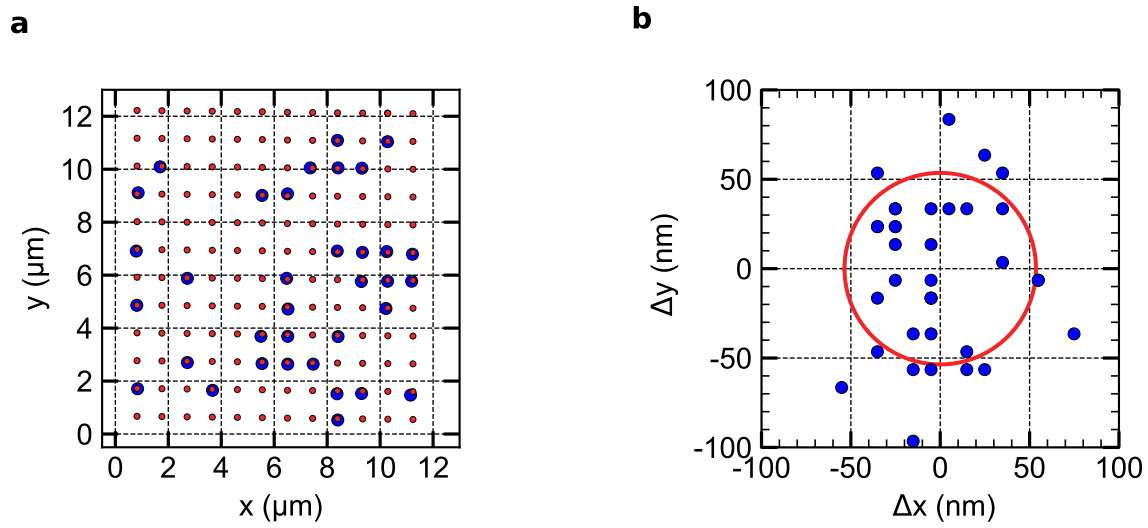

Figure 3.11: **Lateral accuracy of helium-ion implantation.** **a** Fitted positions of the implanted defects via 2D-gaussian functions (blue) and the optimized simulated grid (red). **b** Lateral spatial distribution of the implanted single V2 centers compared to a simulated grid. The red circle represents the 53.6 nm variance of all positions.

accuracy could be reached by reducing the radii of the holes or by using mask-free implantation achieved with a helium FIB or helium ion microscope.

Having demonstrated the high spatial accuracy in all three-dimension of the generation of single V2 centers in SiC using He^+, we have yet to investigate the spin-optical properties of the resulting defects.

3.2.4 Spin-optical properties

For numerous spin defects in solid, it remains unclear whether spin-optical coherences can be maintained after shallow ion implantation [56, 58] as the surface proximity leads to a strong degradation of spin-optical properties [205, 217, 218]. In the following section, we demonstrate that V2 centers do not suffer from those aspects.

Optical

As an initial investigation of the optical properties, we measure the excited state lifetime of a single V2 center at a temperature of $T = 10$ K, similarly to the experiment conducted on the silicon-implanted V2 centers. The protocol is given in FIGURE 3.3**a**. Interestingly, the fluorescence signal reveals only a single-exponential decay, thus we expect crystal damage to be minimum compared to the silicon-implantation case where the lifetime displayed a bi-exponential decay with a broadening of the emission spectra. We extract a 1/e-lifetime of $\tau = 7.05 \pm 0.06$ ns, similar to a previous experiment on V_{Si} [124], thus being promising for the optical properties of the shallow implanted defects. The lifetime limited absorption linewidth is $\Delta\nu = (2\pi\tau)^{-1} = 22.5 \pm 0.2$ MHz,

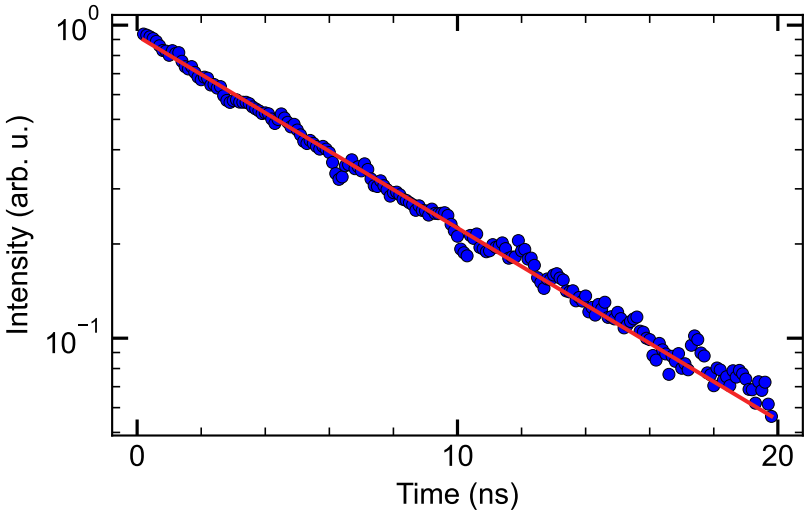

Figure 3.12: **Excited state lifetime (He^+).** Pulsed off-resonant excitation lifetime measurement of a single implantation spot. The fit is based on an exponential decay function, yielding 1/e-lifetimes of $\tau = 7.08 \pm 0.06$ ns.

and allow to benchmark the quality of the resonant absorption linewidths.

Indeed, we now investigate the absorption spectra of the implanted defects. To this end, we scan the frequency of a tunable diode laser (Toptica DL pro) across the spin-conserving optical transitions between the ground and exciting states. As shown previously in FIGURE 1.2, we separate the emission signal from the excitation laser by only collecting the PSB via the usage of a tunable longpass filter. To avoid spin pumping [119] and thus increase the SNR, we additionally provide a microwave drive at 70 MHz (corresponding to the ground state zero-field splitting) to continuously mix the ground state energy levels [40], the protocol is given in FIGURE 3.13**a**. A typical resonant photoluminescence excitation scan is shown in FIGURE 3.13**b**. Strikingly, the spectrum shows two absorption lines spectrally separated by 1 GHz, similar to a V2 center studied in the bulk material [45], even though the defect is shallow and could be prone to spectral diffusion (see section 2.4). Furthermore, the fitted linewidths (least-square method) of the A_1 and A_2 transitions are respectively: $\Delta\nu_{A_1} = 41 \pm 2$ MHz and $\Delta\nu_{A_2} = 24 \pm 1$ MHz; which is remarkably close to the lifetime limit ($\Delta\nu = 22.5 \pm 0.2$ MHz). Thus no spectral diffusion can be observed on the timescale of a single scan, even if the defect is a few tens of nanometer beneath the surface.

To study the long-term stability of the absorption lines, we repeated the resonant photoluminescence excitation scan for an hour, the result is shown in FIGURE 3.13**c**. Every single scan presents the two near transform-limited absorption lines; averaging over the 125 scans displayed in FIGURE 3.13**c**, we obtain a linewidth of 40 ± 10 MHz and 29 ± 5 MHz for the A_1 and A_2 transitions respectively, where the uncertainty is taken from the standard deviation. However, a little drift of the lines can be observed but without any sign of ionization, we assign the drift to surface charge fluctuations.

To characterize the drift speed, we perform a linear regression on the positions of the A_1 transition for the 5 distinctive parts (when no stochastic jump occurs) of the

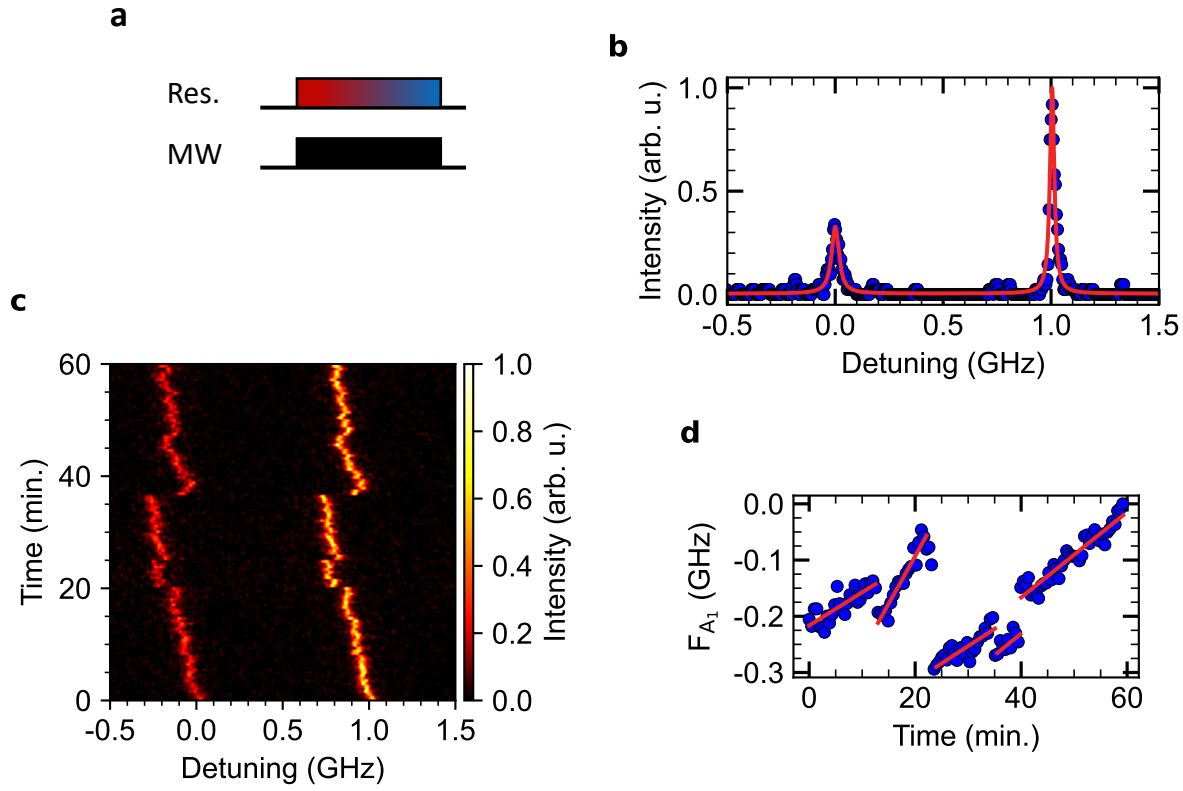

Figure 3.13: **PLE of a single helium-implanted defects.** **a** Sketch of the PLE protocol: the frequency of the resonant laser is scanned across both optical transitions (A_1 and A_2) while the microwave field drives continuously the ground state at 70 MHz (ZFS). **b** Single resonant photoluminescence excitation scan on an implanted V2 center. The optical transitions linewidths are nearly lifetime limited: $\Delta\nu_{A_1} = 41 \pm 2$ MHz and $\Delta\nu_{A_2} = 24 \pm 1$ MHz. **c** Repeated resonant excitation scans during one hour. No ionization is observed, only a slow drift can be seen. This drift is assigned to surface charge fluctuations. **d** Frequency of the A_1 transition over time, fitted from **c**, the red lines are linear regression of different parts of the time-dependent A_1 transition frequency, allowing us to determine a drift rate: here 8.4 MHz/min.

repeated PLE scans. The results are given in FIGURE 3.13**d**, the weighting average of the drift speeds gave us an approximation of the absorption lines drift speed, here 8.4 MHz/min. Thus, according to the measured linewidths of the lines, the laser will drift out of resonance only every few minutes. To counteract the drift, we can stabilize the resonant laser onto the A_2 transitions via our own software protocol, which is given in Appendix C and inspired by previous works [13]. Experimentally, we can stabilize the laser over an infinite amount of time granting access to protocols with long-measurement time as we will see in the next section (3.2.4). The ability to stabilize the laser onto the color center resonant transitions showcases the excellent stability of the shallow V2 center's optical lines.

We highlight that all implanted V2 centers investigated show reproducibly good

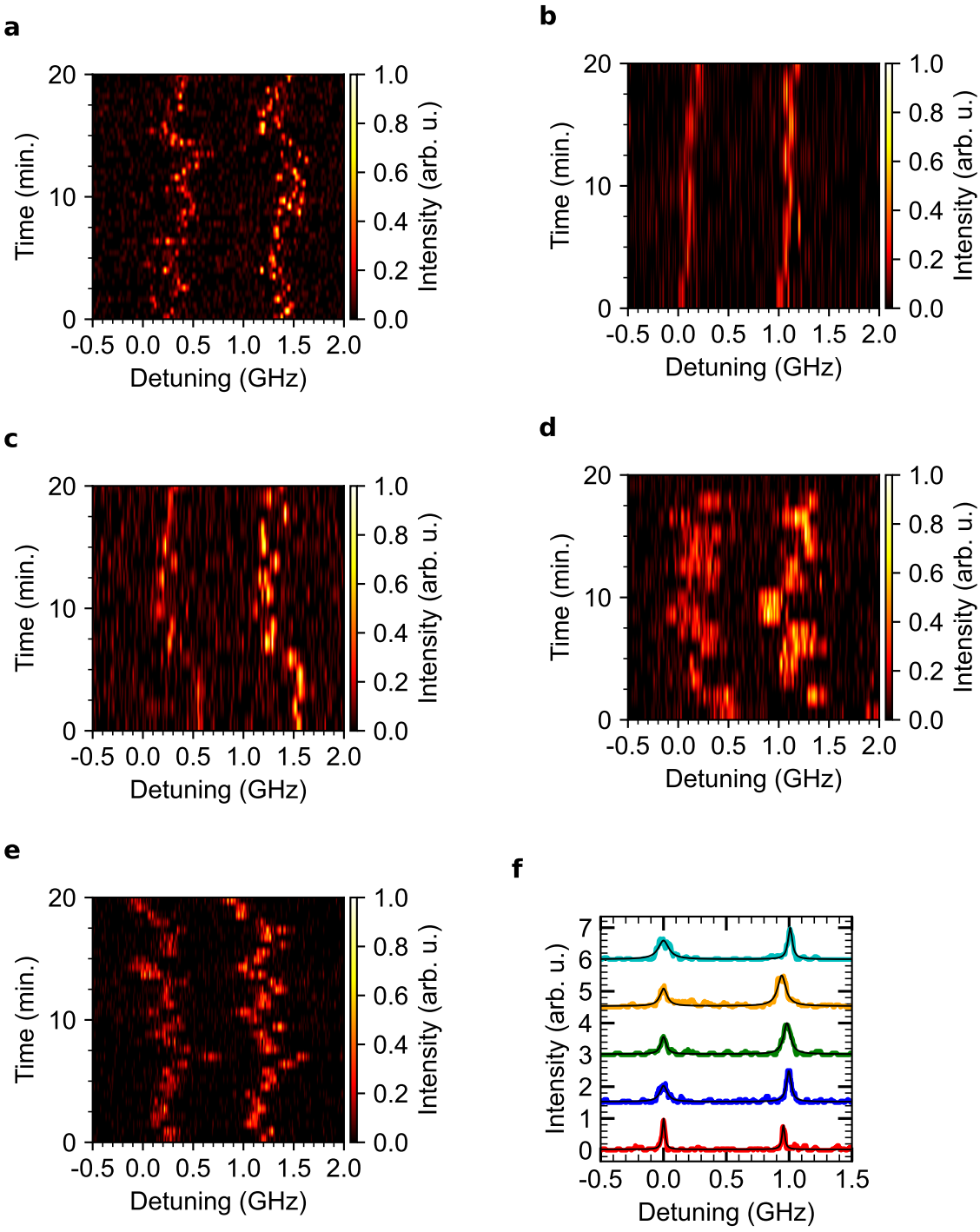

Figure 3.14: **PLE statistics of helium-implanted defects.** **a-e** Repeated resonant excitation scans during 20 minutes for five implanted defects. **f** Single-line resonant excitation scans for the five different V2 centers. For a better visibility, each measurement is offset in the y-direction and the A_1 transition for all spectra is centered at zero detuning. The actual spectral distribution of the defects is ± 10 GHz, comparable to bulk defects [42]. Linewidths are obtained via double-Lorentzian fits to the data (black lines) and given in TABLE 3.1.

spectral stabilities. In particular, we have studied five other implanted defects via repeated PLE scans for 20 minutes, the results are shown in FIGURE 3.14. Remarkably, no defect shows a sign of ionization or blinking, and every single scan results in well-separated spin-selective lines. The small remaining drift rate can be captured by the laser feedback system we have implemented (Appendix C).

In FIGURE 3.14**f**, we display a single absorption line scan for the five additional defects, from which we extract the linewidths of the A2 and A1 transitions via double-Lorentzian fit functions which are given in TABLE 3.1.

Interestingly, we find that all defects presented have close to transform-limited spin-selective optical transitions. The average linewidth of the A_2 transition is 46 ± 20 MHz, where the uncertainty is taken from the standard deviation.

Color in FIGURE 3.14**f**	$\Delta\nu_{A_1}$ (MHz)	$\Delta\nu_{A_2}$ (MHz)
Cyan	101 ± 3	41 ± 1
Yellow	68 ± 4	79 ± 2
Green	52 ± 3	64 ± 2
Royal Blue	70 ± 2	45 ± 1
Red	26 ± 1	26 ± 1

Table 3.1: **Linewidth statistic of helium-implanted defects.** Single line optical linewidths of every studied helium-implanted V2 center shown in FIGURE 3.14**f**. The vertical ordering (from bottom to top) is the same as the one in FIGURE 3.14**f**.

Our results highlight the reproducibility of helium ion-assisted implantation techniques to generate shallow high-quality color centers, with stable narrow optical lines. The high stability of the optical lines allows investigating of the spin properties of the system, via protocols with long measurement-time, namely Ramsey interferometry and Hahn echo measurement.

Spin

In order to investigate the ground state spin dephasing and coherence time, we lift the Kramers degeneracy by aligning an external static magnetic field ($B = 17$ G) along the c-axis of the crystal utilizing our self-developed protocol (see Appendix D). This allows for selective driving of the three ground state spin transitions [40]. A sketch of the resulting ground state energy levels is given in FIGURE 3.15**a**.

To inquire about the spin properties of the implanted defects, we first perform a Ramsey interferometry experiment on the first V2 center investigated in section 3.2.4. The protocol is given in FIGURE 3.15**b** and explained earlier in section 1.4.2. The resulting spin signal is given in FIGURE 3.15**c**, where can be observed, as expected, a decaying oscillation. from the fit of the data, we yield a dephasing time of $T_2^* = 34 \pm 4$ µs, which is comparable to deep-bulk defects in similar SiC crystals [40, 79]. We can thus expect a long coherence time for the shallow implanted defects.

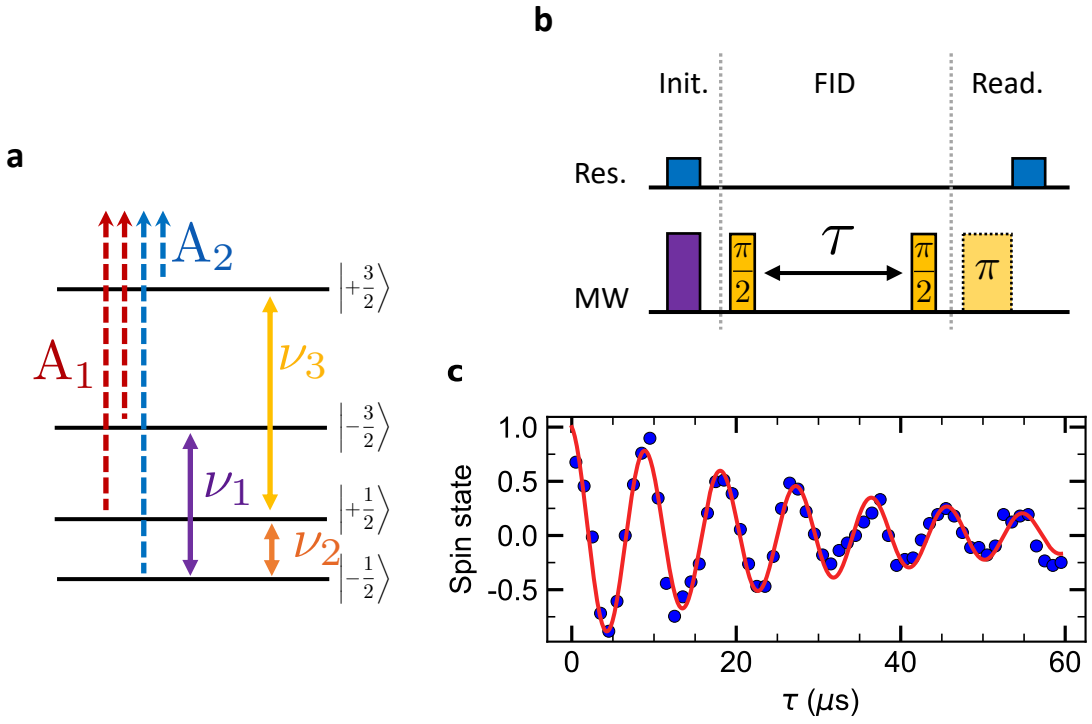

Figure 3.15: **Ramsey interferometry for a helium-implanted defect. a** Energy level diagram of the ground states of a V2 center in an external magnetic field ($B = 17$ G) lifting the Kramers degeneracy. The dashed lines represent the spin-conserving optical transitions and the solid ones the allowed microwave transitions. **b** Sketch of the free induction decay protocol. The electron spin is first initialized in the superposition state ($|+\rangle$) and then freely evolves for a time τ before to be read along $\pm\mathbf{x}$ by either applying an additional π-pulse (here dashed) or not. **c** Spin dephasing time of a helium-implanted V2 center, from the fit to the data we yield $T_2^* = 34 \pm 4$ µs. The spin state $+1$ corresponds to $m_s = 3/2$ and -1 to $m_s = 1/2$.

The coherence time is measured by performing a Hahn echo sequence, protocol in FIGURE 3.16**a**. We fit the spin signal given in FIGURE 3.16**b** with a stretched exponential function:

$$y(\tau) = a \exp\left(-(\frac{\tau}{T_2})^n\right) + y_0. \tag{3.5}$$

The power n allows considering the different sources of dephasing while the offset y_0, as well as the amplitude a, take into account the non-perfect mw-pulses. We yield a coherence time of $T_2 = 1.4 \pm 0.1$ ms, which is to our knowledge and at the time of the redaction of this manuscript, the longest-ever reported Hahn echo coherence time for this system. We explain the long coherence time by the spin-purity of the SiC crystal as well as the magnetic field alignment protocol. The spin properties of shallow ion-implanted V2 centers are on par with the ones from deep bulk electron-implanted V2 centers.

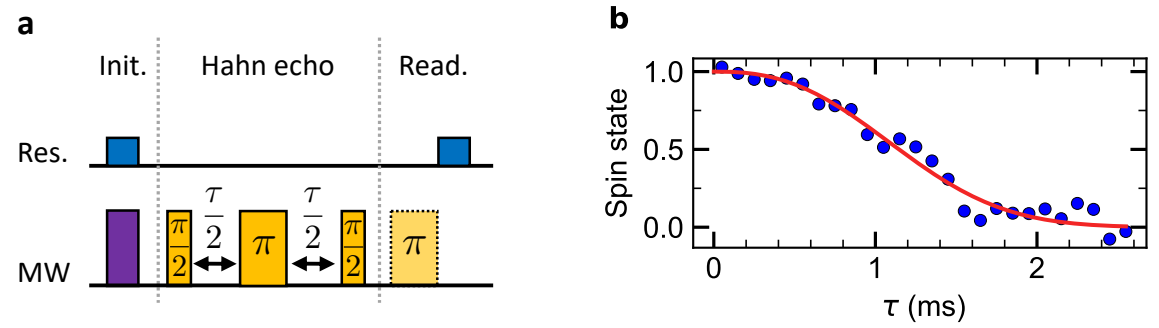

Figure 3.16: **Hahn echo sequence.** **a** Sketch of a Hahn echo sequence. The system undergoes the same protocol as for a free induction decay (FIGURE 3.15**b**) but an additional π-pulse is performed in the middle of the free evolution time. **b** Spin coherence time of a helium-implanted V2 center, from the fit to the data we yield $T_2 = 1.4 \pm 0.1$ ms. The spin state $+1$ corresponds to $m_s = 3/2$ and -1 to $m_s = 1/2$.

In conclusion, implantation of helium ions at low energy into SiC crystal can create, with a high yield and a good spatial accuracy, single V2 centers presenting high spin-optical coherences. We could further increase the accuracy by utilizing mask-free implantation techniques via the use of ion microscopes, where we could implant defects in nanoscale monolithic resonators. Offering unique potential to scale up semiconductor quantum technologies, for quantum information processing [36, 219].

We also studied the possibility to used protons to generate V2 centers. The resulting yield and spatial accuracy, as well as the optical properties of the generated defects, are presented in the next section.

3.3 Proton implantation

As for the helium implantation, we implanted protons through a PMMA mask. A layer of 200 nm thickness is spin-coated on the sample on which 100 nm diameter holes are patterned using electron-beam lithography using the same protocol as before, described in section 3.2.1. The proton implantation has been realized by the group of Prof. Astakhov from the Institute of Ion Beam Physics and Materials Research in Dresden. Protons are implanted at an energy of 12 keV at a dose of $5 \cdot 10^{12}\,\mathrm{cm}^{-2}$. The sample is subsequently annealed at 600°C in an argon atmosphere for 30 minutes to remove some lattice damage and interstitial defects.

3.3.1 Implantation yield and spatial accuracy

In FIGURE 3.17**a** is given a confocal scan of the implanted array. We can use the same approach as previously described in section 3.2 to determine the implantation yield and spatial accuracy. We infer the number of defects per spot by measuring and fitting, with the equation (3.2), the second-order correlation function ($g^{(2)}$). A typical auto-correlation measurement can be seen in FIGURE 3.17**b**. As expected and seen

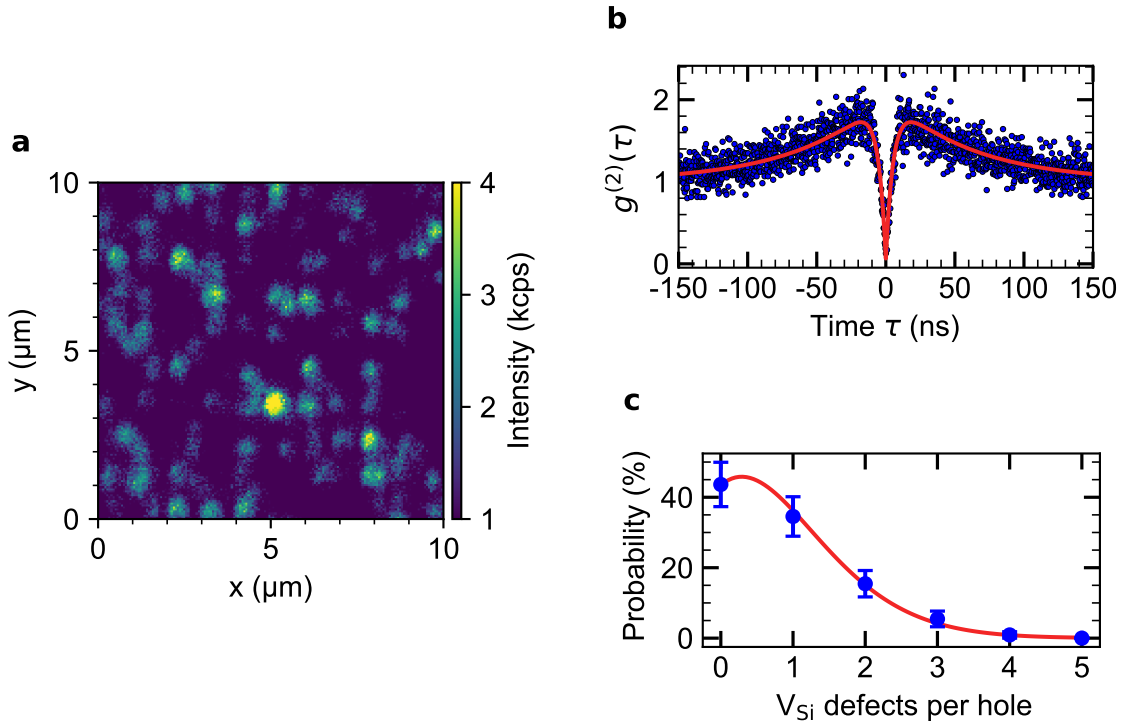

Figure 3.17: **Proton-implanted defects. a** Confocal microscopy scan of the defects generated by proton implantation at an energy of 12 keV at a dose of $5 \cdot 10^{12}$ cm^{-2}, through 100 nm diameter holes. **b** Typical second-order correlation measurement of a single V2 center (signal going below the 0.5 threshold). Blue dots are data and the red line is a fit taking into account the analytical formula of the function $g^{(2)}(\tau)$ (see equation (3.2)). **c** Probability distribution of the number of V2 centers per implantation site. Blue dots are data and error bars correspond to the square root of the number of measurements. The red line is a fit to the data considering a Poissonian distribution (given in equation (3.4)).

previously, we observe a bunching and an anti-bunching behavior, characteristic of a three-level system. Furthermore, the signal goes below the 0.5 threshold: $g^{(2)}(\tau = 0) = 0.06 \pm 0.03$; feature of a single defect.

We subsequently investigate 110 implanted spots to measure the average number of V2 centers created. The resulting distribution is given in FIGURE 3.17**c** as well as the Poissonian fit to the data (equation (3.4)) yielding an average number of V2 centers per spot of 0.83 ± 0.02, which is similar to the helium implantation case. However, we used an implantation dose 50 times higher for the proton implantation study, resulting in a low implantation yield, around 0.2 %, thus being one order of magnitude lower compared to the previous experiment. As we will see in the next section, this low yield seems to lead to decrease spectral stability.

To study the spatial accuracy of the proton implantation technique, we used a similar analysis as used previously, see section 3.2.3. We perform a high-resolution

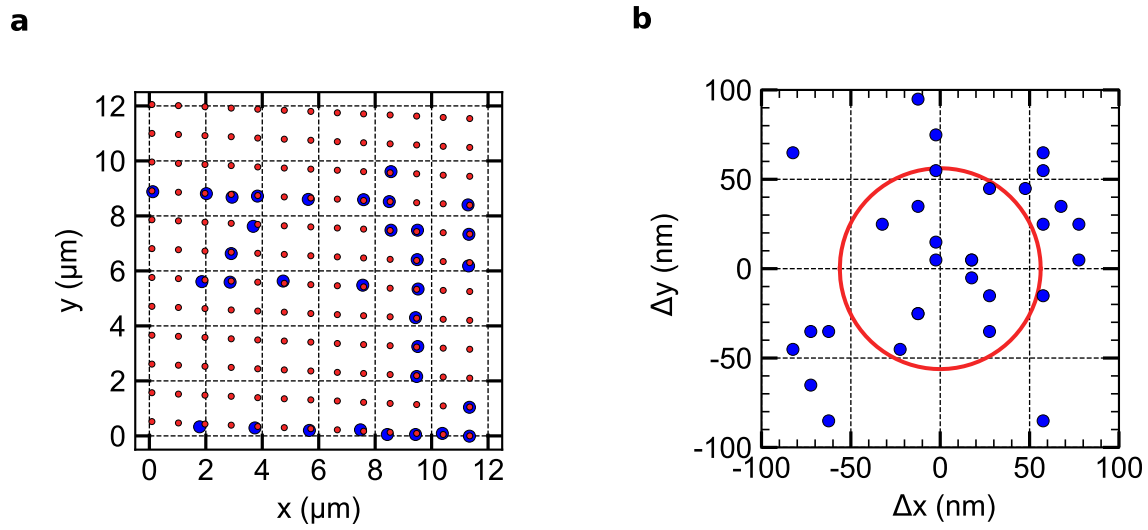

Figure 3.18: **Lateral accuracy of proton implantation.** **a** Fitted positions of the implanted defects via 2D-gaussian functions (blue) and the optimized simulated grid (red). **b** Lateral spatial distribution of the implanted single V2 centers compared to a simulated grid. The red circle represents the 56.2 nm variance of all positions.

confocal scan, using a closed-loop piezo scanner and the fitted positions of the implanted defects are compared to a simulated grid. Via minimizing the error squares, we obtain a lateral spatial variance of 56.2 nm, which is almost entirely dominated by the hole size. The deviation between the measured positions and the simulated grid is shown in FIGURE 3.18**b**, where the red circle symbolizes the variance. As previously, we also conducted a SRIM simulation, which predicts a lateral projected straggle of 33 nm.

For this experiment, we estimated the depth of the generated defects via SRIM simulation from which we extract an average depth of 110 nm for the V_{Si} center generated via proton implantation. The increased depth compare to the helium ion study comes from the higher implantation energy.

In conclusion, compare to the previous study on helium-implantation, protons generate deeper V_{Si} defects with a similar lateral accuracy but with an implantation yield 50 times smaller. In the next section, we will investigate the optical properties of the generated V2 centers.

3.3.2 Optical stability

In FIGURE 3.19**a** is given a single resonant absorption spectrum of five generated V2 defects via proton implantation. Every single-line scan shows two spectrally separated spin-conserving transitions and from the double-Lorentzian fits, we extract optical lines linewidths given in TABLE 3.2. Four fits are revealing nearly lifetime-limited linewidths. Prolonged repeated measurements for 30 minutes, as seen in FIGURE 3.19**b-f**, show no sign of ionization, yet the drift rate seems significantly faster compared to the He^+ ion-implanted defects (FIGURE 3.14).

This is observed despite the fact that proton-implanted defects are generated sub-

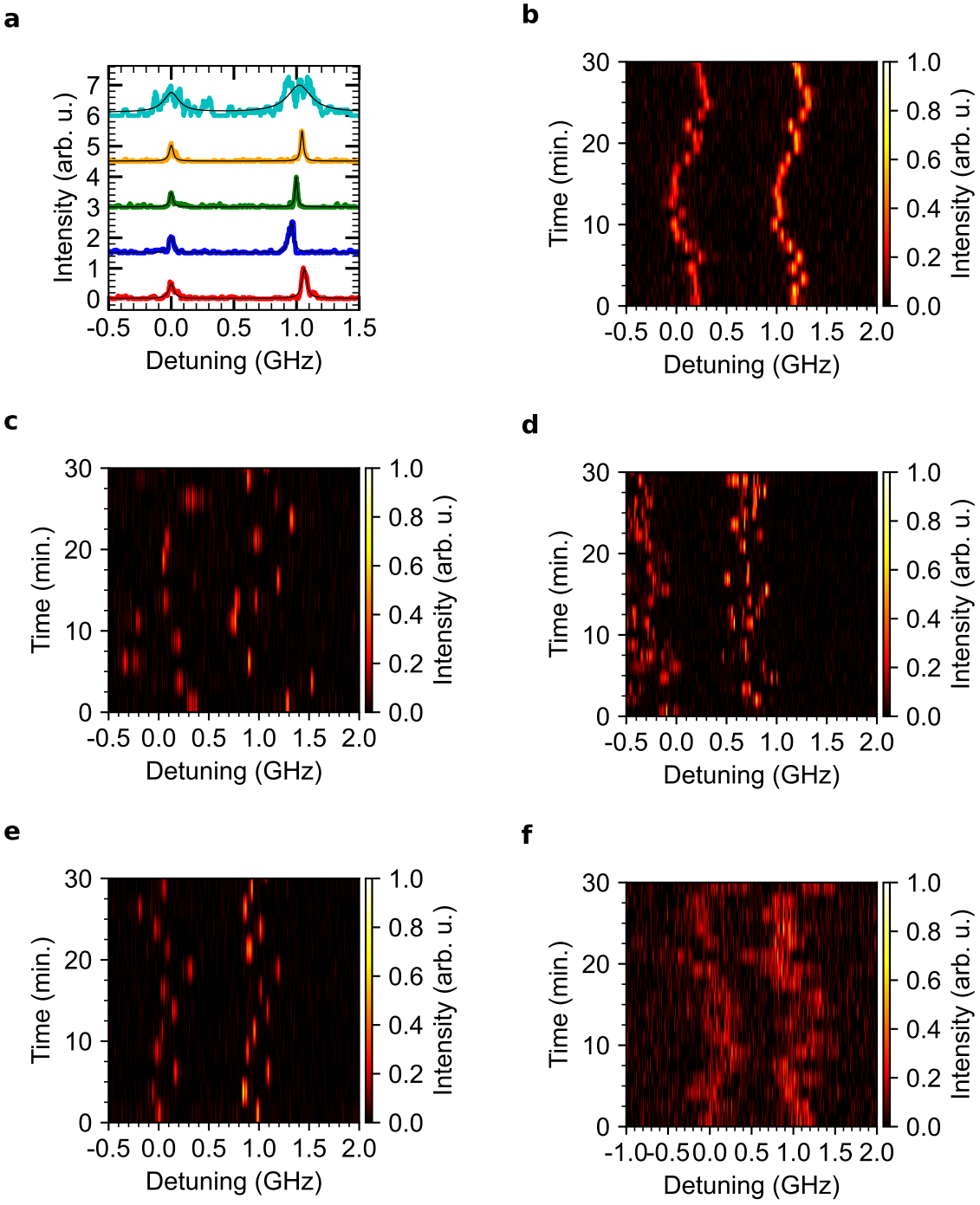

Figure 3.19: **PLE statistics of proton-implanted defects. a** Single-line resonant excitation scans for the five different V2 centers. For better visibility, each measurement is offset in the y-direction and the A_1 transition for all spectra is centered at zero detuning. The actual spectral distribution of the defects is ± 10 GHz, comparable to bulk defects [42]. Linewidths are obtained via double-Lorentzian fits to the data (black lines) and given in TABLE 3.2. **b-f** Repeated resonant excitation scans for the defects presented in **a**. No ionization is observed and the remaining drift is assigned to surface charge fluctuations.

Color in FIGURE 3.19**a**	$\Delta\nu_{A_1}$ (MHz)	$\Delta\nu_{A_2}$ (MHz)
Cyan	147 ± 8	226 ± 6
Yellow	37 ± 1	25.9 ± 0.5
Green	30 ± 1	20.9 ± 0.4
Royal Blue	39 ± 1	43 ± 1
Red	49 ± 2	43.9 ± 0.6

Table 3.2: **Linewidths statistics of proton-implanted defects.** Single line optical linewidths of every identified integrated V2 center shown in FIGURE 3.19**a**. The vertical ordering (from bottom to top) is the same as the one in FIGURE 3.19**a**.

stantially deeper beneath the surface (110 nm for p^+, compared to 40 nm for He^+). As the same SiC crystal is used for both experiments, the increased spectral drifts cannot be explained by surface charge fluctuations. Therefore, we attribute the increased drift rate for proton-implanted defects to the increased relative formation of carbon versus silicon vacancies due to the use of lighter ions.

In conclusion, proton implantation can create single defects deeper in the material compared to the helium implantation techniques, yet with a smaller yield and a reduced spectral stability. Furthermore, helium ions can be implanted with a FIB, whereas protons require a more complex accelerator facility. Thus, helium implantation is more suitable to create shallow (≤ 100 nm) stable defects.

3.4 Conclusion and outlook

To optimize the spin-photon interface of embedded color centers, single color centers with robust spin-optical properties need to be generated with a high spatial resolution. In this chapter, we have studied ion-implantation techniques to generate V2 centers in SiC with three different ion species: silicon, helium, and proton. We were unsuccessful to generate single defects with silicon-ion implantation, even leading to high crystal damages thus the observation of spin-conserving optical transitions was impossible.

We have successfully generated single V2 centers using helium ions (6 keV) and protons (12 keV) implantated through a lithographed PMMA-mask, where the high-spatial accuracy was directly limited by the holes size. Furthermore, both set of defects generated presented spin-conserving optical transitions. However, despite the defects generated via proton implantation being deeper, they presented less stable optical lines compared to the helium-implanted defects. We estimated the drift speed of the helium-implanted defect's optical lines to be around ~ 8 MHz/min. The spectral wandering was then slow enough that we could stabilize the resonant laser onto the drifting lines with a self-developed software-assisted protocol. Thus, allowing the measurement of the spin properties of the generated defects. We recorded the longest-ever measured Hahn echo spin coherence time for the system. He^+ ion-assisted implantation is therefore suitable to create single V2 centers with high spin-optical coherences.

For future investigation, it would be interesting to study the possibility to use helium FIB to generate color centers as it would remove the need to use an implantation mask and allows the implantation into precharacterized nanophotonic resonators.

Chapter 4

Integration of V_{Si} centers in nanophotonic waveguides

Despite their excellent spin-optical properties, solid-state emitters suffer from a poor spin-photon interface leading to slow experimental rates incompatible with network applications [25]. As seen in Chapter 2, the integration of color centers in high cooperativity cavity quantum electrodynamics [26, 220, 221] allows for a high excitation and collection efficiencies, as well as a deterministic spin-photon interaction. However, the low mode volume of cavities needed to reach a high Purcell enhancement requires the spin defects to be close to the surface, where they are prone to spectral diffusion due to surface charge fluctuation. The spin-optical properties can be further degraded due to the coupling to nearby spins and charge traps which can be formed during the nanofabrication of the structures [28, 29, 102, 187, 188, 206, 222]. So far, only centrosymmetric color centers in diamond have been integrated into nanophotonic structures while retaining narrow linewidths [33, 182, 223, 224]. However, inversion symmetry while being a sufficient condition for successful integration, is not necessary for the color centers to present insensitivity to electric fields noise. A low electric dipole moment might be enough, as discussed in Chapter 2 [39]. Additionally, if the host crystal has a low carrier mobility, it would limit the charge fluctuation and as such the spectral diffusion. This second hypothesis might be the reason for the high stability of V_{Si} centers in 4H-SiC at low-temperature, and it is currently under investigation by our collaborators from Erlangen. As seen in the Chapter 3, shallow ion-implanted V2 centers displayed robust spin-optical properties, making it a prime candidate for integration into nanoscale monolithic resonators.

The properties of color centers in cavity quantum electrodynamics are intertwined with the techniques used for device fabrication. Fabry-Pérot microcavities [187, 188, 220, 225], for example, allow the use of polished thin membranes compatible with good spin-optical coherences, but require complex stabilization schemes and result in relatively low optical enhancement. Photoelectrochemical etching [46, 101, 226] can be used to create rectangular cross-section waveguides, however, it deteriorates the spin-optical properties due to material degradation and porosification [102]. We therefore decided to use reactive ion etching, a scalable method for devices fabrication [227, 228, 229, 230] with has lead to minimal degradation of spin-optical coherences of group-IV defects in diamond [30, 33, 182, 211, 231].

In this chapter, we will expand on previous findings on triangular cross-section waveguide designs best suited to harness light-matter interaction via single-mode operation [59]. After, the fabrication recipe of suspended waveguides will be presented. As the photoemission in the nanophotonic structures will be well-separated from parasitic signals from defects beneath the waveguides, we will identify single defects and inquire about their spin-optical properties. We will demonstrate, via a statistical study on 6 different defects, that integrated V2 centers possess excellent optical stability, as well as long spin coherence times. Interestingly, we will also show the coupling between an electron spin and nearby nuclear spins in a nanostructured environment, paving the way towards a memory-based quantum network [22, 31]. Finally, we will propose optimal waveguide designs encompassing all the knowledge obtained in this manuscript.

4.1 Waveguides design

All the waveguide mode simulations presented in this chapter have been done in collaboration with the group of Prof. Radulaski from the University of California using Finite-Difference Time-Domain (FDTD) simulations. This method is particularly suitable for simulating the expected performance of nanophotonic devices and it models the propagation of light by discretizing Maxwell's equations in both time and space coordinates in a leap-frog manner. Owing to high accuracy and broad-frequency response, FDTD method has been widely used as a verification tool for photonic devices over the years. For example, it has been recently employed to simulate nanocavities in triangular diamond waveguides [177, 232] or to analyze color center positioning and Purcell enhancement in triangular SiC waveguides and nanobeam cavities [59]. The simulations were conducted with Lumerical software, an accurate and widely used tool in academia and industry. In the simulations, the color centers are horizontally oriented point dipoles emitting light at 917 nm, placed inside triangular waveguides with a refractive index of $n = 2.6$ and a mesh size of 20 nm. Mode coupling is monitored for the six lowest transverse electric (TE) modes supported in the waveguide and the coupling efficiencies are evaluated after 10 μm of propagation in both directions.

As stated in the introduction, angle-etch-based fabrication techniques are advantageous to create high-quality nanostructures [33, 227]. The resulting devices have an isosceles triangle cross-section, thus characterized by only two parameters: the half-opening angle α and their width d, see the inset of FIGURE 4.1**b**. The angle α is also the etch angle. To obtain highly efficient single-mode light propagation in the waveguide, an optimal set of parameters (α, d) has to be found.

FIGURE 4.1**b** shows the modeled color center emission coupled to the triangular cross-section waveguide for different geometries. For quantum information processing, single-mode fibers are used to ensure the indistinguishability of the interfaced photons [204, 233]. Therefore, to optimize the coupling of light out of the waveguides into single-mode optical fibers, it is important to ensure the single TE mode operation of the emitted light. To this end, we simulated the coupling efficiency of the dipole emission into the fundamental TE mode for the device geometries previously studied, the results are given in FIGURE 4.1**c**. For every etching angle α, the optimal width d (highlighted in red in FIGURE 4.1**b**) provides a coupling efficiency of around 80% (40% in each direction) with a mode shape that appears more rectangular than circular and localized

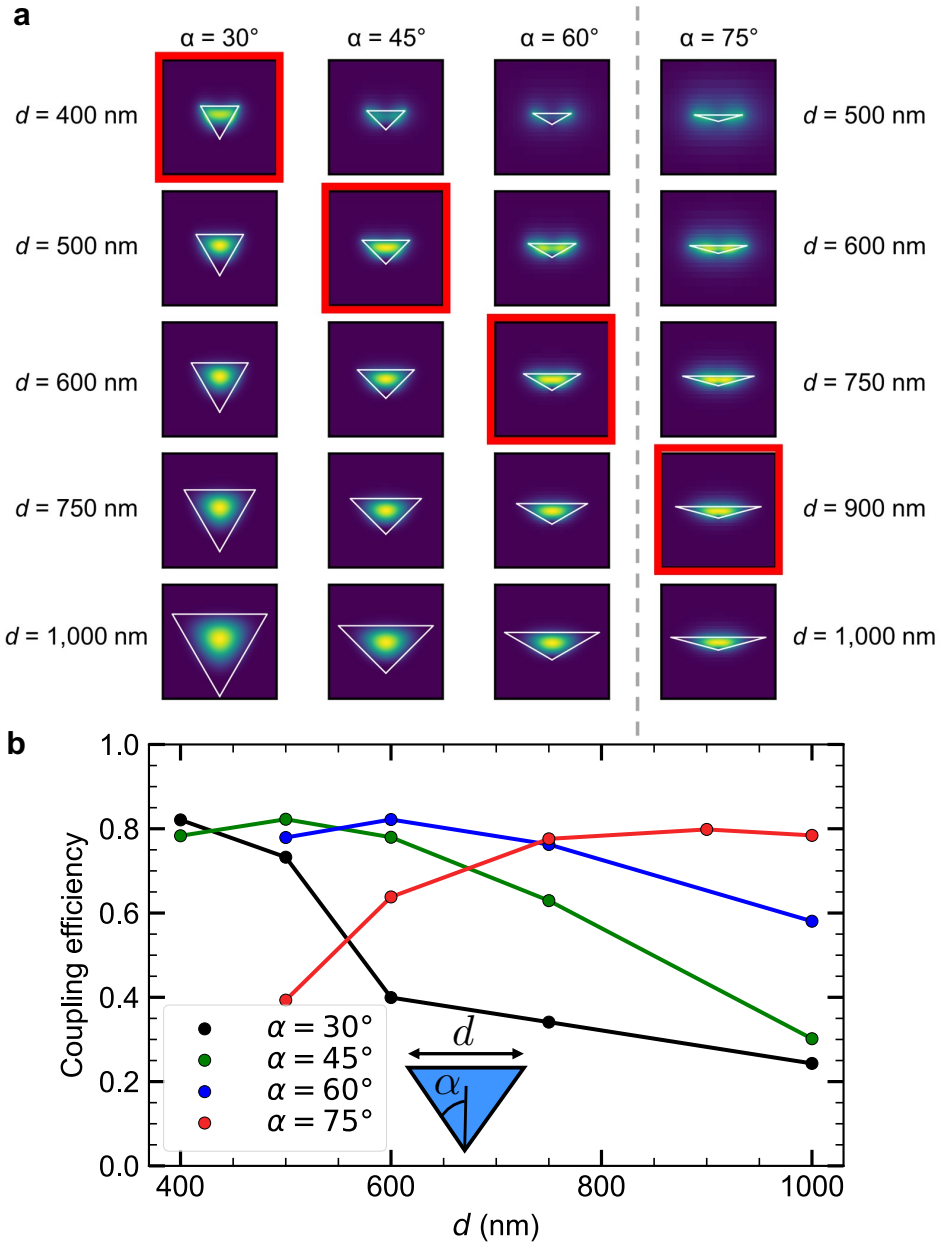

Figure 4.1: **Transverse electric mode profile.** **a** TE mode profiles of triangular waveguides with variable etch angle α and waveguide's width d. The optimal waveguide-coupling efficiency is achieved for the devices that are highlighted in red. Interestingly, the higher is the base angle of the waveguide the higher is the optimal width. **b** The coupling efficiency of light emitted by a centrally located V2 center into the fundamental TE mode for variable waveguide geometry. The simulated couplings are regrouped per color according to the etching angle α. Dots are data and lines are visual guides. Inset: Sketch of the waveguide's cross-section, with the important parameters: the etch angle α and the waveguide's width d.

within silicon carbide. Furthermore, FIGURE 4.1**c** shows that waveguides with steeper etching angle α provide optimal efficiencies over a larger range in d, making them less sensitive to fabrication errors.

Our work was pioneered in the inquiry of spin-optical properties of integrated V_{Si} in SiC and was done while high-quality SiC crystal a-cut samples were not common. In this framework, we decided to create waveguides at a fixed etching-angle $\alpha = 45°$, allowing us to create waveguides with different widths at the same time on the same sample, in our case: 400 and 1000 nm wide waveguides. The former exhibit high light-guiding efficiencies up to 82% and the latter up to 30% in the fundamental TE mode. The out-scattered light will allow us to detect the emitter's fluorescence conveniently from the top of the wider waveguide with our collection optics. In the next section, the techniques to fabricate the nanostructures will be given.

4.2 Fabrication of nanophontonics waveguides

The waveguides were fabricated in an epitaxially grown a-cut SiC layer with a nitrogen concentration of [N] $\sim 3 \cdot 10^{15}$ cm^{-3}. The V2 center dipole is then parallel to the top surface of the final waveguides. To measure the effect of the integration in nanophotonic structures onto the V_{Si} centers independently to the ion-implantation study, we create V2 centers throughout the entire epitaxial layer using electron irradiation [125] at 2 MeV with a dose of 2 kGy (fluence of approximately $5 \cdot 10^{11}$ cm^{-2}). After the irradiation, the sample is annealed at 600°C for 30 min in an argon atmosphere to remove some interstitial-related defects.

A sketch of the fabrication process is given in FIGURE 4.2. It starts with an electron-beam lithography to pattern the structures on a bi-layer of negative photoresist (here PMMA) (FIGURE 4.2**a**). Then a thin layer of nickel (100 nm) is evaporated onto the sample (FIGURE 4.2**b**), defining a mask after the lift-off of the photoresist. The structures are subsequently transferred to the epitaxy layer of SiC via a two-stage process based on reactive ion etching (RIE) with SF_6 gas; a straight-etch of 2.7 µm (FIGURE 4.2**c**) before undercutting the structures using 45° angle-etch with a Faraday cage (FIGURE 4.2**d**). Finally, the nickel mask is dissolved in nitric acid, leaving us with suspended beams of SiC. To fully comprehend the fabrication process, we will explain in more detail each fabrication step in the following subsections.

4.2.1 Photoresist and lithography

To define a mask of the structures, we used electron-beam lithography: the imprinting of a mask onto an electron-sensitive film called resist whose chemical structure is altered through irradiation and thus its solubility to a certain developer. It allows for selective removal of exposed (positive photoresist) or non-exposed (negative photoresist) areas by dissolution in an appropriate solvent. We used in our work a positive photoresist: polymethyl methacrylate (PMMA), such that only the area where the beams will be need to be electron-irradiated.The PMMA layer is spin-coated on top of the SiC: a dissolved resist is spread evenly on the sample via rotation of the sample before being heated up to remove the solvent and thus solidifying the resist. To prevent the charging

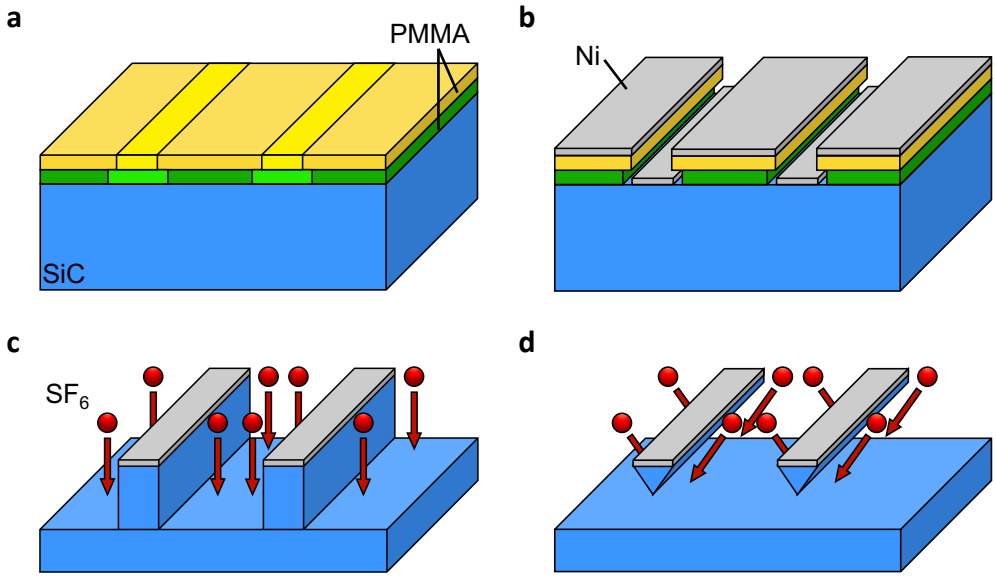

Figure 4.2: **Waveguides fabrication recipe.** **a** Lithography of a spin-coated bi-layer of PMMA mask (950k (yellow) and 200k (green)) a. **b** Developing of the mask and subsequent deposition of a nickel mask. **c** A straight reactive ion etch based on SF_6 plasma creates 2.7 µm deep trenches. **d** Angled SF_6 plasma etch creates suspended triangular cross-section waveguides.

of the surface which could lead to fabrication errors, a conductive layer of an espacer is also spin-coated.

Experimentally, the electron-beam lithography was performed using an eLine from Raith at a dose of 270 $\mu C/cm^2$. After electron-exposure, the sample is immersed, for two minutes, in a mixture of methyl isobutyl ketone (MIBK) and isopropyl alcohol (IPA) to develop the mask.

As a side note, we can briefly mention other lithography techniques. Photolithography allows for large-scale mask creation but is constrained in spatial resolution by the diffraction limit. Extreme ultraviolet lithography using light with a wavelength of few tens of nanometer yields a resolution of few nanometers, but it has been recently developed by the semiconductor industry and remains expensive and not yet widely available; however, it could be used in the future for large scale fabrication of nanostructures.

4.2.2 Metal mask

Electron-beam physical vapor deposition (EBPVD) is used to deposit a thin layer of nickel (100 nm) on top of the sample. A high energy electron-beam causes a targeted metal (here nickel) to evaporate before resolidifying at the surface of the sample, resulting in a metal coating. As seen in FIGURE 4.2**b**, the metal will be either deposited on the resist or directly on the sample, thus by dissolving the PMMA layer, via immersion in acetone, only the metal deposited on the SiC will remain: defining an etching mask.

To improve the efficiency of the PMMA-layer lift-off, two layers of PMMA (200k

and 950k) are spin coated, see FIGURE 4.2**a**. They differ by their sensitivities to the electron-irradiation. The lowest resist is more sensitive, such that a larger volume is exposed leading to a wider gap compared to the top resist. It increases the interaction surface between the resist and the solvent, facilitating the removal of the resists, without affecting the shape of the nickel mask. Additionally, it increases the quality of the metal edges as there is no adjoining resist sidewall affecting the metal deposition. As the desired thickness of the nickel mask is around 100 nm, the spin-coated PMMA-layers are 200 nm and 100 nm thick for the 200k and 950k PMMA respectively.

4.2.3 Reactive ion etching

Once the patterning mask has been defined, it is transferred into the crystal by RIE: a plasma generated via avalanche effect in a strong electric field. The created ions can be accelerated via a secondary DC field towards an isolated electrode. We use SF_6 plasma etching as it was demonstrated to efficiently etch SiC in previous works [234, 235]. To avoid strain in the sample due to the induced heat by the plasma etching, and to ensure a constant etch rate, the etching is done by step of 1 minute separated by 2 minutes of cooling time while the base temperature is kept at $-20°C$. The recipe used is as follow: 20 sccm SF_6, 7.5 mTorr, RIE power of 100 W with no ICP (inductively coupled plasma). After 40 steps of straight-etching, FIGURE 4.2**c**, the area without a nickel mask has been etched by 2.7 µm, as seen in the confocal measurement shown in FIGURE 4.3. The deep etch allows to well-separate the waveguides from the bulk beneath it, avoiding parasitic signals from bulk defects during the study of integrated color centers.

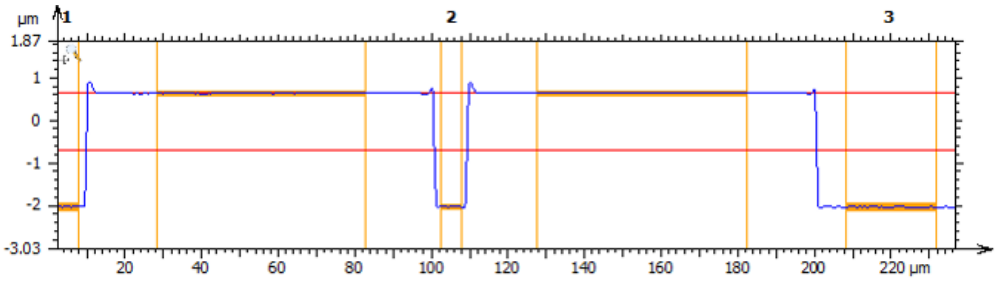

Figure 4.3: **Straight etch.** Confocal measurement of the sample cross-section after 40 steps of straight etching, we can see that 2.7 µm have been etched away.

A second step of etching is then performed to create free-standing triangular cross-section waveguides. To do so, the sample is placed under a graphite Faraday cage, the electric field points perpendicular to its surface and thus deflects the ions, as seen in FIGURE 4.2**d**. After completing both straight and angled etching processes, the nickel mask residuals are removed by immersion into diluted nitric acid (HNO3). Thereafter, the sample is annealed at 600 °C for 30 min in an argon atmosphere to remove some interstitial-related defects.

Scanning electron microscope (SEM) images of both sets of beams (400 and 1000 nm) can be seen in FIGURE 4.4, where the waveguides appear smooth and well undercut; showcasing the high-quality of the fabrication process.

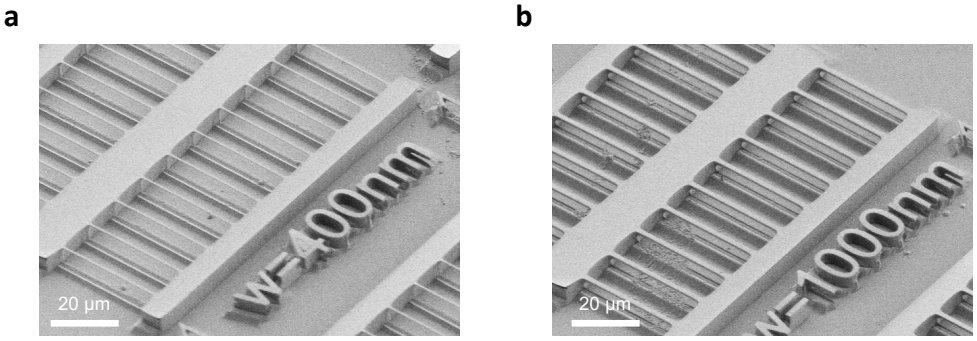

Figure 4.4: **SEM images of the waveguides.** Scanning electron microscope (SEM) images of the created waveguide structures that appear smooth and well undercut. **a** (**b**) corresponds to the waveguides with a width of 400 (1000) nm.

In the next section, the optical properties of the defects present in the created nanophotonic waveguides will be investigated.

4.3 Optical properties of integrated defects

To study the optical properties of integrated V2 centers, the nanofabricated sample is cooled down to 10 Kelvin. In this section, we will see how V2 centers are identified among the fluorescence from the laser back reflection and surface-related defects, as well as the optical properties of the integrated color centers using PLE scans.

4.3.1 Defect identification

As depicted in FIGURE 1.2, we used confocal microscopy to perform spatial scans of the sample. To ensure that optical excitation is performed on waveguide-integrated defects without spurious signal from defects in the SiC bulk substrate beneath, we perform first a confocal depth scan, shown in FIGURE 4.5. Three waveguides are visible, with the fluorescence of defects primarily occurring at the apices. The bulk SiC surface below the waveguides is also visible, including two near-surface defects. Fluorescent spots in waveguides and the bulk of the sample are spatially well-separated, thus confirming that any photoluminescence collected in the experiment is indeed emitted from integrated defects.

A typical photoluminescence map with optical excitation and collection from the top of the 1000 nm wide waveguides reveals multiple bright spots along the waveguides, as seen in FIGURE 4.6.

To decipher the origin of the fluorescence spots, we measured their emission spectra. Unfortunately, most spots are not identified as V2 centers. A typical emission spectrum of these defects can be seen in FIGURE 4.7. There are no distinct features present in the non-V2 center spectrum, despite the low-temperature operation, making it hard for us to attribute the origin of the fluorescence to a particular color center. As the identification of color centers is an ongoing field of research for the relatively new SiC platform and as many studies on unknown defects are performed at room temperature,

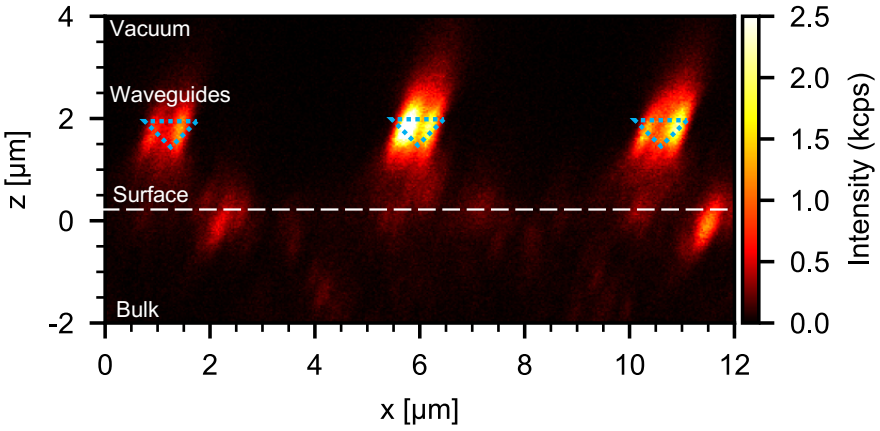

Figure 4.5: **Confocal depth scan of waveguides.** Confocal microscopy depth scan in the waveguides area of the sample. The SiC bulk surface is visible at a depth position $z \approx 0$ µm. Three waveguides can be seen. Fluorescence from the bulk and the waveguides appear spatially well-separated, thus permitting selective excitation without spurious parasitic signals.

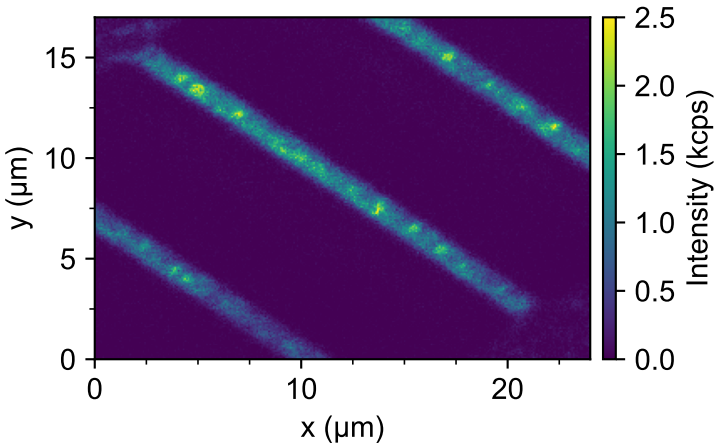

Figure 4.6: **Confocal scan of waveguides.** Confocal fluorescence microscope image of the waveguides. Bright spots are in majority surface-related defects. On average one V2 center is found in every fifth waveguides of width $d = 1000$ nm.

it is a complex task to identify the non-V2 centers at low-temperature. Nevertheless, comparing our spectra to known color centers [35], we can exclude carbon antisite vacancies (CAV), as well as annealing-related defects. The measured emission spectra show some spectral overlap with unknown defects that have been tentatively attributed to surface oxide [236]. Such an oxide layer may form during the sample nanofabrication and/or acid cleaning.

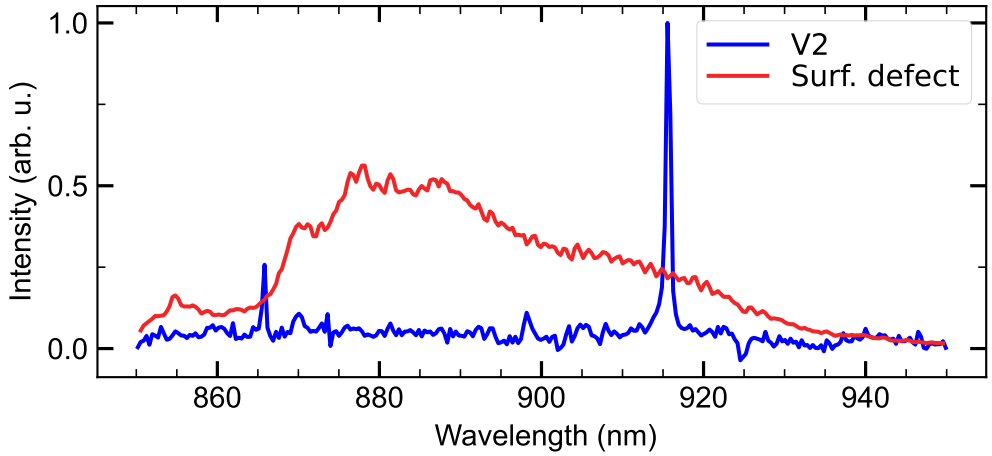

Figure 4.7: **Emission spectra.** Typical emission spectra of color centers in waveguides. The red curve represents a typical non-V2 defect, while the blue curve shows the emission spectrum of a V2 center.

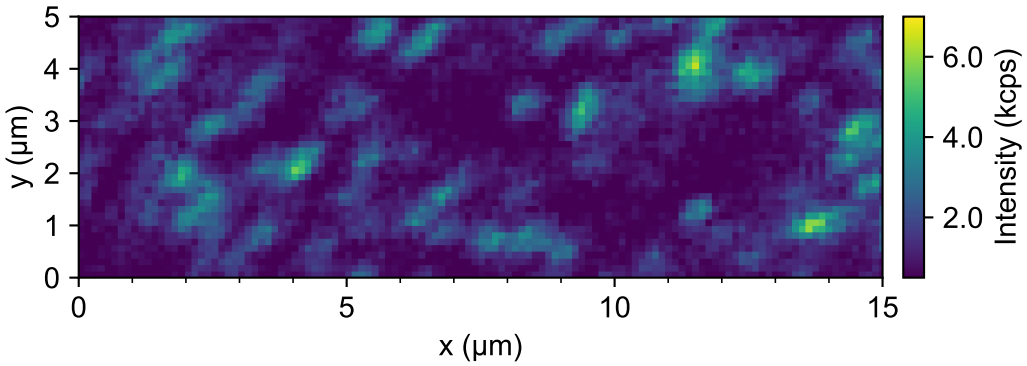

Figure 4.8: **Confocal scan of bulk defects.** Confocal microscopy scan in the bulk next to the waveguides, used to estimate the defect density, here 0.4 μm^{-3}.

Nonetheless, bright[1] single V2 centers can still be found in 1000 nm wide waveguides. They are characterized by a strong component at 917 nm (ZPL) in their emission spectra, as seen in FIGURE 4.7. On average, we found a V2 center in one out of five waveguides. As the waveguides are 20 µm long this would correspond to a defect density of 0.04 μm^{-3}, comparing quite low to the defect density in the bulk material. To estimate the latter, we perform a horizontal confocal scan in an unfabricated area of the sample, displayed in FIGURE 4.8.

The vertical area sensed by our scanning laser is related to the axial resolution. As we used a microscope objective with a numerical aperture of NA = 0.9 and that the refractive index of 4H-SiC is $n = 2.6$, the theoretical axial resolution is:

[1] compared to the waveguide's background fluorescence

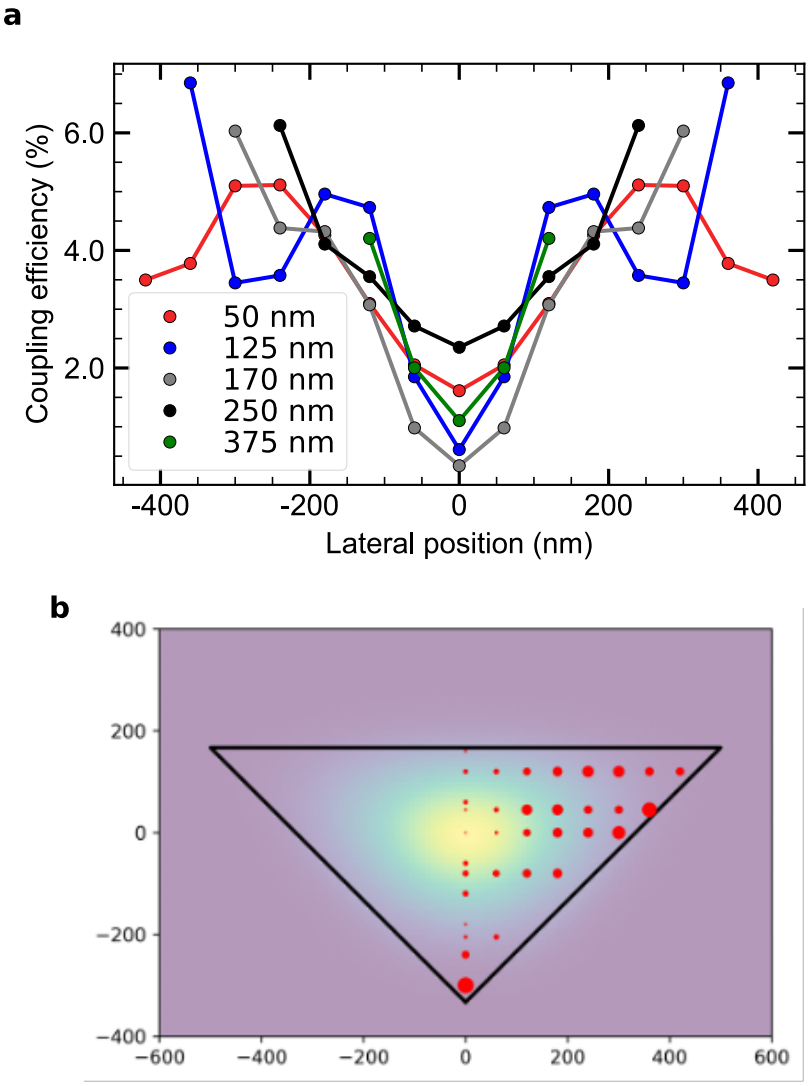

Figure 4.9: **Collection efficiency for integrated defects. a** Simulated collection efficiency for a silicon vacancy located in various positions of a triangular SiC waveguide. The simulated couplings are regrouped per color according to the defect's depth. Collection efficiency into an objective is higher at the edges of the structure than at its center. Dots are data and lines are visual guides. **b** Visualisation of the coupling efficiencies for different positions in the waveguides. The red dot size is proportional to the light collected by the microscope objective, from an emitter at that location.

$$z_{\text{axial}} = \frac{2\,\lambda}{\text{NA}^2} \approx 1.9\,\mu\text{m}. \tag{4.1}$$

As the scanning area is $5 \times 15\,\mu\text{m}^2$, the volume to consider for the estimation of the defect density is $1.9 \times 75 = 142.5\,\mu\text{m}^3$. We count 57 defects in the confocal scan shown in FIGURE 4.8, resulting in a defect density of $\rho_{V_{Si}} \approx 0.4\,\mu\text{m}^{-3}$. The defect density in bulk is then one order of magnitude higher compared to the defect density waveguides.

To comprehend this discrepancy, we simulated the collection efficiency of a dipole placed in various positions in a triangular cross-section waveguide ($\alpha = 45°, d = 1000$ nm) using a microscope objective. As seen in FIGURE 4.9, only color centers close to the waveguides' apices show sizable emission towards our collection optics. This simulation can be corroborated from the depth scan, FIGURE 4.5, where the collected signal seems indeed to come from the apices of the observed waveguides. In reality, the fluorescence of most emitters is guided along the waveguides or out-scattered towards the bottom, thus making it impossible to observe them via our microscope objective placed on top of the sample. Therefore, the actual density is most probably not modified significantly, we can only observe a fraction of the defects. Interestingly, those defects are the ones closest to the surface, the most prompt to spectral diffusion, i.e the worst-case scenario compared to an ideal centrally localized defect.

Moreover, we did not identify any V2 centers in the 400 nm wide devices. We attribute this to the single-mode operation of the 400 nm waveguides, which suppresses out-scattering towards our collection optics. Our experimental and theoretical finding strongly suggests the need for dedicated output couplers such as grating couping [176] or tapered fiber [177], for future experiments.

In summary, we have identified six V2 centers in 1000 nm wide waveguides thanks to their emission spectra. Those defects are estimated to be in the waveguides' apices and their optical properties will be studied using photoluminescence excitation scans.

4.3.2 Absorption lines

Similar to the experiments conducted on the implanted V2 centers, in Chapter 3, we perform resonant PLE scans to study the optical properties of the integrated defects. The experiment is run at 10 Kelvin with the frequency-scanning resonant laser at a fixed power of 1 nW and the ground state transitions ν_1 and ν_3 are continuously driven by a resonant microwave field. A sketch of the protocol can be seen in FIGURE 4.10**a**.

In FIGURE 4.10**b**, a one-hour long PLE recording is plotted, revealing for every single scan two exceptionally narrow absorption lines (A_1 and A_2) with no signs of ionization. The fit of the 198 displayed scans via a two-Lorentzian function yields an average linewidth of 34 ± 8 MHz and 22 ± 5 MHz for the A_1 and A_2 transitions respectively; where the uncertainty is defined as the standard deviation. The transitions are therefore nearly transform-limited ($\sim$ 20 MHz). Furthermore, as for the shallow implanted defects, a slow drift can be observed. Considering that we primarily investigate defects at the waveguides apices, we assign this slow drift to surface charge fluctuations. To demonstrate that the drift is slow enough to perform complex long-term measurements, we stabilize the resonant excitation laser on the optical transitions via software-control [13], the protocol is given in Appendix C.

FIGURE 4.10**c** shows absorption line scans repeated over one hour with the laser feedback activated once per minute and recentring the scanning window after every scan with respect to the position of the A_1 transition. Little to no effective drift is observed: the feedback system manages to refocus the laser on the transitions every time it is out of resonance. In other words, we can perform long-term measurements on the electron spin while keeping the laser in resonance with the drifting optical transitions using our developed laser stabilization protocol. For future works, to interface several

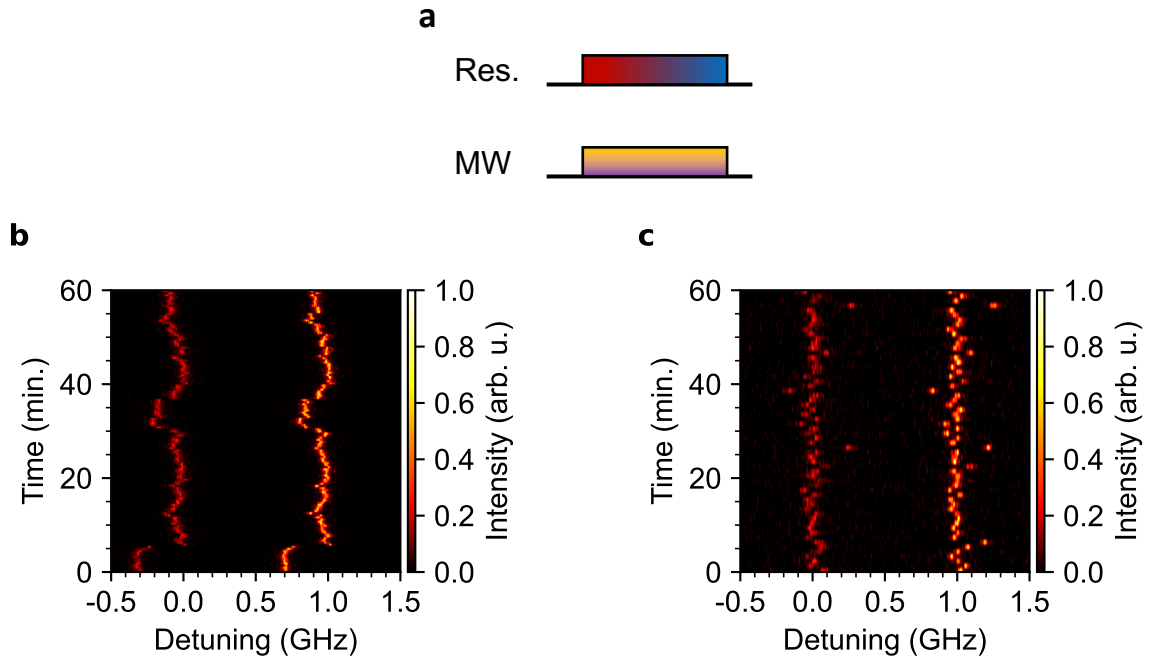

Figure 4.10: **One-hour long PLE measurements of an integrated defect.** **a** Sketch of the PLE protocol: the frequency of the resonant laser is scanned across both optical transitions (A_1 and A_2) while the microwave field drives the ground state transitions $|\pm 3/2\rangle \leftrightarrow |\pm 1/2\rangle$ (ν_1 and ν_3). **b** Repeated resonant excitation scans during one hour. No ionization is observed and the wavelength drift is minimal. A single scan is shown in red in FIGURE 4.11**a**. **c** Repeated resonant excitation scans with the laser feedback software activated once per minute. The scanning window is recentered after every scan with respect to the position of the fitted A_1 transition. No drift is observed.

color centers, we could reverse the protocol, using electrodes to stabilized the optical transitions directly via Stark shift tuning onto a reference laser [60].

It is important to demonstrate the reproducibility of our results on different defects across multiple waveguides. To this end, we conducted PLE measurements on every integrated defects whose have been identified. In FIGURE 4.11**a**, the resonant absorption spectra of V2 centers in six different waveguides are displayed. We find that every defect presents spin-selective optical transitions and that half of them V2 centers show nearly lifetime-limited absorption lines. We extract the optical linewidth of each data set displayed in FIGURE 4.11**a** upon a double Lorentzian fit, which are given in TABLE 4.1. The repeated resonant excitation scans of the defects corresponding to the five upper data sets are shown in FIGURE 4.11**b-f**. All defects exhibit a very slow spectral drift and no ionization is observed, reproducing the results obtained previously.

To characterize the power dependence of the drift rate, we perform repeated PLE scans for the defects presented in FIGURE 4.11**b** at increased resonant power (5 and 10 nW) for 30 minutes. The results are given in FIGURE 4.12**a-b**.

It appears that at a higher resonant power the optical lines are less stable and

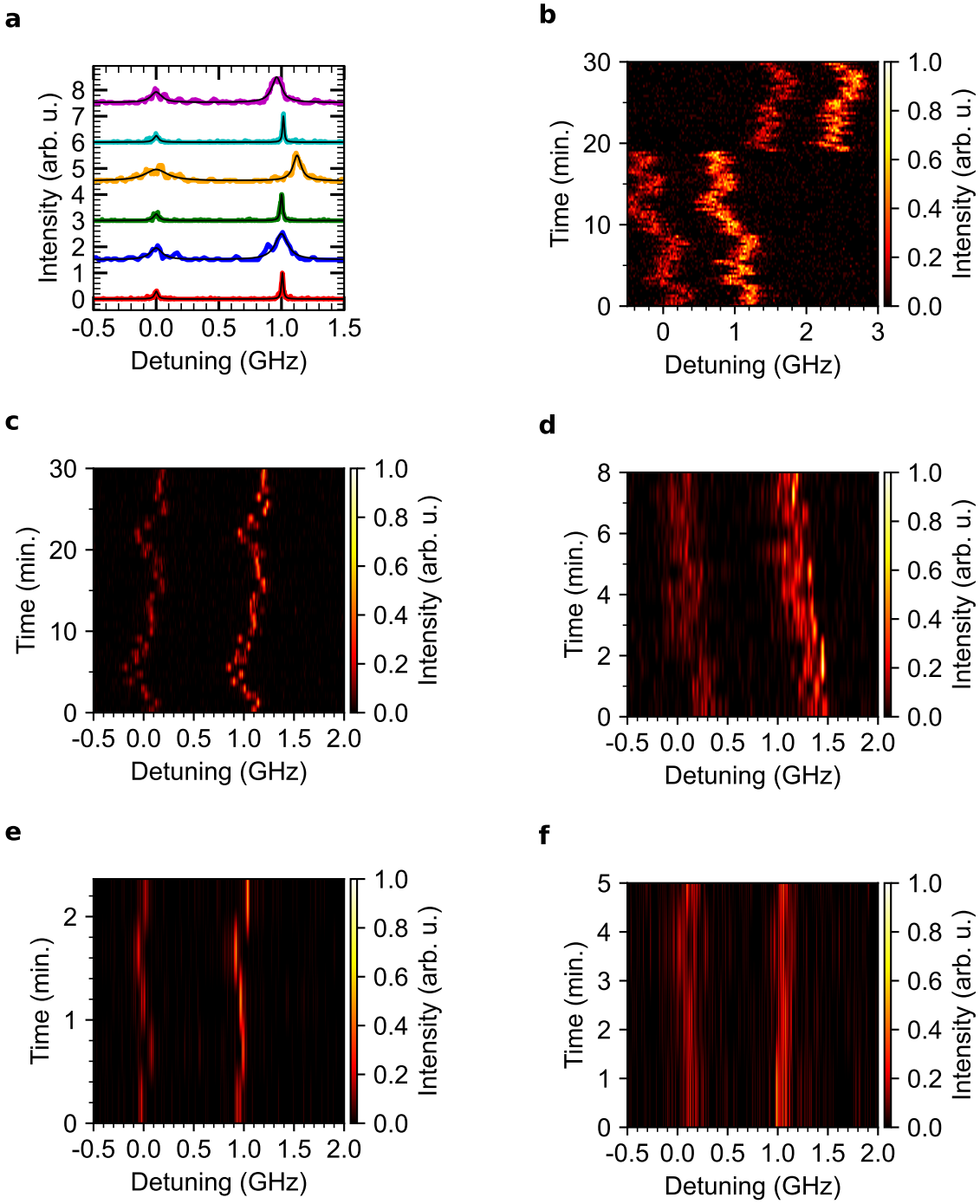

Figure 4.11: **PLE statistics of integrated defects.** **a** Single-line resonant excitation scans for six different V2 centers in waveguides. For better visibility, each measurement is offset in the y-direction and the A_1 transition for all spectra is centered at zero detuning. The actual spectral distribution of the defects is ± 10 GHz, comparable to bulk defects [42]. Linewidths are obtained via double-Lorentzian fits to the data (black lines) and given in TABLE 4.1. **b-f** Repeated resonant excitation scans for the defects presented in **a**. No ionization is observed and the remaining drift is assigned to surface charge fluctuations.

Color in FIGURE 4.11**a**	$\Delta\nu_{A_1}$ (MHz)	$\Delta\nu_{A_2}$ (MHz)
Magenta	100 ± 6	92 ± 1
Cyan	44 ± 2	15 ± 1
Yellow	216 ± 8	78 ± 2
Green	49 ± 2	21 ± 1
Royal Blue	115 ± 20	123 ± 7
Red	32 ± 1	17 ± 1

Table 4.1: **Linewidths statistics of integrated defects.** Single-line optical linewidths of every identified integrated V2 center shown in FIGURE 4.11**a**. The vertical ordering (from bottom to top) is the same as the one in FIGURE 4.11**a**.

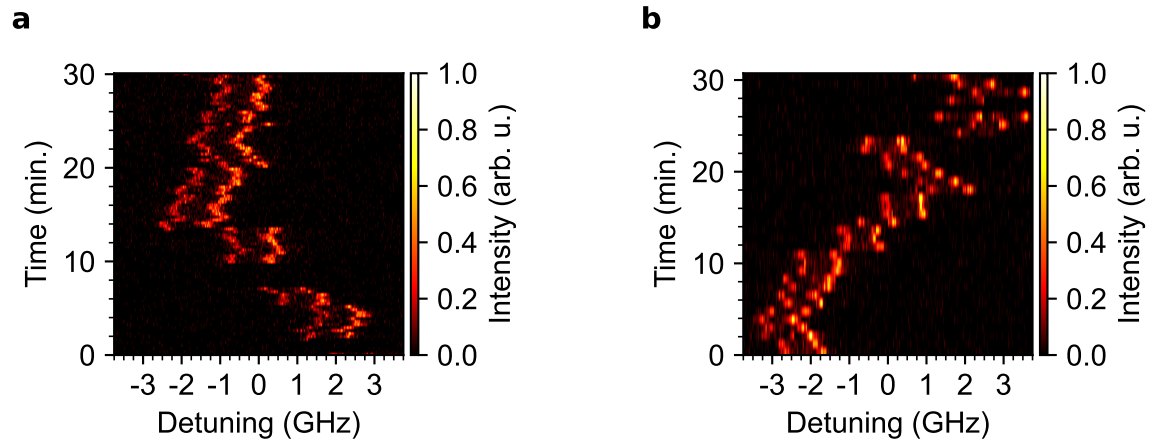

Figure 4.12: **Power dependence of the drift. a** (**b**) Repeated resonant excitation scans for an integrated color center under continuous laser excitation of 5 (10) nW. High drift rate and ionization can be observed.

stochastic jumps are more frequent. For PLE scans performed at 10 nW the frequency range is around 6 GHz, whereas the total range is only 2 GHz when the defect is continuously excited at 1 nW. The use of lower excitation power can then mitigate the spectral drift. However, it also reduces the fluorescence rate of the color center. Thus, a compromise has to be found. In our experiments, we decided to keep the resonant laser power at 1 nW, around a fifth of the saturation power, allowing reasonable count rates and a drift speed at which the optical lines can be easily followed with our stabilization protocol.

In summary, the six integrated defects identified without cherry picking, present minimal degradation of their optical properties, half of them showing nearly lifetime limited absorption lines. The slow remaining wandering of the lines can be explained by charge fluctuations at the surface of the waveguides, as the defects are located

at the apices. Utilizing the demonstrated Stark shift tuning capabilities of the V_{Si} centers [60, 61], stabilization of the transitions onto a reference laser would be possible. Enabling long-distance entanglement between integrated electron spins, guaranteed by the indistinguishability of the emitted photons.

The robust optical properties of single integrated V2 centers showcase the potential of V_{Si} as a stationary qubit for quantum information processing. However, integrated systems have to demonstrate state-of-the-art spin properties with long coherence times to store quantum information during the time of an experimental protocol.

4.4 Spin properties

As we have shown in the Chapter 3, shallow defects retain their high spin coherence times.

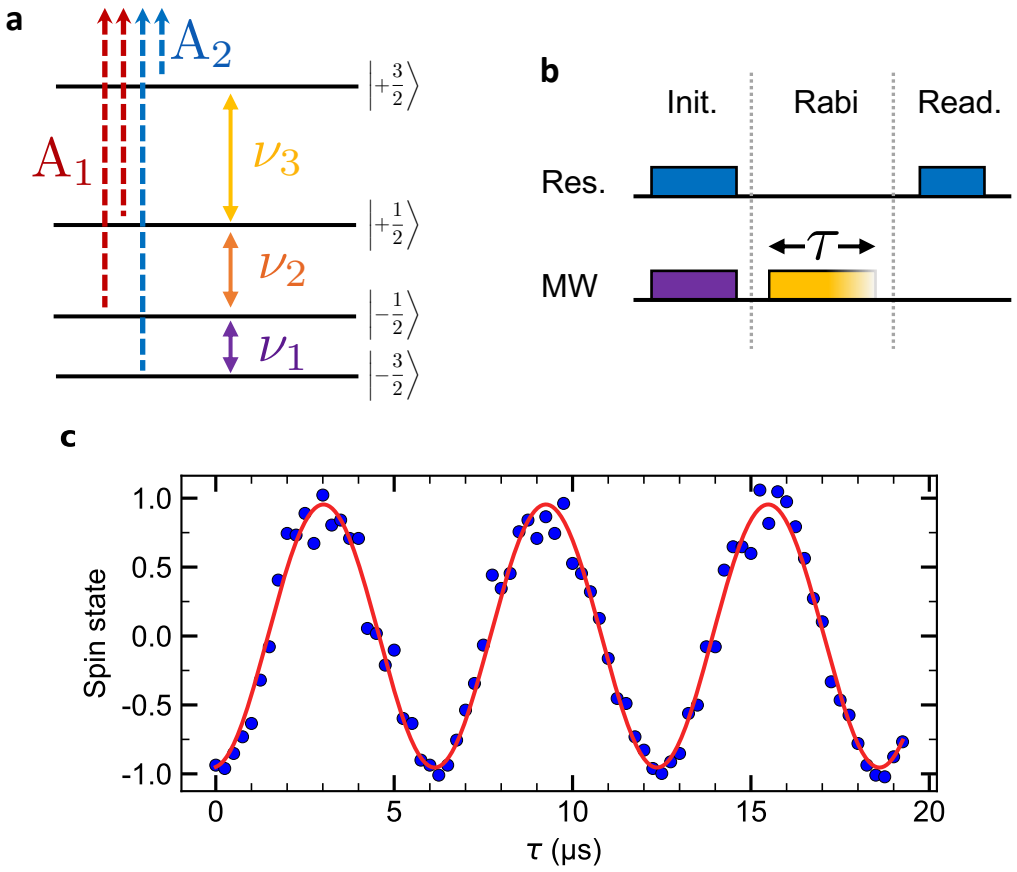

Figure 4.13: **Rabi oscillation.** **a** Energy level diagram of the ground states of a V2 center in an external magnetic field ($B = 36$ G) lifting the Kramers degeneracy. The dashed lines represent the spin-conserving optical transitions and the solid ones the allowed microwave transitions. **b** Sketch of the Rabi cycle protocol, see text. **c** Rabi oscillation for an integrated V2 center. The contrast of 91 % underlines the high control of the integrated electron spin state. The spin state $+1$ corresponds to $m_s = 3/2$ and -1 to $m_s = 1/2$.

However, previous experiments conducted on other platforms have shown that waveguides nanofabrication can still lead to an increased abundance of parasitic spin defects [102, 182], thus, degrading the spin coherence times. To investigate the spin properties of the integrated V2 center, we apply a permanent magnetic field ($B = 36$ G) aligned along the c-axis of the crystal utilizing our self-developed protocol (see Appendix D).The lift of the Kramers degeneracy allows for selective driving of the three ground state spin transitions [40]. A sketch of the resulting ground state's energy levels is given in FIGURE 4.13**a**.

To showcase our ability to control the integrated electron spins state, we performed a Rabi cycle (see section 1.4.1) between the states $|+1/2\rangle$ and $|+3/2\rangle$ while periodically stabilizing the resonant laser onto the optical transition A_2. The experimental protocol is given in FIGURE 4.13**b**, first the spin is deterministically initialized in the state $|+1/2\rangle$, through the resonant excitation along the spin selective A_2 transition and the drive of the transition ν_1 [40]. Then, the transition $|+1/2\rangle \leftrightarrow |+3/2\rangle$ is driven for a varying time τ using a microwave field at 0 dBm at the frequency ν_3. Finally, the spin state is readout via resonant excitation along the A_2 transition. The resulting uncorrected spin signal is given in FIGURE 4.13**c**, revealing fringes with a contrast of 91 %. As the contrast is bounded by the initialization and readout fidelity, our result highlights the high control we have achieved over the integrated electron spin.

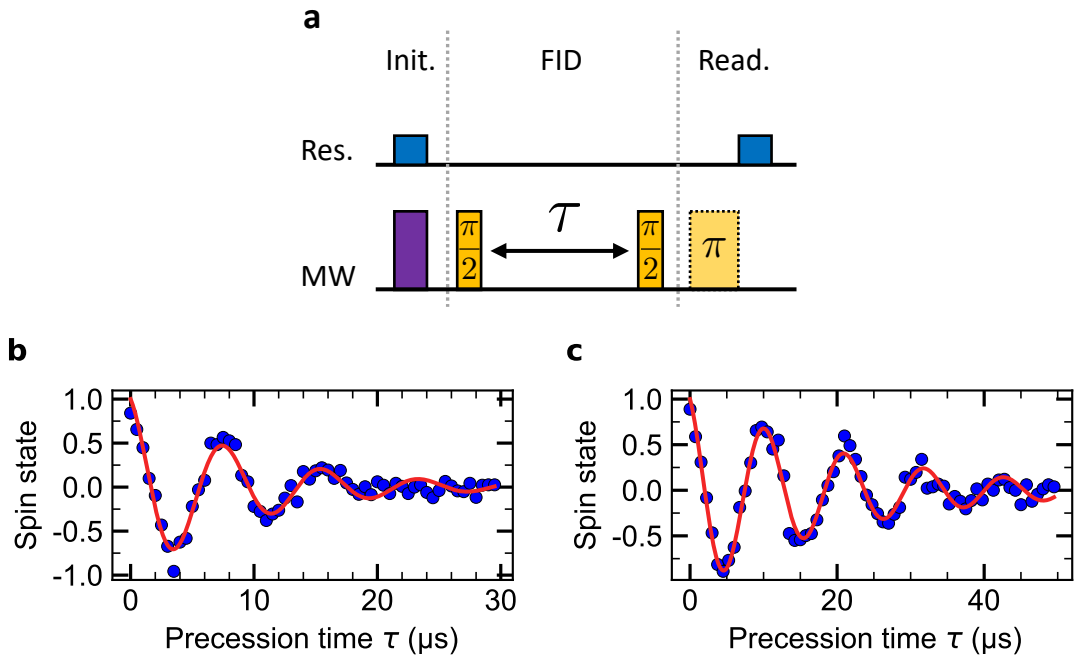

Figure 4.14: **Ramsey interferometry.** **a** Sketch of the free induction decay protocol. The electron spin is first initialized in the superposition state $|+\rangle$ and then freely evolves for a time τ before to be read out along the $\pm\mathbf{x}$ direction by either applying an additional π pulse (here dashed) or not. **b** (**c**) Spin dephasing time of an integrated (bulk) V2 center, from the fit to the data we yield $T^*_{2,\mathrm{wg}} = 9.4 \pm 0.7$ μs ($T^*_{2,\mathrm{bulk}} = 21 \pm 1$ μs). The spin state $+1$ corresponds to $m_s = 3/2$ and -1 to $m_s = 1/2$.

By fitting the signal, we obtain he times for a $\pi/2$, a π and a $3\pi/2$ pulse: 3.03 µs, 6.1 µs and 9.26 µs, respectively. This knowledge allows the deterministic manipulation of the electron spin state and the inquiry of the spin properties: the dephasing time T_2^* and the Hahn echo coherence time T_2.

First, we perform Ramsey interferometry experiments, protocol shown in FIGURE 4.14**a**, on a V2 center in a waveguide. From the fit to the data, FIGURE 4.14**b**, we obtain a dephasing time of $T^*_{2,\mathrm{wg}} = 9.4 \pm 0.7$ µs, which is only two times shorter compared to deep bulk defects in the same sample under the same experimental conditions of $T^*_{2,\mathrm{bulk}} = 21 \pm 1$ µs, FIGURE 4.14**c**. We can thus expect long coherence time for the defect in the nanostructure.

A Hahn echo measurement, protocol shown in FIGURE 4.14**a**, with the integrated defect is presented in FIGURE 4.15**b**. Interestingly, the data display a strong modulation due to dipolar interaction with weakly coupled nuclear spins. In Chapter 5, this particular system will be further investigated and we will demonstrate that the

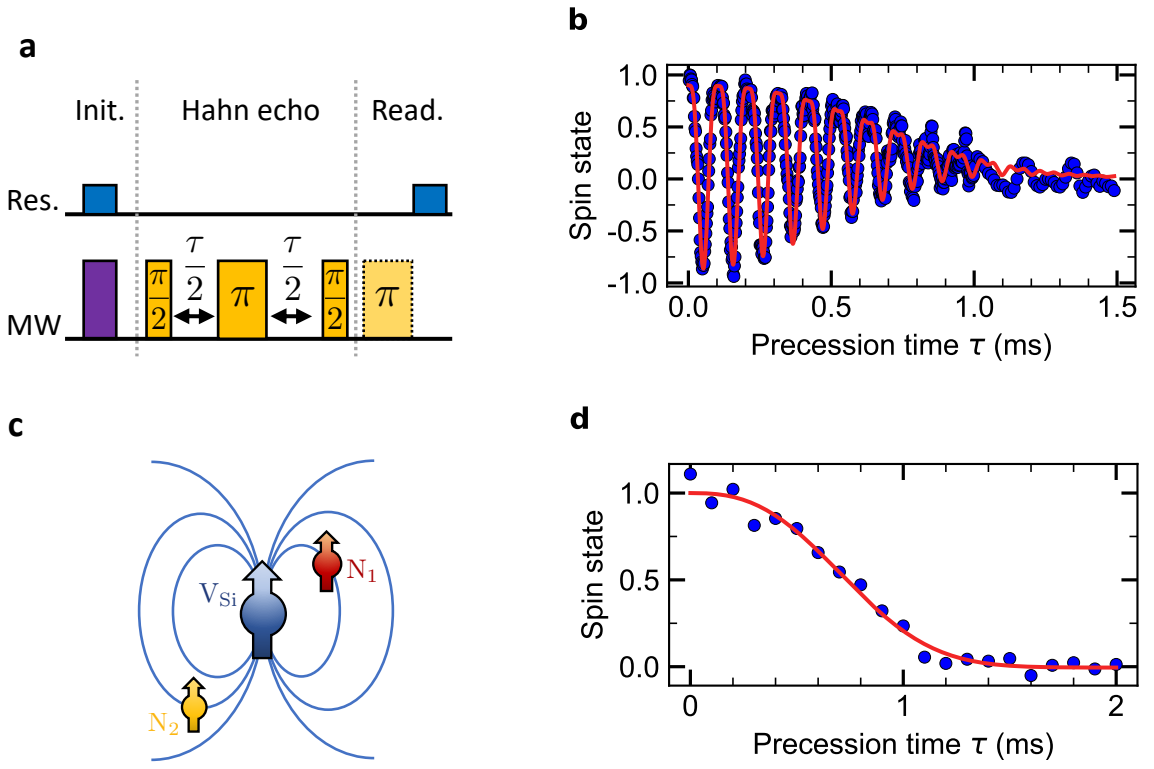

Figure 4.15: **Hahn echo spin signal.** **a** Sketch of the Hahn echo protocol. The system undergoes the same protocol as for a free induction decay, see FIGURE 4.14**b**, but an additional π-pulse is performed in between of the free evolution. **b** (**d**) Spin coherence time of an integrated (bulk) V2 center, from the fit to the data we yield $T_{2,\mathrm{wg}} = 0.84 \pm 0.01$ ms ($T_{2,\mathrm{bulk}} = 0.85 \pm 0.03$ ms). The strong modulation in **d** corroborates coupling to, at least, one nearby nuclear spin. The spin state $+1$ corresponds to $m_s = 3/2$ and -1 to $m_s = 1/2$. **c** Sketch of the coupled electron-nuclear spin triplet identified in a waveguide, further details will be given in Chapter 5.

system is described by one V2 center coupled to two nuclear spins, as depicted in FIGURE 4.15**c**. We will also derivate the analytical formula used to fit the modulated spin signal (equation (5.29)); from which we extract the Hahn echo coherence time $T_{2,\mathrm{wg}} = 0.84 \pm 0.01$ ms. It is comparable to the deep bulk defects in the same sample under the same experimental conditions of $T_{2,\mathrm{bulk}} = 0.85 \pm 0.03$ ms, see FIGURE 4.15**c**. This demonstrates that our nanofabrication recipe induces minimal damage to the crystal lattice and can be used for the creation of high-quality structure without deteriorating the spin properties. The attentive reader will notice the reduced coherence time compared to the helium implanted defects (FIGURE 3.16). This discrepancy most probably originates from the difference in the growth process used for the samples.

In summary, we have demonstrated so far in this manuscript that: ion-implantation to generate V2 centers, as well as the integration of color center in nanofabricated devices, induce minimal degradation of the optical properties and no deterioration of the spin properties. This allows for the deterministic creation of single V2 centers in photonic crystal cavities. However, those structures need to be optimized for defects 30 to 40 nm deep, as this is the depth at which the defects are generated. In the next section, we will describe how the high-quality nanofabrication techniques and high-spatial resolution of defect generation can be combined by studying waveguide designs optimized for shallow implanted defects.

4.5 Implantation & nanophotonic stuctures

In Chapter 3, we have shown that He^+ implantation can be used to generate high-quality V2 centers. However, the technique results in a preferred V2 center creation depth of 30 to 40 nm. To integrate those particular defects, we can simulate the optimal geometry for such shallow defects.

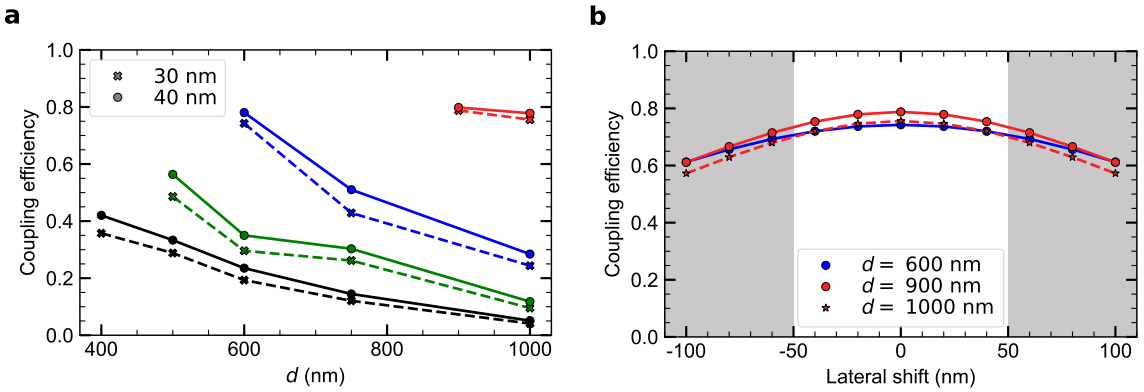

Figure 4.16: **Coupling efficiency for a shallow defect.** The coupling efficiency of light emitted by a V2 center on the vertical symmetry axis for variable emitter depth and waveguide geometry. **b** The coupling efficiency of light emitted by a 30 nm deep V2 center laterally shifted from the central position for variable waveguide geometry. The color legend in FIGURE 4.1**b** applies to both plots. Black corresponds to $\alpha = 30°$, green to $\alpha = 45°$, blue to $\alpha = 60°$, red to $\alpha = 75°$

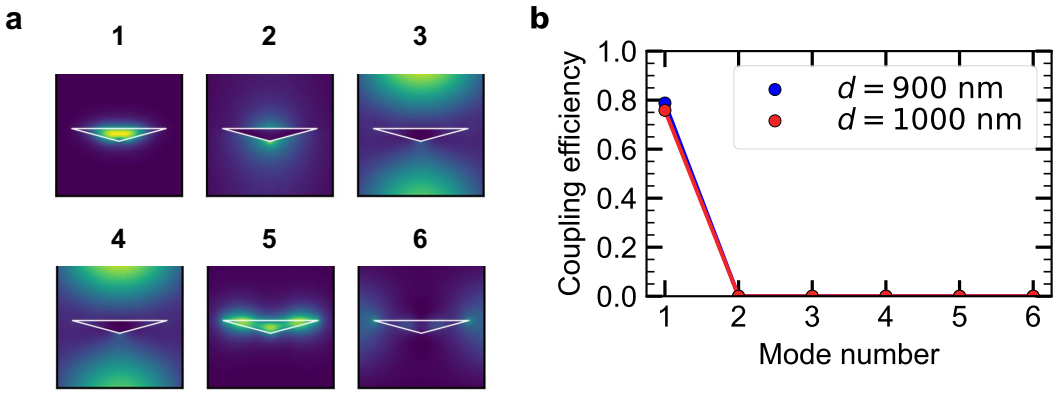

Figure 4.17: **Single-mode operation of optimized triangular waveguides.** **a** Profiles of the six lowest energy modes supported in a triangular waveguide with an etch angle of $\alpha = 75°$ and width of $d = 1000$ nm. Mode #1 is the fundamental TE polarized mode. **b** The coupling efficiency of light emitted by a 30 nm deep horizontally polarized dipole into each of the modes shown in **a**. The coupling efficiency is evaluated after 10 µm of propagation and show single-mode operation.

As presented in FIGURE 4.16**a**, the coupling efficiency does not change significantly in the investigated depth range (30 - 40 nm) for the various device geometries simulated, even if the defects at 40 nm depth coupled systematically better to the waveguides. However, devices with higher etch angles result in consistently better coupling efficiencies (up to 80 %). Remarkably, the $\alpha = 75°$ devices show very robust coupling efficiencies, especially in regards to the waveguide widths d = 900 - 1000 nm. We have also previously shown (see section 3.2.3) that the lateral defect creation accuracy using helium ion-implantation was of 54 nm, mainly limited by the implantation mask's hole size (50 nm radius). As shown in FIGURE 4.16**b**, lateral displacement of the emitters does not play a significant role for the waveguides with an angle of $\alpha = 60 - 75°$. I.e., fundamental TE mode coupling efficiencies of shallow defects remain within 10 % of their peak value even displaced by 50 nm from the central position. The lost photons are coupled to the fundamental transverse magnetic (TM) mode and can, in practice, be filtered out by polarization. Thus, our simulations indicate a reduced demand on alignment of the ion-implanter in single-mode devices with a wide opening angle of $\alpha = 75°$.

In FIGURE 4.17**a**, the simulated profile of the first 6 lowest energy modes in the device with an etch angle of $\alpha = 75°$ and width of $d = 900$ nm are shown. This geometry provides around 80 % coupling efficiency into the first TE mode without noticeable excitation of higher-order modes for defects 30 nm deep, as seen in FIGURE 4.17**b**.

Our model shows that the demonstrated Faraday cage etching techniques and He^+ ion-implantation provide together a rich toolset for integrated SiC color center photonics for quantum information processing. The single TE mode operation of triangular waveguides is highly efficient and robust in multiple degrees of freedom: vertical and lateral emitter displacement, fabrication dimension, and surface roughness imperfections. Moreover, these waveguides can be coupled to triangular photonic crystal cavities

which are known to provide strong Purcell enhancement, boosting the generation of indistinguishable single photons in color centers [33, 59, 232]. They are also compatible with efficient in/out coupling techniques, e.g. tapered fibers [177].

4.6 Conclusion and outlook

Integration of color centers in cavity quantum electrodynamics is a critical approach to increase the spin-photon interface for solid-states spin defects [36]. In this chapter, we have demonstrated the optical stability and state-of-the-art spin coherence times of integrated V2 centers in nanophotonic structures, a milestone experiment towards the integration in more complex structures, namely photonic crystal cavities [46]. All investigated defects possess slowly drifting spin-selective transitions, furthermore half of them displayed near-transform-limited optical lines. The slow drift is assigned to surface-related charge fluctuations, as the defects are found to be close to the waveguides' apices. Our ability to stabilize a laser in resonance with the defects showcases the potential of interfacing several integrated V2 centers [60]. Due to the absence of degradation of the Hahn-echo coherence time, we demonstrated the coupling of an integrated V2 center to nearby nuclear spins. This spin-spin interaction, as well as the utility of nuclear spin as long-lived quantum memory, will be further investigated in the next chapter.

As our RIE-based waveguide fabrication technique is suitable for adapting different waveguide geometries, we simulated the optimal triangular cross-section waveguide design for centrally localized and shallow defects. In future work, the combination of nanofabrication and localized defect generation will be of utmost importance. For that multiple strategies exist, such as waveguide fabrication around precharacterized implanted defect arrays, or depositing He^+ ion-implantation masks on produced waveguides. For the 45° etched waveguides, both strategies require precise alignment in the range of a few 10 nm. However, as simulated here, there are reduced demands on alignment in single-mode devices with a wider opening angle (75° and 900 - 1000 nm width). Such devices could be created with adapted Faraday cages. Based on the success in the diamond platform [26, 176], we believe that mask-free implantation would be ideal to generate single colors centers coupled to the fundamental mode of a triangular cross-section waveguide with an opening angle of $\alpha = 75°$ and a width of $d = 900$ nm [33]. This implantation can be achieved using a helium FIB source or a helium ion microscope operated at fluxes of about 10 He^+ ions per spot, Additionally, to stabilize the optical transitions, further study on surface passivation via graphene deposition would be necessary [76, 77]. This would allow operating the defects at full saturation power, maximizing the count rate without compromising the defects' stability. Finally, utilizing demonstrated efficient in/out coupling techniques such as tapered fibers [177] or grating couplers [176], high collection and excitation efficiencies could be reached.

Chapter 5

Nuclear spin control

In the previous chapters, we have described how the properties of V_{Si} in silicon carbide make it an interesting spin platform. Breakthrough results have been obtained, showcasing the optical stability of V2 centers after generation via ion implantation as well as integrated into nanophpotonic structures. Nonetheless, the scaling of any infrastructures for quantum information processing has to be considered and requires local quantum nodes made of a multi-qubit cluster allowing quantum error correction [23, 237, 238] or memory-based quantum communication [21, 22, 31, 62]. Color centers in the solid can utilize nuclear spins naturally trapped in the crystal lattice to create multi-qubit registers [27, 64]. Given their weak interactions with the environment due to their low gyromagnetic factors, nuclear spins are well suited to be used as memory qubits with long storage time [24]. Yet, on the flipside, the weak coupling to the magnetic field means that direct spin manipulation requires high power radio-frequency (rf) driving, which typically induces additional heat to the system. The cooling power of standard cryogenic systems will therefore be a limiting factor for fast spin control [30, 33]. Additionally, the nuclear spin state cannot be usually read out optically. To counteract those restrictions, a conventional method to interact with nuclear spins is to use the electron spin as an interface using so-called decoupling sequences [66, 67, 239, 240]. The nucleus is indirectly controlled via the hyperfine interaction and entangling the electron and nuclear spins together, allows to read out the latter.

Isotope	Natural Abundance (%)	Quantum Number I	Gyromagnetic Ratio $\tilde{\gamma}_n$ (MHz.T^{-1})
^{13}C	1.1	1/2	10.708
^{29}Si	4.7	1/2	- 8.465

Table 5.1: **Isotopes with nuclear spin in SiC.** Most common nuclei with non-zero nuclear spin present in SiC, with their respective natural abundances, nuclear spins I and reduced gyromagnetic ratios $\tilde{\gamma}_n$ (gyromagnetic ratios divided by 2π).

Silicon carbide, thanks to its diatomic nature, hosts two stable isotopes with a non-zero nuclear spin: ^{13}C and ^{29}Si. Table 5.1 gives the natural abundances of both species

as well as their quantum numbers and gyromagnetic ratios. ^{13}C and ^{29}Si both have a total spin of $I = 1/2$ with gyromagnetic ratios of opposite signs. By engineering the isotope concentration, we can deterministically tune the average of nuclear spins in the vicinity of color centers [79]. In our case, we studied an isotopically purified crystal with the isotope concentrations of [^{12}C]> 99.98% and [^{28}Si]> 99.85%. It allows keeping the number of nuclear spins coupled with any given V_{Si} center to a few in order to simplify our preliminary studies.

In this chapter we first provide the Hamiltonian of the bipartite system composed of an electron spin coupled to a nuclear spin. From this analysis, we will be able to understand the dynamics of the system during a decoupling sequence and specifically during the different resonances of it, which will enable the deterministic control of the system. We will also expand on previous theoretical models [66] with a more accurate description at low magnetic fields. The theoretical predictions will be verified on the integrated V2 center coupled to nuclear spinsn identified previously through the modulation of the spin echo signal (see FIGURE 4.15). With the nuclear spin environment identified, we will demonstrate the control of a nuclear spin with high fidelity. Finally using our theoretical and experimental knowledge we will propose a protocol to reach single-shot readout for a V_{Si} center utilizing a nuclear spin as an ancilla qubit.

5.1 Electron-Nuclear spin systems

The system considered in this chapter is an electron spin ($S = S_e$) coupled to a single nuclear spin ($I = 1/2$), under the action of a static external magnetic field aligned along the z-axis of the electron spin. In the following we will have a look at the most general case, where the electron can be either an integer or a half-integer spin only for the applications will we consider the V2 center with a total spin of 3/2. A sketch of the system is given in FIGURE 5.1.

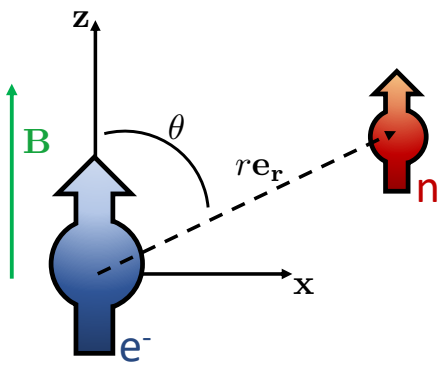

Figure 5.1: **Electron-Nuclear spin systems.** An electron spin (blue) interacting with a single nuclear spin (red) via dipole-dipole coupling. The external magnetic field (B) is assumed to be aligned along the z-axis.

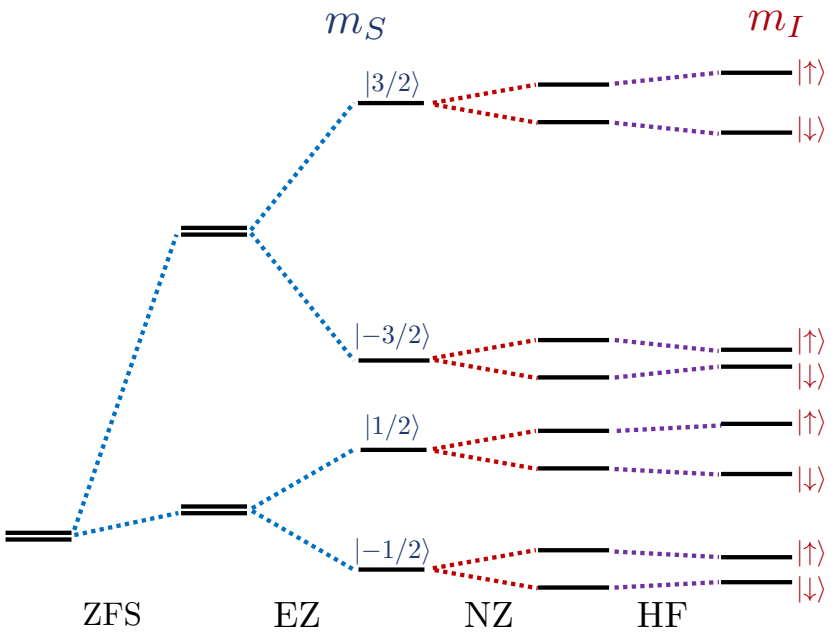

Figure 5.2: **Energy diagram.** Energy levels for the bipartite system V_{Si} - ^{29}Si. Each part of the Hamiltonian is subsequently applied. For clarity, the nuclear-Zeeman and the hyperfine coupling contributions are exaggerated.

5.1.1 Hamiltonian

The Hamiltonian [136, 137] describing the energy levels and dynamics of a nuclear spin coupled to an electron spin is given by:

$$\mathcal{H} = \mathcal{H}_{\text{ZFS}} + \mathcal{H}_{\text{EZ}} + \mathcal{H}_{\text{NZ}} + \mathcal{H}_{\text{HF}}. \tag{5.1}$$

$\mathcal{H}_{\text{ZFS}}$ and $\mathcal{H}_{\text{EZ}}$, respectively the zero-field splitting and electron Zeeman contributions, have been discussed in Chapter 1. The other contributions are the nuclear Zeeman term ($\mathcal{H}_{\text{NZ}}$) describing the action of the external magnetic field onto the nuclear spin and the hyperfine coupling between the electron spin and the nuclear spin ($\mathcal{H}_{\text{HF}}$). The reader will note the omittance of the nuclear quadrupole interaction as this effect only applies to nuclear spins with a quantum number $I > 1/2$. The nuclear Zeeman term is expressed in a similar way as the electron Zeeman splitting:

$$\mathcal{H}_{\text{NZ}} = -\tilde{\gamma}_n \, \mathbf{B}\hat{\mathbf{I}} = -\omega_L \, \hat{I}_z. \tag{5.2}$$

Where $\omega_L = \tilde{\gamma}_n B$ is known as the Larmor frequency. The spin-spin interaction term is described by an anisotropic tensor, $\mathbf{A}$:

$$\mathcal{H}_{\text{HF}} = \widetilde{\mathbf{S}}\mathbf{A}\mathbf{I}. \tag{5.3}$$

This interaction comprises two distinct contributions, the Fermi contact, and the electron-nuclear dipole-dipole coupling. The strength of the Fermi contact is proportional to the electron spin density at the nucleus, therefore it only plays a role for nuclear spins very close to the electron spin. In our case, we will assume the nuclear spin to be several lattice sites away from the color center and thus neglect the Fermi

contact. In this approximation, the two (electron and nuclear) magnetic dipoles are far enough to be treated as point dipoles, and the dipole-dipole interaction can be expressed as:

$$\mathbf{A_{dd}} = \frac{\mu_0}{4\pi\hbar} g_e \mu_b g_n \mu_n \frac{1}{r^3} (3\mathbf{e_r}\widetilde{\mathbf{e_r}} - \mathbf{Id}), \tag{5.4}$$

with $\mathbf{e_r}$ the unit vector connecting the two spins, and r the distance between them, as sketched in FIGURE 5.1. The effect of each Hamiltonian contribution on the energy levels is visualized in FIGURE 5.2. With the hyperfine term, each allowed microwave transition (Δ_{m_S} or $\Delta_{m_I} = \pm 1$), can be addressed independently as the transition's energies are all different. However, the transitions acting on the nuclear spin quantum number ($|s_e, \uparrow\rangle \leftrightarrow |s_e, \downarrow\rangle$), require higher driving power due to the weak interaction of the nuclear spin with the magnetic field. At cryogenic temperature, the induced heat can increase the optical transitions linewidths leading to a reduced spin readout contrast [45], and also can reduce the coherence times of the spin system [30, 33]. Therefore, it has to be kept to a minimum. Other protocols have been developed to manipulate the nuclear spin without the need of a strong rf field, in particular using the electron spin as an intermediate. To understand those protocols, we first need to have a closer look at the interaction between the two spins through the hyperfine interaction.

5.1.2 Secular approximation

In general, the zero-field splitting and the electron-Zeeman terms are around tens to hundreds of MHz[1], whereas the hyperfine interaction is typically orders of magnitude smaller: the dipole-dipole interaction decreases with the distance between the two spins as $1/r^3$, as seen in equation (5.4). Already, if the nuclear spin is 5 angstrom away from the electron spin, the dipole-dipole interaction is less than a hundred kHz. Considering that the lattice constant of 4H-SiC is $a = 3.018$ Å [241], any nuclear spins located more than a few lattice sites away from the electron spin are weakly coupled with low interaction energies. The nuclear Zeeman term is also orders of magnitude smaller due to the reduced nuclear gyromagnetic ratio. To illustrate those estimations, a sketch of the energy range of each term can be seen in FIGURE 5.3.

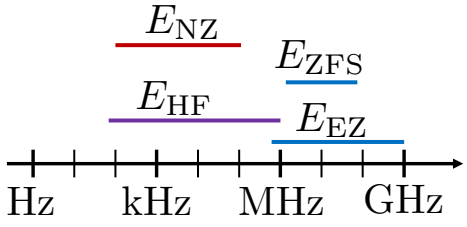

Figure 5.3: **Interaction strength.** Typical energies of the different terms in the Hamiltonian describing the bipartite system electron-nuclear spins. In blue (red) are the contributions concerning only the electron (nuclear) spin, and the hyperfine interaction is labelled in purple.

[1]For V2 (V1), the zero-field splitting is 70 (4) MHz

From this analysis, we can conclude that the nuclear spin plays little to no role in the eigenstates of the electron spin and its dynamics. Neglecting the action of the nuclear spin onto the electron spin's eigenstates is called the *secular approximation*. In this picture, the electron spin creates a spin-dependent magnetic field influencing the nuclear spin eigenstates and dynamics, whereas the nuclear spin only affects the energies of electron spin states and not the eigenstates themselves. Mathematically, this framework allows us to **only** consider terms similar to $\hat{S}_z \otimes \hat{I}_i$ in the calculation of the Hamiltonian. If we assume that $\mathbf{e_r}$ lies in the (X, Z) plane, the hyperfine interaction is described by the Hamiltonian:

$$\mathcal{H}_{HF} = A_{\parallel} \hat{S}_z \otimes \hat{I}_z + A_{\perp} \hat{S}_z \otimes \hat{I}_x, \tag{5.5}$$

where $A_{\parallel}$ and $A_{\perp}$ are called respectively parallel and perpendicular hyperfine coupling coefficients, and their expressions can be deduced from the hyperfine tensor $\mathbf{A_{dd}}$ given in equation (5.4):

$$A_{\parallel} = \frac{T}{r^3}(3\cos^2(\theta) - 1), \tag{5.6}$$

$$A_{\perp} = \frac{T}{r^3}\cos(\theta)\sin(\theta). \tag{5.7}$$

with r, θ describe the position of the nuclear spin according to the electron spin (as seen in FIGURE 5.1) and:

$$T = \frac{\mu_0}{4\pi\hbar}\frac{g_e g_n \mu_b \mu_n}{r^3}. \tag{5.8}$$

By combining everything we have described so far, we obtain the expression of the Hamiltonian, under the secular approximation, of the bipartite system:

$$\mathcal{H} = (D_{gs}\,\hat{S}_z^2 + \tilde{\gamma}_e\,B\,\hat{S}_z) \otimes \hat{\mathbb{1}} + \hat{\mathbb{1}} \otimes (-\omega_L\,\hat{I}_z) + A_{\parallel}\,\hat{S}_z \otimes \hat{I}_z + A_{\perp}\,\hat{S}_z \otimes \hat{I}_x\cdot. \tag{5.9}$$

5.1.3 Free-evolution of the nuclear spin

In the secular approximation, the Hamiltonian, given in equation (5.9), preserves the electron spin states $|s_i\rangle$ ($s_i \in [-S_e \cdots S_e]$) whereas the nuclear spin states are mixing. The effective Hamiltonian acting on the nuclear spin, if the electron spin is in the state $|s_i\rangle$, is:

$$\mathcal{H}_i = \omega_i \mathbf{n}_i \cdot \hat{\mathbf{I}}, \tag{5.10}$$

where:

$$\omega_i = \sqrt{(s_i A_{\parallel} - \omega_L)^2 + (s_i A_{\perp})^2}, \tag{5.11}$$

$$\mathbf{n}_i = \frac{1}{\omega_i}(s_i A_{\perp}, 0, s_i A_{\parallel} - \omega_L). \tag{5.12}$$

ω_i and $\mathbf{n}_i$ are respectively the angular frequency and the rotation axis defining the evolution of the nuclear spin. Indeed, with these notations, we can develop the nuclear spin evolution operator ($\hbar = 1$) as:

$$\hat{U}_i(\tau) = exp\left[-\mathrm{i}\,(\omega_i\tau)\,\mathbf{n}_i \cdot \hat{\mathbf{I}}\right]. \tag{5.13}$$

In the Bloch sphere representation, as pictured in FIGURE 5.4, the free evolution of the nuclear spin is then a rotation around the axis $\mathbf{n}_i$ at an angular frequency ω_i. This rotation is dependent on the electron spin state: the nuclear spin will end up in a different state according to the electron spin state $|s_i\rangle$. In the next section, we will see how we can utilize this characteristic of the hyperfine coupling to deterministically manipulate the nuclear spin.

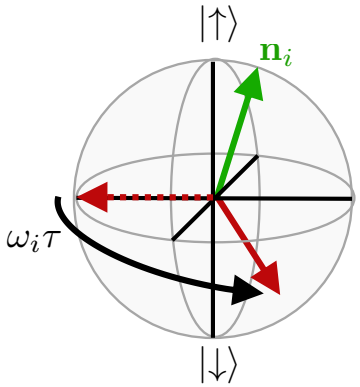

Figure 5.4: **Nuclear spin free-evolution.** Bloch sphere representation of the evolution of the nuclear spin state coupled to an electron spin in the state $|s_i\rangle$ during a time τ. The red dashed (solid) arrow corresponds to the initial (final) state of the nuclear spin. The green line represents the axis of rotation $\mathbf{n}_i$.

5.2 Decoupling sequences

Decoupling sequences were first introduced to actively protect the electron quantum state from the environment [239, 242]. The successive refocusing pulses alternate the Hamiltonian perceived by the nuclear spin bath, decoupling the nuclear spins from the electron spin. It increases the coherence time and therefore the storage time of quantum information on the electron spin. A few seconds of coherence time (several order of magnitudes longer than the Hahn echo time T_2) have been achieved for color centers in the solid [63, 110]. However, the recorded signal can be strongly modulated, as we noticed for the Hahn echo signal of the integrated defects (FIGURE 4.15) where the electron spin population is fully flipped for some precession times. We will see in this chapter how to utilize those resonances to deterministically manipulate the nuclear spin.

Different protocols have been designed over time to mitigate control pulse imperfections in the decoupling sequences [65, 243], e.g. the XY8 sequence [79, 244]. However, we will constrain ourselves to the study of the simplest form of decoupling sequence the

"Carr-Purcell-Meiboom-Gill" (CPMG) sequence [245, 246] which consists of N equally spaced refocusing pulses (π-pulse), as sketched in FIGURE 5.5**a**.

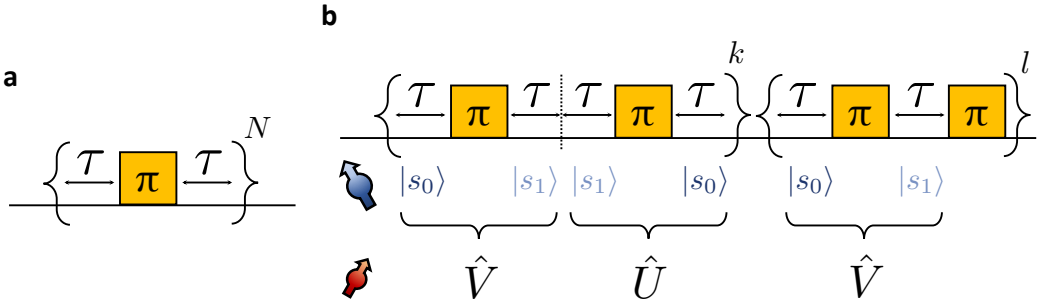

Figure 5.5: **CPMG sequence. a** Representation of a N-pulse CPMG sequence, τ is the waiting time or single precession time and N the number of refocusing pulses. **b** Visualization of the reorganization of the waiting times of the N-pulse CPMG sequence ($N = 2k+l$), helping the derivation of the dynamics of the nuclear spin. A final π-pulse for odd N is present, such that the electron spin state is preserved in the absence of nuclear spin. Below the sequence is shown the successive electron spin states as well as the evolution operators applied on the nuclear spin ($\hat{U}$ and $\hat{V}$ defined in equations (5.17-5.18)), if the electron is initialized in the state $|s_0\rangle$.

5.2.1 Theoretical framework

Let the electron spin be initialized in the state $|s_i\rangle$ ($i \in 0, 1$) and study the action of the electron-spin sequence $(\tau - \pi - \tau)^N$ on the electron-nuclear spin-spin system. Here, τ represents a waiting time, π a spin-flip pulse between the states $|s_0\rangle$ and $|s_1\rangle$, and $N = 2k + l$ is an integer ($k \in \mathbb{N}$, $l \in \{0, 1\}$). To simplify the reading, we assume that an additional π-pulse is performed at the end of the sequence for odd N. Such that the electron spin state is preserved in the absence of nuclear spin. We denote $\hat{U}_{D_i}$, the nuclear spin evolution operator for a full CPMG-sequence when the electron spin is initially in the state $|s_i\rangle$. If the nuclear spin state is initially $|\Psi\rangle$, then the bipartite system's state at the end of the sequence is:

$$|s_i\rangle \otimes (\hat{U}_{D_i} |\Psi\rangle). \tag{5.14}$$

From the definition of the operators $\hat{U}_i$, equation (eq:Ch4_U_i), and using the identity: $\hat{U}_i(2\tau) = \hat{U}_i(\tau)\hat{U}_i(\tau)$, we express the operators $\hat{U}_{D_i}$ as:

$$\hat{U}_{D_0} = (\hat{U}_1(\tau)\hat{U}_0(\tau))^l(\hat{U}_0(\tau)\hat{U}_1(2\tau)\hat{U}_0(\tau))^k = \hat{V}^l(\hat{U}\hat{V})^k, \tag{5.15}$$
$$\hat{U}_{D_1} = (\hat{U}_0(\tau)\hat{U}_1(\tau))^l(\hat{U}_1(\tau)\hat{U}_0(2\tau)\hat{U}_1(\tau))^k = \hat{U}^l(\hat{V}\hat{U})^k. \tag{5.16}$$

Where $\hat{U}$ and $\hat{V}$ are defined as:

$$\hat{U} = \hat{U}_0(\tau)\hat{U}_1(\tau), \tag{5.17}$$
$$\hat{V} = \hat{U}_1(\tau)\hat{U}_0(\tau). \tag{5.18}$$

As a composition of rotations, $\hat{U}$ ($\hat{V}$) is also a rotation in the Bloch representation and thus we can define $\theta_{\hat{U}}$ ($\theta_{\hat{V}}$) and $\mathbf{n}_{\hat{U}}$ ($\mathbf{n}_{\hat{V}}$) the angle and axis of this rotation. The reorganization of the multiplicative terms in the expression of the operators $\hat{U}_{D_i}$ (5.15-5.16) corresponds to the splitting of the 2τ waiting time in two parts, as sketched in FIGURE 5.5**b**, and will be usefull on the analytical derivation of the nuclear spin evolution.

In the case of CPMG, the electron spin is initialized in the state $|s_0\rangle$ just before to be driven, using a $\pi/2$ pulse, in the state: $|+\rangle_e = (|s_0\rangle + |s_1\rangle)/\sqrt{2}$. At the end of the spin-sequence, the bipartite system's state is then the state:

$$\frac{1}{\sqrt{2}}\left(|s_0\rangle \otimes (\hat{U}_{D_0}|\Psi\rangle) + |s_1\rangle \otimes (\hat{U}_{D_1}|\Psi\rangle)\right), \tag{5.19}$$

If $\hat{U}_{D_1}$ and $\hat{U}_{D_0}$ are similar ($\hat{U}_{D_0} = \hat{U}_{D_1} = \hat{U}_D$), then the bipartite quantum state is separable:

$$|+\rangle_e \otimes \hat{U}_D|\Psi\rangle, \tag{5.20}$$

and the electron spin is decoupled from the nuclear spin. Whereas, if $\hat{U}_{D_1}$ and $\hat{U}_{D_0}$ are rotations with different axes[2], e.g. $\pi/2$ rotation in opposite directions, then the electron-nuclear spin system will be entangled (maximally in this case):

$$\frac{1}{\sqrt{2}}(|s_0\rangle_e \otimes |\uparrow\rangle + |s_1\rangle_e \otimes |\downarrow\rangle). \tag{5.21}$$

A representation of both cases can be seen in FIGURE 5.6.

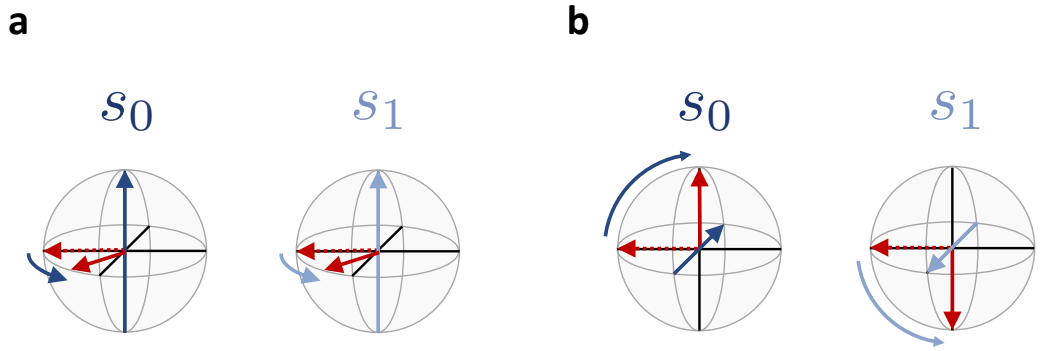

Figure 5.6: **Different dynamics in a decoupling sequence.** Bloch sphere representations of the dynamics of the nuclear spin during a pulse CPMG-sequence for an electron spin state initialized in the state $|s_i\rangle$. The red dashed (solid) arrow corresponds to the initial (final) state of the nuclear spin. The blue solid line represents the axis of rotation. **a** (**b**) corresponds to the case of similar (opposite) evolution of nuclear spin according to the electron spin state, leading to a separable (entangled) two-qubit state.

[2] As we will see later, the angles θ_{D_i} are the same.

In summary, according to the two decoupling sequence parameters, the waiting time τ and the number of refocusing pulses N, we can perform conditional (on the electrons spin state) or unconditional operations on the nuclear spin. As the number of refocusing pulses effectively only increases the rotation angle θ_{D_i}: $\theta_{D_i}(\tau, 2k) = k \cdot \theta_{D_i}(\tau, 2)$, the axis of rotations are unchanged. Therefore only the waiting time τ will determine if the operators $\hat{U}_{D_i}$ are parallels or anti-parallels. The resonances observed in FIGURE 4.15 correspond to the anti-parallel cases $\mathbf{n}_{D_0} \cdot \mathbf{n}_{D_1} = -1$. The specific times at which those operations occur will be theoretically derived in section 5.3.

Experimentally, a final $\pi/2$-pulse is applied onto the electron spin before the reading out of the spin state. By performing a partial trace over the Hilbert space of the nuclear spin states, as it is randomly initialized in our case, we can calculate the probability to preserve the electron spin after a decoupling sequence:

$$P(s_0) = \frac{1 + \cos\left(\frac{\theta_{\hat{U}_{D_0}^\dagger \hat{U}_{D_1}}}{2}\right)}{2}. \tag{5.22}$$

Here, $\theta_{\hat{U}_{D_0}^\dagger \hat{U}_{D_1}}$ is the rotation angle of the nuclear spin during the operation $\hat{U}_{D_0}^\dagger \hat{U}_{D_1}$. As expected, if $\hat{U}_{D_0}$ and $\hat{U}_{D_1}$ are the same, then $\hat{U}_{D_0}^\dagger \hat{U}_{D_1} = \mathbb{1}$ and $P(s_0) = 1$: the electron spin is preserved and decoupled from the nuclear spin.

5.2.2 Spin echo

The Hahn echo sequence introduced previously (section 1.4.2) is a particular case of the decoupling sequence with $N = 1$, in which $\hat{U}_{D_0}$ and $\hat{U}_{D_1}$ are simply:

$$\hat{U}_{D_0} = \hat{V} = \hat{U}_1(\tau)\hat{U}_0(\tau), \tag{5.23}$$
$$\hat{U}_{D_1} = \hat{U} = \hat{U}_0(\tau)\hat{U}_1(\tau). \tag{5.24}$$

To derivate the expression of the operators $\hat{U}_{D_i}$ we will need to use the trigonometric identities of the composition of rotations:

$$\cos(\theta_{ab}/2) = \cos(\theta_a/2)\cos(\theta_b/2) - (\sin(\theta_a/2)\mathbf{n}_a) \cdot (\sin(\theta_b/2)\mathbf{n}_b), \tag{5.25}$$
$$\begin{aligned}\sin(\theta_{ab}/2)\mathbf{n_{ab}} = &\cos(\theta_b/2)\sin(\theta_a/2)\mathbf{n}_a + \cos(\theta_a/2)\sin(\theta_b/2)\mathbf{n}_b \\ &+ (\sin(\theta_b/2)\mathbf{n}_b) \times (\sin(\theta_a/2)\mathbf{n}_a),\end{aligned} \tag{5.26}$$

where "ab" labeled the rotation performed by the composition of the rotation a **then** the rotation b. Applying the identities thrice to the rotations $\hat{U}$, $\hat{V}$ and $\hat{V}^\dagger\hat{U}$, we can derivate the well-known [40, 247] formula:

$$P(s_0) = 1 - \frac{k}{4}\left(2 - 2\cos(\omega_0\tau) - 2\cos(\omega_1\tau) + \cos(\omega_+\tau) + \cos(\omega_-\tau)\right). \tag{5.27}$$

Here, $\omega_\pm = \omega_0 \pm \omega_1$, and k is the so-called modulation depth parameter:

$$k = \left(\frac{\omega_L A_\perp}{\omega_0\,\omega_1}\right)^2. \tag{5.28}$$

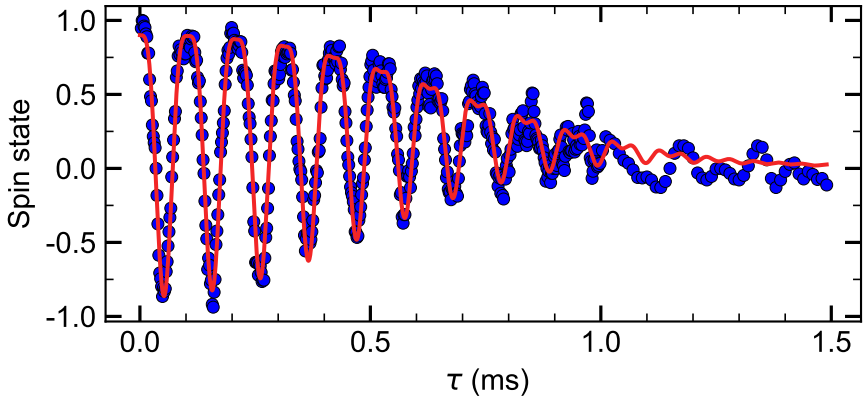

Figure 5.7: **Modulated Hahn echo spin signal.** Spin coherence signal for the integrated V2 center, the fit (in red) is obtained using the model given in equation (5.29). The spin state $+1$ corresponds to $m_s = 3/2$ and -1 to $m_s = 1/2$.

As the name suggests, k corresponds to the the depth of the modulation in the Hahn echo signal. We can use the equation (5.27) to fit the modulation of the Hahn echo signal obtained for the integrated V2 center (experiment conducted at $B = 36$ G) and estimate the nuclear spin environment of the color center. To properly fit the data, we additionally need to take into account experimental errors, such as non-perfect spin-pulses ($\pi/2$, π, and $3\pi/2$) affecting the state preparation and readout, as well as the decaying envelope used to yield the coherence time. In extenso, the equation used to fit the Hahn echo signal is:

$$y(t) = A \cdot P(m_S = 3/2)(t/2) \cdot \exp\left((\frac{t}{T_2})^p\right) + y_0. \tag{5.29}$$

Where t is the full precession time which is twice as long as the waiting time τ. A and y_0 are respectively the amplitude and the offset of the signal, characterizing the experimental errors; while T_2 and p are the coherence time and the decay power describing the decaying envelope. Assuming a single nuclear spin coupled to the integrated electron-spin, we try to fit,using the equation (5.29), the experimental data displayed in FIGURE 5.7. Assuming the nuclear spin to be a ^{13}C does not allow a fit of the modulation. The nucleus is a ^{29}Si, which fits with the experimental data, see FIGURE 5.7. In regards to the isotope concentration in the sample ([^{29}Si]>99.85%, [^{13}C]>99.98%), it was expected as the number of ^{29}Si nuclear is far greater than the number of ^{13}C nuclear. We yield the following hyperfine parameters[3]:

$$\begin{aligned} A_{\parallel} &= -23.35 \pm 0.02\,\text{kHz}, \\ A_{\perp} &= 12.09 \pm 0.01\,\text{kHz}. \end{aligned} \tag{5.30}$$

Therefore, the nuclear spin is weakly coupled ($A \lesssim 1/T_2^* = 100$ kHz) to the electron spin. Thanks to the low magnetic field, the Larmor frequency (~ 30 kHz) is comparable

[3]Those are the reduced hyperfine parameters, i.e divided by 2π.

to the hyperfine coupling coefficients, which explains the strong modulation of the signal. From this fit, we also yield the Hahn echo coherence time of the integrated V2 center, which was discussed in Chapter 4.

To improve the description of the spin bath surrounding the integrated electron spin, we will increase the number of refocusing pulses.

5.2.3 CPMG sequence

Hahn echo sequences show a limited precision to estimate and sense a nuclear spin bath surrounding an electron spin state. Different protocols have been developed over the years to sense complex spin baths such as nuclear magnetic resonance (NMR) [27, 248, 249], DEER [250, 251, 252], or DDrF [24] sequences, some requiring rf-drive capabilities. However, as the sample used in our experiment is isotopically purified, we expect the nuclear spin bath to be composed of a few weakly coupled nuclear spins, as seen by the ability to fit the Hahn echo signal (FIGURE 5.7) assuming only a single nuclear spin. Therefore the spin bath can be resolved by simply performing CPMG-sequences with higher N. In particular, we perform an 8-pulse CPMG-sequence at an elevated magnetic field ($B = 81$ G), thus keeping the hyperfine coupling strength comparable to the nuclear spin Larmor frequency while optimizing the contrast of the signal. The result can be seen in FIGURE 5.8: we observe once again a strong modulation of the signal (near unity contrast) with various dips of different depths.

Obtaining an analytical formula for an arbitrary number of π-pulses is not straightforward, as equations get exponentially more complex. To simulate the results using multiplications of the free-evolution as given in (5.13) is also not computationally efficient as the exponentiation of matrices for every waiting time τ would be too long. We, therefore, use the Taylor-development of the exponential function and the identities for Pauli matrices to express the operators $\hat{U}_i$ as:

$$\hat{U}_i(\tau) = \cos(\omega_i \tau/2)\, \hat{\mathbb{1}} - i \sin(\omega_i \tau/2)\, \mathbf{n}_i \cdot \hat{\mathbf{I}}. \tag{5.31}$$

Pauli matrices form a group with simple multiplication identities, thus the multiplication of an arbitrary number of operators $\hat{U}_i$ at any given waiting time τ is now computationally simple. This process of expressing the composition of rotations through a four-dimensional group is also used in 3D animation, in this context the Pauli matrices are called quaternions: the expansion of complex numbers in four-dimension. Using our simplified model and with the hyperfine coupling parameters extracted from the Hahn echo, we simulate the expected 8-pulse CPMG signal. Although the simulated signal shows a good overlap with the data, we find additional dips at $\tau = 3.7$ µs, 11.1 µs, and 18.5 µs, which cannot be explained by the presence of a single nuclear spin. A fit to the additional dips with a second ^{29}Si nuclear spin shows a very good qualitative overlap.

Subsequently, all four hyperfine coupling terms are fine-tuned to minimize the error squares between the simulation and the experimental data. Due to its low strength, the nuclear-nuclear interaction is neglected, the probabilities $P_j(m_S = 3/2)$ given by the equation (5.22) for each nuclear spin N_j are then simply multiplied to obtain the probability for the electron spin to be preserved:

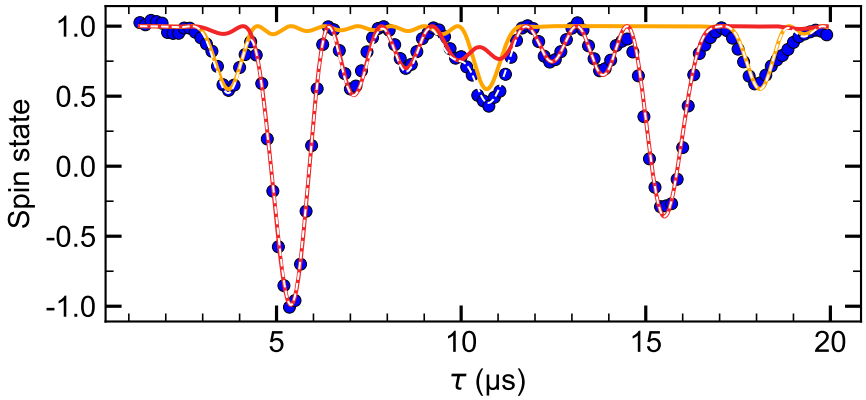

Figure 5.8: **8-pulse CPMG spin signal.** Spin signal for the 8-pulse CPMG-sequence at $B = 81$ G (blue dots). The red and orange lines correspond to the (independent) spin signals obtained for the first and second nucleus, respectively. The fit to the data (white dashed line) is based on the product of both contributions (equation (5.32)). The spin state $+1$ corresponds to $m_s = 3/2$ and -1 to $m_s = 1/2$.

.

$$P(m_S = 3/2)(\tau) = \prod_j P_j(m_S = 3/2)(\tau). \tag{5.32}$$

Using the hyperfine parameters obtained prior as starting parameters of the fit research, we obtain the following hyperfine coupling coefficients for the nucleus N_1 and N_2:

$$A_{\parallel,1} = -23.5\,\text{kHz},\ A_{\perp,1} = 12.0\text{kHz}, \tag{5.33}$$
$$A_{\parallel,2} = 0.2\,\text{kHz},\ A_{\perp,2} = 8.5\,\text{kHz}. \tag{5.34}$$

As the overlap between the experimental data and its fit, seen in FIGURE 5.8, shows essentially no residuals, we consider that the coupling to additional nuclear spins is very weak compared to the electron spin coherence time, and thus negligible. The system is therefore fully described by one electron and two nuclear spins. An artistic design of the system identified in the waveguide is given in FIGURE 5.9.

In summary, we have identified our system and acquired the possibility to simulate an arbitrary CPMG-sequence. The nice agreement between the fit and the experimental data, in FIGURE 5.7 and FIGURE 5.8, assesses the validity of the theoretical model derivated so far. However, we have yet to give an accurate description of the resonances (dips) observed in the spin signal. In the next section, we will give an analytical formula of the waiting times at which the resonances occur and the validity range of those. We will also study the action performed on the nuclear spin at those resonances.

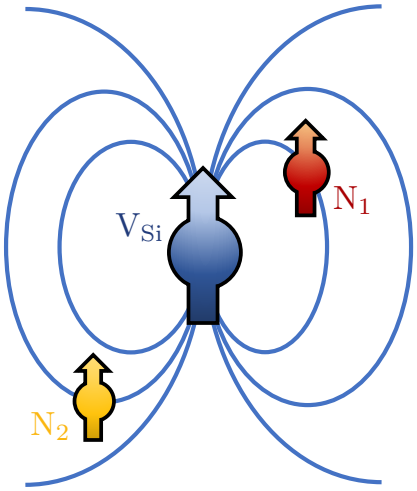

Figure 5.9: **Multi-spin system.** Artistic representation of the coupled electron-nuclear spin triplet identified in a waveguide. The blue arrow corresponds to the electron spin while the red (orange) one corresponds to the nuclear spin N_1 (N_2).

.

5.3 CPMG resonances

5.3.1 Theoretical derivation

For the remaining of the calculation, we will focus on the case of even number of refocusing pulses: $N = 2k$, such that:

$$\hat{U}_{D_0} = (\hat{U}\hat{V})^k, \tag{5.35}$$
$$\hat{U}_{D_1} = (\hat{V}\hat{U})^k. \tag{5.36}$$

At the end of a CPMG-sequence, the electron spin state is decoupled from the nuclear spin if and only if the rotations axis of the operators $\hat{U}_{D_i}$ are the same, as seen in FIGURE 5.6, whereas both spins will be maximally entangled for anti-parallel rotation axis: $\mathbf{n}_{D_0} \cdot \mathbf{n}_{D_1} = -1$. As $(\hat{U}\hat{V})^k$ and $\hat{U}\hat{V}$ share the same rotation axis, the useful resonances (anti-parallel case) of the decoupling sequence arise when: $\mathbf{n}_{\hat{U}\cdot\hat{V}} = -\mathbf{n}_{\hat{V}\cdot\hat{U}}$. Utilizing the equation (5.26), we have:

$$\begin{aligned}\sin\left(\theta_{\hat{U}\cdot\hat{V},\hat{V}\cdot\hat{U}}\right)\mathbf{n}_{\hat{U}\cdot\hat{V},\hat{V}\cdot\hat{U}} = &\cos(\theta_{\hat{U}}/2)\sin(\theta_{\hat{V}}/2)\mathbf{n}_{\hat{V}} + \cos(\theta_{\hat{V}}/2)\sin(\theta_{\hat{U}}/2)\mathbf{n}_{\hat{U}} \\ &\pm \sin(\theta_{\hat{U}}/2)\sin(\theta_{\hat{V}}/2)\mathbf{n}_{\hat{U}} \times \mathbf{n}_{\hat{V}}.\end{aligned} \tag{5.37}$$

If $\mathbf{n}_{\hat{U}} \times \mathbf{n}_{\hat{V}} = \mathbf{0}$, then $\mathbf{n}_{\hat{U}\cdot\hat{V}} = \mathbf{n}_{\hat{V}\cdot\hat{U}}$. Therefore, we have to assume that $\mathbf{n}_{\hat{U}} \times \mathbf{n}_{\hat{V}} \neq \mathbf{0}$. Under this hypothesis the equation $\mathbf{n}_{\hat{U}\cdot\hat{V}} = -\mathbf{n}_{\hat{V}\cdot\hat{U}}$ is equivalent to:

$$\begin{cases} \cos(\theta_{\hat{U}}/2)\sin(\theta_{\hat{V}}/2) = 0, \\ \cos(\theta_{\hat{V}}/2)\sin(\theta_{\hat{U}}/2) = 0, \\ \sin(\theta_{\hat{U}}/2)\sin(\theta_{\hat{V}}/2) \neq 0. \end{cases}$$

i.e:

$$\cos(\theta_{\hat{U}}/2) = \cos(\theta_{\hat{V}}/2) = 0. \tag{5.38}$$

With the definition of $\hat{U}$ and $\hat{V}$ (5.17,5.18), and the equation (5.25), we obtain the condition for anti-parallel rotation axes:

Theorem 3 *The resonances of a decoupling sequence occur for the waiting time τ_r respecting the following identity:*

$$\cos(\omega_0\tau_r/2)\cos(\omega_1\tau_r/2) = (\mathbf{n}_0 \cdot \mathbf{n}_1) \cdot \sin(\omega_0\tau_r/2)\sin(\omega_1\tau_r/2). \tag{5.39}$$

Where ω_i and $\mathbf{n}_i$ are respectively the angular frequency and the rotation axis of the nuclear free evolution according to the electron spin state $|s_i\rangle$ and given in equations (5.11-5.12).

Interestingly, for the periodic waiting times:

$$\tau_{2k+1} = \frac{(2k+1)\pi}{\omega_0 + \omega_1}, \tag{5.40}$$

with $k \in \mathbb{N}$, we have:

$$\cos\left(\frac{\omega_i\tau_{2k+1}}{2}\right) = (-1)^k \sin\left(\frac{\omega_{1-i}\tau_{2k+1}}{2}\right). \tag{5.41}$$

Further, we find that in the case of negligible perpendicular hyperfine coupling ($|A_\perp| \ll |A_\parallel|, \omega_L$), both rotation axes $\mathbf{n}_i$ are along the z-axis. The inner product is then $\mathbf{n}_0 \cdot \mathbf{n}_1 \approx 1$. Therefore, in this case, we find that the periodic times τ_{2k+1} are solutions of the equation (5.39).

These solutions are the zero-order approximations and are exact in the asymptotic cases $B \to \infty$ or $A_\perp \to 0$. These solutions, or the one obtained for $A_\perp = 0$, are well accepted in the literature [34, 67]. However, in our experiment, we have used a magnetic field such that $\omega_L \sim A_\perp \sim A_\parallel$. Therefore, the solutions need to be refined with a correction term.

We assume the correction to the resonant times τ_{2k+1} (5.40) to be as: $\tau_r = \tau_{2k+1}(1+\epsilon_\tau)$, with $|\epsilon_\tau| \ll 1$. After rearranging the equation (5.39) as product of tangents and expanding them in the first-order in ϵ_τ, we obtain:

$$\tan(\omega_0\tau/2)\tan(\omega_1\tau/2) = 1 + \epsilon_\tau \cdot \frac{(2k+1)\pi}{\sin(\omega_0\tau_{2k+1}/2)} + \mathcal{O}(\epsilon_\tau^2). \tag{5.42}$$

Then, solving the equation (5.39) for ϵ_τ results in:

$$\epsilon_\tau = \sin(\omega_0\tau_{2k+1}/2)\frac{(\mathbf{n}_0 \cdot \mathbf{n}_1)^{-1} - 1}{(2k+1)\pi}. \tag{5.43}$$

In extenso, the resonance times are:

$$\tau_k^{(1)} = \frac{(2k+1)\pi}{\omega_0 + \omega_1}\left(1 + \sin\left(\frac{(2k+1)\pi\cdot\omega_0}{2(\omega_0+\omega_1)}\right)\frac{(\mathbf{n}_0 \cdot \mathbf{n}_1)^{-1} - 1}{(2k+1)\pi}\right). \tag{5.44}$$

As $(\mathbf{n}_0 \cdot \mathbf{n}_1) \to 1$ when $B \to \infty$, then $\epsilon_\tau \to 0$, as expected. To determine if the correction term suffices to express the resonant times for our experimental conditions, we now develop an expression to define the magnetic field range $B_{\text{crit}} \leq B \leq \infty$ in which the approximation is valid. In other words, given a nuclear spin with coupling terms $A_\parallel$ and $A_\perp$, what is the minimum required magnetic field B_{crit} in which the approximation $\tau_r = \tau_{2k+1}(1 + \epsilon_\tau)$ is valid?

5.3.2 Validity range

To have a negligible contribution from all higher order terms in $\mathcal{O}(\epsilon_\tau^2)$, we want $\epsilon_\tau^2 \ll |\epsilon_\tau|$, which translates to $(\mathbf{n}_0 \cdot \mathbf{n}_1)^{-1} - 1 \ll \pi$. From equation (5.12), we can write:

$$(\mathbf{n}_0 \cdot \mathbf{n}_1)^{-1} = \sqrt{1 + \Big(\frac{A_\perp \cdot \omega_L}{s_1 s_0 \cdot (A_\perp^2 + A_\parallel^2) - (s_0 + s_1) \cdot A_\parallel \cdot \omega_L + \omega_L^2}\Big)^2}. \tag{5.45}$$

Therefore, we can define the following equivalence:

$$(\mathbf{n}_0 \cdot \mathbf{n}_1)^{-1} - 1 \leq \epsilon_n \Leftrightarrow \Big|\frac{A_\perp \cdot \omega_L}{s_0 s_1 \cdot (A_\perp^2 + A_\parallel^2) - (s_0 + s_1) \cdot A_\parallel \cdot \omega_L + \omega_L^2}\Big| \leq \sqrt{(1+\epsilon_n)^2 - 1}. \tag{5.46}$$

Here, $\epsilon_n \ll 1$ is a parameter that is related to the magnitude of the correction term ϵ_τ given in equation (5.43):

$$(\mathbf{n}_0 \cdot \mathbf{n}_1)^{-1} - 1 \leq \epsilon_n \Rightarrow |\epsilon_\tau| \leq \frac{|\sin(\omega_0 \tau_{2k+1}/2)|}{(2k+1)\pi} \cdot \epsilon_n. \tag{5.47}$$

The second inequality in equation (5.46) is solved for two sets of solutions respecting the equations:

$$\omega_L + A_- + s_0 s_1 \frac{A_\perp^2 + A_\parallel^2}{\omega_L} \geq 0 \text{ or} \tag{5.48}$$

$$\omega_L + A_+ + s_0 s_1 \frac{A_\perp^2 + A_\parallel^2}{\omega_L} \leq 0, \tag{5.49}$$

with $A_\pm = (s_0 + s_1)A_\parallel \pm \frac{|A_\perp|}{\sqrt{(1+\epsilon_n)^2 - 1}}$. As required above, we are interested in the solutions that cover the case $B \to \infty$, $B_{\text{crit}} \leq B \leq \infty$. Because $\omega_L = \tilde{\gamma}_n B$, the correct set of solutions depends on the sign of the gyromagnetic ratio γ_n. If γ_n is positive (negative), the inequality to solve is the equation (5.48) (equation (5.49)). To determine the critical magnetic field B_{crit}, we therefore use the following equation:

$$\omega_L^2 + A_{\text{sign}(\gamma_n)} \cdot \omega_L + s_0 s_1 (A_\perp^2 + A_\parallel^2) = 0, \tag{5.50}$$

in which $\text{sign}(\gamma_n) = \gamma_n / |\gamma_n|$. Finally, we obtain the following identity:

$$(\mathbf{n}_0 \cdot \mathbf{n}_1)^{-1} - 1 \leq \epsilon_n \Leftrightarrow B \geq B_{\text{crit}} = \frac{A_{\text{sign}(\gamma_n)} + \text{sign}(\gamma_n)\sqrt{A^2_{\text{sign}(\gamma_n)} - 4s_0 s_1 (A_\perp^2 + A_\parallel^2)}}{2\tilde{\gamma}_n}. \tag{5.51}$$

Where $A_{\text{sign}(\gamma_n)}$ is defined as:

$$A_{\text{sign}(\gamma_n)} = (s_0 + s_1)A_\parallel + \text{sign}(\gamma_n)\frac{|A_\perp|}{\sqrt{(1+\epsilon_n)^2 - 1}}. \tag{5.52}$$

To keep higher order terms at a negligible level, the first-order correction has to be limited to 10 % ($\epsilon_\tau \leq 0.1$). This can be reached for $\epsilon_n = 0.1\pi$. With this, we can express the denominator in equation (5.52) as $1/\sqrt{(1+\epsilon_n)^2 - 1} \approx 1.17$. Hence, the following theorem for the first-order approximation of the CPMG resonance times τ_r:

Theorem 4 *For a given nuclear spin with hyperfine coupling terms $A_\parallel$ and $A_\perp$, and in an external magnetic field along the z-axis with strength B, the CPMG resonances occur at:*

$$\tau^{(1)}_{2k+1} = \frac{(2k+1)\pi}{\omega_0 + \omega_1}\left(1 + \sin\left(\frac{(2k+1)\pi \cdot \omega_0}{2(\omega_0 + \omega_1)}\right)\frac{(\mathbf{n}_0 \cdot \mathbf{n}_1)^{-1} - 1}{(2k+1)\pi}\right), \tag{5.53}$$

with $k \in \mathbb{N}$. This equation is valid as long as $B \geq B_{crit}$, with:

$$B_{crit} = \frac{A_{sign(\gamma_n)} + sign(\gamma_n)\sqrt{A^2_{sign(\gamma_n)} - 4s_0 s_1 (A_\perp^2 + A_\parallel^2)}}{2\tilde{\gamma}_n}, \tag{5.54}$$

$$A_{sign(\gamma_n)} = (s_0 + s_1)A_\parallel + 1.17 \cdot sign(\gamma_n)|A_\perp|. \tag{5.55}$$

We now apply the theorem to the nuclear spin configuration identified in this work, i.e., ($A_\parallel = -23.6\,\text{kHz}$, $A_\perp = 12.2\,\text{kHz}$, $\tilde{\gamma}_n = -84.65$ kHz/G). For these parameters, we obtain a critical magnetic field strength of $B_{\text{crit}} = 60.5\,\text{G}$ with an ϵ_τ of the first resonance of $0.083 < 0.1$. Comparing the approximated value $\tau_k^{(1)}$ to the numerically solved equation (5.39), we find that the relative error is very small, $(\tau_r - \tau_k^{(1)})/\tau_r = 0.003$. This stands as a clear confirmation for the quality and validity of our first-order approximation and the criteria used to determine the minimum required magnetic field B_{crit}. Further considering the magnetic field used for the experiment in this work ($B = 81$ G), we find that the first-order approximation describes the CPMG resonance time within an error of 0.0026.

FIGURE 5.10 shows the relative error of the approximation: $((\tau_r - \tau_k^{(1)})/\tau_r)$ for varying magnetic field strengths. The horizontal line represents the maximum acceptable error threshold of 0.003, obtained with the constraint: $\epsilon_n \leq 0.1$. The vertical line represents the critical magnetic field strength (B_{crit}). Importantly, the error is below the threshold for any magnetic field exceeding B_{crit}, thus validating our theorem.

This shows that our analytic expression to determine the resonance times of decoupling sequences can be applied even in low magnetic field conditions in which $|\omega_L| \sim |A_\perp|$, unlike the zero-order term τ_{2k+1}.

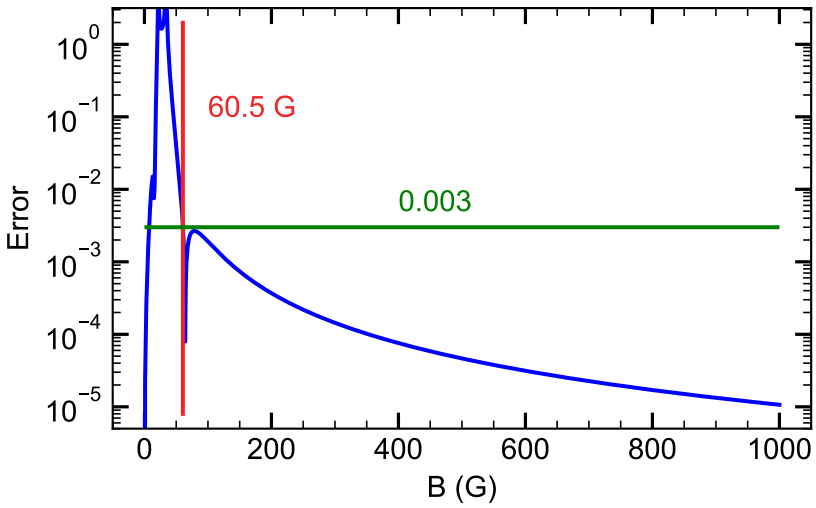

Figure 5.10: **Error in the CPMG resonance times.** Relative error between the approximated resonance time $\tau_k^{(1)}$ and the numerical solution of equation (5.39). The red line represents the critical magnetic field from which on the error is always below the defined threshold value (represented by the green line).

In summary, in this section we have derivated a refined solution to the CPMG resonances, corresponding to anti-parallel electron-spin-dependent rotations of the nuclear spin states, as well as its application range. The conditional rotations applied on the nuclear spin at the resonances, will be studied in the next section.

5.3.3 Conditional rotations

FIGURE 5.11**a** displays the inner product of $\mathbf{n}_{D_0}$ and $\mathbf{n}_{D_1}$ for the system studied experimentally (N_1 nucleus at $B = 81$ G) with the resonance times ($\tau_{2k+1}^{(1)}$) marked by the arrows. These times fit the dips observed in FIGURE 5.8, and correspond to anti-parallel rotations ($\mathbf{n}_{D_0} \cdot \mathbf{n}_{D_1} = -1$), as expected. FIGURE 5.11**b** shows the x component of each vector, at the resonances the rotations axes are along the x-axis ($|n_x| \sim 1$) with opposite direction. A Bloch sphere representation of the electron-spin-control dynamics of the nuclear spin is then as described prior in FIGURE 5.6**b**. From an analysis of the graphs given in FIGURE 5.11, it also seems that exactly in the middle of two resonances, the rotations are parallel and along the x-axis, this property will be investigated in section 5.4.1.

We will now demonstrate formally that indeed, at the resonances, the rotation vectors ($\mathbf{n}_{D_i}$) are along the x-axis. As previously mentioned, we only need to study the case $N = 2$, as the operators $\hat{U}_i(\tau)$ for $N = 2k$ share the same rotation axis. To simplify the equation's expressions in the different proofs, we introduce the following notation:

$$C_i = \cos(\theta_i/2), S_i = \sin(\theta_i/2) \text{ for } i \in \{0, 1, \hat{U}, \hat{V}, D_0, D_1\}. \tag{5.56}$$

We will assume, to reduce the calculation complexity, that the first-order correction

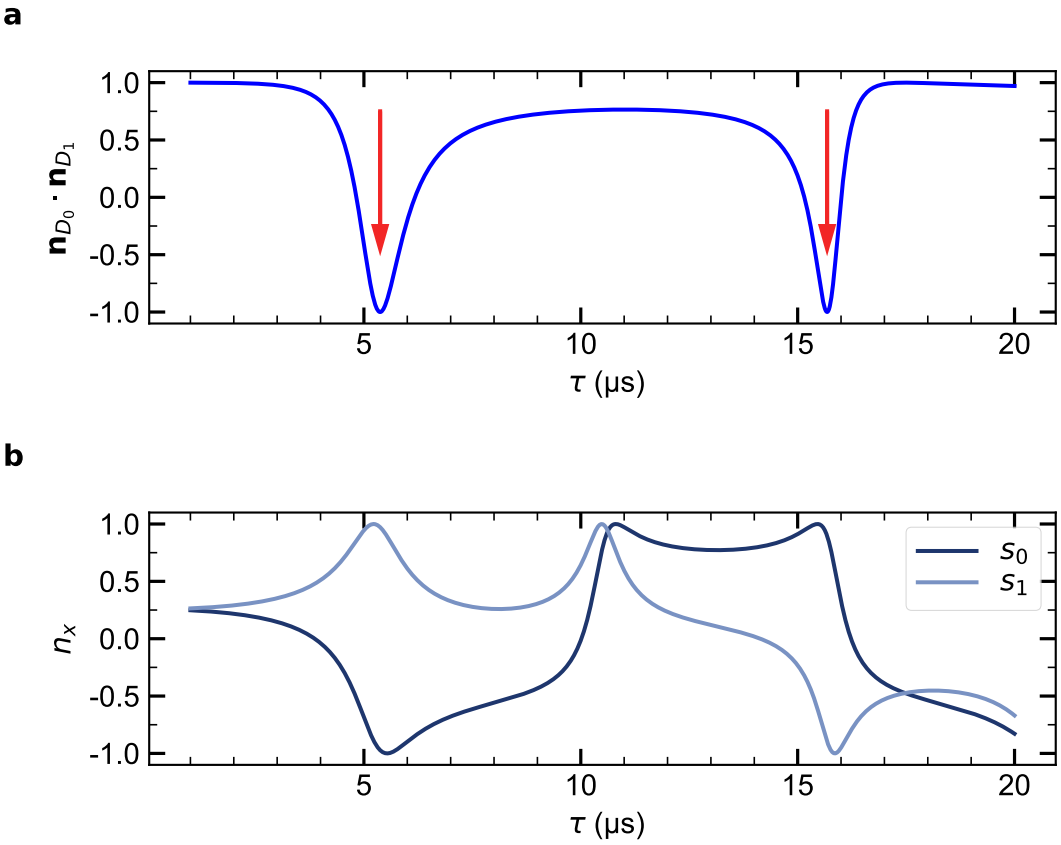

Figure 5.11: **Simulations of rotation axes. a** The inner product $\mathbf{n}_{D_0} \cdot \mathbf{n}_{D_1}$ of the two rotation axes defining the evolution of a full spin sequence. The resonances (antiparallel axes, $\mathbf{n}_{D_0} \cdot \mathbf{n}_{D_1} = -1$) are indicated with red arrows. **b** The x components of the vectors $\mathbf{n}_{D_i}$ of the rotation axis when the electron spin is initialized in the state $|s_i\rangle$. The dark (light) blue curve corresponds to the case $|s_0\rangle$ ($|s_1\rangle$). At the resonances and exactly in the middle of two resonances, the x components are nearly one indicating rotations around the x axis.

can be neglected, i.e: $(\mathbf{n}_0 \cdot \mathbf{n}_1)^{-1} - 1 \ll 1$, such as: $\tau_r \sim \tau^{(1)}_{2k+1} \sim \tau_{2k+1}$. This corresponds to the strong magnetic field regime, but as we will see, the conclusions will also hold for lower magnetic field strength. Using the equation (5.41), we have in this approximation the rotations $\hat{U}$ and $\hat{V}$ described by:

$$C_{\hat{U}} = C_{\hat{V}} = (-1)^k S_0 C_0 (1 - \mathbf{n}_0 \cdot \mathbf{n}_1), \tag{5.57}$$

$$S_{\hat{U},\hat{V}} \mathbf{n}_{\hat{U},\hat{V}} = (-1)^k [(S_0^2 \mathbf{n}_0 + C_0^2 \mathbf{n}_1) \pm C_0 S_0 (\mathbf{n}_0 \times \mathbf{n}_1)]. \tag{5.58}$$

We can deduce from equation (5.58) that $\mathbf{n}_{\hat{U}} \times \mathbf{n}_{\hat{U}} \neq 0$ condition sine qua non to obtain the theorem 3 (see section 5.3.1). Utilizing the equations (5.25-5.26) and the identity:

$$|\mathbf{n}_0 \times \mathbf{n}_1|^2 = 1 - (\mathbf{n}_0 \cdot \mathbf{n}_1)^2, \tag{5.59}$$

we can derivate the full rotation $\hat{U}_{D_i}$, for $N = 2$,

$$C_{D_0} = C_{D_1} = -1 + 4S_0^2C_0^2(1 - \mathbf{n}_0 \cdot \mathbf{n}_1), \tag{5.60}$$

$$\begin{aligned} S_{D_{0,1}}\mathbf{n}_{D_{0,1}} = 2C_0S_0[&(1 - \mathbf{n}_0 \cdot \mathbf{n}_1)(S_0^2\mathbf{n}_0 + C_0^2\mathbf{n}_1) \\ &\pm (\mathbf{n}_0 \times \mathbf{n}_1) \times (S_0^2\mathbf{n}_0 + C_0^2\mathbf{n}_1)]. \end{aligned} \tag{5.61}$$

The first equation proves that both angles θ_{D_i} are the same. To simplify the expression of the second equation, we can define ϕ as the angle between $\mathbf{n}_0$ and $\mathbf{n}_1$ such as, by definition of the inner and vector products, we have: $\mathbf{n}_0 \cdot \mathbf{n}_1 = \cos(\phi)$ and $|\mathbf{n}_0 \times \mathbf{n}_1| = |\sin(\phi)|$. We are in the small angle regime ($\mathbf{n}_0 \cdot \mathbf{n}_1 \sim 1$) such that $|\mathbf{n}_0 \times \mathbf{n}_1| = \phi$ and $\mathbf{n}_0 \cdot \mathbf{n}_1 = 1 - \phi^2/2 = 1 - |\mathbf{n}_0 \times \mathbf{n}_1|^2/2$. The contributions of each term in equation (5.61) can now be compared:

$$\frac{|(1 - \mathbf{n}_0 \cdot \mathbf{n}_1)(S_0^2\,\mathbf{n}_0 + C_0^2\,\mathbf{n}_1)|^2}{|(\mathbf{n}_0 \times \mathbf{n}_1) \times (S_0^2\,\mathbf{n}_0 + C_0^2\,\mathbf{n}_1)|^2} \propto |\mathbf{n}_0 \times \mathbf{n}_1]^2. \tag{5.62}$$

As $|\mathbf{n}_0 \times \mathbf{n}_1|^2 \ll 1$, the first term in the equation (5.61) can then be neglected in front of the second, i.e:

$$S_{D_{0,1}}\mathbf{n}_{D_{0,1}} = \pm 2\,C_0\,S_0 \cdot (\mathbf{n}_0 \times \mathbf{n}_1) \times (S_0^2\,\mathbf{n}_0 + C_0^2\,\mathbf{n}_1). \tag{5.63}$$

Two observations can be done. First of all, $\mathbf{n}_{D_0}$ and $\mathbf{n}_{D_1}$ are indeed anti-parallel, confirming our theorem 4. Second of all, as by definition, $\mathbf{n}_0$ and $\mathbf{n}_1$ lie in the plane (X,Z), then $\mathbf{n}_0 \times \mathbf{n}_1$ is along the y-axis, and as the main components of $\mathbf{n}_i$ are along the z-axis (in the same direction) for strong magnetic fields, then we have $(\mathbf{n}_0 \times \mathbf{n}_1) \times (S_0^2\,\mathbf{n}_0 + C_0^2\,\mathbf{n}_1) \propto \mathbf{e}_x$. We can then conclude:

Theorem 5 *For strong magnetic field ($A_\perp \ll \omega_L$), during the decoupling sequence $(\tau - \pi - \tau)^N$ at the waiting time $\tau = \tau^{(1)}_{2k+1}$, the nuclear spin undergoes a rotation around the x-axis in a direction conditioned by the initial electron spin state $|s_i\rangle$. Furthermore, the angle of rotation is the same for both cases. For $N = 2$, we have the angles (θ_{D_i}) and axes of rotations ($\mathbf{n}_{D_i}$) given by:*

$$\begin{aligned} C_{D_0} = C_{D_1} &= -1 + 4S_0^2C_0^2(1 - \mathbf{n}_0 \cdot \mathbf{n}_1), \\ S_{D_{0,1}}\mathbf{n}_{D_{0,1}} &= \pm 2\,C_0\,S_0 \cdot (\mathbf{n}_0 \times \mathbf{n}_1) \times (S_0^2\,\mathbf{n}_0 + C_0^2\,\mathbf{n}_1). \end{aligned}$$

Experimentally, the control of the nuclear spin rotation is demonstrated by varying the number N of refocusing pulses at the calculated resonant time: $\tau_{\text{CPMG}} = \tau_0^{(1)} = 5.38$ µs. The uncorrected raw data, shown in FIGURE 5.12, reveal that the electron spin signal is modulated due to electron spin-controlled nuclear spin rotations with near-unity fringe contrast, in excellent accord with the simulated signal with no free parameters (red curve).

From our simulation, we find that the rotation axes and rotation angles for the operators $\hat{U}$ and $\hat{V}$ are:

$$\mathbf{n}_{\hat{U}} \approx \sqrt{0.943} \cdot \mathbf{e_x} + \sqrt{0.057} \cdot \mathbf{e_z}, \tag{5.64}$$

$$\mathbf{n}_{\hat{V}} \approx \sqrt{0.941} \cdot \mathbf{e_x} - \sqrt{0.059} \cdot \mathbf{e_z}, \tag{5.65}$$

$$\theta_{\hat{U}} = \theta_{\hat{V}} \approx 0.49 \cdot \pi. \tag{5.66}$$

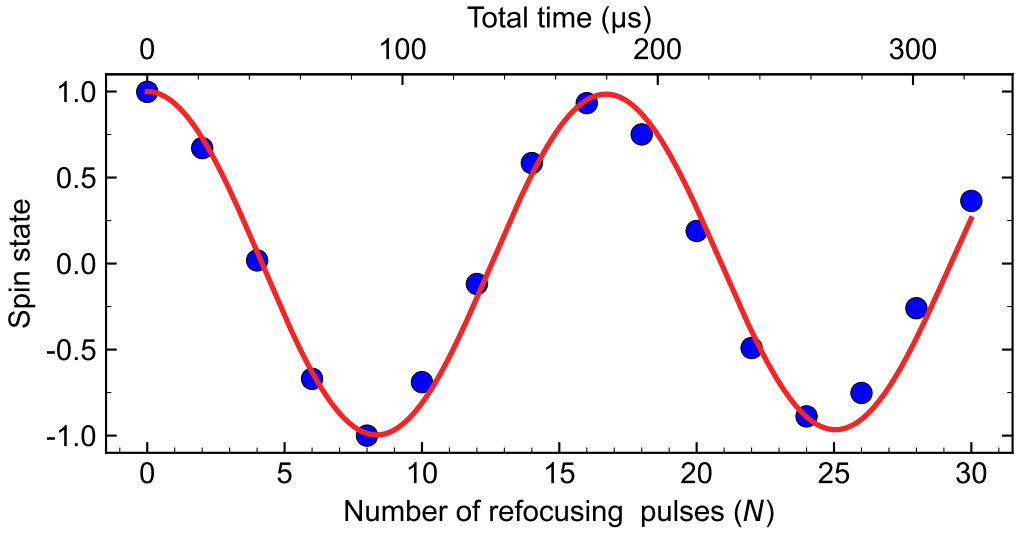

Figure 5.12: **CPMG spin signal for a fix waiting time.** Electron-spin signal for different number N of refocusing pulses at $\tau_{\mathrm{CPMG}} = 5.38$ µs. Strong oscillations stem from electron spin-dependent rotations of N_1. Blue dots are uncorrected raw data. The red curve is a simulation based on the two nuclear spins (N_1 and N_2) without any free parameters. The spin state $+1$ corresponds to $m_s = 3/2$ and -1 to $m_s = 1/2$.

Therefore:

- The rotation axes are essentially perfectly anti-parallel: $\mathbf{n}_{\hat{U}} \cdot \mathbf{n}_{\hat{V}} = -0.999994$.
- The axis of rotation are (almost entirely) oriented along the $\mathbf{e_x}$ axis.
- The rotation angles are the same.

The first point confirms the theorem 4, and the two last the theorem 5, which seems to hold even for low magnetic fields ($\omega_L \sim A$). The Bloch spheres in FIGURE 5.13, visualize the electron spin-dependent rotations of the first nucleus for the interesting number of refocusing pulses, $N = 4, 8, 16$. The net result, for $N = 4$, is an opposite rotation around the x-axis, which can be used to implement an entangling Hadamard gate. By increasing the number of refocusing pulses, we can rotate the nucleus further to implement additional gates: for $N = 8$ we are perfoming a σ_x-gate and the identity operation for $N = 16$. The latest is effectively keeping the system unchanged over time, and protecting the electron-nuclear state from any interactions.

We can simulate the fidelity of the three gates. To do so, we initialize the bipartite system in one of the four spin-eigenstates and simulate the spin state $|\Psi_f\rangle$ at the end of the sequence. We then calculate the overlap with the target spin-state as $\mathcal{F} = |\langle \Psi_{\mathrm{target}} | \Psi_f \rangle|^2$, and obtain the following fidelities:

- For $N = 4$, the fidelity for the creation of the Bell state $\left|\Phi_{\mathrm{i}}^{\pm}\right\rangle$ and $\left|\Psi_{\mathrm{i}}^{\pm}\right\rangle$ is $\mathcal{F} = 97\%\cdot$.
- For $N = 8$, the fidelity for performing the σ_x-gate on the nuclear spin is $\mathcal{F} = 94\%\cdot$.

- For $N = 16$, the fidelity for performing the identity-gate on the bipartite system is $\mathcal{F} = 99\%$·.

These high fidelities are due to the fast implementation of gates using only a small number of refocusing pulses for which electron spin decoherence is negligible, as well as the magnetic field strength optimization to reach a rotation angle of $\pi/2$ for $N = 4$. In this sense, the small signal decrease in FIGURE 5.12 for high pulse numbers ($N > 20$) is not associated with the electron spin decoherence. The signal decrease stems from a minimal remaining spin-dependent rotation of the second nuclear spin (N_2), which can be suppressed with stronger external magnetic fields [22, 79], or other manipulation protocols utilizing extra rf-driving to target a single nuclear spin [24, 251, 252]. The high-quality of our results underline that waveguide-integrated V2 centers can be used for controlling the nuclear spin state with a high fidelities at convenient cryogenic temperatures ($T = 10$ K).

So far, only conditional rotations have been demonstrated, yet to reach an universal set of quantum gates for a two-qubit system, more operations need to be achieved by the bipartite system. In the next section, unconditional control of the nuclear spin state through decoupling sequence will be studied.

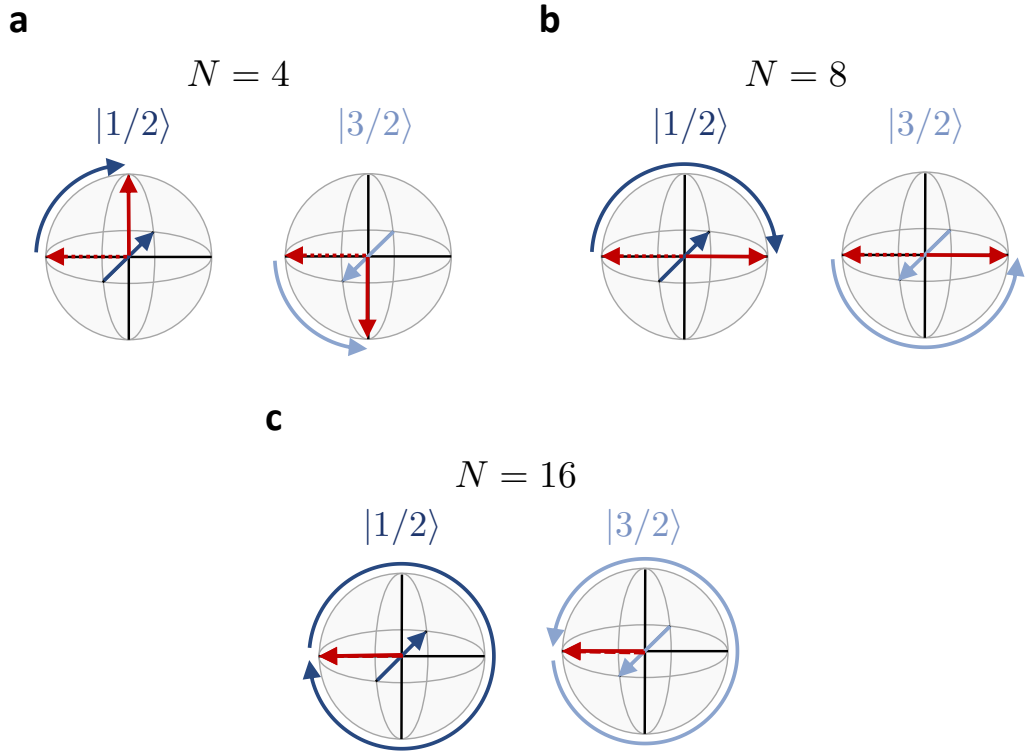

Figure 5.13: **Dynamics for a varying number of refocusing pulses.** Bloch sphere representation displaying the dynamics of the nuclear spin during the N-pulse CPMG-sequence for $\tau = \tau_0^{(1)}$ shown in FIGURE 5.12, while the electron spin state is initialized either in the state $|1/2\rangle$ or $|3/2\rangle$. The red dashed (solid) arrow corresponds to the initial (final) state of the nuclear spin. The blue line represents the axis of rotations. **a**, **b** and **c** correspond to 4, 8, and 16 refocusing pulses respectively.

5.4 Implementation of two-qubit gates

As stated prior, by investigating the FIGURE 5.11 we see that exactly in the middle of two resonances of the decoupling sequence ($\tau_2^{(1)} \sim 10$ µs), the axes of the rotations $\hat{U}_{D_i}$ seems to be parallel and along the x-axis. However, this presupposed rule is not perfect as the peaks of the x component in FIGURE 5.11**b** are not at the same position. In FIGURE 5.14, we plotted the x and z components of the vectors $\mathbf{n}_{D_i}$, as well as the inner product between them, for stronger magnetic field ($B = 175$ G), such as $A_\perp \ll \omega_L$ ($\mathbf{n}_0 \cdot \mathbf{n}_1 - 1 \ll 1$).

At the same time as the resonances get sharper as the magnetic field increases, the axes get more parallel ($\mathbf{n}_{D_0} \cdot \mathbf{n}_{D_1} \sim 1$) in between the resonances. Even if for most of the waiting times τ the rotations are along the z-axis, exactly in the middle of two resonances ($\tau = \tau_{2k}$) the rotations are along the x-axis. These characteristics would allow performing unconditional rotations around both x and z axis. In the next subsection, we will rigorously demonstrate the first statement.

5.4.1 Unconditional X rotation

Let's investigate the rotations $\hat{U}_{D_i}$ at the times $\tau = \tau_{2k} = 2k\pi/(\omega_0 + \omega_1)$, at which we have:

$$C_1 = (-1)^k C_0 \text{ and } S_1 = (-1)^{k+1} S_0. \tag{5.67}$$

With C_i and S_i described in equation (5.56). We can simplify the expression of the rotations $\hat{U}$ and $\hat{V}$ in:

$$C_{\hat{U}} = C_{\hat{V}} = (-1)^k [1 - s_0^2(1 - \mathbf{n}_0 \cdot \mathbf{n}_1)], , \tag{5.68}$$

$$S_{\hat{U},\hat{V}} \mathbf{n}_{\hat{U},\hat{V}} = (-1)^k S_0 [C_0(\mathbf{n}_0 - \mathbf{n}_1) \mp S_0(\mathbf{n}_0 \times \mathbf{n}_1)]. \tag{5.69}$$

Using the rules of composition of rotations (5.25-5.26) and equation (5.59), the full rotations $\hat{U}_{D_i}$ can be expressed as:

$$C_{D_0} = C_{D_1} = (1 - 2s_0^2)^2 + 4C_0^2 S_0^2 (\mathbf{n}_0 \cdot \mathbf{n}_1), \tag{5.70}$$

$$\begin{aligned} S_{D_{0,1}} \mathbf{n}_{D_{0,1}} = 2C_0 S_0 [&(1 + S_0^2(\mathbf{n}_0 \cdot \mathbf{n}_1 - 1))(\mathbf{n}_0 - \mathbf{n}_1) \\ &\mp 2S_0^2 (\mathbf{n}_0 - \mathbf{n}_1) \times (\mathbf{n}_0 \times \mathbf{n}_1)]. \end{aligned} \tag{5.71}$$

Assuming a strong magnetic field, we have $1 - (\mathbf{n}_0 \cdot \mathbf{n}_1) \ll 1$ as well as $|\mathbf{n}_0 \times \mathbf{n}_1|^2 \ll 1$, i.e the latest equation can be simplified in:

$$S_{D_{0,1}} \mathbf{n}_{D_{0,1}} = 2C_0 S_0 (\mathbf{n}_0 - \mathbf{n}_1). \tag{5.72}$$

As $\mathbf{n}_{D_0} = \mathbf{n}_{D_1}$, the rotations are indeed parallel. Furthermore, the vectors $\mathbf{n}_i$ lie in the plane (X, Z) so does the vector $\mathbf{n} = \mathbf{n}_0 - \mathbf{n}_1$. We can compare the norm of both x and z components of the vector $\mathbf{n}$, to know along which axis $\mathbf{n}$ preferentially is:

$$\left| \frac{n_x}{n_z} \right| = \left| \frac{A_\perp (s_0\omega_1 - s_1\omega_0)}{A_\parallel (s_0\omega_1 - s_1\omega_0) - \omega_L(\omega_1 - \omega_0)} \right|. \tag{5.73}$$

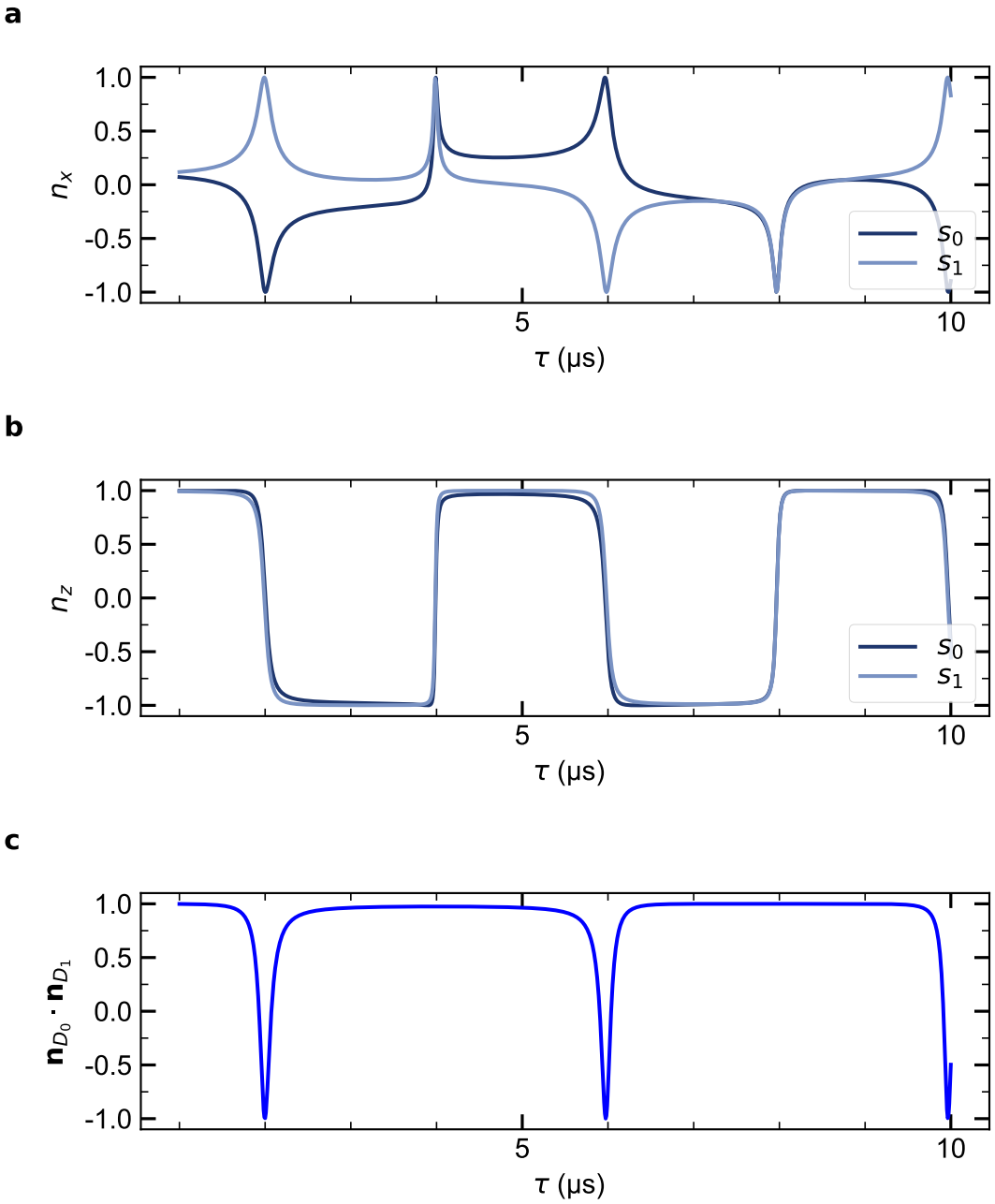

Figure 5.14: **Simulations of rotation axes for strong magnetic field ($B =$ 175 G). a** (**b**) The x (z) component of the vectors $\mathbf{n}_{D_i}$ when the electron spin is initialized in the state $|s_i\rangle$. The dark and light blue curves correspond respectively to the case $|s_0\rangle$ and $|s_1\rangle$. **c** The inner product of $\mathbf{n}_{D_0} \cdot \mathbf{n}_{D_1}$ of the two rotation axis indicates if the rotations are unconditional (parallel axes, $\mathbf{n}_{D_0} \cdot \mathbf{n}_{D_1} = 1$) or conditional (anti-parallel axes, $\mathbf{n}_{D_0} \cdot \mathbf{n}_{D_1} = -1$).

To simplify the expression of $\frac{n_x}{n_z}$, we can Taylor expand the pulsations ω_i:

$$\begin{aligned}\omega_i &= (s_i A_\parallel - \omega_L)\Big(1 + \frac{s_i^2 A_\perp^2}{2(s_i A_\parallel - \omega_L)^2}\Big) + o((\omega_L)^{-1}),\\ \omega_i &= -\omega_L + s_i A_\parallel - \frac{s_i^2 A_\perp^2}{2\,\omega_L} + o((\omega_L)^{-1}).\end{aligned} \tag{5.74}$$

Therefore we have the following identities (with $s_1 = s_0 + 1$):

$$\omega_1 - \omega_0 = A_\parallel - \frac{(s_1^2 - s_0^2)A_\perp^2}{2\,\omega_L}, \tag{5.75}$$

$$s_0\omega_1 - s_1\omega_0 = \omega_L + \frac{s_0 s_1 A_\perp^2}{2\,\omega_L}. \tag{5.76}$$

Using these expressions in the ratio n_x/n_z, obtained in equation (5.73), we have:

$$\Big|\frac{n_x}{n_z}\Big| = \Big|\frac{2\,\omega_L A_\perp + (s_0 s_1)A_\perp^3}{(s_1^2 - s_0^2)A_\perp^2 + \frac{s_0 s_1 A_\perp^2 A_\parallel}{\omega_L}}\Big| \sim \Big|\frac{2\,\omega_L}{(s_1^2 - s_0^2)A_\perp}\Big|. \tag{5.77}$$

As we are in the approximation $A_\perp \ll \omega_L$, we obtain $\frac{n_x}{n_z} \gg 1$. In other words the vector $\mathbf{n}_0 - \mathbf{n}_1$ is mainly along the x-axis.

Theorem 6 *For strong magnetic field ($A_\perp \ll \omega_L$), during the decoupling sequence $(\tau - \pi - \tau)^N$ at the waiting time τ_{2k}, the nuclear spin undergoes a* ***unconditional*** *rotation around the x-axis. For $N = 2$, we have the angle $\theta_{D_0} = \theta_{D_1} = \theta_D$ and axis of rotation $\mathbf{n}_{D_0} = \mathbf{n}_{D_1} = \mathbf{n}_D$ given by:*

$$\begin{aligned}\cos\Big(\frac{\theta_D}{2}\Big) &= (1 - 2\sin^2(\frac{\omega_0\tau_{2k}}{2}))^2 + 4\cos^2(\frac{\omega_0\tau_{2k}}{2})\sin^2(\frac{\omega_0\tau_{2k}}{2})(\mathbf{n}_0 \cdot \mathbf{n}_1),\\ \sin\Big(\frac{\theta_D}{2}\Big)\mathbf{n}_D &= 2\cos\Big(\frac{\omega_0\tau_{2k}}{2}\Big)\sin\Big(\frac{\omega_0\tau_{2k}}{2}\Big)(\mathbf{n}_0 - \mathbf{n}_1).\end{aligned}$$

In summary, we can perform unconditional x-rotations onto the nuclear spin without the need for high power rf-driving. Notably, from the equation (5.77), if $s_1 = -s_0 = -1/2$ then the ratio n_x/n_z would be in the order of $(\omega_L/A_\perp)^2$, such that the axis of rotations would have a stronger overlap with the x-axis. As seen in FIGURE 5.14, we can also perform unconditional z-rotations for half-integer waiting times: $\tau_{k+1/2}$. Utilizing the conditional and unconditional rotations, we will now describe how to implement some of the most useful single and two-qubit gates for quantum information processing.

5.4.2 CNOT gates

The purpose of the decoupling sequence is to manipulate the nuclear spin and create one and two-qubit gates. For a V_{Si} center coupled to a ^{29}Si, we define the qubits as: $|0\rangle_e = |1/2\rangle_e$, $|1\rangle_e = |3/2\rangle_e$ and $|0\rangle_n = |\downarrow\rangle_n$, $|1\rangle_n = |\uparrow\rangle_n$.

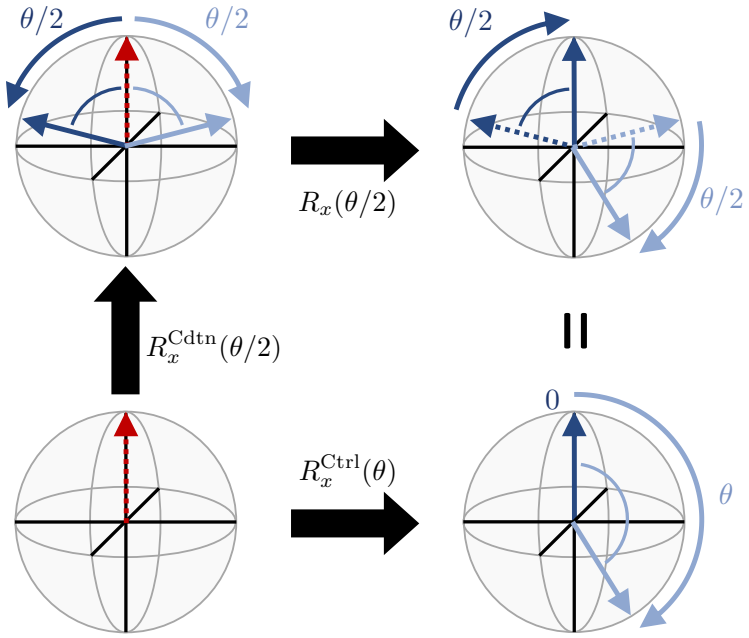

Figure 5.15: **Realization of electron spin-control x-rotation.** Depiction of the identity given in equation (5.78) for the nuclear spin initialized in the state $|\uparrow\rangle$. The dark (light) blue arrow is the result of the operations if the electron spin is in the state $|s_0\rangle$ ($|s_1\rangle$). First, we apply a conditional x-rotation of an angle $\theta/2$, then an unconditional x-rotation of the same angle. The rotations are obtained for odd and even resonant times respectively. Therefore if the electron spin is in the state $|s_1\rangle$ ($|s_0\rangle$) the qubit is unchanged (rotated around the x-axis by an angle θ): it is a control x-rotation of an angle θ. The CNOT gate is achieved for $\theta = \pi$.

Using mw-driving and optical pulses we can deterministically initialize and coherently drive the electron spin and create any 1-qubit gate. As seen previously, we can utilize the waiting times τ_{2k} and $\tau_{k+1/2}$ of the decoupling sequence to perform unconditional rotations along the x ($R_x(\theta)$) and z ($R_z(\theta)$) axis. The first set of rotations allows to implement the Hadamard and σ_x gates, the second set, as we will see later, will be required to initialize the nuclear spin state. However, another important gate to be able to perform on any two-qubit system is the CNOT gate:

It is a qubit spin-flip controlled by the second qubit state. As depicted in FIGURE 5.15, by simply composing a conditional rotation ($R_x^{\mathrm{Cdtn}}(\theta/2)$) of an angle $\theta/2$ reached for the odd waiting times (τ_{2k+1}) and an unconditional rotation ($R_x(\theta/2)$) of the same angle reached for the even waiting times ($\tau_{2k'}$), we can obtain an electron-control x-rotation of an angle θ ($R_x^{\mathrm{Ctrl}}(\theta)$) i.e:

$$R_x^{\mathrm{Ctrl}}(\theta) = R_x(\theta/2) \cdot R_x^{\mathrm{Cdtn}}(\theta/2). \tag{5.78}$$

The nuclear CNOT gate will be obtained for $\theta = \pi$. The CNOT gate applied on the electron depending on the nuclear spin state cannot be achieved by simply using CPMG-sequences. However, using the gate identity:

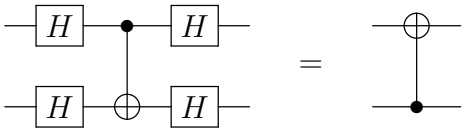

A nuclear-control NOT gate can be achieved on the electron using four Hadamard gates, two on each spins, and a CNOT gate on the nuclear spin, which have all been described previously. Building on this knowledge, we can initialize the nuclear spin state by initializing the electron spin and transferring its state to the nuclear spin via a 2-CNOT-gate protocol:

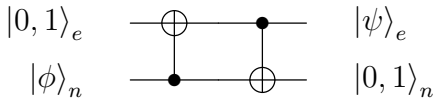

This would correspond to the series of rotations:

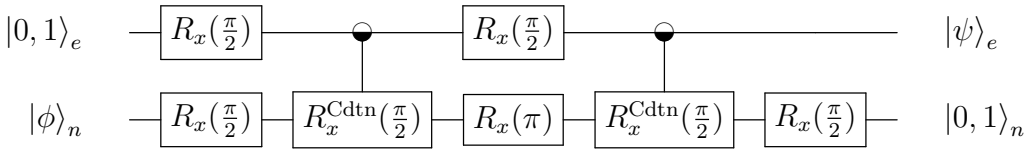

Where the half-filled controls are conditional gates. Here, it corresponds to opposite x-rotation on the nuclear spin according to the electron spin state. However, following the work presented in [67], we can rearrange the circuit in:

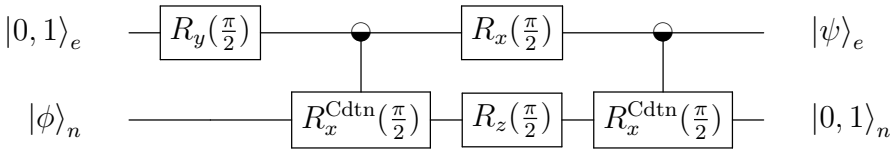

With the ensemble of gates at our disposal and the ability to initialize both electron and nuclear spins states, we are now able to implement various two-qubit quantum protocols: single-shot readout (SSR), quantum Fourier transform, quantum error correction, etc... As a way to showcase the strength and usefulness of nuclear spin based protocols, we will explain how to achieve SSR.

5.5 Single-shot readout

Being able to deterministically read the electron spin state in every recurrence of an experimental protocol is crucial for any quantum technologies [143], especially for quantum information processing based on Bell-state measurements [13, 145]. For our system (V_{Si}) no SSR is within reach: the lack of highly cycling optical transitions, due to the strong coupling of the excited states with the ISC limits the number of emitted photons at each spin readout before the loss of the electron spin-information. As stated

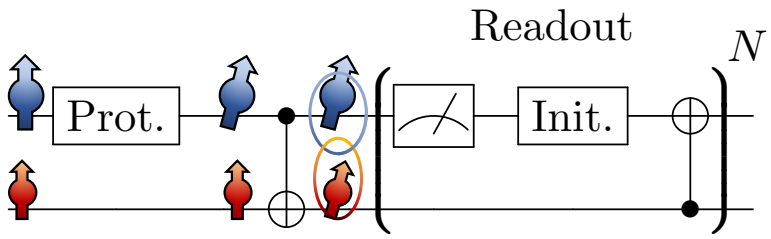

Figure 5.16: **Single-shot readout protocol.** Sketch of the protocol for achieving SSR of the electron spin state. Description in the text.

in Chapter 2, the integration of the V2 center in a cavity is a sine qua non condition to unfold the full potential of solid-states color centers by increasing the number of emitted photons in a single readout via Purcell enhancement at the same time as the coupling efficiency to the detection path. However, the resulting optical line broadening should not exceed the intrinsic line-splitting of 1 GHz, limiting the emission rate improvement. Using the nuclear spin as an ancilla qubit could help mitigate the absence of SSR. The protocol to read out the electron spin state $|\Psi\rangle_e = a\,|s_0\rangle_e + b\,|s_1\rangle_e$ after a given protocol, is show in FIGURE 5.16, and is as follow:

- The nuclear spin is initialized in the state $|\uparrow\rangle$ prior to the protocol and entangled with the electron spin at the end of the protocol using a CNOT gate: $|\Phi\rangle = a\,|s_0\rangle_e\,|\uparrow\rangle_n + b\,|s_1\rangle_e\,|\downarrow\rangle_n$.
- The electron spin is readout optically, projecting the nuclear spin state in either $|\uparrow\rangle_n$ or $|\downarrow\rangle_n$ according to the measurement outcome while the electron spin state information is lost via transit through the metastable states' manifold.
- The nuclear spin state is then repeatedly (classically) copied to the reinitialized electron spin.

Repeating the readout increases the photon statistics, aiming toward spin-dependent average counts separated by three standard deviations. Yet, the protocol can not be repeated indefinitely, it is bounded by the relaxation time (T_1) of the nuclear spin. For bulk V_{Si} center, on average 0.010 (0.001) photons are measured when the spin system is in the state $|1/2\rangle$ ($|3/2\rangle$) and resonantly excited along the A_1 transition. Then, at least 1 000 repetitions are required to obtain a SSR of the electron spin state. For the NV-center in diamond, this protocol has been successfully demonstrated at room-temperature with 2 000 repetitions [68]. As all gates needed are achievable for the V_{Si} center in SiC, we are confident in the possibility to implement such a SSR protocol. However, preliminary investigations should be conducted, for example, the mixing of the nuclear spin state happening while the electron spin is in the ISC could limit the number of repetitions.

One could also note the possibility to achieve SSR of the electron spin states via spin-to-charge conversion: mapping the spin state to the charge state of the V_{Si} center using resonant laser pulses combined with an ionization laser [110, 207, 253, 254].

5.6 Conclusion and outlook

To scale-up quantum networks, nuclear spin quantum memories and processors represent a critical technology [17]. In this chapter, we have studied the system formed by a nuclear spin weakly coupled to an arbitrary electron spin in a weak magnetic field. We looked at how to utilize pulse-sequences on the electron spin to deterministically manipulate the nuclear spin state, via three types of resonances. The two-qubit set of gates toolset presented allowed us to describe a protocol to reach SSR.

Capitalizing on our refine model, we have experimentally demonstrated the coupling of a waveguide-integrated defect to two nearby nuclear spins. It also allowed us to opitimize the magnetic field to coherently manipulate, with a high fidelity, a single nuclear spin via decoupling sequences at cryogenic temperature without any heating issue. In future work, the amount of controllable nuclear spins can be directly scaled up in isotopically engineered samples [79]. For a higher number of nuclear spins, more complex protocols could be investigated to target single nuclear spins from the spin bath [27, 249, 251].

Chapter 6

Phase estimation via squeezed states of light

In this chapter, we will study a novel interferometry scheme utilizing squeezed states of light [73] combining the stability of a classical interferometer and the sensitivity enhancement of a non-linear interferometer Capitalizing on previous scientific projects I participated in, I provided a theoretical description of the measurement scheme developed by MSc Raphael Nold.

As this experiment doesn't concern spins in the solid, we will begin this chapter with a brief introduction of the framework of phase sensing via optical interferometry. Even though the scheme utilizes non-linear (NL) components, we will be able to comprehend the novel aspects of the measurement scheme by giving a simplified theoretical model based on the Fock space representation. A more complete description will then be given, utilizing the Heisenberg picture, allowing us to study the loss-dependent interferometric signal and noise at any squeezing strength. Finally, our theoretical results will be confronted with the experimental results comparing the novel scheme operating at a low photon flux to a state-of-the-art Michelson interferometer. From the fringe visibilities measured at each detector, our model will perfectly predict the phase sensitivity enhancement observed. Building on our findings, we will explore the potential offered by the experimental scheme and demonstrate even greater robustness to losses as the squeezing parameter increases.

6.1 Optical interferometry

Optical interferometry represents the gold-standard for measuring phase differences between two optical paths: spatial displacement, refractive indices or surface properties. A sketch of a typical Michelson interferometer is shown in FIGURE 6.1**a**, where the phase sensitivity is given by the shot-noise limit (SNL) [255, 256]:

$$\Delta\Phi_{\mathrm{SNL}} = \frac{1}{\sqrt{N}}, \tag{6.1}$$

where N is the number of independently measured photons (uncorrelated). Quantum schemes can improve on this classical limit, using N correlated photons (N00N-

state) [257] resulting in a single measurement event leading to a phase sensitivity of:

$$\Delta\Phi_{\mathrm{HL}} = \frac{1}{N}, \tag{6.2}$$

called the Heisenberg limit, the ultimate sensitivity limit[1] [255, 256]. However, reaching such sensitivity experimentally using N00N-state requires photon number resolving detectors, which are slow with low optical saturation [258]. Squeezed states of light are another set of interesting non-classical states for quantum metrology [73], allowing a phase sensitivity beyond the SNL. Yet, their coherences exponentially decrease with losses in the optical paths, rendering them complex to manipulate. Limitations which can be overcome in SU(1,1) interferometer arrangements [259, 260], but these schemes are prone to common mode noise (pump laser power fluctuations), which compromises phase sensitivity and reliability [261].

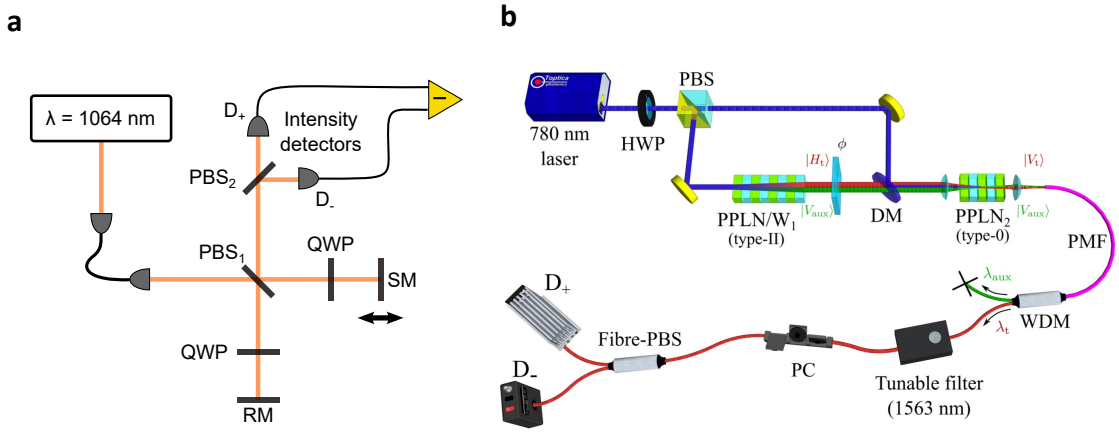

Figure 6.1: **Optical interferometer.** **a** Classical Michelson interferometer. PBS: Polarization beam-splitter. QWP: Quarter-wave plate. RM/SM: reference/sample mirror. D: Detector. **b** Experimental setup used in [83], it resembles a Mach-Zehnder interferometer, with NL crystals (PPLN) in one of the interferometer arms and at the output path. A refined measurement scheme, FIGURE 6.2**a** will be explained in more details in section 6.2.

In [83] a novel approach was proposed where a two-photon phase contribution was projected onto a single-photon state resulting in super-resolution: twice the number of interference fringes for the same phase shift compared to a classical interferometer. This was achieved by overlapping a two-photon-pair contribution created in one path of an interferometer with a second one created after the interferometer, see FIGURE 6.1**a**. In this scientific publication, I built the theoretical framework linking the interferometer losses to the visibility of the fringes. The scheme was further improved, using the polarization of the photon-pair contribution to achieve phase sensitivity beyond the SNL. In the next section, we will explain how this was accomplished.

[1] In the quantum realm as we know it.

6.2 Novel scheme

The interferometer studied is depicted FIGURE 6.2**a** and resembles a Mach-Zehnder interferometer, with a coherent light source (green laser) as an input. While the input beam splitter (BS) is let unchanged, the output one is replaced by a dichroic mirror (DM), which reflects the green laser but transmits infrared photons.

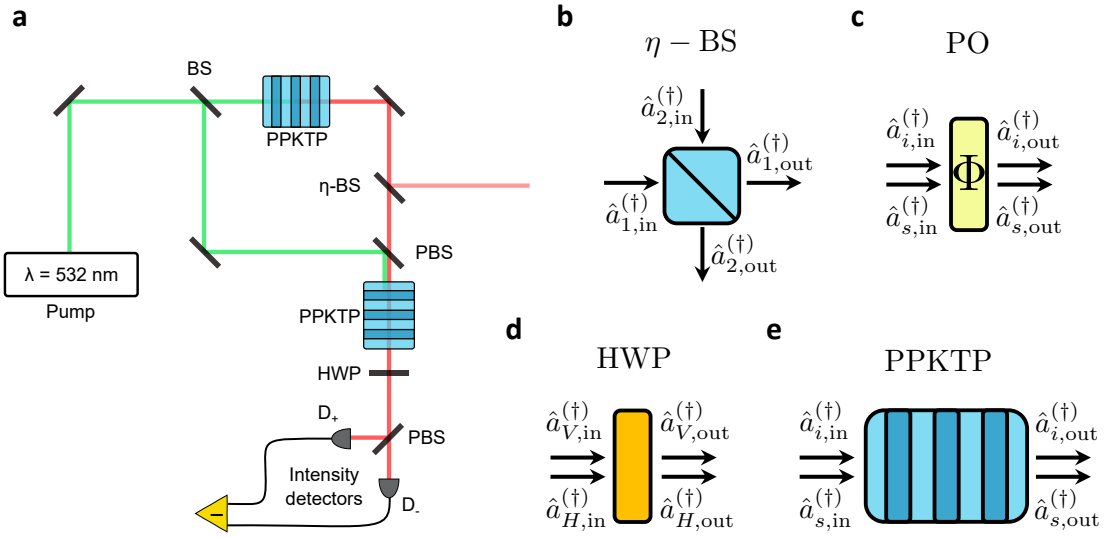

Figure 6.2: **Quantum sensor and Heisenberg picture. a** Sketch of the quantum sensor. The virtual beam-splitter (BS) of transmissivity η (η-BS) simulates losses inside the interferometer. A detailed explaination is given in the manuscript. PPKTP: NL crystal. DM: Dichroic mirror. HWP: Half-wave plate. **b-e** Creation and annihilation operators corresponding to the modes of the different optical elements. PO: Phase object.

Further, a NL crystal is placed in one of the interferometer arms, as well as at the output path of the interferometer. The first NL crystal is used to frequency convert pump laser photons, via type-0 spontaneous parametric down-conversion (SPDC), to photon-pairs:

$$|V\rangle_p \xrightarrow[\mathrm{NL}_1]{} |V\rangle_i \otimes |V\rangle_s \,, \tag{6.3}$$

V (H) corresponds to a vertically (horizontally) polarized photon, and the subscripts denote the photons mode (wavelength): pump (p, 532 nm), idler (i, 1023 nm) and signal (s, 1109 nm). The second NL crystal used type-II SPDC:

$$|V\rangle_p \xrightarrow[\mathrm{NL}_2]{} |V\rangle_i \otimes |H\rangle_s \,. \tag{6.4}$$

The remaining pump laser in the interferometer arm with the NL crystal is filtered out, and a phase difference is applied on the photon-pairs within the interferometer: $2\Phi = \Phi_i + \Phi_s$, the sum of the phases applied to each photon. Where Φ is the phase shift applied to a photon at the average energy between the idler and the signal photon.

In this section, the virtual beam splitter with transmissivity η, which simulates losses in the interferometer, will not be considered. Furthermore, we will only study the phase measurement scheme at a low photon-pair flux regime, where the probability of the occurrence of two-photon-pairs per coherence time of the laser photons is low. The signal dependency on the losses and on an arbitrary pump power regime will be studied in the section.

The pump laser from the reference arm is overlapped with the photon-pairs created in the interferometer, via a DM, and can generate another two-photon contribution through the second NL crystal. As we can consider each photon-pair contribution as distinct, and as the photons from both NL crystals are assumed indistinguishable in every aspect except polarization, after spectral filtering of the pump laser, the quantum state of the photon-pairs is:

$$\frac{|V\rangle_i \otimes |V\rangle_s + \exp(i2\,\Phi)\,|V\rangle_i \otimes |H\rangle_s}{\sqrt{2}} = |V\rangle_i \otimes \frac{|V\rangle_s + \exp(i2\Phi)\,|H\rangle_s}{\sqrt{2}}. \tag{6.5}$$

Such that the idler photon does not contain any information, and if filtered out project the two-photon phase information $(2\,\Phi)$ on a single-photon state. This phase information can be accessed via a projective measurement in the σ_x basis, using a half-waveplate (HWP) and a polarization beam splitter (PBS):

$$\frac{|V\rangle_s + \exp(i2\Phi)\,|H\rangle_s}{\sqrt{2}} \xrightarrow[\text{HWP, PBS}]{} |\Psi\rangle = \cos(\Phi)\,|H\rangle_1 + \sin(\Phi)\,|V\rangle_2\,, \tag{6.6}$$

where the $\{1, 2\}$ subscripts denote the output paths of the PBS. Subtracting the signal measured on each detector gives us:

$$S_{\mathrm{q}} = (S_1 - S_2) = (|\langle H|_1\,|\Psi\rangle\,|^2 - |\langle V|_2\,|\Psi\rangle\,|^2) = \cos(2\,\Phi). \tag{6.7}$$

On average, two photons are used per protocol and one is send through the phase object and read out. Such that, if the protocol is repeated N times, the signal would be:

$$S_{\mathrm{q}} = (S_1 - S_2) = N\cos(2\,\Phi). \tag{6.8}$$

As the N measurements are independent, the measurement noise is $\Delta S_q = \sqrt{N}$. The maximum phase sensitivity, occurring at the steepest slope of the signal, is then:

$$\Delta\Phi_{\mathrm{q}} = \frac{1}{2\sqrt{N}}. \tag{6.9}$$

We compare this sensitivity to the one achieved by classical Michelson interferometer utilizing the same number of photons $(2N)$. In this case, the interferometric signal is:

$$S_{\mathrm{c}} = 2N\cos(\Phi), \tag{6.10}$$

with a phase sensitivity shot-noise limited:

$$\Delta\Phi_{\mathrm{c}} = \Delta\Phi_{\mathrm{SNL}} = \frac{1}{\sqrt{2N}}. \tag{6.11}$$

The quantum phase estimation is then more sensitive by a factor $\sqrt{2}$:

$$f = \frac{\Delta\Phi_{\mathrm{c}}}{\Delta\Phi_{\mathrm{q}}} = \sqrt{2}. \tag{6.12}$$

The quantum scheme allows sub-shot-noise sensitivity. Furthermore, the quantum signal is twice as fast (super-resolution [83]) with half the intensity (as only half as many photons are measured). However, as this interferometer used NL source of light, the sensitivity might degrade rapidly with losses in the interferometer. In the next section, we will introduce an exact theoretical framework, taking into account losses and which can be used at any squeezing regime.

6.3 Heisenberg picture

6.3.1 Matrix representation of optical elements

Let a_i, and $\mathrm{a}_i^\dagger$, denote the annihilation and creation operators for photons in the mode i, which could refer to the photon paths, polarizations or wavelengths. Those operators satisfy the boson commutation relations:

$$[\hat{a}_i, \hat{a}_j] = \left[\hat{a}_i^\dagger, \hat{a}_j^\dagger\right] = 0, \left[\hat{a}_i, \hat{a}_j^\dagger\right] = \delta_{ij}. \tag{6.13}$$

The basis of the theoretical framework developed in this section is to study the experimental scheme in the Heisenberg picture, where each optical element will act onto the operators $\hat{a}_i^{(\dagger)}$ of each photon mode. For example, in this picture a BS (of transmitivity η) leads to the operators transformation:

$$\hat{a}_{1,\mathrm{out}}^{(\dagger)} = \sqrt{\eta}\,\hat{a}_{1,\mathrm{in}}^{(\dagger)} + \sqrt{1-\eta}\,\hat{a}_{2,\mathrm{in}}^{(\dagger)}, \tag{6.14}$$

$$\hat{a}_{2,\mathrm{out}}^{(\dagger)} = -\sqrt{1-\eta}\,\hat{a}_{1,\mathrm{in}}^{(\dagger)} + \sqrt{\eta}\,\hat{a}_{2,\mathrm{in}}^{(\dagger)}. \tag{6.15}$$

The subscript in (out) corresponds to the input (output) channel, and 1 (2) to the specific path, see FIGURE 6.2**b**. Thus, if we define the input and output vectors as:

$$\hat{A}_{\mathrm{in}} = \begin{pmatrix} \hat{a}_{1,\mathrm{in}} \\ \hat{a}_{1,\mathrm{in}}^\dagger \\ \hat{a}_{2,\mathrm{in}} \\ \hat{a}_{2,\mathrm{in}}^\dagger \end{pmatrix}, \quad \hat{A}_{\mathrm{out}} = \begin{pmatrix} \hat{a}_{1,\mathrm{out}} \\ \hat{a}_{1,\mathrm{out}}^\dagger \\ \hat{a}_{2,\mathrm{out}} \\ \hat{a}_{2,\mathrm{out}}^\dagger \end{pmatrix}, \tag{6.16}$$

we can express the equations (6.14,6.15) as:

$$\hat{A}_{\mathrm{out}} = \hat{O}_\eta \cdot \hat{A}_{\mathrm{in}}, \tag{6.17}$$

where $\hat{O}_\eta$ is the matrix:

$$\hat{O}_\eta = \frac{1}{\sqrt{2}} \begin{pmatrix} \sqrt{\eta} & 0 & \sqrt{1-\eta} & 0 \\ 0 & \sqrt{\eta} & 0 & \sqrt{1-\eta} \\ -\sqrt{1-\eta} & 0 & \sqrt{\eta} & 0 \\ 0 & -\sqrt{1-\eta} & 0 & \sqrt{\eta} \end{pmatrix}. \tag{6.18}$$

We can define similar matrices for the phase object (PO, FIGURE 6.2**c**) and the HWP (FIGURE 6.2**d**) , where the subscript i ($i \in \{1, 2\}$) corresponds to the polarization and the wavelength respectively:

$$\hat{O}_{\text{PO}} = \begin{pmatrix} e^{i\Phi_1} & 0 & 0 & 0 \\ 0 & e^{-i\Phi_1} & 0 & 0 \\ 0 & 0 & e^{i\Phi_2} & 0 \\ 0 & 0 & 0 & e^{-i\Phi_2} \end{pmatrix}, \tag{6.19}$$

$$\hat{O}_{\text{HWP}} = \frac{1}{\sqrt{2}} \begin{pmatrix} 1 & 0 & -1 & 0 \\ 0 & 1 & 0 & -1 \\ 1 & 0 & 1 & 0 \\ 0 & 1 & 0 & 1 \end{pmatrix}. \tag{6.20}$$

Finally, as seen earlier, the photon-pairs are generated via spontaneous parametric down-conversion, such that the NL crystal is described by a two-mode *squeezing operator*:

$$\hat{S}_2(r) = \exp\left[r\hat{a}_1^\dagger \hat{a}_2^\dagger - r^* \hat{a}_1 \hat{a}_2\right], \tag{6.21}$$

where $r = |r|e^{i\theta}$ is the squeezing parameter:

$$r = i\chi^{(2)}\sqrt{I_p}\, t. \tag{6.22}$$

$\chi^{(2)}$ is the 2$^{\text{rd}}$ order component of the electric susceptibility of the crystal, I_p the pump laser intensity and t the time-of-flight of the pump photon in the crystal. Using the Baker-Campbell-Hausdorff formula, the action of the squeezing operator on the operators $\hat{a}_{i,s}^{(\dagger)}$ (FIGURE 6.2**e**) can be obtained:

$$\hat{S}^\dagger \hat{a}_{i,\text{out}} S = \text{ch}(|r|)\, \hat{a}_{i,\text{in}} - e^{i\theta}\text{sh}(|r|)\, \hat{a}_{s,\text{in}}^\dagger, \tag{6.23}$$

$$\hat{S}^\dagger \hat{a}_{s,\text{out}} S = \text{ch}(|r|)\, \hat{a}_{s,\text{in}} - e^{i\theta}\text{sh}(|r|)\, \hat{a}_{i,\text{in}}^\dagger. \tag{6.24}$$

ch and sh are the hyperbolic functions. Thus we have the matrix $\hat{O}_{\text{NL}}$ acting on the operators vector $\hat{A}_{\text{in}}$:

$$\hat{O}_{\text{NL}} = \begin{pmatrix} \text{ch}(|r|) & 0 & 0 & -e^{i\theta}\text{sh}(|r|) \\ 0 & \text{ch}(|r|) & -e^{i\theta}\text{sh}(|r|) & 0 \\ 0 & -e^{i\theta}\text{sh}(|r|) & \text{ch}(|r|) & 0 \\ -e^{i\theta}\text{sh}(|r|) & 0 & 0 & \text{ch}(|r|) \end{pmatrix} \tag{6.25}$$

For the rest of this manuscript, we will assume that r is real, i.e: $\theta = 0$ and $r = |r|$, this will coincide with the highest sensitivity. Using the operator $\hat{O}_{\text{NL}}$, we can also estimate the number of photons going through the phase object for a given squeezing strength (r), which will illustrate the advantage of the Heisenberg picture. Both idler and signal photons are not present before the NL crystal, such that the number of signal photons after the NL crystal can be obtained by calculating the expecting value of the operator $\hat{S}^\dagger \left(\hat{a}_{s,\text{out}}^\dagger \hat{a}_{s,\text{out}}\right) \hat{S}$ on the vacuum state:

$$N_s = \langle 0|_s \hat{S}^\dagger \left(\hat{a}^\dagger_{s,\text{out}} \hat{a}_{s,\text{out}}\right) \hat{S} |0\rangle_s , \tag{6.26}$$

$$N_s = \langle 0|_s \left(\hat{S}^\dagger \hat{a}^\dagger_{s,\text{out}} \hat{S}\right) \left(\hat{S}^\dagger \hat{a}_{s,\text{out}} \hat{S}\right) |0\rangle_s . \tag{6.27}$$

Then by utilizing the bosonic commutation relations (6.13), the equations given in (6.23,6.24) and the action of the creation and annihilation operators on the Fock states ($|n\rangle$):

$$\hat{a}\,|n\rangle = \sqrt{n}\,|n-1\rangle\,,\ \hat{a}^\dagger\,|n\rangle = \sqrt{n+1}\,|n+1\rangle\,, \tag{6.28}$$

we can simplify the equation (6.27) in:

$$N_s = \text{sh}^2(r). \tag{6.29}$$

The same goes for the number of created idler photons, such that the total number of photons going through the phase object is:

$$N = 2\,\text{sh}^2(r). \tag{6.30}$$

6.3.2 Theoretical derivation of quantum interferometry

Even though calculations for various locations of the virtual beam splitter have been done, in the following derivation only the placement of the η-BS shown in FIGURE 6.2**a** will be discussed. The reason is that losses outside of the interferometer, behave exactly as in a classical interferometer, which can be attributed to the fact that (like its classical counterpart) we only detect single-photon states. Loss of an idler photon outside of the interferometer does not affect the single-photon state and a loss of a signal photon just results in a decrease of the measured number of photons, thus does not lead to decoherence as no information is leaked to the environment.

For the theoretical derivation, we need to consider for the quantum sensor all the modes present: $|V\rangle_{s,i}$, $|H\rangle_s$ and the modes introduced by the virtual beam splitter $|V\rangle_{s,i,L}$, $|H\rangle_{s,L}$. This forms a six-dimensional Hilbert space and leads us to consider a twelve-dimensional operators vector ($\hat{A}$) comprising all the creation and annihilation operators. The two-dimensional transfer matrices of every optical element described in the previous section are then expanded to 12-dimensional matrices including the non-interacting modes with the unity matrices. The total transfer matrix modeling the full quantum sensor is then:

$$\hat{O}_\text{q} = \hat{O}_\text{HWP}\,\hat{O}_{\text{NL}_2}\hat{O}_\eta\,\hat{O}_\text{PO}\,\hat{O}_{\text{NL}_1}, \tag{6.31}$$

and the creation and annihilation operators at the output can be expressed as a function of the inputs ones in respect to:

$$\hat{A}_\text{out} = \hat{O}_\text{q}\hat{A}_\text{in}. \tag{6.32}$$

The intensity operators at each detectors are $\hat{I}_1 = \hat{a}^\dagger_{H,s,\text{out}}\hat{a}_{H,s,\text{out}}$ and $\hat{I}_2 = \hat{a}^\dagger_{V,s,\text{out}}\hat{a}_{V,s,\text{out}}$ and can then by expressed as a function of the operators $\hat{a}^{(\dagger)}_\text{in}$ using the equations

(6.31,6.32). Similarly to the photon numbers going through the phase object, we can then estimate the signals I_i:

$$I_{1,2} = \langle 0|\, \hat{I}_{1,2}\, |0\rangle = \frac{\sinh^2(r)}{2}\left(1 + \eta\, \cosh^2(r) \pm 2\eta\, \cosh(r)\, \cos(2\,\Phi)\right). \tag{6.33}$$

We expect then a fringes visibility of:

$$V_{\mathrm{q}} = \frac{2\,\eta\,\mathrm{ch}(r)}{\eta\,\mathrm{ch}^2(r) + 1}. \tag{6.34}$$

Furthermore, the signal operator is the subtraction of both the detectors signals: $\hat{S} = \hat{I}_1 - \hat{I}_2$, such that the expecting value and uncertainty are:

$$S = \langle 0|\, \hat{S}\, |0\rangle = \alpha \cos(2\,\Phi), \tag{6.35}$$

$$\Delta S^2 = \langle 0|\, \hat{S}^2\, |0\rangle - S^2 = \frac{\alpha^2}{2}\cos(4\Phi) + \beta, \tag{6.36}$$

with α and β being:

$$\alpha = 2\,\eta\,\mathrm{sh}^2(r)\,\mathrm{ch}(r) \tag{6.37}$$

$$\beta = \eta\,(3 - 2\,\eta)\,\mathrm{sh}^2(r)\,\mathrm{ch}^2(r) + \eta^2\,\mathrm{sh}^6(r) + \eta^2\,\mathrm{sh}^2(r)\,\mathrm{ch}^4(r) + (1-\eta)^2\,\mathrm{sh}^2(r) \tag{6.38}$$

Interestingly, the frequency doubling (or super-resolution) is conserved for any squeezing strength, as seen in equation (6.35). Furthermore, the signal is still proportional to the number of photons going through the phase object ($N = 2\,\mathrm{sh}^2(r)$), yet an additional term is present: $\mathrm{ch}(r)$, coming from stimulated emission in the second crystal.

The maximum sensitivity is achieved when the ratio $\Delta S/(\partial_\Phi S)$ is minimized, i.e when the smaller phase change results in a signal change greater than the uncertainty. Here, it is reached for $\Phi = \pi/2,\, 3\pi/2$, as seen from equations (6.35,6.36), and is:

$$\Delta\Phi_{\mathrm{q}} = \min\left|\frac{\Delta S}{\partial_\Phi S}\right| = \frac{1}{2}\sqrt{\frac{\beta}{\alpha^2} - \frac{1}{2}}, \tag{6.39}$$

While for a non-perfect classical interferometer with $2N$ photons inserted (N photons through the phase object) the phase sensitivity is:

$$\Delta\Phi_{\mathrm{c}} = \frac{1}{V_{\mathrm{c}}\sqrt{2N}} \tag{6.40}$$

With V_{c} the visibility of the fringes on each detector outputs of the classical interferometer. Therefore, the quantum setup achieves a higher sensitivity if and only if:

$$f = \frac{\Delta\Phi_{\mathrm{c}}}{\Delta\Phi_{\mathrm{q}}} > 1 \tag{6.41}$$

In the next section, we will study for various squeezing regimes when a sub-shot-noise sensitivity is reached depending on the internal losses and compare our theoretical model to experimental data.

6.4 Discussion

6.4.1 Low squeezing regime

In the case of low squeezing parameter, $r \ll 1$, the squeezed state is equivalent to uncorrelated photon-pairs ($|r\rangle \sim |0\rangle + r\,|2\rangle$) and as such corresponds to the study performed in section 6.2. In this approximation, we have $\mathrm{sh}(r) \sim r$, $\mathrm{ch}(r) \sim 1$, and the visibility reduces to:

$$V_\mathrm{q} = \frac{2\,\eta}{\eta + 1}. \tag{6.42}$$

Furthermore, the expression of the phase sensitivity of the quantum sensor is simplified to:

$$\Delta\Phi_\mathrm{q} = \frac{1}{2\sqrt{V_\mathrm{q}\,\eta\,N}}. \tag{6.43}$$

The phase sensitivity enhancement expected compared to a classical Michelson interferometer of visibility V_c is then:

$$f = \frac{\Delta\Phi_\mathrm{c}}{\Delta\Phi_\mathrm{q}}, \tag{6.44}$$

$$f = \frac{V_\mathrm{q}}{V_\mathrm{c}}\sqrt{\frac{2}{2 - V_\mathrm{q}}}, \tag{6.45}$$

$$f = \frac{2\eta}{V_\mathrm{c}\sqrt{1+\eta}}. \tag{6.46}$$

If both interferometers are perfect ($\eta = V_\mathrm{q} = V_\mathrm{c} = 1$), then we recover, as expected, the enhancement factor $f = \sqrt{2}$. Yet, this model takes into account losses within the interferometers, and is as such more precise and can be compared to real-world experiments, here performed by MSc Raphael Nold.

The quantum sensor used experimentally is slightly different to the one presented earlier, as seen in FIGURE 6.3**a**, but is formally equivalent. First of all, a single NL crystal is used to increase the interferometer stability and photon indistinguishability. A wavelength selective wave plate is used to engineer the polarization states of the first photon-pair contribution. Additionally, the crystal birefringence causes a time difference between the photons ($\sim$ 3 ps), compensate by a polarization delay stage. Finally, the phase shift is introduced using the displacement of a piezoelectric actuator. The classical interferometer to benchmark the experiment is a Michelson interferometer, as depicted in FIGURE 6.1. In FIGURE 6.3**b** the detectors signals for both the classical and quantum sensors are shown. A fit to the signals yields the raw visibilities: $V_\mathrm{c} = 0.98 \pm 0.002$ and $V_\mathrm{q} = 0.85 \pm 0.02$. Thus the classical interferometer is nearly-perfect, and we estimate the upper limit of losses in the quantum sensor to be around $1 - \eta = 0.26$. The transmissivity η is here estimated by inverting the equation (6.42):

$$\eta = \frac{V_\mathrm{q}}{2 - V_\mathrm{q}}. \tag{6.47}$$

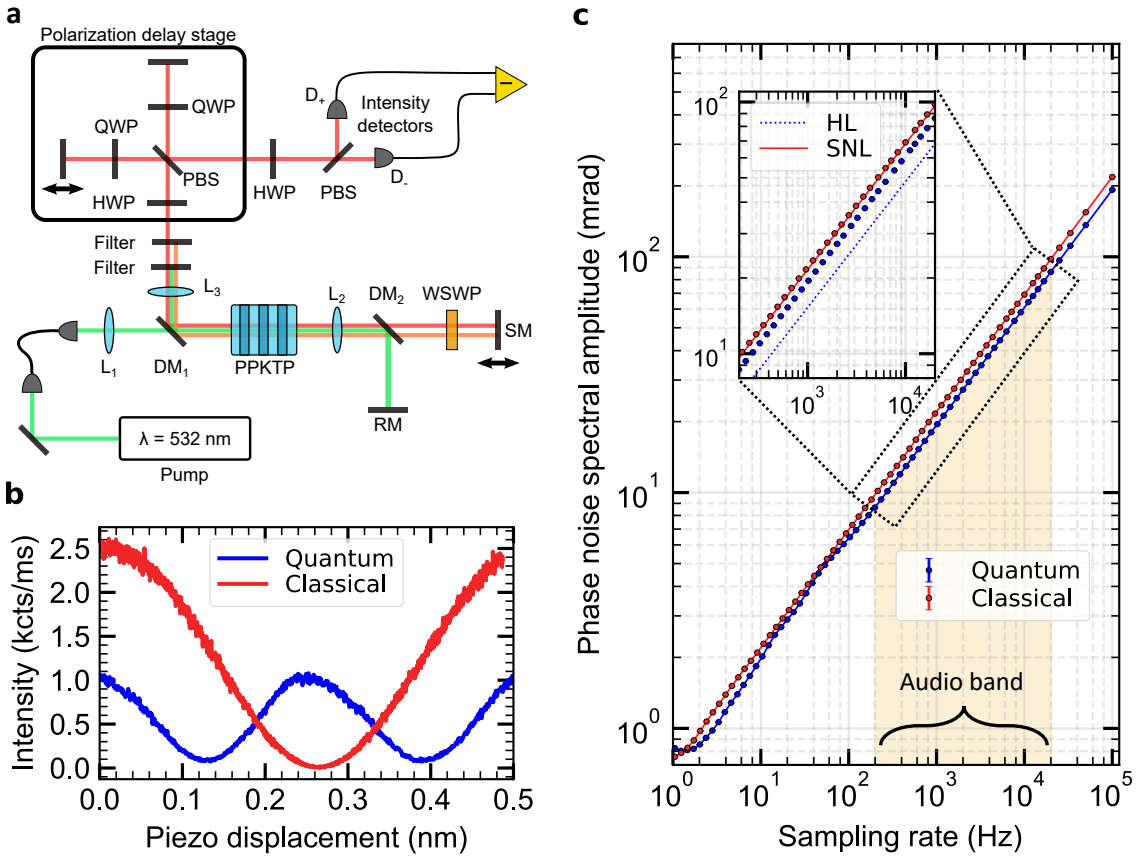

Figure 6.3: **Experimental results.** **a** A detailed sketch of the experimental setup. Compared to the setup shown in FIGURE 6.2**a**, the pump laser passes twice in a single NL crystal and an additional compensation stage is placed. Furthermore, a wavelength selective wave plate (WSWP) rotates, after a dual passage, the polarization of the signal photon by 90° while letting the idler photon unchanged. L: Lens. **b** The raw data of a single-detector (I_1) of the quantum (blue) and classical sensor (red), with the same number of photons (N) going through the phase object. The visibilities, yielded from a sinusoidal fit, are $V_\mathrm{q} = 0.85 \pm 0.02$ and $V_\mathrm{c} = 0.98 \pm 0.002$. **c** Frequency-dependent phase noise spectral amplitudes of the classical (red) and quantum (blue) sensor. Both measurements are performed at identical photon fluxes, prior to any loss inside the interferometer. Above 200 Hz, the quantum sensor surpasses the classical sensor by a factor of 1.13 ± 0.02. The inset shows a zoom-in of the signal in the audio band, in which the solid (dotted) line represents the theoretical limits of the classical (quantum) sensor according to the photon rate $R = 2.14 \cdot 10^6$ s^{-1}.

Furthermore, for the same piezo displacement, the quantum sensor presents twice as many fringes, thus corroborating the phase sensing with super-resolution, as expected. Utilizing the equation (6.45), we can also predict the expected enhancement

$$f = \frac{\Delta\Phi_\mathrm{c}}{\Delta\Phi_\mathrm{q}} = \frac{V_\mathrm{q}}{V_\mathrm{c}}\sqrt{\frac{2}{2 - V_\mathrm{q}}} = 1.14 \pm 0.01. \tag{6.48}$$

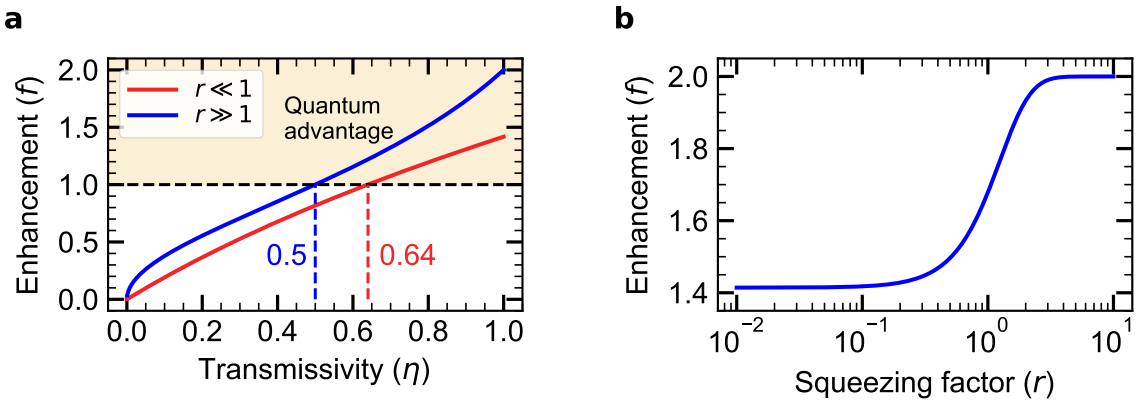

Figure 6.4: **Enhancement dependency.** **a** Losses-dependent enhancement factor at low (blue) and strong (red) squeezing regime. A sub-shot-noise sensitivity (yellow area) is achieved for losses below 36 % and 50 % for each case. For strong regime, the enhancement is more robust to losses. **b** Squeezing-strength-dependent enhancement factor, for a lossless quantum interferometer. For any given squeezing regime a quantum advantage is present: from $\sqrt{2}$, for low r, up to 2 for high r.

To experimentally infer the phase sensitivity of both sensors, we measure the spectral amplitudes of the phase noise for both the quantum and classical sensor (using Allan deviation), at a piezo position with the maximum phase (displacement) sensitivity. As shown in FIGURE 6.3**c**, for sampling frequencies above 1 Hz, both sensors show the expected phase noise increase with a square root power scaling. The fit to the data shows that the classical sensor operates merely 1.5 % above the fundamental shot-noise limit, confirming the high quality of the classical sensor. Additionally, above 200 Hz, the quantum sensor surpasses the classical interferometer by a factor of 1.13 ± 0.02, which fits perfectly with the prediction made by our theoretical model (equation (6.48)), demonstrating the validity of our calculation. Furthermore, a sub-shot-noise quantum advantage is present for transmissivities above $\eta_{\text{crit}} = 0.64$, as seen in FIGURE 6.4**a**. The quantum sensor is then resilient against losses in the interferometer (linear dependency) despite using squeezed states of light whose coherences are often prone to exponential dependency to the losses.

Quite remarkably, the sub-shot-noise quantum advantage is maintained for sampling rates up to 100 kHz, as seen in FIGURE 6.4**a**, which is four orders of magnitude higher than previously obtained [262, 263, 264]. Capitalizing on the robustness and high sampling rates of the device, MSc Raphael Nold implemented a quantum optical microphone in the audio band from the quantum sensor and made the quantum advantage audible. This claim has been confirmed by a standardized medically-approved speech recognition test on 45 subjects. In summary, we have developed a theoretical model for the quantum sensor and confirm its validity by predicting, from the fringes visibilities, the expecting phase sensitivity enhancement, which fitted the experimental value perfectly. Furthermore, the quantum sensor is robust against losses: even with 36 % of losses, the sensor still presents an advantage over a perfect classical interferometer without losses. In the next section, we will explore the enhancement reached at different squeezing regimes.

6.4.2 Strong squeezing regime

As seen in FIGURE 6.4**b**, the enhancement factor increases with the squeezing strength, up to $f = 2$ for a high squeezing parameter ($r \gg 1$). This regime can be achieved, as seen in equation (6.22), by increasing the pump laser power (I_P) or its interaction with the NL crystal (t), e.g. by integration of the crystal in a cavity [265]. Experimentally, squeezing factors around 15 dB ($r \sim 1.7$) have been already observed [266]. In the strong squeezing regime we have $\mathrm{sh}(r) \sim \mathrm{ch}(r) \sim \exp(r)/2$ and the quantum phase sensitivity achieved is:

$$\Delta\Phi_{\mathrm{q}} = \frac{1}{2\sqrt{N}}\sqrt{\frac{3-2\eta}{2\eta}}, \tag{6.49}$$

leading to an enhancement factor of:

$$f = \frac{\Delta\Phi_{\mathrm{c}}}{\Delta\Phi_{\mathrm{q}}} = \frac{2}{V_{\mathrm{c}}}\sqrt{\frac{\eta}{3-2\eta}} \tag{6.50}$$

Therefore, if no losses are present in the quantum interferometer ($\eta = 1$), we indeed have a phase sensitivity enhancement of $f = 2$ compare to a perfect classical interferometer ($V_{\mathrm{c}} = 1$). Furthermore, the enhancement factor is more resilient to losses at higher squeezing regime. Indeed a sub-shot-noise sensitivity is still observed for losses of 50 % in the strong squeezing regime, as seen in FIGURE 6.4**a**, while only 36% of losses was allowed for small squeezing parameters.

6.5 Conclusion and outlook

In this chapter, we have explored a novel phase measurement scheme based on squeezed states of light. We first gave a theoretical description using the Fock space to develop an intuition on the scheme, before using the Heisenberg representation to refine the model. We have demonstrated that sub-shot-noise sensitivity was achieved for any squeezing regimes, with an enhancement bounded between $\sqrt{2}$ ($r \ll 1$) and 2 ($r \gg 1$), and robust against losses within the interferometer. Our model predicted from the visibility of the fringes, with perfect accuracy, the expected enhancement compared to a state-of-the-art classical interferometer. The robustness and high sampling rates of the device allowed the implementation of a quantum optical microphone in the audio band and made the quantum advantage audible.

It would be interesting to study whether our concepts could be applied to suppress common mode intensity noise in SU(1,1) interferometers [259, 260, 267]. Furthermore, in future experiments we could consider miniaturizing the free space optical setup in an integrated on-chip system, utilizing NL optical properties of some crystals (e.g. PPKTP, SiC) [48, 98], to increase further the stability of the sensor and the applicability range of the scheme.

Appendix A

List of Abbreviations

arb. u.	Arbitrary units
BS	Beam splitter
CB	Conduction band
CPMG	Carr-Purcell-Meiboom-Gill sequence
cQED	Cavity quantum electrodynamics
DEER	Double electron-electron resonance
DFT	Density functional theory
DM	Dichroic mirror
DWF	Debye-Waller factor
EBPVD	Electron-beam physical vapor deposition
ESLAC	Excited state level anticrossing
FIB	Focused ion beam
FID	Free induction decay
FWHM	Full width at half maximum
GSLAC	Ground state level anticrossing
HOM	Hong-Ou-Mandel (effect)
HWP	Half-waveplate
ICP	Inductively coupled plasma
IPA	Isopropyl alcohol
ISC	Intersystem crossing states
LED	Light-Emitting Diode
MIBK	Methyl isobutyl ketone
MW	Microwace
NL	Non-linear

NV	Nitrogen-vacancy (center)
ODMR	Optically detected magnetic resonance
PBS	Polarization beam splitter
PD	Photodiode
PhD	Philosophiæ doctor
PLE	Photoluminescence excitation (scan)
PMMA	Polymethyl methacrylate
PSB	Phonon sideband
Qubit	Quantum bit
QWP	Quarter-waveplate
RF	Radiofrequency
RIE	Reactive ion etching
SEM	Scanning electron microscope
SiC	Silicon carbide
SIL	Solid immersion lense
SNL	Shot noise limit
SNR	Signal to noise ratio
SNSPD	Superconducting nanowire single-photon detector
SPDC	Spontaneous parametric down-conversion
SRIM	Stopping and Range of Ions in Matter
V_{Si}	Silicon vacancy (center)
VB	Valence band
ZFS	Zero-Field Splitting
ZPL	Zero-phonon line

Appendix B

List of Symbols

^{13}C	Carbon 13 isotope
^{29}Si	Silicon 29 isotope
$\mathbf{A}_{\mathrm{dd}}$	Hyperfine tensor
$A_{\parallel}$	Parallel hyperfine coupling coefficient
$A_{\perp}$	Perpendicular hyperfine coupling coefficient
$\mathbb{B}$	External magnetic field
B_i	i-component of $\mathbf{B}$
cps	Counts per second
D	Longitudinal crystal field splitting parameters
D_{es}	Ground state zero-field splitting parameter
D_{gs}	Excited state zero-field splitting parameter
E	Transversal crystal field splitting parameters
$\tilde{\gamma}_e$	Gyromagnetic ratio for an isotated electron, 28.024 GHz·T^{-1}
$\tilde{\gamma}_e$	Gyromagnetic ratio for an nucleus: ^{13}C: 10.708 MHz·T^{-1}; ^{29}Si: -8.465 MHz·T^{-1}
g_e	Electron Landé factor, 2.0028
g_n	Nuclear Landé factor, dependent of the nuclear species: ^{13}C Landé factor: 1.4048236; ^{29}Si Landé factor: -1.11058
$\mathcal{H}$	Hamiltonian
$\hbar$	Reduced Planck contant, 1.054 571...10^{-34} J·s
$\mathbf{I}$	Nuclear spin angular momentum operator (here: spin 1/2)
$\hat{I}_i$	i-component of $\mathbf{I}$ (here: spin 1/2)
m_s	Electron spin quantization number along the z-axis

μ_0	Vacuum permeability, $4\pi\ 10^7$ T·m·A^{-1}
μ_B	Bohr magneton, $9.274009994\ 10^{-24}$ J·T^{-1}
μ_n	Nuclear magneton, $5.05078317\ 10^{-27}$ J·T^{-1}
ω_L	Larmor frequency
$\mathbf{S}$	Electron spin angular momentum operator (here: spin 3/2)
$\hat{S}_i$	i-component of $\mathbf{S}$ (here: spin 3/2)

Appendix C

Laser stabilization protocol

As we have seen through this manuscript: the optical lines of shallow V2 centers tend to drift over time. Therefore we created a protocol to refocus the resonant laser onto the resonant transitions (here A_2). The refocusing period is typically chosen on a time scale of a few to several minutes. The employed protocol is schematically depicted in FIGURE C.1. During all steps in the protocol, we provide a microwave (MW) drive resonant with the ground state transitions $m_s = +1/2 \leftrightarrow m_s = +3/2$ and $m_s = -1/2 \leftrightarrow m_s = -3/2$ to counteract spin pumping by mixing the ground state populations. The laser feedback protocol goes as follows:

(1) We probe whether the absorption lines drifted by applying a resonant excitation on the A_2 optical transition for 500 ms. Provided that more than 300 photons are detected, we consider that no drift occurred, and the main measurement is continued. If less than 300 photons are detected, we proceed with step (2).

(2) We perform up to two resonant excitation scans (PLE), by tuning the resonant excitation laser over a frequency range of 3 GHz. The resulting fluorescence signal is fitted with a double-Lorentzian function. The goodness of the fit is evaluated by several criteria, such as the peak separation that must be within $0.9-1.1$ GHz, the peak ratio that must be in the range of $\frac{1}{3}$ to 3, the peak width that must be in the range of 10 to 100 MHz, and the signal-to-background ratio that must exceed 5. If all criteria are met, we fix the laser on the high-frequency transition (A_2 line) and resume the main measurement. The laser scanning window is also reset such that the A_2 transition occurs at 2/3 of the (potential) next scan. If the above criteria are not met, we repeat step (2) one more time. If the criteria are not met after the second attempt, we proceed to step (3).

(3) An off-resonant laser pulse (1 mW, 1 s, 785 nm) is applied to modify/reset the charge environment of the V2 center. Then, we perform up to two resonant excitation scans with a frequency range of 13 GHz. If the signal can be fitted by a double-Lorentzian function with the same fit criteria as mentioned in (2), we continue with step (2). Note that we do not resume the main measurement directly due to laser drift and hysteresis after extended scan ranges. If step (3) is not successful after two attempts, we proceed with step (4).

(4) Similar to step (3), we step (4) employs the same off-resonant excitation pulse, however followed by a resonant excitation scan covering 20 GHz. This scan range is sufficient to always identify the absorption lines, e.g., we have never observed spectral wandering and distribution beyond this range [42]. Once step (4) is successful, we proceed with step (2).

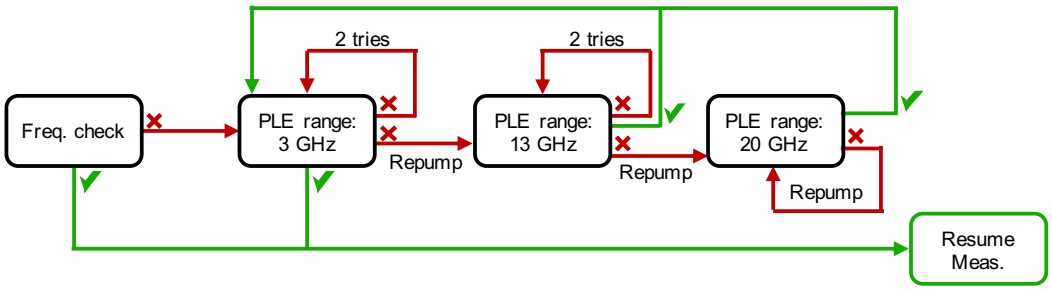

Figure C.1: **Laser stabilization protocol.**Schematic of the protocol to periodically refocus the resonant laser on the A_2 optical transition of the waveguide-integrated V2 centers. The green (red) arrows correspond to successful (unsuccessful) steps in finding the A_2 transition.

Appendix D

Magnetic field alignment protocol

To lift the Kramers degeneracy and deterministically control the V_{Si} centers spin state, a magnet is placed next to the cryostat with its north pole pointing toward the c-axis of the SiC crystal. The magnet position is reliably controlled with two motorized translation stages. The magnetic field has to be precisely aligned to avoid a mixing of the spin eigenstates of the Hamiltonian, see equation (**??**). Previous protocols, based on off-resonant ODMR signals of V2 centers ensemble, were slow due to the low spin signal contrast. We improved upon these protocols, allowing to align roughly the magnetic field in a matter of minutes and precisely in a few hours.

A rough alignment is first obtained by minimizing the photon count rate of a single V2 center under continuous resonant excitation along the A_2 transition. When the color center does not fluoresce anymore, $|+1/2\rangle_{gs}$ has become a steady state of the system and the perpendicular Zeeman term ($\tilde{\gamma}_e B \sin(\theta)$) is negligible compared to ν_3, i.e. $\theta \ll \frac{\nu_3}{\tilde{\gamma}_e B}$. Yet, the state $|-1/2\rangle_{gs}$ and $|-3/2\rangle_{gs}$ can still be mixing. A second alignment step is done by repeating the same protocol with an additional mw field resonant with the ν_2 transition, such that the color center becomes dark if and only if the magnetic does not induce any spin mixing anymore. After this protocol we have:

$$\theta \ll \theta_{\text{rough}} = \left| \frac{2D_{gs}}{\tilde{\gamma}_e B} - 1 \right| \tag{D.1}$$

The alignment is then the most accurate, at the GSLAC when $2D_{gs} \sim \tilde{\gamma}_e B$ and any tilt of the magnetic field induces an significant spin mixing. The precision of this protocol is around $\theta_{\text{rough}}/10$, which even at a strong magnetic field ($\tilde{\gamma}_e B \gg 2D_{gs}$) correspond to only a few degrees ($\sim 6°$). Thanks to the motorized translation stages, we can reach a higher precision by determining the optimal magnet position via a fit of the position-dependent count rate. With each data point being acquired only for a few ten seconds, we obtain a first magnetic field alignment in a few minutes with a degree precision.

An higher precision is reached by performing a series of ODMR measurements on the three ground state transitions, protocol given in FIGURE 1.8**c**. The magnet is once again scanned along each axis, while the frequencies of the three fluorescence peaks are monitored. As the frequency depends on the magnetic field, to not lose track of the resonances, the scanning window of each ODMR scan is adjusted to the fitted values of the resonance of the previous scan, i.e. at the previous position. This second

method proves to be more accurate, yet more time consuming. However, owing to the high contrast of resonant ODMR and the motorization of the stages, the protocol is automatically performed in a few hours, which can be easily done overnight and unsupervised.

Appendix E

Rotating wave approximation

E.1 Two-level system

Let us define the free Hamiltonian of a two-level system ($|g\rangle, |e\rangle$) as:

$$\mathcal{H}_0 = -\frac{\omega_0}{2}|g\rangle\langle g| + \frac{\omega_0}{2}|e\rangle\langle e| = \frac{\omega_0}{2}\hat{\sigma}_z. \tag{E.1}$$

where ω_0 is the energy difference between the two states $|g\rangle$ and $|e\rangle$, under the assumption $\hbar = 1$. In FIGURE E.1 is given a sketch of the system.

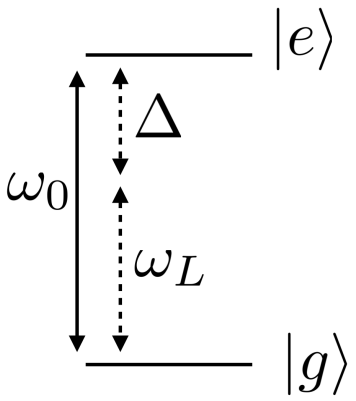

Figure E.1: **Two-level system** Energy level composed of an excited state $|e\rangle$ a ground state $|g\rangle$ separated by an energy difference ω_0. ω_L is the pulsation of the electromagnetic radiation and Δ is the detuning, i.e. $\Delta = \omega_0 - \omega_L$

.

We assume the existence of an electric[1] dipole moment that coupled the energy levels to one another. The quantum operator ($\hat{\mathbf{d}}$) for the transition dipole is:

$$\hat{\mathbf{d}} = \mathrm{d}\,\mathbf{n}_d\,(|e\rangle\langle g| + |g\rangle\langle e|) = \mathrm{d}\,\mathbf{n}_d\,\sigma_x. \tag{E.2}$$

Here, d is the amplitude of the dipole and $\mathbf{n}_\mathrm{d}$ the unitary vector which carries the information of the dipole orientation. For the V_{Si} centers in SiC, this vector is along

[1] the explanation is similar for a magnetic dipole moment

the c-axis of the crystal. The dipole couples to external electromagnetic waves with the interaction energy Hamiltonian given by:

$$\mathcal{H}_{\text{int}} = -\mathbf{d} \cdot \mathbf{E} \cdot \tag{E.3}$$

Here, $\mathbf{E}$ is the electric field, assumed as a wave plane of amplitude E, direction $\mathbf{n}_L$, an angular frequency ω_L and a phase ϕ. i.e $\mathbf{E} = \mathrm{E}\,\mathbf{n}_L \cos(\omega_L t + \phi)$.[2] The full Hamiltonian of the qubit under the perturbation of the radiation is then:

$$\mathcal{H} = \mathcal{H}_0 + \mathcal{H}_{int} = \frac{\omega_0}{2}\hat{\sigma}_z - \Omega \cos(\omega_L t + \phi)\hat{\sigma}_x \cdot \tag{E.4}$$

Where $\Omega = \mathrm{d}\,\mathrm{E}\,(\mathbf{n}_L \cdot \mathbf{n}_d)$ is the Rabi frequency. The evolution of the qubit state is thus given by the Schrödinger equation:

$$i\frac{\partial}{\partial t}\left|\Psi(t)\right\rangle = \mathcal{H}\left|\Psi(t)\right\rangle \cdot \tag{E.5}$$

The Hamiltonian (E.5) is time-dependent, therefore we will study the time evolution of the qubit in the interaction picture.

E.2 Rotating wave approximation

The interaction picture connects the Schrödinger and Heisenberg pictures, where the state vectors and the operators carry a part of the time dependence, we rearrange the Hamiltonian as: $\mathcal{H} = \mathcal{H}_0' + \mathcal{H}_{int}' = (\frac{\omega_L}{2}\hat{\sigma}_z) + (\frac{\Delta}{2}\hat{\sigma}_z - \Omega\cos(\omega_L t + \phi)\hat{\sigma}_x)$. Where Δ is the detuning of the electromagnetic wave frequency with respect to ω_0. See FIGURE E.1. Therefore, we can define the interacting evolution operator as[3]:

$$\hat{U}_0(t) = exp\left(-\frac{i\mathcal{H}_0' t}{\hbar}\right) = \begin{pmatrix} e^{-\frac{i\omega_L t}{2}} & 0 \\ 0 & e^{+\frac{i\omega_L t}{2}} \end{pmatrix} \cdot \tag{E.6}$$

In the rotation frame, the states are defined as: $\left|\Psi_I\right\rangle = \hat{U}_0^\dagger \left|\Psi_S\right\rangle$ and the operator as: $\hat{O}_I = \hat{U}_0^\dagger(t)\hat{O}_S\hat{U}_0(t)$, where the index S (I) design the state or the operator in the Schrödinger (interaction) picture. From the Schrodinger equation (E.5), we can derivate the evolution equation in the interacting frame:

$$i\frac{\partial}{\partial t}\left|\Psi_I\right\rangle = \mathcal{H}_{int,I}'\left|\Psi_I\right\rangle \cdot \tag{E.7}$$

The interacting part of the Hamiltonian in the rotation frame is given by:

$$\mathcal{H}_{int,I}' = \frac{1}{2}\begin{pmatrix} \Delta & -\Omega(e^{i(2\omega_L t+\phi)} + e^{-i\phi}) \\ -\Omega(e^{-i(2\omega_L t+\phi)} + e^{+i\phi}) & -\Delta \end{pmatrix} \cdot \tag{E.8}$$

The off-diagonal terms are made of a time-dependent (rotating at the frequency $2\omega_L$) term and a time-independent one. The first contribution is canceling out itself,

[2] All the calculations can also be done using a quantum field representation of the electric field.
[3] The matrix representation is written in the basis $\{\left|e\right\rangle, \left|g\right\rangle\}$

oscillating too fast compared to the speed of the state changes. This approximation is the so-called rotating wave approximation. The effective Hamiltonian can be rewritten as: $\mathcal{H}_{int}^{\prime,RWA} = \frac{\Omega'}{2}\mathbf{n}\cdot\boldsymbol{\sigma}$, where $\mathbf{n}$ is a unitary vector defined as:

$$\mathbf{n} = \begin{pmatrix} -\frac{\omega_L}{\Omega'}\cos\phi \\ -\frac{\omega_L}{\Omega'}\sin\phi \\ \frac{\Delta}{\Omega'} \end{pmatrix} \tag{E.9}$$

And $(\Omega')^2 = \Delta^2 + \Omega^2$ is the effective Rabi frequency. If we shine a resonant Laser ($\Delta = 0$), the evolution operator in the rotating frame is:

$$\hat{U}^{I,RWA} = \exp\left(-i\mathcal{H}_{int}^{\prime I,RWA}t\right) = \begin{pmatrix} \cos\left(\frac{\Omega' t}{2}\right) & \sin\left(\frac{\Omega' t}{2}\right) \\ \sin\left(\frac{\Omega' t}{2}\right) & \cos\left(\frac{\Omega' t}{2}\right) \end{pmatrix} \tag{E.10}$$

From this expression, we can derivate the evolution operator in the Schrödinger frame, and compute the probability to find the qubit in the state $|e\rangle$ if this one is initially in the ground state:

$$P(|e\rangle) = |\langle e|\,\hat{U}^{RWA}\,|g\rangle\,|^2 = \sin^2\left(\frac{\Omega' t}{2}\right). \tag{E.11}$$

Therefore, an resonant electromagnetic wave induces coherent oscillation of the system between its ground and excited states [144].

Bibliography

[1] R. P. Feynman, "Simulating physics with computers," *International Journal of Theoretical Physics*, vol. 21, no. 6, pp. 467–488, 1982.

[2] L. K. Grover, "A fast quantum mechanical algorithm for database search," in *Proceedings of the twenty-eighth annual ACM symposium on Theory of computing*, pp. 212–219, 1996.

[3] D. Deutsch and R. Jozsa, "Rapid solution of problems by quantum computation," *Proceedings of the Royal Society of London. Series A: Mathematical and Physical Sciences*, vol. 439, no. 1907, pp. 553–558, 1992.

[4] R. Cleve, A. Ekert, C. Macchiavello, and M. Mosca, "Quantum algorithms revisited," *Proceedings of the Royal Society of London. Series A: Mathematical, Physical and Engineering Sciences*, vol. 454, no. 1969, pp. 339–354, 1998.

[5] P. W. Shor, "Algorithms for quantum computation: discrete logarithms and factoring," in *Proceedings 35th Annual Symposium on Foundations of Computer Science*, pp. 124–134, 1994.

[6] D. Bernstein, J. Buchmann, and E. Dahmen, *Post-Quantum Cryptography*. Springer.

[7] C. H. Bennett and G. Brassard, "Quantum cryptography: Public key distribution and coin tossing," *Theoretical Computer Science*, vol. 560, pp. 7–11, 2014.

[8] N. Gisin, G. Ribordy, W. Tittel, and H. Zbinden, "Quantum cryptography," *Reviews of Modern Physics*, vol. 74, no. 1, pp. 145–195, 2002.

[9] M. Dušek, N. Lütkenhaus, and M. Hendrych, "Quantum cryptography," *Progress in Optics*, vol. 49, pp. 381–454, 2006.

[10] E. Peter, P. Senellart, D. Martrou, A. Lemaître, J. Hours, J. M. Gérard, and J. Bloch, "Exciton-photon strong-coupling regime for a single quantum dot embedded in a microcavity," *Physical Review Letters*, vol. 95, p. 067401, 2005.

[11] S. Barz, E. Kashefi, A. Broadbent, J. F. Fitzsimons, A. Zeilinger, and P. Walther, "Demonstration of blind quantum computing," *Science*, vol. 335, no. 6066, pp. 303–308, 2012.

[12] M. H. Devoret and R. J. Schoelkopf, "Superconducting circuits for quantum information: An outlook," *Science*, vol. 339, no. 6124, pp. 1169–1174, 2013.

[13] B. Hensen, H. Bernien, A. E. Dréau, A. Reiserer, N. Kalb, M. S. Blok, J. Ruitenberg, R. F. L. Vermeulen, R. N. Schouten, C. Abellán, W. Amaya, V. Pruneri, M. W. Mitchell, M. Markham, D. J. Twitchen, D. Elkouss, S. Wehner, T. H. Taminiau, and R. Hanson, "Loophole-free bell inequality violation using electron spins separated by 1.3 kilometres," *Nature*, vol. 526, no. 7575, pp. 682–686, 2015.

[14] M. Bock, P. Eich, S. Kucera, M. Kreis, A. Lenhard, C. Becher, and J. Eschner, "High-fidelity entanglement between a trapped ion and a telecom photon via quantum frequency conversion," *Nature Communications*, vol. 9, no. 1, p. 1998, 2018.

[15] C. Neill, , *et al.*, "A blueprint for demonstrating quantum supremacy with superconducting qubits," *Science*, vol. 360, no. 6385, pp. 195–199, 2018.

[16] B. Bartlett and S. Fan, "Universal programmable photonic architecture for quantum information processing," *Physical Review A*, vol. 101, p. 042319, 2020.

[17] J. Borregaard, H. Pichler, T. Schröder, M. D. Lukin, P. Lodahl, and A. S. Sørensen, "One-way quantum repeater based on near-deterministic photon-emitter interfaces," *Physical Review X*, vol. 10, p. 021071, 2020.

[18] G. Stein, V. Bushmakin, Y. Wang, A. W. Schell, and I. Gerhardt, "Narrow-band fiber-coupled single-photon source," *Physical Review Applied*, vol. 13, p. 054042, 2020.

[19] G. Wolfowicz, F. J. Heremans, C. P. Anderson, S. Kanai, H. Seo, A. Gali, G. Galli, and D. D. Awschalom, "Quantum guidelines for solid-state spin defects," *Nature Reviews Materials*, vol. 6, no. 10, pp. 906–925, 2021.

[20] D. D. Awschalom, R. Hanson, J. Wrachtrup, and B. B. Zhou, "Quantum technologies with optically interfaced solid-state spins," *Nature Photonics*, vol. 12, no. 9, pp. 516–527, 2018.

[21] N. Kalb, A. A. Reiserer, P. C. Humphreys, J. J. W. Bakermans, S. J. Kamerling, N. H. Nickerson, S. C. Benjamin, D. J. Twitchen, M. Markham, and R. Hanson, "Entanglement distillation between solid-state quantum network nodes," *Science*, vol. 356, no. 6341, pp. 928–932, 2017.

[22] M. Pompili, S. L. N. Hermans, S. Baier, H. K. C. Beukers, P. C. Humphreys, R. N. Schouten, R. F. L. Vermeulen, M. J. Tiggelman, L. dos Santos Martins, B. Dirkse, S. Wehner, and R. Hanson, "Realization of a multinode quantum network of remote solid-state qubits," *Science*, vol. 372, no. 6539, pp. 259–264, 2021.

[23] G. Waldherr, Y. Wang, S. Zaiser, M. Jamali, T. Schulte-Herbrüggen, H. Abe, T. Ohshima, J. Isoya, J. F. Du, P. Neumann, and J. Wrachtrup, "Quantum error correction in a solid-state hybrid spin register," *Nature*, vol. 506, pp. 204–207, 2014.

[24] C. E. Bradley, J. Randall, M. H. Abobeih, R. C. Berrevoets, M. J. Degen, M. A. Bakker, M. Markham, D. J. Twitchen, and T. H. Taminiau, "A ten-qubit solid-state spin register with quantum memory up to one minute," *Physical Review X*, vol. 9, pp. 1–12, 2019.

[25] F. Rozpędek, R. Yehia, K. Goodenough, M. Ruf, P. C. Humphreys, R. Hanson, S. Wehner, and D. Elkouss, "Near-term quantum-repeater experiments with nitrogen-vacancy centers: Overcoming the limitations of direct transmission," *Physical Review A*, vol. 99, p. 052330, 2019.

[26] E. Janitz, M. K. Bhaskar, and L. Childress, "Cavity quantum electrodynamics with color centers in diamond," *Optica*, vol. 7, no. 10, pp. 1232–1252, 2020.

[27] M. H. Abobeih, J. Randall, C. E. Bradley, H. P. Bartling, M. A. Bakker, M. J. Degen, M. Markham, D. J. Twitchen, and T. H. Taminiau, "Atomic-scale imaging of a 27-nuclear-spin cluster using a quantum sensor," *Nature*, vol. 576, pp. 411–415, 2019.

[28] B. A. Myers, A. Das, M. C. Dartiailh, K. Ohno, D. D. Awschalom, and A. C. Bleszynski Jayich, "Probing surface noise with depth-calibrated spins in diamond," *Physical Review Letters*, vol. 113, p. 027602, 2014.

[29] T. Schröder, S. L. Mouradian, J. Zheng, M. E. Trusheim, M. Walsh, E. H. Chen, L. Li, I. Bayn, and D. Englund, "Quantum nanophotonics in diamond," *Journal of the Optical Society of America B*, vol. 33, no. 4, pp. B65–B83, 2016.

[30] C. Bradac, W. Gao, J. Forneris, M. E. Trusheim, and I. Aharonovich, "Quantum nanophotonics with group iv defects in diamond," *Nature Communications*, vol. 10, no. 1, p. 5625, 2019.

[31] M. K. Bhaskar, R. Riedinger, B. Machielse, D. S. Levonian, C. T. Nguyen, E. N. Knall, H. Park, D. Englund, M. Lončar, D. D. Sukachev, and M. D. Lukin, "Experimental demonstration of memory-enhanced quantum communication," *Nature*, vol. 580, no. 7801, pp. 60–64, 2020.

[32] E. N. Knall, C. M. Knaut, R. Bekenstein, D. R. Assumpcao, P. L. Stroganov, W. Gong, Y. Q. Huan, P.-J. Stas, B. Machielse, M. Chalupnik, D. Levonian, A. Suleymanzade, R. Riedinger, H. Park, M. Lončar, M. K. Bhaskar, and M. D. Lukin, "Efficient source of shaped single photons based on an integrated diamond nanophotonic system," 2022.

[33] C. T. Nguyen, D. D. Sukachev, M. K. Bhaskar, B. Machielse, D. S. Levonian, E. N. Knall, P. Stroganov, C. Chia, M. J. Burek, R. Riedinger, H. Park, M. Lončar, and M. D. Lukin, "An integrated nanophotonic quantum register based on silicon-vacancy spins in diamond," *Physical Review B*, vol. 100, p. 165428, 2019.

[34] C. T. Nguyen, D. D. Sukachev, M. K. Bhaskar, B. Machielse, D. S. Levonian, E. N. Knall, P. Stroganov, R. Riedinger, H. Park, M. Lončar, and M. D. Lukin,

"Quantum network nodes based on diamond qubits with an efficient nanophotonic interface," *Physical Review Letters*, vol. 123, p. 183602, 2019.

[35] S. Castelletto and A. Boretti, "Silicon carbide color centers for quantum applications," *Journal of Physics: Photonics*, vol. 2, no. 2, p. 022001, 2020.

[36] D. M. Lukin, M. A. Guidry, and J. Vučković, "Integrated quantum photonics with silicon carbide: Challenges and prospects," *PRX Quantum*, vol. 1, p. 020102, 2020.

[37] N. T. Son, C. P. Anderson, A. Bourassa, K. C. Miao, C. Babin, M. Widmann, M. Niethammer, J. Ul Hassan, N. Morioka, I. G. Ivanov, F. Kaiser, J. Wrachtrup, and D. D. Awschalom, "Developing silicon carbide for quantum spintronics," *Applied Physics Letters*, vol. 116, no. 19, p. 190501, 2020.

[38] D. Simin, H. Kraus, A. Sperlich, T. Ohshima, G. V. Astakhov, and V. Dyakonov, "Locking of electron spin coherence above 20 ms in natural silicon carbide," *Physical Review B*, vol. 95, p. 161201, 2017.

[39] P. Udvarhelyi, R. Nagy, F. Kaiser, S.-Y. Lee, J. Wrachtrup, and A. Gali, "Spectrally stable defect qubits with no inversion symmetry for robust spin-to-photon interface," *Physical Review Applied*, vol. 11, p. 044022, 2019.

[40] R. Nagy, M. Niethammer, M. Widmann, Y.-C. Chen, P. Udvarhelyi, C. Bonato, J. U. Hassan, R. Karhu, I. G. Ivanov, N. T. Son, J. R. Maze, T. Ohshima, Ö. O. Soykal, Á. Gali, S.-Y. Lee, F. Kaiser, and J. Wrachtrup, "High-fidelity spin and optical control of single silicon-vacancy centres in silicon carbide," *Nature Communications*, vol. 10, no. 1, p. 1954, 2019.

[41] C. Babin, R. Stöhr, N. Morioka, T. Linkewitz, T. Steidl, R. Wörnle, D. Liu, E. Hesselmeier, V. Vorobyov, A. Denisenko, M. Hentschel, C. Gobert, P. Berwian, G. V. Astakhov, W. Knolle, S. Majety, P. Saha, M. Radulaski, N. T. Son, J. Ul-Hassan, F. Kaiser, and J. Wrachtrup, "Fabrication and nanophotonic waveguide integration of silicon carbide colour centres with preserved spin-optical coherence," *Nature Materials*, vol. 21, no. 1, pp. 67–73, 2022.

[42] R. Nagy, D. B. R. Dasari, C. Babin, D. Liu, V. Vorobyov, M. Niethammer, M. Widmann, T. Linkewitz, I. Gediz, R. Stöhr, H. B. Weber, T. Ohshima, M. Ghezellou, N. T. Son, J. Ul-Hassan, F. Kaiser, and J. Wrachtrup, "Narrow inhomogeneous distribution of spin-active emitters in silicon carbide," *Applied Physics Letters*, vol. 118, no. 14, p. 144003, 2021.

[43] M. Widmann, S.-Y. Lee, T. Rendler, N. T. Son, H. Fedder, S. Paik, L.-P. Yang, N. Zhao, S. Yang, I. Booker, A. Denisenko, M. Jamali, S. A. Momenzadeh, I. Gerhardt, T. Ohshima, A. Gali, E. Janzén, and J. Wrachtrup, "Coherent control of single spins in silicon carbide at room temperature," *Nature Materials*, vol. 14, no. 2, pp. 164–168, 2015.

[44] N. Morioka, C. Babin, R. Nagy, I. Gediz, E. Hesselmeier, D. Liu, M. Joliffe, M. Niethammer, D. Dasari, V. Vorobyov, R. Kolesov, R. Stöhr, J. Ul-Hassan, N. T. Son, T. Ohshima, P. Udvarhelyi, G. Thiering, A. Gali, J. Wrachtrup, and F. Kaiser, "Spin-controlled generation of indistinguishable and distinguishable photons from silicon vacancy centres in silicon carbide," *Nature Communications*, vol. 11, no. 1, p. 2516, 2020.

[45] P. Udvarhelyi, G. Thiering, N. Morioka, C. Babin, F. Kaiser, D. Lukin, T. Ohshima, J. Ul-Hassan, N. T. Son, J. Vučković, J. Wrachtrup, and A. Gali, "Vibronic states and their effect on the temperature and strain dependence of silicon-vacancy qubits in 4*h*-SiC," *Physical Review Applied*, vol. 13, p. 054017, 2020.

[46] D. O. Bracher, X. Zhang, and E. L. Hu, "Selective purcell enhancement of two closely linked zero-phonon transitions of a silicon carbide color center," *Proceedings of the National Academy of Sciences*, vol. 114, no. 16, pp. 4060–4065, 2017.

[47] D. M. Lukin, C. Dory, M. A. Guidry, K. Y. Yang, S. D. Mishra, R. Trivedi, M. Radulaski, S. Sun, D. Vercruysse, G. H. Ahn, and J. Vučković, "4h-silicon-carbide-on-insulator for integrated quantum and nonlinear photonics," *Nature Photonics*, vol. 14, no. 5, pp. 330–334, 2020.

[48] M. A. Guidry, K. Y. Yang, D. M. Lukin, A. Markosyan, J. Yang, M. M. Fejer, and J. Vučković, "Optical parametric oscillation in silicon carbide nanophotonics," *Optica*, vol. 7, no. 9, pp. 1139–1142, 2020.

[49] E. Waks and J. Vuckovic, "Dipole induced transparency in drop-filter cavity-waveguide systems," *Physical Review Letters*, vol. 96, p. 153601, 2006.

[50] A. Reiserer and G. Rempe, "Cavity-based quantum networks with single atoms and optical photons," *Reviews of Modern Physics*, vol. 87, pp. 1379–1418, 2015.

[51] J. Borregaard, A. S. Sørensen, and P. Lodahl, "Quantum networks with deterministic spin–photon interfaces," *Advanced Quantum Technologies*, vol. 2, p. 1800091, 2019.

[52] R. E. Evans, M. K. Bhaskar, D. D. Sukachev, C. T. Nguyen, A. Sipahigil, M. J. Burek, B. Machielse, G. H. Zhang, A. S. Zibrov, E. Bielejec, H. Park, M. Lončar, and M. D. Lukin, "Photon-mediated interactions between quantum emitters in a diamond nanocavity," *Science*, vol. 362, no. 6415, pp. 662–665, 2018.

[53] S. Yamada, B.-S. Song, S. Jeon, J. Upham, Y. Tanaka, T. Asano, and S. Noda, "Second-harmonic generation in a silicon-carbide-based photonic crystal nanocavity," *Optics Letters*, vol. 39, no. 7, pp. 1768–1771, 2014.

[54] X. Shi, W. Fan, Y. Lu, A. K. Hansen, M. Chi, A. Yi, X. Ou, K. Rottwitt, and H. Ou, "Polarization and spatial mode dependent four-wave mixing in a 4h-silicon carbide microring resonator," *APL Photonics*, vol. 6, no. 7, p. 076106, 2021.

[55] Y.-C. Chen, P. S. Salter, M. Niethammer, M. Widmann, F. Kaiser, R. Nagy, N. Morioka, C. Babin, J. Erlekampf, P. Berwian, M. J. Booth, and J. Wrachtrup, "Laser writing of scalable single color centers in silicon carbide," *Nano Letters*, vol. 19, no. 4, pp. 2377–2383, 2019.

[56] J.-F. Wang, Q. Li, F.-F. Yan, H. Liu, G.-P. Guo, W.-P. Zhang, X. Zhou, L.-P. Guo, Z.-H. Lin, J.-M. Cui, X.-Y. Xu, J.-S. Xu, C.-F. Li, and G.-C. Guo, "On-demand generation of single silicon vacancy defects in silicon carbide," *ACS Photonics*, vol. 6, no. 7, pp. 1736–1743, 2019.

[57] T. Ohshima, T. Satoh, H. Kraus, G. V. Astakhov, V. Dyakonov, and P. G. Baranov, "Creation of silicon vacancy in silicon carbide by proton beam writing toward quantum sensing applications," *Journal of Physics D: Applied Physics*, vol. 51, no. 33, p. 333002, 2018.

[58] S. P. Pavunny, A. L. Yeats, H. B. Banks, E. Bielejec, R. L. Myers-Ward, M. T. DeJarld, A. S. Bracker, D. K. Gaskill, and S. G. Carter, "Arrays of si vacancies in 4h-sic produced by focused li ion beam implantation," *Scientific Reports*, vol. 11, no. 1, p. 3561, 2021.

[59] S. Majety, V. A. Norman, L. Li, M. Bell, P. Saha, and M. Radulaski, "Quantum photonics in triangular-cross-section nanodevices in silicon carbide," *Journal of Physics: Photonics*, vol. 4, p. 034008, 2021.

[60] D. M. Lukin, A. D. White, R. Trivedi, M. A. Guidry, N. Morioka, C. Babin, Ö. O. Soykal, J. Ul-Hassan, N. T. Son, T. Ohshima, P. K. Vasireddy, M. H. Nasr, S. Sun, J.-P. W. MacLean, C. Dory, E. A. Nanni, J. Wrachtrup, F. Kaiser, and J. Vučković, "Spectrally reconfigurable quantum emitters enabled by optimized fast modulation," *npj Quantum Information*, vol. 6, no. 1, p. 80, 2020.

[61] M. Rühl, L. Bergmann, M. Krieger, and H. B. Weber, "Stark tuning of the silicon vacancy in silicon carbide," *Nano Letters*, vol. 20, no. 1, pp. 658–663, 2020.

[62] N. Lo Piparo, M. Razavi, and W. J. Munro, "Memory-assisted quantum key distribution with a single nitrogen-vacancy center," *Physical Review A*, vol. 96, p. 052313, 2017.

[63] M. H. Abobeih, J. Cramer, M. A. Bakker, N. Kalb, M. Markham, D. J. Twitchen, and T. H. Taminiau, "One-second coherence for a single electron spin coupled to a multi-qubit nuclear-spin environment," *Nature Communications*, vol. 9, no. 1, p. 2552, 2018.

[64] M. A. Nielsen, "Cluster-state quantum computation," *Reports on Mathematical Physics*, vol. 57, no. 1, pp. 147–161, 2006.

[65] M. A. Ali Ahmed, G. A. Álvarez, and D. Suter, "Robustness of dynamical decoupling sequences," *Physical Review A*, vol. 87, p. 042309, 2013.

[66] T. H. Taminiau, J. J. Wagenaar, T. V. D. Sar, F. Jelezko, V. V. Dobrovitski, and R. Hanson, "Detection and control of individual nuclear spins using a weakly coupled electron spin," *Physical Review Letters*, vol. 109, p. 137602, 2012.

[67] T. H. Taminiau, J. Cramer, T. van der Sar, V. V. Dobrovitski, and R. Hanson, "Universal control and error correction in multi-qubit spin registers in diamond," *Nature Nanotechnology*, vol. 9, no. 3, pp. 171–176, 2014.

[68] P. Neumann, J. Beck, M. Steiner, F. Rempp, H. Fedder, P. R. Hemmer, J. Wrachtrup, and F. Jelezko, "Single-shot readout of a single nuclear spin," *Science*, vol. 329, no. 5991, pp. 542–544, 2010.

[69] Z. Y. Ou, S. F. Pereira, H. J. Kimble, and K. C. Peng, "Realization of the einstein-podolsky-rosen paradox for continuous variables," *Physical Review Letters*, vol. 68, pp. 3663–3666, 1992.

[70] C. Gerry, P. Knight, and P. L. Knight, *Introductory quantum optics*. Cambridge university press, 2005.

[71] J. Aasi and et. al., "Enhanced sensitivity of the ligo gravitational wave detector by using squeezed states of light," *Nature Photonics*, vol. 7, no. 8, pp. 613–619, 2013.

[72] V. Giovannetti, S. Lloyd, and L. Maccone, "Quantum-enhanced measurements: Beating the standard quantum limit," *Science*, vol. 306, no. 5700, pp. 1330–1336, 2004.

[73] R. Schnabel, "Squeezed states of light and their applications in laser interferometers," *Physics Reports*, vol. 684, pp. 1–51, 2017.

[74] X.-C. Yao, T.-X. Wang, P. Xu, H. Lu, G.-S. Pan, X.-H. Bao, C.-Z. Peng, C.-Y. Lu, Y.-A. Chen, and J.-W. Pan, "Observation of eight-photon entanglement," *Nature Photonics*, vol. 6, no. 4, pp. 225–228, 2012.

[75] J. P. Dowling and K. P. Seshadreesan, "Quantum optical technologies for metrology, sensing, and imaging," *Journal of Lightwave Technology*, vol. 33, no. 12, pp. 2359–2370, 2015.

[76] C. Riedl, C. Coletti, and U. Starke, "Structural and electronic properties of epitaxial graphene on sic(0 0 0 1): a review of growth, characterization, transfer doping and hydrogen intercalation," *Journal of Physics D: Applied Physics*, vol. 43, no. 37, p. 374009, 2010.

[77] N. Mishra, J. Boeckl, N. Motta, and F. Iacopi, "Graphene growth on silicon carbide: A review," *Physica Status Solidi A*, vol. 213, pp. 2277–2289, 2016.

[78] C. P. Anderson, A. Bourassa, K. C. Miao, G. Wolfowicz, J. Mintun, Peter, A. L. Crook, H. Abe, H. J. Ul, N. T. Son, T. Ohshima, and D. D. Awschalom, "Electrical and optical control of single spins integrated in scalable semiconductor devices," *Science*, vol. 366, no. 6470, pp. 1225–1230, 2019.

[79] A. Bourassa, C. P. Anderson, K. C. Miao, M. Onizhuk, H. Ma, A. L. Crook, H. Abe, J. Ul-Hassan, T. Ohshima, N. T. Son, G. Galli, and D. D. Awschalom, "Entanglement and control of single nuclear spins in isotopically engineered silicon carbide," *Nature Materials*, vol. 19, pp. 1319–1325, 2020.

[80] K. Jung, M. H. Abobeih, J. Yun, G. Kim, H. Oh, A. Henry, T. H. Taminiau, and D. Kim, "Deep learning enhanced individual nuclear-spin detection," *npj Quantum Information*, vol. 7, no. 1, p. 41, 2021.

[81] V. Vorobyov, S. Zaiser, N. Abt, J. Meinel, D. Dasari, P. Neumann, and J. Wrachtrup, "Quantum fourier transform for nanoscale quantum sensing," *npj Quantum Information*, vol. 7, no. 1, p. 124, 2021.

[82] J. Randall, C. Bradley, F. van der Gronden, A. Galicia, M. Abobeih, M. Markham, D. Twitchen, F. Machado, N. Yao, and T. Taminiau, "Many-body–localized discrete time crystal with a programmable spin-based quantum simulator," *Science*, vol. 374, no. 6574, pp. 1474–1478, 2021.

[83] P. Vergyris, C. Babin, R. Nold, E. Gouzien, H. Herrmann, C. Silberhorn, O. Alibart, S. Tanzilli, and F. Kaiser, "Two-photon phase-sensing with single-photon detection," *Applied Physics Letters*, vol. 117, no. 2, p. 024001, 2020.

[84] M. Bhatnagar and B. J. Baliga, "Comparison of 6h-sic, 3c-sic, and si for power devices," *IEEE Transactions on Electron Devices*, vol. 40, pp. 645–655, 1993.

[85] H. Matsunami, "Technological breakthroughs in growth control of silicon carbide for high power electronic devices," *Japanese Journal of Applied Physics*, vol. 43, no. 10, pp. 6835–6847, 2004.

[86] H. Matsunami, "Current sic technology for power electronic devices beyond si," *Microelectronic Engineering*, vol. 83, no. 1, pp. 2–4, 2006.

[87] T. Kimoto, "Material science and device physics in sic technology for high-voltage power devices," *Japanese Journal of Applied Physics*, vol. 54, no. 4, p. 040103, 2015.

[88] X. Ding, M. Du, T. Zhou, H. Guo, and C. Zhang, "Comprehensive comparison between silicon carbide mosfets and silicon igbts based traction systems for electric vehicles," *Applied Energy*, vol. 194, pp. 626–634, 2017.

[89] H. J. Round, "A note on carborundum," *Electrical World*, vol. 49, 1907.

[90] N. Zheludev, "The life and times of the led —a 100-year history," *Nature Photonics*, vol. 1, no. 4, pp. 189–192, 2007.

[91] S. Vlaskina, "Silicon carbide led," *Semiconductor Physics, Quantum Electronics and Optoelectronics*, vol. 5, pp. 71–75, 2002.

[92] R. Cheung, *Silicon Carbide Microelectromechanical Systems for Harsh Environments*. Imperial College Press.

[93] S. Karmann, R. Helbig, and R. A. Stein, "Piezoelectric properties and elastic constants of 4h and 6h sic at temperatures 4–320 k," *Journal of Applied Physics*, vol. 66, no. 8, pp. 3922–3924, 1989.

[94] M. Yamanaka, H. Daimon, E. Sakuma, S. Misawa, and S. Yoshida, "Temperature dependence of electrical properties of n-and p-type 3c-sic," *Journal of Applied Physics*, vol. 61, no. 2, pp. 599–603, 1987.

[95] A. O. Evwaraye, S. R. Smith, and W. C. Mitchel, "Shallow and deep levels in n-type 4h-sic," *Journal of Applied Physics*, vol. 79, no. 10, pp. 7726–7730, 1996.

[96] M. Widmann, M. Niethammer, D. Y. Fedyanin, I. A. Khramtsov, T. Rendler, I. D. Booker, J. Ul Hassan, N. Morioka, Y.-C. Chen, I. G. Ivanov, N. T. Son, T. Ohshima, M. Bockstedte, A. Gali, C. Bonato, S.-Y. Lee, and J. Wrachtrup, "Electrical charge state manipulation of single silicon vacancies in a silicon carbide quantum optoelectronic device," *Nano Letters*, vol. 19, no. 10, pp. 7173–7180, 2019.

[97] S. Wang, M. Zhan, G. Wang, H. Xuan, W. Zhang, C. Liu, C. Xu, Y. Liu, Z. Wei, and X. Chen, "4h-sic: a new nonlinear material for midinfrared lasers," *Laser & Photonics Reviews*, vol. 7, no. 5, pp. 831–838, 2013.

[98] H. Sato, M. Abe, I. Shoji, J. Suda, and T. Kondo, "Accurate measurements of second-order nonlinear optical coefficients of 6h and 4h silicon carbide," *Journal of the Optical Society of America B*, vol. 26, no. 10, pp. 1892–1896, 2009.

[99] P. Xing, D. Ma, K. J. A. Ooi, J. W. Choi, A. M. Agarwal, and D. Tan, "Cmos-compatible pecvd silicon carbide platform for linear and nonlinear optics," *ACS Photonics*, vol. 6, no. 5, pp. 1162–1167, 2019.

[100] A. Yi, Y. Zheng, H. Huang, J. Lin, Y. Yan, T. You, K. Huang, S. Zhang, C. Shen, M. Zhou, W. Huang, J. Zhang, S. Zhou, H. Ou, and X. Ou, "Wafer-scale 4h-silicon carbide-on-insulator (4h–sicoi) platform for nonlinear integrated optical devices," *Optical Materials*, vol. 107, 2020.

[101] D. O. Bracher and E. L. Hu, "Fabrication of high-q nanobeam photonic crystals in epitaxially grown 4h-sic," *Nano Letters*, vol. 15, no. 9, pp. 6202–6207, 2015.

[102] A. L. Crook, C. P. Anderson, K. C. Miao, A. Bourassa, H. Lee, S. L. Bayliss, D. O. Bracher, X. Zhang, H. Abe, T. Ohshima, E. L. Hu, and D. D. Awschalom, "Purcell enhancement of a single silicon carbide color center with coherent spin control," *Nano Letters*, vol. 20, no. 5, pp. 3427–3434, 2020.

[103] M. Radulaski, M. Widmann, M. Niethammer, J. L. Zhang, S.-Y. Lee, T. Rendler, K. G. Lagoudakis, N. T. Son, E. Janzén, T. Ohshima, J. Wrachtrup, and J. Vučković, "Scalable quantum photonics with single color centers in silicon carbide," *Nano Letters*, vol. 17, no. 3, pp. 1782–1786, 2017.

[104] H. Itoh, M. Yoshikawa, I. Nashiyama, L. Wei, S. Tanigawa, S. Misawa, H. Okumura, and S. Yoshida, "Defects in electron-irradiated 3c-sic epilayers observed by positron annihilation," *Hyperfine Interactions*, vol. 79, no. 1, pp. 725–729, 1993.

[105] E. Sörman, N. T. Son, W. M. Chen, O. Kordina, C. Hallin, and E. Janzén, "Silicon vacancy related defect in 4h and 6h sic," *Physical Review B*, vol. 61, pp. 2613–2620, 2000.

[106] W. F. Koehl, B. B. Buckley, F. J. Heremans, G. Calusine, and D. D. Awschalom, "Room temperature coherent control of defect spin qubits in silicon carbide," *Nature*, vol. 479, no. 7371, pp. 84–87, 2011.

[107] D. J. Christle, A. L. Falk, P. Andrich, P. V. Klimov, J. U. Hassan, N. T. Son, E. Janzén, T. Ohshima, and D. D. Awschalom, "Isolated electron spins in silicon carbide with millisecond coherence times," *Nature Materials*, vol. 14, no. 2, pp. 160–163, 2015.

[108] D. J. Christle, P. V. Klimov, C. F. de las Casas, K. Szász, V. Ivády, V. Jokubavicius, J. Ul Hassan, M. Syväjärvi, W. F. Koehl, T. Ohshima, N. T. Son, E. Janzén, A. Gali, and D. D. Awschalom, "Isolated spin qubits in sic with a high-fidelity infrared spin-to-photon interface," *Physical Review X*, vol. 7, p. 021046, 2017.

[109] Q. Li *et al.*, "Room temperature coherent manipulation of single-spin qubits in silicon carbide with a high readout contrast," *National Science Review*, 2021. nwab122.

[110] A. C. P., G. E. O., Z. Cyrus, B. Alexandre, J. Yu, Z. Yizhi, V. Christian, C. A. L., A. Hiroshi, U.-H. Jawad, O. Takeshi, S. N. T., G. Giulia, and A. D. D., "Five-second coherence of a single spin with single-shot readout in silicon carbide," *Science Advances*, vol. 8, no. 5, p. eabm5912.

[111] N. T. Son, A. Ellison, B. Magnusson, M. F. MacMillan, W. M. Chen, B. Monemar, and E. Janzén, "Photoluminescence and zeeman effect in chromium-doped 4h and 6h sic," *Journal of Applied Physics*, vol. 86, no. 8, pp. 4348–4353, 1999.

[112] W. F. Koehl, B. Diler, S. J. Whiteley, A. Bourassa, N. T. Son, E. Janzén, and D. D. Awschalom, "Resonant optical spectroscopy and coherent control of Cr^{4+} spin ensembles in sic and gan," *Physical Review B*, vol. 95, p. 035207, 2017.

[113] B. Diler, S. J. Whiteley, C. P. Anderson, G. Wolfowicz, M. E. Wesson, E. S. Bielejec, F. Joseph Heremans, and D. D. Awschalom, "Coherent control and high-fidelity readout of chromium ions in commercial silicon carbide," *npj Quantum Information*, vol. 6, no. 1, p. 11, 2020.

[114] L. Spindlberger, A. Csóré, G. Thiering, S. Putz, R. Karhu, J. Hassan, N. Son, T. Fromherz, A. Gali, and M. Trupke, "Optical properties of vanadium in 4h silicon carbide for quantum technology," *Physical Review Applied*, vol. 12, p. 014015, 2019.

[115] G. Wolfowicz, C. P. Anderson, B. Diler, O. G. Poluektov, F. J. Heremans, and D. D. Awschalom, "Vanadium spin qubits as telecom quantum emitters in silicon carbide," *Science Advances*, vol. 6, no. 18, p. eaaz1192, 2020.

[116] M. Wagner, B. Magnusson, W. M. Chen, E. Janzén, E. Sörman, C. Hallin, and J. L. Lindström, "Electronic structure of the neutral silicon vacancy in $4h$ and $6h$ sic," *Physical Review B*, vol. 62, pp. 16555–16560, 2000.

[117] E. Janzén, A. Gali, P. Carlsson, A. Gällström, B. Magnusson, and N. T. Son, "The silicon vacancy in sic," *Physica B: Condensed Matter*, vol. 404, no. 22, pp. 4354–4358, 2009.

[118] R. Nagy, M. Widmann, M. Niethammer, D. B. R. Dasari, I. Gerhardt, O. O. Soykal, M. Radulaski, T. Ohshima, J. Vučković, N. T. Son, I. G. Ivanov, S. E. Economou, C. Bonato, S.-Y. Lee, and J. Wrachtrup, "Quantum properties of dichroic silicon vacancies in silicon carbide," *Physical Review Applied*, vol. 9, p. 034022, 2018.

[119] H. B. Banks, O. O. Soykal, R. L. Myers-Ward, D. K. Gaskill, T. Reinecke, and S. G. Carter, "Resonant optical spin initialization and readout of single silicon vacancies in 4*h*-SiC," *Physical Review Applied*, vol. 11, p. 024013, 2019.

[120] I. D. Breev, Z. Shang, A. V. Poshakinskiy, H. Singh, Y. Berencén, M. Hollenbach, S. S. Nagalyuk, E. N. Mokhov, R. A. Babunts, P. G. Baranov, D. Suter, S. A. Tarasenko, G. V. Astakhov, and A. N. Anisimov, "Inverted fine structure of a 6h-sic qubit enabling robust spin-photon interface," 2021.

[121] V. Ivády, J. Davidsson, N. T. Son, T. Ohshima, I. A. Abrikosov, and A. Gali, "Identification of si-vacancy related room-temperature qubits in 4*h* silicon carbide," *Physical Review B*, vol. 96, p. 161114, 2017.

[122] H. Kraus, D. Simin, C. Kasper, Y. Suda, S. Kawabata, W. Kada, T. Honda, Y. Hijikata, T. Ohshima, V. Dyakonov, and G. V. Astakhov, "Three-dimensional proton beam writing of optically active coherent vacancy spins in silicon carbide," *Nano Letters*, vol. 17, no. 5, pp. 2865–2870, 2017.

[123] H. L. Heinisch, L. R. Greenwood, W. J. Weber, and R. E. Williford, "Displacement damage in silicon carbide irradiated in fission reactors," *Journal of Nuclear Materials*, vol. 327, no. 2, pp. 175–181, 2004.

[124] F. Fuchs, B. Stender, M. Trupke, D. Simin, J. Pflaum, V. Dyakonov, and G. V. Astakhov, "Engineering near-infrared single-photon emitters with optically active spins in ultrapure silicon carbide," *Nature Communications*, vol. 6, no. 1, p. 7578, 2015.

[125] C. Kasper, D. Klenkert, Z. Shang, D. Simin, A. Gottscholl, A. Sperlich, H. Kraus, C. Schneider, S. Zhou, M. Trupke, W. Kada, T. Ohshima, V. Dyakonov, and G. V. Astakhov, "Influence of irradiation on defect spin coherence in silicon carbide," *Physical Review Applied*, vol. 13, p. 044054, 2020.

[126] S. Castelletto, A. F. M. Almutairi, K. Kumagai, T. Katkus, Y. Hayasaki, B. C. Johnson, and S. Juodkazis, "Photoluminescence in hexagonal silicon carbide by direct femtosecond laser writing," *Optics Letters*, vol. 43, no. 24, pp. 6077–6080, 2018.

[127] O. O. Soykal, P. Dev, and S. E. Economou, "Silicon vacancy center in 4*h*-sic: Electronic structure and spin-photon interfaces," *Physical Review B*, vol. 93, p. 081207, 2016.

[128] P. G. Baranov, A. P. Bundakova, A. A. Soltamova, S. B. Orlinskii, I. V. Borovykh, R. Zondervan, R. Verberk, and J. Schmidt, "Silicon vacancy in sic as a promising quantum system for single-defect and single-photon spectroscopy," *Physical Review B*, vol. 83, p. 125203, 2011.

[129] T. C. Hain, F. Fuchs, V. A. Soltamov, P. G. Baranov, G. V. Astakhov, T. Hertel, and V. Dyakonov, "Excitation and recombination dynamics of vacancy-related spin centers in silicon carbide," *Journal of Applied Physics*, vol. 115, no. 13, p. 133508, 2014.

[130] J. S. Pelc, L. Yu, K. De Greve, P. L. McMahon, C. M. Natarajan, V. Esfandyarpour, S. Maier, C. Schneider, M. Kamp, S. Höfling, R. H. Hadfield, A. Forchel, Y. Yamamoto, and M. M. Fejer, "Downconversion quantum interface for a single quantum dot spin and 1550-nm single-photon channel," *Optics Express*, vol. 20, no. 25, pp. 27510–27519, 2012.

[131] B.-S. Song, T. Asano, S. Jeon, H. Kim, C. Chen, D. D. Kang, and S. Noda, "Ultrahigh-q photonic crystal nanocavities based on 4h silicon carbide," *Optica*, vol. 6, no. 8, pp. 991–995, 2019.

[132] K. Huang, A. Rhys, and N. F. Mott, "Theory of light absorption and non-radiative transitions in f-centres," *Proceedings of the Royal Society of London. Series A. Mathematical and Physical Sciences*, vol. 204, no. 1078, pp. 406–423, 1950.

[133] A. Gali, T. Demján, M. Vörös, G. Thiering, E. Cannuccia, and A. Marini, "Electron–vibration coupling induced renormalization in the photoemission spectrum of diamondoids," *Nature Communications*, vol. 7, no. 1, p. 11327, 2016.

[134] A. Alkauskas, B. B. Buckley, D. D. Awschalom, and C. G. Van de Walle, "First-principles theory of the luminescence lineshape for the triplet transition in diamond nv centres," *New Journal of Physics*, vol. 16, no. 7, p. 073026, 2014.

[135] Z. Shang, A. Hashemi, Y. Berencén, H.-P. Komsa, P. Erhart, S. Zhou, M. Helm, A. V. Krasheninnikov, and G. V. Astakhov, "Local vibrational modes of si vacancy spin qubits in sic," *Physical Review B*, vol. 101, p. 144109, 2020.

[136] J. A. Weil, J. R. Bolton, and J. E. Wertz, *Electron Paramagnetic Resonance: Elementary Theory and Practical Applications*. John Wiley & Sons, Inc., 1994. ISBN: 0-471-57234-9.

[137] A. Schweiger and G. Jeschke, *Principles of pulse electron paramagnetic resonance*. Oxford University Press, 2001. ISBN: 0-19-850634-1.

[138] O. O. Soykal and T. L. Reinecke, "Quantum metrology with a single spin-$\frac{3}{2}$ defect in silicon carbide," *Physical Review B*, vol. 95, p. 081405, 2017.

[139] S. B. Orlinski, J. Schmidt, E. N. Mokhov, and P. G. Baranov, "Silicon and carbon vacancies in neutron-irradiated sic: A high-field electron paramagnetic resonance study," *Physical Review B*, vol. 67, p. 125207, 2003.

[140] S. G. Carter, O. O. Soykal, P. Dev, S. E. Economou, and E. R. Glaser, "Spin coherence and echo modulation of the silicon vacancy in $4h-$SiC at room temperature," *Physical Review B*, vol. 92, p. 161202, 2015.

[141] S. A. Tarasenko, A. V. Poshakinskiy, D. Simin, V. A. Soltamov, E. N. Mokhov, P. G. Baranov, V. Dyakonov, and G. V. Astakhov, "Spin and optical properties of silicon vacancies in silicon carbide – a review," *Physica Status Solidi B*, vol. 255, p. 1700258, 2017.

[142] D. Simin, V. A. Soltamov, A. V. Poshakinskiy, A. N. Anisimov, R. A. Babunts, D. O. Tolmachev, E. N. Mokhov, M. Trupke, S. A. Tarasenko, A. Sperlich, P. G. Baranov, V. Dyakonov, and G. V. Astakhov, "All-optical dc nanotesla magnetometry using silicon vacancy fine structure in isotopically purified silicon carbide," *Physical Review X*, vol. 6, p. 031014, 2016.

[143] D. P. DiVincenzo, "The physical implementation of quantum computation," *Fortschritte der Physik*, vol. 48, no. 9-11, pp. 771–783, 2000.

[144] M. Fox, *Quantum optics: an introduction*, vol. 15 OUP Oxford, 2006.

[145] H. Bernien, B. Hensen, W. Pfaff, G. Koolstra, M. S. Blok, L. Robledo, T. H. Taminiau, M. Markham, D. J. Twitchen, L. Childress, and R. Hanson, "Heralded entanglement between solid-state qubits separated by three metres," *Nature*, vol. 497, no. 7447, pp. 86–90, 2013.

[146] E. Togan, Y. Chu, A. S. Trifonov, L. Jiang, J. Maze, L. Childress, M. V. G. Dutt, A. S. Sørensen, P. R. Hemmer, A. S. Zibrov, and M. D. Lukin, "Quantum entanglement between an optical photon and a solid-state spin qubit," *Nature*, vol. 466, no. 7307, pp. 730–734, 2010.

[147] K. Nemoto, M. Trupke, S. J. Devitt, A. M. Stephens, B. Scharfenberger, K. Buczak, T. Nöbauer, M. S. Everitt, J. Schmiedmayer, and W. J. Munro, "Photonic architecture for scalable quantum information processing in diamond," *Physical Review X*, vol. 4, p. 031022, 2014.

[148] S. Yang, Y. Wang, D. D. B. Rao, T. Hien Tran, A. S. Momenzadeh, M. Markham, D. J. Twitchen, P. Wang, W. Yang, R. Stöhr, P. Neumann, H. Kosaka, and J. Wrachtrup, "High-fidelity transfer and storage of photon states in a single nuclear spin," *Nature Photonics*, vol. 10, no. 8, pp. 507–511, 2016.

[149] D. P. Peter Lambropoulos Peter Lambropoulos, *Fundamentals of Quantum Optics and Quantum Information*. Springer-Verlag Berlin Heidelberg, 2007.

[150] J. Benhelm, G. Kirchmair, C. F. Roos, and R. Blatt, "Experimental quantum-information processing with $^{43}Ca^{+}$ ions," *Physical Review A*, vol. 77, p. 062306, 2008.

[151] X. Xu, B. Sun, P. R. Berman, D. G. Steel, A. S. Bracker, D. Gammon, and L. J. Sham, "Coherent population trapping of an electron spin in a single negatively charged quantum dot," *Nature Physics*, vol. 4, no. 9, pp. 692–695, 2008.

[152] C. G. Yale, B. B. Buckley, D. J. Christle, G. Burkard, F. J. Heremans, L. C. Bassett, and D. D. Awschalom, "All-optical control of a solid-state spin using coherent dark states," *Proceedings of the National Academy of Sciences*, vol. 110, no. 19, p. 7595, 2013.

[153] B. Pingault, J. N. Becker, C. H. H. Schulte, C. Arend, C. Hepp, T. Godde, A. I. Tartakovskii, M. Markham, C. Becher, and M. Atatüre, "All-optical formation of coherent dark states of silicon-vacancy spins in diamond," *Physical Review Letters*, vol. 113, p. 263601, 2014.

[154] GMW, "https://www.gmw.com."

[155] danfysik, "http://www.danfysik.com."

[156] C. K. Hong, Z. Y. Ou, and L. Mandel, "Measurement of subpicosecond time intervals between two photons by interference," *Physical Review Letters*, vol. 59, pp. 2044–2046, 1987.

[157] C. Santori, D. Fattal, J. Vučković, G. S. Solomon, and Y. Yamamoto, "Indistinguishable photons from a single-photon device," *Nature*, vol. 419, no. 6907, pp. 594–597, 2002.

[158] O. Gazzano, S. Michaelis de Vasconcellos, C. Arnold, A. Nowak, E. Galopin, I. Sagnes, L. Lanco, A. Lemaître, and P. Senellart, "Bright solid-state sources of indistinguishable single photons," *Nature Communications*, vol. 4, no. 1, p. 1425, 2013.

[159] M. Gschrey, A. Thoma, P. Schnauber, M. Seifried, R. Schmidt, B. Wohlfeil, L. Krüger, J. H. Schulze, T. Heindel, S. Burger, F. Schmidt, A. Strittmatter, S. Rodt, and S. Reitzenstein, "Highly indistinguishable photons from deterministic quantum-dot microlenses utilizing three-dimensional in situ electron-beam lithography," *Nature Communications*, vol. 6, no. 1, p. 7662, 2015.

[160] N. Somaschi, V. Giesz, L. De Santis, J. C. Loredo, M. P. Almeida, G. Hornecker, S. L. Portalupi, T. Grange, C. Antón, J. Demory, C. Gómez, I. Sagnes, N. D. Lanzillotti-Kimura, A. Lemaítre, A. Auffeves, A. G. White, L. Lanco, and P. Senellart, "Near-optimal single-photon sources in the solid state," *Nature Photonics*, vol. 10, no. 5, pp. 340–345, 2016.

[161] D. Fattal, K. Inoue, J. Vučković, C. Santori, G. S. Solomon, and Y. Yamamoto, "Entanglement formation and violation of bell's inequality with a semiconductor single photon source," *Physical Review Letters*, vol. 92, p. 037903, 2004.

[162] R. B. Patel, A. J. Bennett, K. Cooper, P. Atkinson, C. A. Nicoll, D. A. Ritchie, and A. J. Shields, "Quantum interference of electrically generated single photons from a quantum dot," *Nanotechnology*, vol. 21, no. 27, p. 274011, 2010.

[163] M. Rezai, J. Wrachtrup, and I. Gerhardt, "Polarization-entangled photon pairs from a single molecule," *Optica*, vol. 6, no. 1, pp. 34–40, 2019.

[164] A. V. Krukau, O. A. Vydrov, A. F. Izmaylov, and G. E. Scuseria, "Influence of the exchange screening parameter on the performance of screened hybrid functionals," *The Journal of Chemical Physics*, vol. 125, no. 22, p. 224106, 2006.

[165] J. Heyd, G. E. Scuseria, and M. Ernzerhof, "Hybrid functionals based on a screened coulomb potential," *The Journal of Chemical Physics*, vol. 118, no. 18, pp. 8207–8215, 2003.

[166] J. P. Perdew, K. Burke, and M. Ernzerhof, "Generalized gradient approximation made simple," *Physical Review Letters*, vol. 77, pp. 3865–3868, 1996.

[167] K. D. Jahnke, A. Sipahigil, J. M. Binder, M. W. Doherty, M. Metsch, L. J. Rogers, N. B. Manson, M. D. Lukin, and F. Jelezko, "Electron–phonon processes of the silicon-vacancy centre in diamond," *New Journal of Physics*, vol. 17, no. 4, p. 043011, 2015.

[168] A. Dréau, M. Lesik, L. Rondin, P. Spinicelli, O. Arcizet, J.-F. Roch, and V. Jacques, "Avoiding power broadening in optically detected magnetic resonance of single nv defects for enhanced dc magnetic field sensitivity," *Physical Review B*, vol. 84, p. 195204, 2011.

[169] V. Zwiller and G. Björk, "Improved light extraction from emitters in high refractive index materials using solid immersion lenses," *Journal of Applied Physics*, vol. 92, no. 2, pp. 660–665, 2002.

[170] P. Siyushev, F. Kaiser, V. Jacques, I. Gerhardt, S. Bischof, H. Fedder, J. Dodson, M. Markham, D. Twitchen, F. Jelezko, and J. Wrachtrup, "Monolithic diamond optics for single photon detection," *Applied Physics Letters*, vol. 97, no. 24, p. 241902, 2010.

[171] M. Jamali, I. Gerhardt, M. Rezai, K. Frenner, H. Fedder, and J. Wrachtrup, "Microscopic diamond solid-immersion-lenses fabricated around single defect centers by focused ion beam milling," *Review of Scientific Instruments*, vol. 85, no. 12, p. 123703, 2014.

[172] J. P. Hadden, J. P. Harrison, A. C. Stanley-Clarke, L. Marseglia, Y. L. D. Ho, B. R. Patton, J. L. O'Brien, and J. G. Rarity, "Strongly enhanced photon collection from diamond defect centers under microfabricated integrated solid immersion lenses," *Applied Physics Letters*, vol. 97, no. 24, p. 241901, 2010.

[173] L. Marseglia, J. P. Hadden, A. C. Stanley-Clarke, J. P. Harrison, B. Patton, Y. L. D. Ho, B. Naydenov, F. Jelezko, J. Meijer, P. R. Dolan, J. M. Smith, J. G. Rarity, and J. L. O'Brien, "Nanofabricated solid immersion lenses registered to single emitters in diamond," *Applied Physics Letters*, vol. 98, no. 13, p. 133107, 2011.

[174] F. Sardi, T. Kornher, M. Widmann, R. Kolesov, F. Schiller, T. Reindl, M. Hagel, and J. Wrachtrup, "Scalable production of solid-immersion lenses for quantum emitters in silicon carbide," *Applied Physics Letters*, vol. 117, no. 2, p. 022105, 2020.

[175] A. Sipahigil, R. E. Evans, D. D. Sukachev, M. J. Burek, J. Borregaard, M. K. Bhaskar, C. T. Nguyen, J. L. Pacheco, H. A. Atikian, C. Meuwly, R. M. Camacho, F. Jelezko, E. Bielejec, H. Park, M. Lončar, and M. D. Lukin, "An integrated diamond nanophotonics platform for quantum-optical networks," *Science*, vol. 354, no. 6314, pp. 847–850, 2016.

[176] C. Dory, D. Vercruysse, K. Y. Yang, N. V. Sapra, A. E. Rugar, S. Sun, D. M. Lukin, A. Y. Piggott, J. L. Zhang, M. Radulaski, K. G. Lagoudakis, L. Su, and J. Vučković, "Inverse-designed diamond photonics," *Nature Communications*, vol. 10, no. 1, p. 3309, 2019.

[177] M. J. Burek, C. Meuwly, R. E. Evans, M. K. Bhaskar, A. Sipahigil, S. Meesala, B. Machielse, D. D. Sukachev, C. T. Nguyen, J. L. Pacheco, E. Bielejec, M. D. Lukin, and M. Lončar, "Fiber-coupled diamond quantum nanophotonic interface," *Physical Review Applied*, vol. 8, p. 024026, 2017.

[178] E. M. Purcell, "Spontaneous emission probabilities at radio frequencies," *Physical Review*, vol. 69, pp. 674–674, 1946.

[179] H. Kaupp, C. Deutsch, H.-C. Chang, J. Reichel, T. W. Hänsch, and D. Hunger, "Scaling laws of the cavity enhancement for nitrogen-vacancy centers in diamond," *Physical Review A*, vol. 88, p. 053812, 2013.

[180] L. C. Andreani, G. Panzarini, and J.-M. Gérard, "Strong-coupling regime for quantum boxes in pillar microcavities: Theory," *Physical Review B*, vol. 60, pp. 13276–13279, 1999.

[181] L. Li, T. Schröder, E. H. Chen, M. Walsh, I. Bayn, J. Goldstein, O. Gaathon, M. E. Trusheim, M. Lu, J. Mower, M. Cotlet, M. L. Markham, D. J. Twitchen, and D. Englund, "Coherent spin control of a nanocavity-enhanced qubit in diamond," *Nature Communications*, vol. 6, no. 1, p. 6173, 2015.

[182] A. E. Rugar, C. Dory, S. Aghaeimeibodi, H. Lu, S. Sun, S. D. Mishra, Z.-X. Shen, N. A. Melosh, and J. Vučković, "Narrow-linewidth tin-vacancy centers in a diamond waveguide," *ACS Photonics*, vol. 7, no. 9, pp. 2356–2361, 2020.

[183] B.-S. Song, S. Yamada, T. Asano, and S. Noda, "Demonstration of two-dimensional photonic crystals based on silicon carbide," *Optics Express*, vol. 19, no. 12, pp. 11084–11089, 2011.

[184] G. Calusine, A. Politi, and D. D. Awschalom, "Silicon carbide photonic crystal cavities with integrated color centers," *Applied Physics Letters*, vol. 105, no. 1, p. 011123, 2014.

[185] J. Cardenas, M. Zhang, C. T. Phare, S. Y. Shah, C. B. Poitras, B. Guha, and M. Lipson, "High q sic microresonators," *Optics Express*, vol. 21, no. 14, pp. 16882–16887, 2013.

[186] T. Fan, X. Wu, A. A. Eftekhar, M. Bosi, H. Moradinejad, E. V. Woods, and A. Adibi, "High-quality integrated microdisk resonators in the visible-to-near-infrared wavelength range on a 3c-silicon carbide-on-insulator platform," *Optics Letters*, vol. 45, no. 1, pp. 153–156, 2020.

[187] D. Riedel, I. Söllner, B. J. Shields, S. Starosielec, P. Appel, E. Neu, P. Maletinsky, and R. J. Warburton, "Deterministic enhancement of coherent photon generation from a nitrogen-vacancy center in ultrapure diamond," *Physical Review X*, vol. 7, p. 031040, 2017.

[188] M. Ruf, M. Weaver, S. van Dam, and R. Hanson, "Resonant excitation and purcell enhancement of coherent nitrogen-vacancy centers coupled to a fabry-perot microcavity," *Physical Review Applied*, vol. 15, p. 024049, 2021.

[189] M. N. Gadalla, A. S. Greenspon, R. K. Defo, X. Zhang, and E. L. Hu, "Enhanced cavity coupling to silicon vacancies in 4h silicon carbide using laser irradiation and thermal annealing," *Proceedings of the National Academy of Sciences*, vol. 118, no. 12, 2021.

[190] J. T. Robinson, C. Manolatou, L. Chen, and M. Lipson, "Ultrasmall mode volumes in dielectric optical microcavities," *Physical Review Letters*, vol. 95, p. 143901, 2005.

[191] S. Hu and S. M. Weiss, "Design of photonic crystal cavities for extreme light concentration," *ACS Photonics*, vol. 3, no. 9, pp. 1647–1653, 2016.

[192] J. McKeever, A. Boca, A. D. Boozer, R. Miller, J. R. Buck, A. Kuzmich, and H. J. Kimble, "Deterministic generation of single photons from one atom trapped in a cavity," *Science*, vol. 303, no. 5666, pp. 1992–1994, 2004.

[193] J. I. Cirac, P. Zoller, H. J. Kimble, and H. Mabuchi, "Quantum state transfer and entanglement distribution among distant nodes in a quantum network," *Physical Review Letters*, vol. 78, pp. 3221–3224, 1997.

[194] L.-M. Duan and H. J. Kimble, "Scalable photonic quantum computation through cavity-assisted interactions," *Physical Review Letters*, vol. 92, p. 127902, 2004.

[195] F. Jelezko and J. Wrachtrup, "Single defect centres in diamond: A review," *Physica Status Solidi A*, vol. 203, no. 6415, pp. 3207–3225, 2006.

[196] J. Riedrich-Möller, C. Arend, C. Pauly, F. Mücklich, M. Fischer, S. Gsell, M. Schreck, and C. Becher, "Deterministic coupling of a single silicon-vacancy color center to a photonic crystal cavity in diamond," *Nano Letters*, vol. 14, no. 9, pp. 5281–5287, 2014.

[197] M. K. Koch, M. Hoese, V. Bharadwaj, J. Lang, J. P. Hadden, R. Ramponi, F. Jelezko, S. M. Eaton, and A. Kubanek, "On-chip single-photon subtraction by individual silicon vacancy centers in a laser-written diamond waveguide," 2021.

[198] J. N. Becker and C. Becher, "Coherence properties and quantum control of silicon vacancy color centers in diamond," *Physica Status Solidi (a)*, vol. 214, p. 1700586, 2017.

[199] A. Majumdar, E. D. Kim, and J. Vučković, "Effect of photogenerated carriers on the spectral diffusion of a quantum dot coupled to a photonic crystal cavity," *Physical Review B*, vol. 84, p. 195304, 2011.

[200] A. Gali and J. R. Maze, "Ab initio study of the split silicon-vacancy defect in diamond: Electronic structure and related properties," *Physical Review B*, vol. 88, p. 235205, 2013.

[201] A. Sipahigil, K. D. Jahnke, L. J. Rogers, T. Teraji, J. Isoya, A. S. Zibrov, F. Jelezko, and M. D. Lukin, "Indistinguishable photons from separated silicon-vacancy centers in diamond," *Physical Review Letters*, vol. 113, p. 113602, 2014.

[202] Y. Shen, T. M. Sweeney, and H. Wang, "Zero-phonon linewidth of single nitrogen vacancy centers in diamond nanocrystals," *Physical Review B*, vol. 77, p. 033201, 2008.

[203] H. Bernien, L. Childress, L. Robledo, M. Markham, D. Twitchen, and R. Hanson, "Two-photon quantum interference from separate nitrogen vacancy centers in diamond," *Physical Review Letters*, vol. 108, p. 043604, 2012.

[204] P. C. Humphreys, N. Kalb, J. P. J. Morits, R. N. Schouten, R. F. L. Vermeulen, D. J. Twitchen, M. Markham, and R. Hanson, "Deterministic delivery of remote entanglement on a quantum network," *Nature*, vol. 558, no. 7709, pp. 268–273, 2018.

[205] T. Ishikawa, K.-M. C. Fu, C. Santori, V. M. Acosta, R. G. Beausoleil, H. Watanabe, S. Shikata, and K. M. Itoh, "Optical and spin coherence properties of nitrogen-vacancy centers placed in a 100 nm thick isotopically purified diamond layer," *Nano Letters*, vol. 12, no. 4, pp. 2083–2087, 2012.

[206] S. Sangtawesin, B. L. Dwyer, S. Srinivasan, J. J. Allred, L. V. H. Rodgers, K. De Greve, A. Stacey, N. Dontschuk, K. M. O'Donnell, D. Hu, D. A. Evans, C. Jaye, D. A. Fischer, M. L. Markham, D. J. Twitchen, H. Park, M. D. Lukin, and N. P. de Leon, "Origins of diamond surface noise probed by correlating single-spin measurements with surface spectroscopy," *Physical Review X*, vol. 9, p. 031052, 2019.

[207] D. M. Irber, F. Poggiali, F. Kong, M. Kieschnick, T. Lühmann, D. Kwiatkowski, J. Meijer, J. Du, F. Shi, and F. Reinhard, "Robust all-optical single-shot readout of nitrogen-vacancy centers in diamond," *Nature Communications*, vol. 12, no. 1, p. 532, 2021.

[208] L. Robledo, L. Childress, H. Bernien, B. Hensen, P. F. A. Alkemade, and R. Hanson, "High-fidelity projective read-out of a solid-state spin quantum register," *Nature*, vol. 477, no. 7366, pp. 574–578, 2011.

[209] J. R. Weber, W. F. Koehl, J. B. Varley, A. Janotti, B. B. Buckley, C. G. Van de Walle, and D. D. Awschalom, "Quantum computing with defects," *Proceedings of the National Academy of Sciences*, vol. 107, no. 19, pp. 8513–8518, 2010.

[210] D. McCloskey, D. Fox, N. O'Hara, V. Usov, D. Scanlan, N. McEvoy, G. S. Duesberg, G. L. W. Cross, H. Z. Zhang, and J. F. Donegan, "Helium ion microscope generated nitrogen-vacancy centres in type ib diamond," *Applied Physics Letters*, vol. 104, no. 3, p. 031109, 2014.

[211] R. E. Evans, A. Sipahigil, D. D. Sukachev, A. S. Zibrov, and M. D. Lukin, "Narrow-linewidth homogeneous optical emitters in diamond nanostructures via silicon ion implantation," *Physical Review Applied*, vol. 5, p. 044010, 2016.

[212] R. Hanbury-Brown and R. Q. Twiss, "Correlation between photons in two coherent beams of light," *Nature*, vol. 177, no. 4497, pp. 27–29, 1956.

[213] I. Jakobi, S. A. Momenzadeh, F. F. de Oliveira, J. Michl, F. Ziem, M. Schreck, P. Neumann, A. Denisenko, and J. Wrachtrup, "Efficient creation of dipolar coupled nitrogen-vacancy spin qubits in diamond," *Journal of Physics: Conference Series*, vol. 752, no. 1, p. 012001, 2016.

[214] T. Schröder, M. E. Trusheim, M. Walsh, L. Li, J. Zheng, M. Schukraft, A. Sipahigil, R. E. Evans, D. D. Sukachev, C. T. Nguyen, J. L. Pacheco, R. M. Camacho, E. S. Bielejec, M. D. Lukin, and D. Englund, "Scalable focused ion beam creation of nearly lifetime-limited single quantum emitters in diamond nanostructures," *Nature Communications*, vol. 8, no. 1, p. 15376, 2017.

[215] W. Li, L. Wang, L. Bian, F. Dong, M. Song, J. Shao, S. Jiang, and H. Guo, "Threshold displacement energies and displacement cascades in 4h-sic: Molecular dynamic simulations," *AIP Advances*, vol. 9, no. 5, p. 055007, 2019.

[216] J. F. Ziegler, M. D. Ziegler, and J. P. Biersack, "Srim –the stopping and range of ions in matter (2010)," *Nuclear Instruments and Methods in Physics Research Section B: Beam Interactions with Materials and Atoms*, vol. 268, no. 11, pp. 1818–1823, 2010.

[217] F.-F. Yan, A.-L. Yi, J.-F. Wang, Q. Li, P. Yu, J.-X. Zhang, A. Gali, Y. Wang, J.-S. Xu, X. Ou, C.-F. Li, and G.-C. Guo, "Room-temperature coherent control of implanted defect spins in silicon carbide," *npj Quantum Information*, vol. 6, no. 1, p. 38, 2020.

[218] S. B. van Dam, M. Walsh, M. J. Degen, E. Bersin, S. L. Mouradian, A. Galiullin, M. Ruf, M. IJspeert, T. H. Taminiau, R. Hanson, and D. R. Englund, "Optical coherence of diamond nitrogen-vacancy centers formed by ion implantation and annealing," *Physical Review B*, vol. 99, p. 161203, 2019.

[219] S. Majety, P. Saha, V. A. Norman, and M. Radulaski, "Quantum information processing with integrated silicon carbide photonics," 2021.

[220] D. Hunger, T. Steinmetz, Y. Colombe, C. Deutsch, T. W. Hänsch, and J. Reichel, "A fiber fabry–perot cavity with high finesse," *New Journal of Physics*, vol. 12, no. 6, p. 065038, 2010.

[221] A. Faraon, P. E. Barclay, C. Santori, K.-M. C. Fu, and R. G. Beausoleil, "Resonant enhancement of the zero-phonon emission from a colour centre in a diamond cavity," *Nature Photonics*, vol. 5, no. 5, pp. 301–305, 2011.

[222] Y. Chu, N. P. de Leon, B. J. Shields, B. Hausmann, R. Evans, E. Togan, M. J. Burek, M. Markham, A. Stacey, A. S. Zibrov, A. Yacoby, D. J. Twitchen, M. Loncar, H. Park, P. Maletinsky, and M. D. Lukin, "Coherent optical transitions in implanted nitrogen vacancy centers," *Nano Letters*, vol. 14, no. 4, pp. 1982–1986, 2014.

[223] B. Machielse, S. Bogdanovic, S. Meesala, S. Gauthier, M. J. Burek, G. Joe, M. Chalupnik, Y. I. Sohn, J. Holzgrafe, R. E. Evans, C. Chia, H. Atikian, M. K. Bhaskar, D. D. Sukachev, L. Shao, S. Maity, M. D. Lukin, and M. Lončar, "Quantum interference of electromechanically stabilized emitters in nanophotonic devices," *Physical Review X*, vol. 9, p. 031022, 2019.

[224] N. H. Wan, T.-J. Lu, K. C. Chen, M. P. Walsh, M. E. Trusheim, L. De Santis, E. A. Bersin, I. B. Harris, S. L. Mouradian, I. R. Christen, E. S. Bielejec, and D. Englund, "Large-scale integration of artificial atoms in hybrid photonic circuits," *Nature*, vol. 583, no. 7815, pp. 226–231, 2020.

[225] E. Janitz, M. Ruf, M. Dimock, A. Bourassa, J. Sankey, and L. Childress, "Fabry-perot microcavity for diamond-based photonics," *Physical Review A*, vol. 92, p. 043844, 2015.

[226] A. P. Magyar, D. Bracher, J. C. Lee, I. Aharonovich, and E. L. Hu, "High quality sic microdisk resonators fabricated from monolithic epilayer wafers," *Applied Physics Letters*, vol. 104, no. 5, p. 051109, 2014.

[227] M. J. Burek, N. P. de Leon, B. J. Shields, B. J. M. Hausmann, Y. Chu, Q. Quan, A. S. Zibrov, H. Park, M. D. Lukin, and M. Lončar, "Free-standing mechanical and photonic nanostructures in single-crystal diamond," *Nano Letters*, vol. 12, no. 12, pp. 6084–6089, 2012.

[228] S. A. Momenzadeh, R. J. Stöhr, F. F. de Oliveira, A. Brunner, A. Denisenko, S. Yang, F. Reinhard, and J. Wrachtrup, "Nanoengineered diamond waveguide as a robust bright platform for nanomagnetometry using shallow nitrogen vacancy centers," *Nano Letters*, vol. 15, no. 1, pp. 165–169, 2015.

[229] P. Latawiec, M. J. Burek, Y.-I. Sohn, and M. Lončar, "Faraday cage angled-etching of nanostructures in bulk dielectrics," *Journal of Vacuum Science & Technology B*, vol. 34, no. 4, p. 041801, 2016.

[230] J. Liu, R. Su, Y. Wei, B. Yao, S. F. C. d. Silva, Y. Yu, J. Iles-Smith, K. Srinivasan, A. Rastelli, J. Li, and X. Wang, "A solid-state source of strongly entangled photon pairs with high brightness and indistinguishability," *Nature Nanotechnology*, vol. 14, no. 6, pp. 586–593, 2019.

[231] A. E. Rugar, S. Aghaeimeibodi, D. Riedel, C. Dory, H. Lu, P. J. McQuade, Z.-X. Shen, N. A. Melosh, and J. Vučković, "Quantum photonic interface for tin-vacancy centers in diamond," *Physical Review X*, vol. 11, p. 031021, 2021.

[232] J. L. Zhang, S. Sun, M. J. Burek, C. Dory, Y.-K. Tzeng, K. A. Fischer, Y. Kelaita, K. G. Lagoudakis, M. Radulaski, Z.-X. Shen, N. A. Melosh, S. Chu, M. Lončar, and J. Vučković, "Strongly cavity-enhanced spontaneous emission from silicon-vacancy centers in diamond," *Nano Letters*, vol. 18, no. 2, pp. 1360–1365, 2018.

[233] D. L. Moehring, P. Maunz, S. Olmschenk, K. C. Younge, D. N. Matsukevich, L. M. Duan, and C. Monroe, "Entanglement of single-atom quantum bits at a distance," *Nature*, vol. 449, no. 7158, pp. 68–71, 2007.

[234] F. A. Khan and I. Adesida, "High rate etching of sic using inductively coupled plasma reactive ion etching in sf6-based gas mixtures," *Applied Physics Letters*, vol. 75, no. 15, pp. 2268–2270, 1999.

[235] L. Jiang, R. Cheung, R. Brown, and A. Mount, "Inductively coupled plasma etching of sic in sf6/o2 and etch-induced surface chemical bonding modifications," *Journal of Applied Physics*, vol. 93, no. 3, pp. 1376–1383, 2003.

[236] M. Widmann, M. Niethammer, T. Makino, T. Rendler, S. Lasse, T. Ohshima, J. Ul Hassan, N. Tien Son, S.-Y. Lee, and J. Wrachtrup, "Bright single photon sources in lateral silicon carbide light emitting diodes," *Applied Physics Letters*, vol. 112, no. 23, p. 231103, 2018.

[237] S. J. Devitt, W. J. Munro, and K. Nemoto, "Quantum error correction for beginners," *Reports on Progress in Physics*, vol. 76, no. 7, p. 076001, 2013.

[238] M. H. Abobeih, Y. Wang, J. Randall, S. J. H. Loenen, C. E. Bradley, M. Markham, D. J. Twitchen, B. M. Terhal, and T. H. Taminiau, "Fault-tolerant operation of a logical qubit in a diamond quantum processor," 2021.

[239] L. Viola, E. Knill, and S. Lloyd, "Dynamical decoupling of open quantum systems," *Physical Review Letters*, vol. 82, pp. 2417–2421, 1999.

[240] C. A. Ryan, J. S. Hodges, and D. G. Cory, "Robust decoupling techniques to extend quantum coherence in diamond," *Physical Review Letters*, vol. 105, p. 200402, 2010.

[241] Y. Goldberg, M. Levinshtein, and S. L. Rumyantsev, *Properties of Advanced Semiconductor Materials: GaN, AIN, InN, BN, SiC, SiGe*. John Wiley & Sons, Inc., 2001. ISBN: 978-0-471-35827-5.

[242] P. Zanardi, "Symmetrizing evolutions," *Physics Letters A*, vol. 258, no. 2, pp. 77–82, 1999.

[243] Z.-H. Wang, G. de Lange, D. Ristè, R. Hanson, and V. V. Dobrovitski, "Comparison of dynamical decoupling protocols for a nitrogen-vacancy center in diamond," *Physical Review B*, vol. 85, p. 155204, 2012.

[244] T. Gullion, D. B. Baker, and M. S. Conradi, "New, compensated carr-purcell sequences," *Journal of Magnetic Resonance (1969)*, vol. 89, no. 3, pp. 479–484, 1990.

[245] H. Y. Carr and E. M. Purcell, "Effects of diffusion on free precession in nuclear magnetic resonance experiments," *Physical Review*, vol. 94, pp. 630–638, 1954.

[246] S. Meiboom and D. Gill, "Modified spin-echo method for measuring nuclear relaxation times," *Review of Scientific Instruments*, vol. 29, no. 8, pp. 688–691, 1958.

[247] L. G. Rowan, E. L. Hahn, and W. B. Mims, "Electron-spin-echo envelope modulation," *Physical Review*, vol. 137, pp. A61–A71, 1965.

[248] C. Müller, X. Kong, J. M. Cai, K. Melentijević, A. Stacey, M. Markham, D. Twitchen, J. Isoya, S. Pezzagna, J. Meijer, J. F. Du, M. B. Plenio, B. Naydenov, L. P. McGuinness, and F. Jelezko, "Nuclear magnetic resonance spectroscopy with single spin sensitivity," *Nature Communications*, vol. 5, no. 1, p. 4703, 2014.

[249] N. Aslam, M. Pfender, P. Neumann, R. Reuter, A. Zappe, F. F. de Oliveira, A. Denisenko, H. Sumiya, S. Onoda, J. Isoya, and J. Wrachtrup, "Nanoscale nuclear magnetic resonance with chemical resolution," *Science*, vol. 357, no. 6346, pp. 67–71, 2017.

[250] A. Milov, A. Ponomarev, and Y. Tsvetkov, "Electron-electron double resonance in electron spin echo: Model biradical systems and the sensitized photolysis of decalin," *Chemical Physics Letters*, vol. 110, no. 1, pp. 67–72, 1984.

[251] H. S. Knowles, D. M. Kara, and M. Atatüre, "Observing bulk diamond spin coherence in high-purity nanodiamonds," *Nature Materials*, vol. 13, no. 1, pp. 21–25, 2014.

[252] M. J. Degen, S. J. H. Loenen, H. P. Bartling, C. E. Bradley, A. L. Meinsma, M. Markham, D. J. Twitchen, and T. H. Taminiau, "Entanglement of dark electron-nuclear spin defects in diamond," *Nature Communications*, vol. 12, no. 1, p. 3470, 2021.

[253] M. Niethammer, M. Widmann, T. Rendler, N. Morioka, Y.-C. Chen, R. Stöhr, J. U. Hassan, S. Onoda, T. Ohshima, S.-Y. Lee, A. Mukherjee, J. Isoya, N. T. Son, and J. Wrachtrup, "Coherent electrical readout of defect spins in silicon carbide by photo-ionization at ambient conditions," *Nature Communications*, vol. 10, no. 1, p. 5569, 2019.

[254] B. J. Shields, Q. P. Unterreithmeier, N. P. de Leon, H. Park, and M. D. Lukin, "Efficient readout of a single spin state in diamond via spin-to-charge conversion," *Physical Review Letters*, vol. 114, p. 136402, 2015.

[255] V. Giovannetti, S. Lloyd, and L. Maccone, "Quantum metrology," *Physical Review Letters*, vol. 96, p. 010401, 2006.

[256] R. Demkowicz-Dobrzański, M. Jarzyna, and J. Kołodyński, "Quantum limits in optical inter- ferometry.," *Progress in Optics*, vol. 60, pp. 345–435, 2015.

[257] J. P. Dowling, "Quantum optical metrology –the lowdown on high-n00n states," *Contemporary Physics*, vol. 49, pp. 125–143, 03 2008.

[258] X.-C. Yao, T.-X. Wang, P. Xu, H. Lu, G.-S. Pan, X.-H. Bao, C.-Z. Peng, C.-Y. Lu, Y.-A. Chen, and J.-W. Pan, "Observation of eight-photon entanglement," *Nature Photonics*, vol. 6, no. 4, pp. 225–228, 2012.

[259] M. V. Chekhova and Z. Y. Ou, "Nonlinear interferometers in quantum optics," *Advances in Optics and Photonics*, vol. 8, no. 1, pp. 104–155, 2016.

[260] Z. Y. Ou and X. Li, "Quantum su(1,1) interferometers: Basic principles and applications," *APL Photonics*, vol. 5, no. 8, p. 080902, 2020.

[261] S. S. Szigeti, R. J. Lewis-Swan, and S. A. Haine, "Pumped-up su(1,1) interferometry," *Physical Review Letters*, vol. 118, p. 150401, 2017.

[262] T. Ono, R. Okamoto, and S. Takeuchi, "An entanglement-enhanced microscope," *Nature Communications*, vol. 4, no. 1, p. 2426, 2013.

[263] G. J. Pryde, S. Slussarenko, M. M. Weston, H. M. Chrzanowski, L. K. Shalm, V. B. Verma, and S. W. Nam, "Unconditional shot-noise-limit violation in photonic quantum metrology," in *CLEO Pacific Rim Conference 2018*, OSA Technical Digest, p. Th4J.1, Optica Publishing Group, 2018.

[264] V. Cimini, M. Mellini, G. Rampioni, M. Sbroscia, L. Leoni, M. Barbieri, and I. Gianani, "Adaptive tracking of enzymatic reactions with quantum light," *Optics Express*, vol. 27, no. 24, pp. 35245–35256, 2019.

[265] M. S. Stefszky, C. M. Mow-Lowry, S. S. Y. Chua, D. A. Shaddock, B. C. Buchler, H. Vahlbruch, A. Khalaidovski, R. Schnabel, P. K. Lam, and D. E. McClelland, "Balanced homodyne detection of optical quantum states at audio-band frequencies and below," *Classical and Quantum Gravity*, vol. 29, no. 14, p. 145015, 2012.

[266] H. Vahlbruch, M. Mehmet, K. Danzmann, and R. Schnabel, "Detection of 15 db squeezed states of light and their application for the absolute calibration of photoelectric quantum efficiency," *Physical Review Letters*, vol. 117, p. 110801, 2016.

[267] B. Yurke, S. L. McCall, and J. R. Klauder, "Su(2) and su(1,1) interferometers," *Physical Review A*, vol. 33, pp. 4033–4054, 1986.

Eidesstattliche Erklärung, Declaration on oath

Hiermit erkläre ich,Charles Babin, geboren in Chambray-lès-Tours, dass die eingereichte Dissertation zum Thema "Integrating silicon carbide spintronics quantum systems" meine eigenständig erbrachte Leistung darstellt. Ich habe ausschließlich die angegebenen Quellen und Hilfsmittel benutzt. Wörtlich oder inhaltlich aus anderen Werken übernommene Angaben habe ich als solche kenntlich gemacht. Die Richtigkeit der hier getätigten Angaben bestätige ich und versichere, nach bestem Wissen die Wahrheit erklärt zu haben.

Hiermit erkläre ich,Charles Babin, dass das von mir eingereichte pdf-Dokument zur Dissertation mit dem Thema "Integrating silicon carbide spintronics quantum systems" in Inhalt und Wortlaut der ebenfalls eingereichten Printversion meiner Dissertationsschrift entspricht.

I, Charles Babin, born at Chambray-lès-Tours, hereby declare that the dissertation submitted on the topic "Integrating silicon carbide spintronics quantum systems" constitutes my independent work.I have used only the sources and aids indicated. I have marked information taken over verbatim or in content from other works as such.I confirm the correctness of the information given here and assure that I have declared the truth to the best of my knowledge.

I, Charles Babin, hereby declare that the pdf document I submitted for the dissertation with the topic "Integrating silicon carbide spintronics quantum systems" is identical in content and wording to the print version of my dissertation paper that was also submitted.

Stuttgart, den (the) 31/01/2022

Unterschrift/Signature: Charles Babin .....

À la fin de l'envoie je touche, Cyrano de Bergerac

Abstract

As the second quantum revolution is unfolding, the investigation and development of individual quantum systems best-suited to lead this revolution is thriving. In the surge of new platforms, our work aims to decipher the role that silicon carbide's color centers could play in the near-future. In this dissertation, we demonstrate that ion-assisted implantation and integration in nanophotonic waveguides preserve the silicon vacancy center spin-optical properties. Further, high-fidelity coherent manipulation of integrated nuclear spins via decoupling sequences is shown, which is a critical resource for mutli-qubit local registers. Our work paves the way towards integration into nanophotonic resonators, overcoming the inherent low light collection efficiency of optically active spins in the solid.

Zussamenfassung

Während sich die zweite Quantenrevolution entfaltet, blüht die Forschung und Entwicklung von Quantensystemen, die am besten geeignet sind, diese Revolution anzuführen, auf. In der Flut neuer Plattformen zielt unsere Arbeit darauf ab, herauszufinden, welche Rolle Farbzentren von Siliziumkarbid in naher Zukunft spielen könnten. In dieser Dissertation zeigen wir, dass durch ionengestützte Implantation und Integration in nanophotonische Wellenleiter, die spinoptischen Eigenschaften der Silizium-Fehlstellen erhalten bleiben. Darüber hinaus wird gezeigt, dass die kohärente Manipulation integrierter Kernspins durch Entkopplungssequenzen mit hoher Genauigkeit möglich ist, was eine wichtige Ressource für lokale Mutli-Qubit-Register darstellt. Unsere Arbeit ebnet den Weg zur Integration von Silizium-Fehlstellen in nanophotonische Resonatoren, um die inhärent geringe Lichtsammeleffizienz optisch aktiver Spins im Festkörper zu überwinden.

Résumé

Alors que la deuxième révolution quantique est en cours, l'identification de systèmes quantiques isolés les mieux adaptés pour mener cette révolution bat son plein. Notre travail vise à évaluer le potentiel des centres colorés du carbure de silicium, en tant que noeuds d'un réseau de communication quantique. Dans cette thèse, nous démontrons que ni la génération des centres *lacune de silicium* par implantation d'ions ni l'intégration dans des guides d'ondes nanophotoniques ne détériorent les propriétés optique ou de spin de ces centre colorés. De plus, nous manipulons de manière cohérente des spins nucléaires spatialement confinés, via des séquences d'impulsions de découplage, étape nécessaire à la réalisation de clusters pluri-qubit locaux. Nos travaux ouvrent la voie à l'intégration de défauts cristallins dans des cavités nanophotoniques, surmontant ainsi l'inhérente faible collection de la fluorescensce émise par les atomes artificiels à l'état solide.